Characterisation of FAGE apparatus for HOx detection and application in an environmental chamber

Frank Alexander Frederick Winiberg

Submitted in accordance with the requirements for the degree of Doctor of Philosophy

The University of Leeds

School of Chemistry

The candidate confirms that the work submitted is his own and that appropriate credit has been given where reference has been made to work of others.

Acknowledgments

So this is where I’m supposed to write something nice about people…

Well… I tried.

Hello. I'm sat writing this with a large Ardmore whiskey at 1.45 am on the day before I'm going to submit, so hopefully by the end, things will still be coherent. I've been to a lot of cool places and met a load of interesting people along the way. I'm sure in the rush I'll forget someone. If it's you, then there's a blank page before this one

First and foremost, Paul and Dwayne: thank you for offering me the opportunity to stay on after my masters. I've had a load of fun within the groups and learnt a lot along the way. Hopefully I've not been too much of a burden.

Shona: You helped field far too many of my stupid questions in my first couple of years. Thanks for being my personal organiser and providing me with helpful criticism, like "yuk" and "eurgh". I didn't flounce out of the room once whilst writing up. Honest.

Jess: I honestly can't believe how patient you've been. I think I've been living in work and on my laptop for the last two years, and for some reason you've understood, let me get on with it and tried to offer me help. You're clearly as crazy as I originally thought.

Mark and Trev: Cheers for the help in the lab. A lot of time was lost on my endless questions about lasers and FAGE, I'm sure.

Pete: Cheers for giving me a place to live right at the start of my PhD dude. The North View Hostel was a fun (if cold) place to live. Oh, and the endless Blackadder quotes will never get old, despite what Jenny thinks. Maaaaah!

Mum and Dad (a.k.a Gut Bucket): I did it! All that effort you put in to raising the perfect son finally paid off… Yes I am getting a job now (hopefully). No I'm not moving home. Yes I realise so-and-so left uni and dossed around for a year and sponged of his/her parents. Please stop asking. Thanks for being so understanding this last year.

Basement guys: Thanks for making that rather Vitamin-D-deficient office a fun place to work. The random conversations and endless cups of tea and coffee have helped me develop a healthy caffeine habit. I think we definitely have more fun than that horrible Dainton lot upstairs.

Dainton people: Thanks for letting me get away from those annoying basement dwellers. They're so chatty and force me to have endless cups of tea. You guys were awesome. Pub trips and late night records/arguments/arguments about records. Fun times. The motivational dances were particularly helpful in the final weeks.

Abstract

The hydroxyl radical, OH, and the hydroperoxy radical, HO_2 (known collectively as HOx), play a key role in tropospheric chemistry and are intricately related to chemical cycles that control the concentration of greenhouse gases and have important implications for air quality. Through accurate measurements of these two important radicals, and thorough investigation of the chemical mechanisms that control their formation and removal, we can develop a better understanding of atmosphere. Simulation chambers offer the unique ability to study these processes under atmospherically relevant conditions, using a wide variety of instrumentation to probe many different species. The Highly Instrumented Reactor for Atmospheric Chemistry (HIRAC) is a stainless steel chamber based at the University of Leeds and was previously designed to operate over a range of temperatures and pressures. HIRAC was implemented to validate important oxidation mechanisms of volatile organic compounds, furthering mechanism databases, such as the Master Chemical Mechanism (MCM).

This thesis concentrates on the continued development of a dedicated HOx radical detection instrument, based on laser induced fluorescence spectroscopy at low pressure (fluorescence assay by gas expansion (FAGE)), for use in an atmospheric simulation chamber. In the field, FAGE instruments are designed to operate on board aircraft, which subject the instrument to a range of external operating pressures. Thorough characterisation and calibration of the FAGE instrument was performed using traditional methods, accounting for several factors known to affect instrument sensitivity. This calibration procedure was successfully validated using two newly developed calibration methods for OH and HO_2, which take advantage of the HIRAC chamber and its ability to operate over a range of temperatures and pressures.

After thorough calibration, the instrument was implemented in the investigation of direct OH radical production from the reaction of HO_2 with acetylperoxy radicals in the HIRAC chamber. Reactions of RO_2 radicals with HO_2 have previously been thought to be a radical sink in atmospherically pristine environments (i.e., low NOx). However, more recently, higher than anticipated concentrations of OH have been observed in areas where biogenic loadings are high. Recycling of OH from reactions of RO_2 with HO_2 could provide part of the current mechanism shortfall. Acetyl peroxy radicals are

of particular importance as they are formed directly from the oxidation of MVK, a major product of isoprene oxidation. Reported here is the first study sensitive to products from all three branching pathways of the reaction.

Table of Contents

List of Figures

Chapter 1. The tropospheric chemistry of OH and HO_2 radicals

1.1 Motivation and project aims

The study of atmospheric chemistry is extremely important in the modern world. The extent to which anthropogenic emissions are irreversibly affecting our climate and health is rapidly becoming more apparent. Pressure is being put on governments to act and kerb the rise in greenhouse gases and pollutants, with policy change is directed by complex climate models that aim to predict the future of our climate. These models rely on the various physical and chemical processes at work in our atmosphere. For example, the atmospheric lifetimes of certain greenhouse gases, particularly methane, are controlled by chemical oxidation, while anthropogenic emissions of particulate matter and gaseous species in densely populated areas have adverse effects on human health. The chemical ageing of particulates, through oxidation and photolysis, can enhance the production of further toxic products and aerosols and hence, a comprehensive understanding of the oxidative species and reactions in our atmosphere is important in furthering our ability to model future properties of the atmosphere.

The importance of the hydroxyl radical, OH, and its role in our atmosphere cannot be overstated. OH acts as the primary daytime oxidant, initiating the degradation of most trace gases emitted into the atmosphere, which can go on to form an array of secondary species, such as secondary organic aerosols (SOA). Air quality and climate are also affected by OH as it is responsible for the removal of greenhouse gases and anthropogenic pollutants emitted into the troposphere, thereby controlling the concentrations and lifetimes of many volatile organic compounds (VOCs). Hydroxyl radicals are linked to the hydroperoxy radical, HO_2, through a series of further oxidation steps that depend on the local chemistry *in situ* (see following section and Figure 1.1). These highly reactive radicals, known collectively as HOx, have short tropospheric lifetimes (~1 s and ~100 s for OH and HO_2 respectively) and their concentrations are therefore uninfluenced by transport processes. Close monitoring of HOx concentrations can therefore provide useful information on the oxidative capacity of a local environment at a specific point in time.

The high reactivity of HOx radicals results in low ambient steady state concentrations (~10^6 and ~10^8 molecule cm^{-3} for OH and HO_2 respectively) and hence detection techniques need to be highly sensitive. Several methods exist by which OH can be

measured directly and indirectly (see section 1.6), however the accuracy of these techniques is underpinned by the accuracy of the calibration processes they depend on. Validation of the calibration through alternative methods (section 1.6.1) or intercomparisons with other instruments (section 1.6.3) are therefore of vital importance.

Reproducing observed HOx concentrations using zero-dimensional box models (i.e., models where transport of species in and out of the box is not considered) is very informative and an excellent test of current chemical kinetics and mechanisms. The models are, however, only as good as the reactions and mechanisms that drive them. There are databases that have been created with the aim to review relevant chemical mechanisms and kinetics, organising the reactions in a format that can easily be applied to a range of different modelling packages. One such database is the Master Chemical Mechanism (MCM v3.2) at the University of Leeds, which contains over 17,000 reactions. As field work campaigns employ more varied detection techniques that are sensitive to a wider variety of trace species, discrepancies between measured and modelled data using the MCM highlight areas of chemistry that are poorly understood, directing future laboratory based kinetic and mechanistic studies.

Both small scale kinetic studies and larger, chamber based investigations play a key role in developing a more detailed understanding of lesser known processes over a range of atmospheric conditions. Chambers offer the advantage of multiple species detection using several detection techniques on longer timescales, bridging the gap between field work and small scale kinetic studies. Conducting experiments in atmospherically relevant gas mixtures (e.g., air, O_3, NOx, H_2O), and temperature and pressure ranges, chambers are able to control more variables than fieldwork. The Highly Instrumented Reactor for Atmospheric Chemistry (HIRAC) at Leeds is such a chamber. Temperature and pressure control has been combined with direct HOx radical detection using a dedicated Fluorescence Assay by Gas Expansion (FAGE) instrument to create a unique test-bed for atmospheric radical based chemistry and instrument development.

This thesis concentrates on the characterisation, calibration and implementation of a laser induced fluorescence (LIF) based HOx radical detection instrument using a new medium pulse repetition frequency (PRF) laser source at 200 Hz for use in an atmospheric reactor. First, the HIRAC chamber and supporting instrumentation are

discussed in chapter 2 while the HOx instrument design and operation are discussed in chapter 4. Secondly, the standard calibration procedure is described in detail in chapter 5, which has shown that low-cost medium PRF laser sources operate efficiently and at a high enough sensitivity for chamber based HOx radical measurements. The instrument was thoroughly characterised to account for the operating chamber conditions the instrument would be exposed to (e.g., pressure and temperature). The calibration and characterisation procedure was also completed with a more widely used high PRF laser light source (5 kHz) and comparisons were drawn between the two. Thirdly, using HIRAC, alternative calibration methods for both OH and HO_2 detection were developed to independently validate the instrument sensitivity as a function of pressure. This work was completed in collaboration with the University of Leeds airborne HOx detection instrument, which was able to further validate the newly developed HO_2 calibration technique. The fourth and final part of the project was to implement the instrument in the HIRAC chamber, directly detecting OH radicals in the study of the topical reaction of acetylperoxy radicals with HO_2. Central to this work was the analysis of complex convoluted FTIR spectra, for which a fitting procedure was developed to provide a free method of fast, quantitative analysis of spectra taken in the HIRAC chamber, and this is discussed in chapter 3.

1.2 Tropospheric chemistry of the hydroxyl radical: an outline

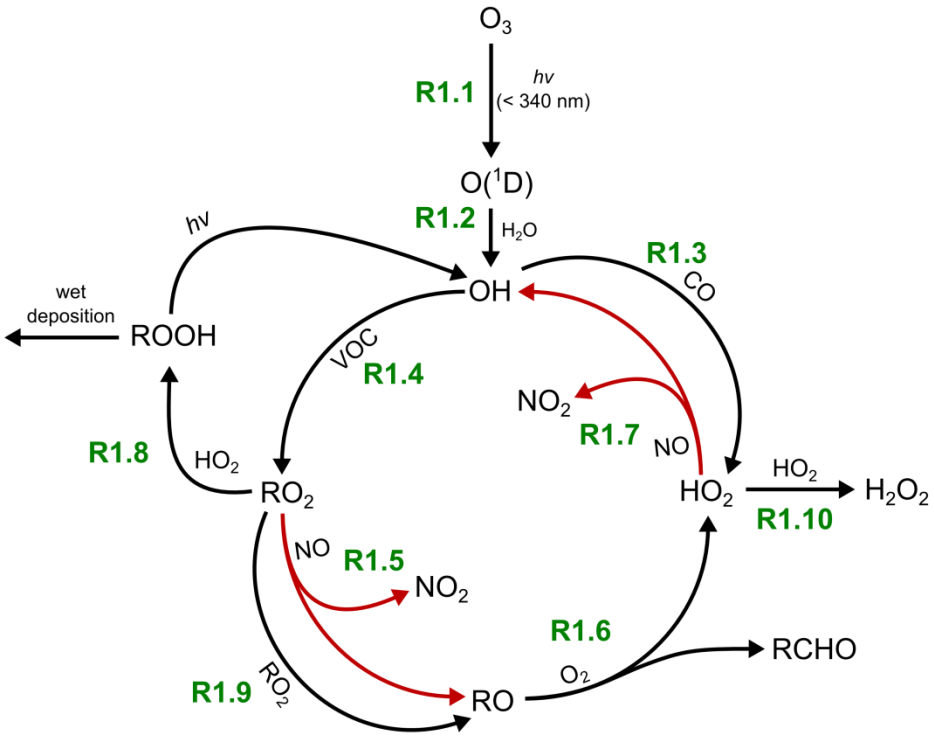

Figure 1.1: The key species and reactions involved in the closely linked chemistry of the OH and HO_2 radicals. Red arrows indicate reactions that only occur under high NOx conditions (see text for definition), and reactions described in more detail in the text are referenced in green.

A general and simplified depiction of the closely linked chemistry between the OH and HO_2 radicals is displayed in Figure 1.1, and reaction references are displayed therein. A full description of the tropospheric chemistry of OH is beyond the scope of this introduction, and has been covered in two recent reviews in the literature (Heard and Pilling, 2003; Stone et al., 2012). The main source of daytime OH is through the photolysis of O_3 ($\lambda < 340$ nm), producing $O(^1D)$, which in turn reacts with H_2O to form OH (R 1.1 - R 1.2).

$$O_3 + h\nu\ (< 340\ \text{nm}) \rightarrow O(^1D) + O_2 \qquad \text{R 1.1}$$

$$O(^1D) + H_2O \rightarrow 2OH \qquad \text{R 1.2}$$

Various reaction pathways exist for OH, including the reaction with CO to form HO_2 (R 1.3) or reaction with VOCs (RH) to form RO_2 radicals (R 1.4).

$$OH + CO\ (+O_2) \rightarrow HO_2 + CO_2 \qquad \text{R 1.3}$$

$$OH + RH + O_2 \rightarrow RO_2 + H_2O \qquad \text{R 1.4}$$

RO_2 radicals have two main destruction pathways: (i) reaction with NO and (ii) reaction with HO_2 or other RO_2 radicals. In areas where reaction with NO dominates RO_2 loss (typically when [NO] > 2×10^{10} molecule cm^{-3} or 0.8 ppbv), RO_2 radicals rapidly react with NO forming NO_2 and recycling OH (R 1.5 - R 1.7), through the creation and destruction of HO_2. NO_2 formation is extremely important in tropospheric chemistry as it is the only known source of O_3 *via* photolysis, a primary component in photochemical smog.

$$RO_2 + NO \rightarrow RO + NO_2 \qquad \text{R 1.5}$$

$$RO + O_2 \rightarrow RCHO + HO_2 \qquad \text{R 1.6}$$

$$HO_2 + NO \rightarrow OH + NO_2 \qquad \text{R 1.7}$$

However, in low NOx environments (e.g., remote forested areas), loss of RO_2 is dominated by reaction with other RO_2 and HO_2 radicals (R 1.8 and R 1.9), forming organic peroxides, ROOH, and RO radicals. R 1.8 is considered a radical loss pathway as a fraction of the peroxide formed is removed from the gas phase through wet deposition before photolysis can occur. The RO radicals generated in R 1.9 produce HO_2 as in R 1.6, however HO_2 loss is now dominated *via* self-reaction, producing H_2O_2 (R 1.10), the chemistry of which is analogous to the organic peroxide counterparts, ROOH.

$$RO_2 + HO_2 \rightarrow ROOH + O_2 \qquad \text{R 1.8}$$

$$RO_2 + RO_2 \rightarrow 2RO + O_2 \qquad \text{R 1.9}$$

$$HO_2 + HO_2 \rightarrow H_2O_2 + O_2 \qquad \text{R 1.10}$$

As mentioned previously, the high reactivity of HOx radicals leads to short atmospheric lifetimes (~1 s and ~100 s for OH and HO_2 respectively), chemistry that does not involve transport and steady state concentrations that are dependent on the balance between the sources and sinks of the local environment. Therefore, HOx measurements are indicative not only of the oxidative capacity but also of the magnitude of sources and sinks of the troposphere in a specific location (e.g., forest canopy or marine

boundary layer). More detailed information on specific sinks and sources can be gained through close examination of the comparison between measurements and computer simulated chemical models.

1.3 Comparison of field work with comprehensive reaction mechanisms

Comparisons of measurements with comprehensive chemical mechanisms help to identify potential missing sources and sinks. Models are often highly constrained to the observed concentrations of more stable, longer lived species, and spectral radiometer measurements (which are used to calculate photolysis rates). The models used often cover a wide range of oxidative chemistry and are therefore highly complex. Databases documenting thousands of reviewed reactions exist to aid model construction, depending on the application. One such database is the Master Chemical Mechanism (MCM) at the University of Leeds. The MCM v3.2 (MCM, 2014) represents ~17,000 gas phase oxidation reactions from ~6000 VOCs covering alkenes, alkanes and aromatics, to name but a few. The mechanism is constantly reviewed and new reaction schemes are added based on recent and relevant research. However, it should be noted that most of the reaction product branching ratios and kinetics are based on structural activity relationships (SARs) as not all the listed reactions have been studied directly. This does not diminish the use of the MCM in comparison to modelled data, as discrepancies between measurements and comprehensive reaction mechanisms highlight areas of atmospheric chemistry that are important and require further study. Through constant comparison between measured and modelled data, a better understanding of missing radical sources and sinks can be developed.

However, good model agreement with observed data does not necessarily mean that all chemistry has been accounted for, as misrepresentation of both HOx sources and sinks in the model could lead to a coincidental good agreement. These erroneous assignments can be improved as new detection techniques are developed, enabling a wider range of VOC speciation. This, in turn, provides a more comprehensive constraint for models to evaluate data. One such technique that has enjoyed recent success in the field is OH

reactivity, k'_{OH}. Measurements have been completed in both urban (Kovacs et al., 2003; Sadanaga et al., 2005), and forested environments (Di Carlo et al., 2004; Ingham et al., 2009; Sinha et al., 2010) and the technique has become a powerful tool in the elucidation of HOx sinks through comparison with modelled reactivities. While the comparison is useful, it is unable to provide direct confirmation of specific missing VOCs from the model mechanism.

Several field measurement campaigns have been conducted in various different environments, including: (i) the marine boundary layer, where halogenated species play a key role in the HOx cycle, (ii) polluted areas, where anthropogenic VOC and NOx emissions are high, causing large amounts of radical recycling and (iii) pristine forested environments, where VOC type, concentration and oxidation are controlled by biogenic emissions. Models have reproduced measurements with varying success and each campaign has identified new potential sources and sinks of OH and HO_2 for further investigation.

Campaigns in the marine boundary layer have been conducted to examine the effect of halogenated emissions from sea spray, seaweeds etc. on the HOx cycle, using models to better understand these interactions. Typically, NOx sources are limited in remote coastal regions and HOx chemistry is influenced by the reactions with oxygenated halogens. HO_2 can react with OX (where X = Br or I), to form HOX which can be photolysed, recycling OH and producing highly oxidative halogen atoms. The impact of this reaction was studied in the NAMBLEX campaign (North Atlantic Marine Boundary Layer Experiment) at Mace Head, Ireland (Bloss et al., 2005; Heard et al., 2006; Smith et al., 2006; Sommariva et al., 2006a; Sommariva et al., 2007). BrO, IO, OIO and I_2 were measured using DOAS (Saiz-Lopez et al., 2006) with supporting measurements of OIO and I_2 using broadband cavity ringdown spectroscopy (Bitter et al., 2005). Direct HOx detection was completed using the University of Leeds ground based FAGE instrument (Smith et al., 2006). Steady state calculations were conducted that were able to reproduce OH measurements ($[OH]_{mod}$ / $[OH]_{meas}$ = 1.04 ± 0.36), however a large discrepancy of 3.22 ± 0.69 was observed between calculated and measured HO_2. A possible cause for this over prediction was the lack of quantification of HO_2 and IO uptake on aerosol surfaces and a non-uniform distribution of iodine species in the DOAS long path cell (Smith et al., 2006), which reduced the discrepancy to 1.87 ± 0.61. Bloss et al. (2005) was able to show through calculations based on the various dominant

sinks of HO_2 in the region (reaction with IO, CH_3O_2, HO_2, NO and O_3 as well as aerosol uptake) that reaction with IO could account for ~40% of total HO_2 loss and that the HOX produced could account for 15% of the total OH production through photolysis. A comprehensive modelling study was also completed (Sommariva et al., 2006a; Sommariva et al., 2007) which reproduced OH to within 25% of measured concentrations for model runs with limited and more comprehensive representation of a wide variety of VOCs (see Figure 1.2). This demonstrates the dominance of CO, CH_4 and H_2 as OH sinks, over VOCs in the region. However, modelled concentrations of HO_2 were over predicted a factor of two, due to an underestimation in the HO_2 uptake efficiency onto aerosols.

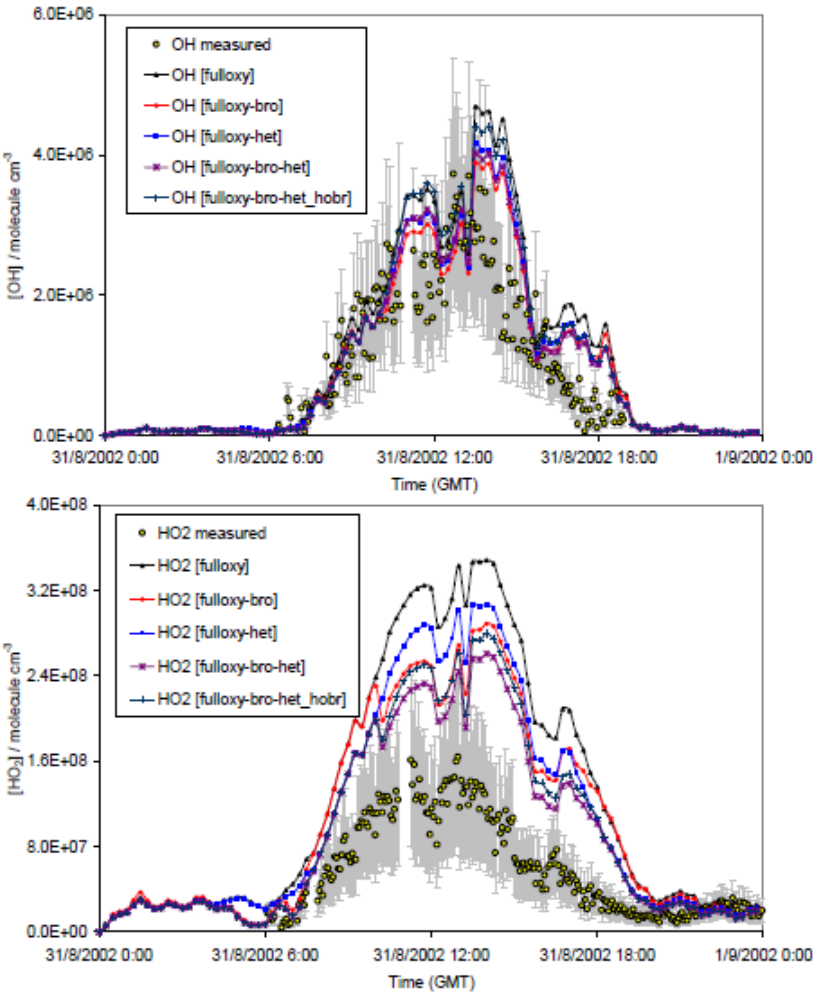

Figure 1.2: Comparison between measured and modelled HOx data taken during the NAMBLEX campaign. Yellow points represent average measured concentration with error bars indicative of uncertainties to ± 2σ. Different coloured lines are representative of models of varying complexity. Reproduced from Sommariva et al. (2006b).

Comparisons between measured HOx data and the current best understanding of reactive chemistry through the application of box models is essential to the continuing development of a better understanding of our atmosphere. The information gathered and presented drives the direction of future research. The example above showed that in remote environments, HOx levels can be reproduced using chemical models with a reasonable level of accuracy (~25 %). The largest discrepancy observed during NAMBLEX, however, corresponded to a time at which isoprene emissions were high, and this has been a particular topic of interest in other remote regions in recent years.

1.4 HOx chemistry in areas with high biogenic VOC emissions

The largest biogenic emission is isoprene (~500 Tg C $year^{-1}$), however the accurate determination of the OH oxidation mechanism remains elusive. Campaigns aimed at measuring HOx radicals in remote areas where NOx concentrations are low and biogenic VOC (BVOC) emissions are high (such as forests) have been extensively compared to box models which have highlighted large sections of unknown chemistry. Early campaigns (Cantrell et al., 1997; McKeen et al., 1997; Stevens et al., 1997) reported modelled OH concentrations approximately four times higher than those measured. A lack of HOx sinks in the chemical mechanism was responsible for the over prediction, and since then, models have consistently under predicted OH measurements where biogenic VOC emissions were high, particularly isoprene. The largest discrepancies were reported when NOx levels fell below a certain threshold (< 100 pptv) and reactivity measurements were able to show that there were still OH sinks unaccounted for in these areas. Di Carlo et al. (2004) were able to identify a missing terpene source, and inclusion of OH yields in models (Tan et al., 2001) based on existing terpene knowledge, brought the model closer to the measured values. The evidence for a correlation between high BVOCs and model underprediction of OH was growing, and other campaigns were able to show this for isoprene explicitly (Creasey et al., 2001; Tan et al., 2001; Ren et al., 2008). The implications of a missing OH source in the oxidation mechanisms of BVOCs is highly important as the dominant removal of methane, a major greenhouse gas, in equatorial regions is through reaction with OH.

Being able to predict OH is therefore crucial in our continued assessment of the CH_4 contribution to the global radiative forcing potential.

Hofzumahaus et al. (2009) showed that a box model constrained to VOC measurements was unable to account for measured OH levels in the isoprene rich environment, and a discrepancy of up to a factor of eight was reported, shown here in Figure 1.3. However, good correlation was observed between measured and modelled OH around sunrise, when NO levels were greater than 1 ppbv. Similar discrepancies were observed in the Amazonian rain forest, where comprehensive models (Butler et al., 2008; Lelieveld et al., 2008; Kubistin et al., 2010) based on the chemistry described in the MCM, significantly underestimated HOx concentrations by factors of 12.2 ± 3.3 and 3.1 ± 1.4 for OH and HO_2 respectively. These discrepancies were, again, closely correlated with the measured isoprene profile.

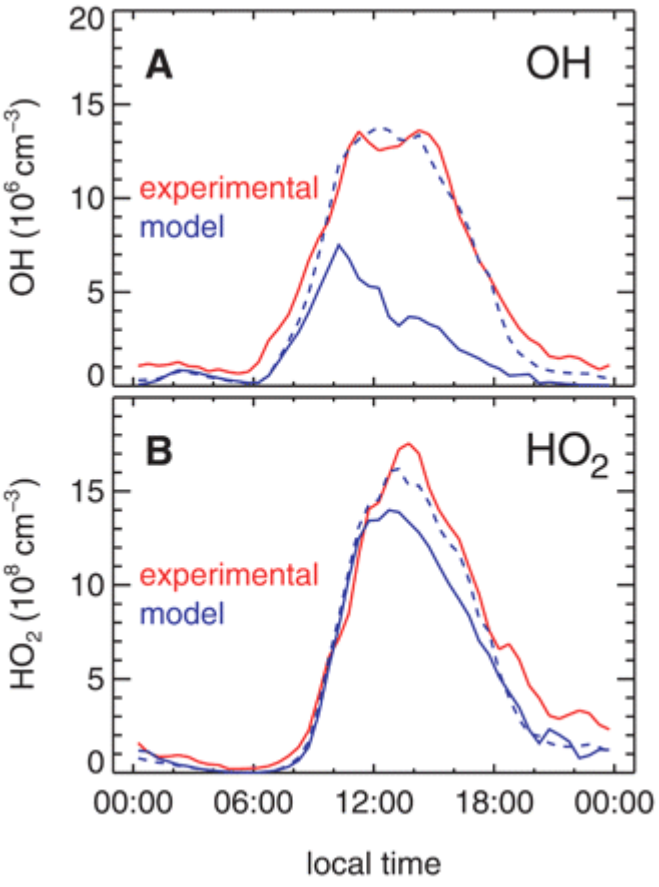

Figure 1.3: Comparison of measured and modelled OH and HO_2 from the Pearl River Delta. Reproduced from Hofzumahaus et al. (2009).

Ground based (Whalley et al., 2011) and airborne (Stone et al., 2011) HOx measurements in the Borneo rainforest (Hewitt et al., 2010) painted a similar picture, reporting a mean OH discrepancy of approximately five when isoprene concentrations were high, and NOx concentrations low. Interestingly, HO_2 concentrations were reasonably well represented by the models with a mean mod:meas ratio of 1.18, and this slight over prediction could be explained by recently reported HO_2 interference in the detection technique used (Fuchs et al., 2011). This is discussed in more detail in section 1.6.2.

Clearly, from the work examined above, there remains some uncertainty in the community as to the source of these discrepancies between measured and modelled HOx concentrations. Unlike the marine boundary layer example given in the previous section, a measurement of a wider number of species, namely BVOCs, has not enabled models to account for the low HOx concentrations under high BVOC loadings. Recycling of radicals from BVOC oxidation could help to explain the discrepancy, and the most abundant of these is isoprene. Studies into the atmospheric oxidation of isoprene could help close the gap between modelled and measured HOx concentrations. Through theoretical calculations, several mechanisms have been proposed, and chamber based studies under atmospherically relevant conditions offer an ideal environment to probe these reactions through comparisons with chemical box models. Another possible cause for the discrepancy between measured and modelled HOx concentrations could be interferences in the measurement techniques. The most common HOx measurement techniques and their validation are discussed in section 1.6.

1.5 Mechanism of the OH initiated oxidation of isoprene

The growing disparity between measured and modelled HOx concentrations has led to the novel identification of detailed isoprene oxidation mechanisms amongst the atmospheric community. These mechanisms have aimed to solve the discrepancies solely through providing a significant source of OH under high BVOC loadings. Atmospheric chambers have been instrumental in the identification of potential OH sources in VOC oxidation, as the reactions could be studied under atmospherically relevant conditions ([H_2O], [NOx] etc.) and primary and secondary oxidation products could be detected using a variety of instrumentation. A discussion of the advantages of chamber based kinetic and mechanistic studies is covered in chapter 2.

Based on direct OH measurements by Dillon and Crowley (2008), Lelieveld et al. (2008) proposed that HO_2 + RO_2 reactions could provide the missing OH source for measurements conducted in the Suriname. Production of OH from RO_2 radicals with carbonyl functionality has been inferred in several product studies (Hasson et al., 2004; Jenkin et al., 2007; Jenkin et al., 2008; Hasson et al., 2012), and the oxidation of isoprene proceeds *via* many RO_2 intermediates which could represent a significant source. Inclusion of these parameters in modelling studies improved the correlation with measured results for both OH and HO_2 in the Suriname study (Lelieveld et al., 2008; Kubistin et al., 2010), however the model included unreasonably high branching ratios for OH (200 to 400%) and Hofzumahaus et al. (2009) showed that with a more reasonable upper limit of 6%, HO_2 + RO_2 chemistry was unable to account for the total modelling shortfall observed in the Pearl River Delta. Interestingly, good correlation was observed when an NO equivalent was introduced into the model that converted HO_2 to OH without producing O_3, a method that was also found to improve model correlation with data taken by Whalley et al. (2011) in the Borneo rainforest. The accurate determination of the OH yield from RO_2 + HO_2 reactions is important, however, for the development of the understanding of the HOx budget, and chapter 7 details the recent investigation into the directly measured OH yields of acetylperoxy + HO_2 in the HIRAC chamber.

Continuing the work into reactions of HO_2 with isoprene derived RO_2 ($ISOPO_2$), Paulot et al. (2009) have conducted chamber studies into the OH initiated oxidation of isoprene-hydroxy-hydroperoxides and observed the formation of epoxide species. Epoxides were shown to regenerate OH under low NOx conditions, and supporting theoretical calculations showed that unimoleculear decomposition of the dominant β-$ISOPO_2$ radicals could produce OH (Da Silva et al., 2010). However, *ab initio* calculations predicted a slow rate of decomposition, and a faster 1,6-H shift isomerisation process was proposed by Peeters et al. (2009) which has become known as the Peeters Mechanism or Leuven Isoprene Mechanism (LIM). Isomerisation of $ISOPO_2$ radicals produces hydroperoxy-aldehydes (HPALDs). Structurally similar HPALDS to those from isoprene oxidation have been synthesised and laboratory studies have reported an OH photolysis quantum yield of ~1 (Mao et al., 2012; Wolfe et al., 2012). The subsequent products, such as peroxy-acid-aldehydes are also expected to produce OH (Peeters et al., 2009; Nguyen et al., 2010; Peeters and Muller, 2010), starting a chain that could buffer OH concentrations (Taraborrelli et al., 2012).

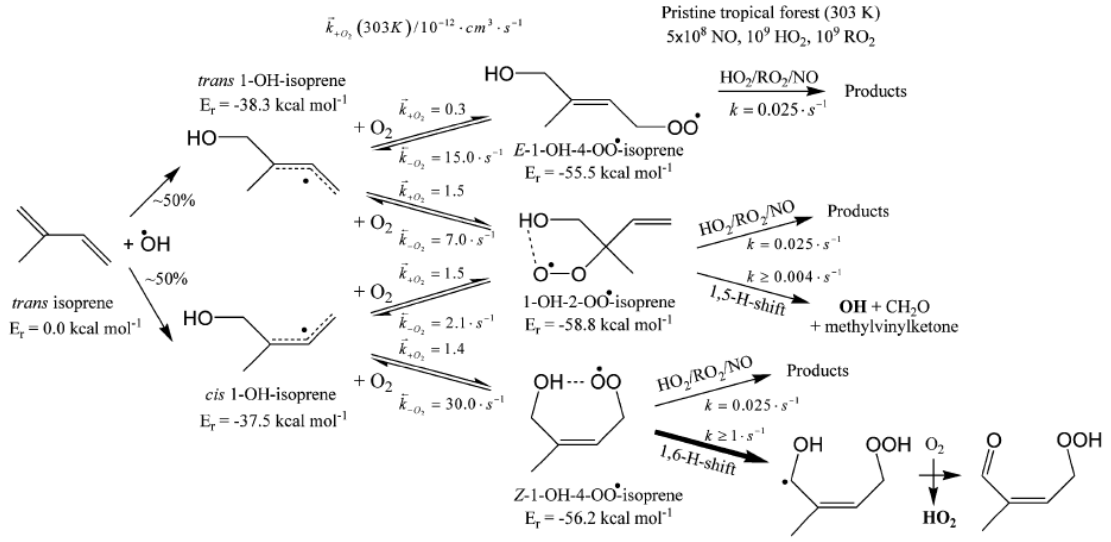

Figure 1.4: Example mechanism of HPALD production through a fast 1,6-H shift as proposed by Peeters et al. (2009) for the *cis*-1-OH-isoprene isomer. A similar pathway was also reported for the *cis*-4-OH-isoprene isomer.

Modelling based investigations have been conducted to assess the impact of these proposed mechanisms. Stavrakou et al. (2010) incorporated the LIM and epoxide formation mechanisms into an existing transport model framework and compared the results to data taken in Suriname. The epoxide formation mechanism and subsequent OH production was unable to replicate the measured OH concentrations, providing only a 25% increase in predicted OH. Using the LIM, better agreement was observed for OH (within 30% of the measured concentration). The included 1,6-H shift isomerisation of $ISOPO_2$ radicals, however, also produces HO_2 and so predicted concentrations for HO_2 were also increased by a factor of ~3. For this reason, Hofzumahaus et al. (2009) and others (Stone et al., 2011; Whalley et al., 2011) were cautious of the additional HOx formation pathways from Peeters based on the poor agreement with measured HO_2 data. Chamber based experiments have now provided evidence of the formation of HPALDs (Crounse et al., 2011), however the rate of production was estimated to be ~50 times slower than the proposed mechanism by Peeters et al. (2009).

Clearly more laboratory studies into the low NOx oxidation mechanism of isoprene are required to determine the impact of the Peeters Mechanism on OH and HO_2 yields through comparison with comprehensive chemical models. Another potential source for the discrepancies observed in the field is instrumental interference, whereby OH and HO_2 are being observed at high concentration with high isoprene loadings due to OH and HO_2 generation inside the instrument. Instrumentation used to detect HOx radicals are thoroughly characterised and calibrated before use, and a discussion on the different methods available, their validation through calibration techniques and intercomparisons, and potential interferences are discussed in the following section.

1.6 HOx radical measurement techniques

The two most common instruments used for OH radical detection at the time of writing are fluorescence assay by gas expansion (FAGE) and chemical ionisation mass spectrometry (CIMS). CIMS relies on the titration of OH to isotopically labelled $H_2{}^{34}SO_4$ with $^{34}SO_2$ (R 1.11 - R 1.13), which can be readily distinguished from the naturally occurring $H_2{}^{32}SO_4$ using mass spectrometry. $H_2{}^{34}SO_4$ is then chemically

ionised using $NO_3^-\cdot HNO_3$ cluster ions (R 1.14), produced in a separate sheath using a radioactive source and vapour phase HNO_3.

$$OH + {}^{34}SO_2 \ (+M) \rightarrow H^{34}SO_3 + O_2 \ (+M) \qquad \text{R 1.11}$$

$$H^{34}SO_3 + O_2 \rightarrow {}^{34}SO_3 + HO_2 \qquad \text{R 1.12}$$

$${}^{34}SO_3 + H_2O \ (+M) \rightarrow H_2{}^{34}SO_4 \ (+M) \qquad \text{R 1.13}$$

$$H_2{}^{34}SO_4 + NO_3^-\cdot HNO_3 \rightarrow H^{34}SO_4^-\cdot HNO_3 + HNO_3 \qquad \text{R 1.14}$$

After fragmentation of the $H^{34}SO_4^-\cdot HNO_3$ cluster using collision-induced dissociation (CID), the $H^{34}SO_4^-$ and NO_3^- ions are detected using a quadrapole mass spectrometer. The CIMS technique is extremely sensitive, offering the best detection limit of any HOx instrumentation at $< 10^5$ molecule cm^{-3} at 1 min averaging (Eisele and Tanner, 1991; Berresheim et al., 2002; Sjostedt et al., 2007; Kukui et al., 2008).

The majority of field measurements have been made using FAGE (Brune et al., 1999; Kubistin et al., 2008; Dusanter et al., 2009; Commane et al., 2010; Whalley et al., 2011), and is used in both SAPHIR and EUPHORE reactions chambers (Siese et al., 2001; Karl et al., 2004) and in the HIRAC chamber at the University of Leeds (Glowacki et al., 2007; Malkin et al., 2010). A full description of the FAGE technique and its application for measurements in the HIRAC chamber are discussed in chapter 4, and as such, only an overview will be given here. Laser induced fluorescence (LIF) spectroscopy is used to excite OH radicals at $\lambda = 308$ nm. The excited state of OH can either: (i) be collisionally quenched to the ground state or (ii) fluoresce upon relaxation, which produces a photon at the same wavelength. Operating a fluorescence cell at low pressure extends the fluorescence lifetime by reducing the number density, and hence the collisional quenching efficiency. High pulse repetition frequency (PRF) lasers are typically used (e.g., 5 kHz), however a 200 Hz PRF system has been characterised herein and is compared to two 5 kHz systems in chapters 4, 5 and 6. Typical FAGE detection limits to are $\sim 2 - 5 \times 10^5$ molecule cm^{-3} (Stone et al., 2012), however this is highly dependent on instrument design and the measurement averaging time.

Long path differential optical absorption spectroscopy (DOAS) was, until recently, used to detect OH in the field (Brauers et al., 1996; Dorn et al., 1996), however now the only instrument still in use is operated in the SAPHIR chamber (Schlosser et al., 2009).

DOAS is a direct and absolute OH measurement technique that relies on structured differential absorption spectra to act as a fingerprint for detection (Plane and Saiz-Lopez, 2006). A 0.26 nm spectral bandwidth laser light source centred around 308 nm is usually used to simultaneously monitor several OH rotational lines, and concentrations are calculated using the rearranged Beer-Lambert law, E 1.1:

$$[x] = \frac{\ln\left(\frac{I_0}{I}\right)}{\sigma_x \, l} \qquad \text{E 1.1}$$

where $[x]$ is the concentration of the target species, $\ln(I_0/I)$ is the optical density (OD), σ_x is the absorption cross-section for the species, x, and l is the pathlength of the light through the sample.

Sample spectra are analysed by removing the contribution to the OD without the laser light source (e.g., scattered light) and fitting reference spectra of absorbers in the region of 308 nm (e.g., HCHO and SO_2), before finally using an OH cross-section to calculate [OH]. The detection limit is dependent on the absorber and the pathlength and hence DOAS measurements require well collimated laser beams to be used over $l \approx 10$ km to achieve sub-pptv level detection (Plane and Saiz-Lopez, 2006).

Both CIMS and FAGE can be used to detect HO_2 indirectly through titration with NO (R 1.15), producing OH which is detected in the usual way by LIF spectroscopy.

$$HO_2 + NO \rightarrow OH + NO_2 \qquad \text{R 1.15}$$

For CIMS, the titration is conducted at ambient pressures and hence simultaneous RO_2 conversion to OH is possible and can only be limited through careful manipulation of the NO injection. Therefore, typically, CIMS measurements are reported as the sum of $[HO_2]$ and $[RO_2]$.

The deployment of the FAGE and CIMS technique for aircraft-based measurements (Eisele et al., 2001; Commane et al., 2010) raises some issues. The need to sample air from outside of the fuselage of the aircraft means that a significant length of flowtube is required before the sample is interrogated or converted, leading to potential losses. Also, the pressure in the FAGE cell will vary as the aircraft changes altitude, altering the instrumental sensitivity (Commane et al., 2010; Martinez et al., 2010) owing to changes, for example, in the nature of the initial expansion into the FAGE apparatus.

1.6.1 Calibration methods

Measurement of HOx radicals using the FAGE and CIMS techniques relies on an accurate calibration method. The standard and sole calibration technique uses the photolysis of H_2O vapour in a turbulent flow of air at 184.9 nm. An Hg lamp is used to produce OH and HO_2 through reactions R 1.16 - R 1.17:

$$H_2O + h\nu \rightarrow OH + H \qquad \text{R 1.16}$$

$$H + O_2 + M \rightarrow HO_2 + M \qquad \text{R 1.17}$$

The radicals are then sampled by the HO_x instrument at atmospheric pressure; the concentrations of OH and HO_2 produced can be determined using equation E 1.2:

$$[OH] = [HO_2] = [H_2O]\, \sigma_{H2O}\, \Phi_{OH}\, F_{184.9\,nm}\, \Delta t \qquad \text{E 1.2}$$

where $[H_2O]$ is the water vapour concentration, σ_{H2O} is the absorption cross-section of H_2O vapour at 184.9 nm, Φ_{OH} is the photodissociation quantum yield of OH and HO_2, $F_{184.9\,nm}$ is the photon flux of 184.9 nm light and Δt is the exposure time of the air to the Hg lamp output. There are two main methodologies used for obtaining the product $F_{184.9\,nm}\,\Delta t$ in equation E 1.2. In the first, $F_{184.9\,nm}$ can be measured using a calibrated phototube and Δt calculated using knowledge of the volumetric flowrate and geometric parameters of the flowtube (Stevens et al., 1994). In the second, a chemical actinometer can be used to obtain the product directly, with either O_2 or N_2O photolysis at 184.9 nm to generate either O_3 or NO respectively, both of which can be subsequently detected with reasonable sensitivity (Creasey et al., 1997; Hofzumahaus et al., 1997; Heard and Pilling, 2003; Faloona et al., 2004). The HIRAC FAGE instrument has been calibrated using H_2O vapour photolysis and the full calibration, N_2O and O_2 chemical actinometry methods are discussed in detail in chapter 5. It should be noted that the measurement of $F_{184.9\,nm}$ is very important as the total uncertainty in the calibration procedure is weighted to the greater uncertainty of the $F_{184.9\,nm}$ term (see chapter 5).

The current design of the flowtube calibration method is limited to delivering the calibrated [OH] at atmospheric pressure, however, by using different nozzle pinhole diameters (typically 0.2 – 1.0 mm) it is possible to alter the pressure in the FAGE cell over the range typically encountered during a flight or chamber experiment. This method does not compensate for the changing pressure differential across the inlet

nozzle experienced during a flight and what effect this might have on the expanding gas before it reaches the FAGE cell (Faloona et al., 2004). Potential systematic uncertainties around the application of atmospheric calibrations to HOx data obtained at low pressures highlight the need to obtain calibrations at relevant pressures.

Alternative OH calibration methods have also been developed, but typically not deployed in the field. An evaluation of calibration techniques has been presented by Dusanter et al. (2008) and examples of these will be discussed in more detail in chapter 6. In some of the earliest field measurements, Hard et al. (1995) developed a calibration method based on hydrocarbon decays upon reaction with OH. The rate of loss of a hydrocarbon (HC) is given by E 1.3:

$$-\frac{d[\mathrm{HC}]}{dt} = k[\mathrm{OH}][\mathrm{HC}] \qquad \text{E 1.3}$$

The concentration of a hydrocarbon (1,3,5-trimethylbenzene) with a known and well-characterised rate coefficient for reaction with OH, was measured as a function of time using gas chromatography allowing determination of all the parameters in E 1.3 with the exception of [OH]. This methodology has also been applied more recently to measurements in the EUPHORE chamber (Bloss et al., 2004) which were able to validate the H_2O vapour photolysis calibration method using a series of hydrocarbons. To date, no alternative HO_2 calibration methods have been reported.

Reported in chapter 6 is an intercomparison of HOx calibrations based on the flow tube methodology using different inlet nozzle diameters to vary the internal FAGE cell pressure compared to hydrocarbon decays for OH, and on the kinetics of HO_2 decay by self reaction following the photolysis of formaldehyde for HO_2. The experiments described therein aim to validate the H_2O photolysis calibration method, improving confidence in measured HOx concentrations

1.6.2 HOx measurement interferences

Until recently, the low pressure of FAGE cells was thought to limit RO_2 conversion to OH (through reactions R 1.5 - R 1.7), as the RO + O_2 reaction is slow and number density is reduced at ~1 Torr. However, Fuchs et al. (2011) and Whalley et al. (2013) have shown an appreciable conversion to OH for certain alkene and aromatic derived RO_2 radicals. Both studies have shown that the interference is highly dependent on instrument design and the concentration of NO used. Fuchs et al. (2011) was able to demonstrate that for their FAGE instrument, a change in inlet pinhole size from 0.2 to 0.4 mm increased the conversion efficiency for ethene derived RO_2 considerably from 0.17 to 0.95. The increased residence time through the FAGE cell when using the larger inlet pinhole diameter, resulted in a longer mixing time for the NO with RO_2, increasing the conversion efficiency. Whalley et al. (2013) tested the RO_2 conversion efficiency of different FAGE cell designs and found that for the ground-based FAGE cell, used previously in campaigns (Whalley et al., 2010; Whalley et al., 2011), the conversion efficiency was < 0.10 for all the RO_2 measured at NO concentrations used in the field in Borneo, validating the measured HO_2. However, for a cell of similar design to the University of Leeds aircraft and HIRAC FAGE instrument designs, interference of ethene derived RO_2 reached 0.95.

Both studies were able to show that the RO_2 conversion depends on various factors that are instrument specific such as residence time in the cell (which defines NO mixing times), the concentration of NO added to the cell, the method of injection and position of the injector (i.e., close to the HO_2 detection axis), distance of the supersonic jet expansion from the pinhole (as mixing is presumed poorer in this region) and the proximity of the walls to NO injection. These factors considered, it is likely that every instrument will have flow and NO mixing dynamics that are unique and hence determination of the RO_2 conversion efficiency for all HO_2 measurement capable FAGE cells is essential. Preliminary results for the HIRAC FAGE instrument are described in chapter 5.

Recent work by Mao et al. (2012) has identified a possible OH interference in the FAGE instrument used in a recent study of biogenic VOC oxidation in a Californian forest. Typically, measurements of background laser scatter and possible interferences from broadly absorbing species around 308 nm are accounted for by moving the laser

wavelength away from the single rotational OH transition used in LIF (see chapter 4 for a more detailed description). Mao et al. (2012) sprayed C_3F_6, perfluoropropene, just before the inlet of the FAGE instrument, which scavenged the ambient OH, creating a chemical method of measuring the "offline" signal. Comparisons showed that upon injection of C_3F_6, some OH was observed above the wavelength determined OH offline measurement. Laser generated photolysis was ruled out *via* a series of measurements and Mao et al. (2012) postulated that a BVOC was creating OH inside the instrument inlet before reaching the OH detection cell. Correcting for the interference, OH concentrations measured in the Ponderosa pine forest were reduced by up to 50%. Identification of the potential interfering species has not yet been achieved, and so it is hard to extrapolate to other environments. The interference is likely dependent on instrument design and hence all FAGE instruments may not be affected equally. The University of Leeds ground-based FAGE cells, for example, have a comparatively short inlet (~10 cm compared to ~30 cm), and hence the interference, if generated chemically, is unlikely to be as great.

As CIMS relies on the indirect measurement of OH through chemical conversion to $H_2{}^{34}SO_4$, any reactions that could lead to OH production inside the instrument could produce an enhanced positive bias. For example, the HO_2 generated in reaction R 1.12, could react with ambient O_3 or NO to produce OH, leading to a positive bias (Eisele and Tanner, 1991; Berresheim et al., 2000). The production of OH in this manner is suppressed by an injection of excess propane into the system further downstream in the reaction chamber. The propane injector is carefully positioned so that ambient OH is able to react with $^{34}SO_2$ before it encounters propane. However, any reaction that can oxidise $^{34}SO_2$ to form $^{34}SO_3$ that is not suppressed by the propane injection could lead to a positive OH bias. Recent measurements have shown that Criegee intermediates can quickly react with SO_2 (Welz et al., 2012), and have been proposed as a significant oxidant of SO_2 in the atmosphere (Mauldin et al., 2012), which could potentially lead to an interference in CIMS measurements.

1.6.3 Validation through intercomparison

Close comparison of instruments in a range of field and controlled chamber environments can help to identify potential interferences and detection biases. A ground-based intercomparison of ambient OH measurements was conducted at Fritz Peak, Colorado, between DOAS and CIMS instruments (Mount and Eisele, 1992). Results from both techniques were found to be in good agreement, and the worst discrepancy (factor of ~2 - 3) was attributed to the sampling of different air masses. A close intercomparison of airborne Penn State University (PSU) FAGE and National Centre for Atmospheric Research (NCAR) CIMS instruments has also been completed twice (Eisele et al., 2001; Eisele et al., 2003) and good agreement, within the combined uncertainty (~16%), was observed on both occasions. However, it should be noted that the studies identified a potential uncertainty in the H_2O photolysis calibration methods used as the CIMS instrument measured repeatedly higher concentrations of OH (see Figure 1.5).

Several HOx detection instruments have been compared in the HOxCOMP project conducted at the SAPHIR chamber (Schlosser et al., 2009; Fuchs et al., 2012). SAPHIR is a Teflon-made atmospheric simulation chamber equipped with a DOAS instrument to act as an absolute standard for OH measurements. The HOxCOMP comparison consisted of three FAGE and one CIMS instruments and was conducted over a range of different starting conditions, including humidity, NO and O_3. Correlations between instruments were linear with slopes between 1.01 and 1.13 and high correlation coefficients (R^2 = 0.75 - 0.96). During the campaign, HO_2 measurements between the three FAGE instruments were also compared and were found to be more variable than OH with linear slopes between 0.69 and 1.26 (R^2 = 0.82 and 0.98). Parameters were found to be in better correlation when grouped together into subsets of similar humidity, indicating a slight HO_2 measurement bias in the presence of H_2O.

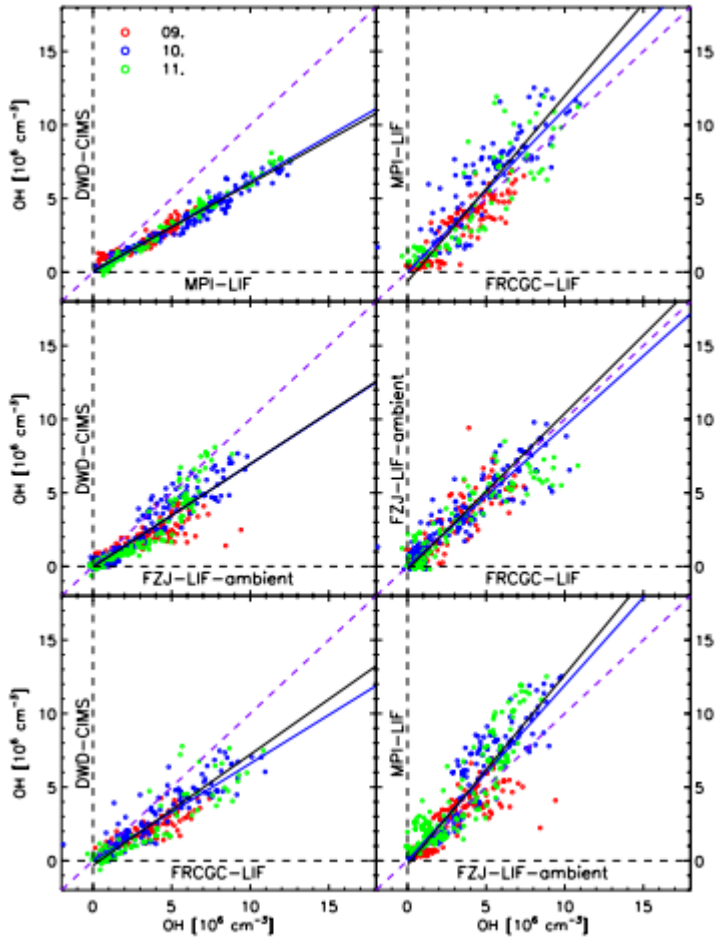

Figure 1.5: OH measurements taken during HOxCOMP at the SAPHIR chamber site using CIMS and FAGE (LIF) instrumentation. Data points represent 300 s averaged data and the dashed line represents the unity slope for comparison. FZJ = Forschungzentrum Jülich, MPI = Max Plank Institute für Chemie, FRCGC = Frontier Research for Global Change and DWD = Deutscher Wetterdienst.

1.7 References

Berresheim, H., T. Elste, C. Plass-Dülmer, F. L. Eiseleb and D. J. Tannerb (2000). "Chemical ionization mass spectrometer for long-term measurements of atmospheric OH and H2SO4." International Journal of Mass Spectrometry **202**(1-3): 91-109.

Berresheim, H., T. Elste, H. G. Tremmel, A. G. Allen, H. C. Hansson, K. Rosman, M. Dal Maso, J. M. Makela, M. Kulmala and C. D. O'Dowd (2002). "Gas-aerosol relationships of H_2SO_4, MSA, and OH: Observations in the coastal marine boundary layer at Mace Head, Ireland." Journal of Geophysical Research-Atmospheres **107**(D19): art. no.-8100.

Bitter, M., S. M. Ball, I. M. Povey and R. L. Jones (2005). "A broadband cavity ringdown spectrometer for in-situ measurements of atmospheric trace gases." Atmospheric Chemistry and Physics **5**: 2547-2560.

Bloss, W. J., J. D. Lee, C. Bloss, D. E. Heard, M. J. Pilling, K. Wirtz, M. Martin-Reviejo and M. Siese (2004). "Validation of the calibration of a laser-induced fluorescence instrument for the measurement of OH radicals in the atmosphere." Atmospheric Chemistry and Physics **4**: 571-583.

Bloss, W. J., J. D. Lee, G. P. Johnson, R. Sommariva, D. E. Heard, A. Saiz-Lopez, J. M. C. Plane, G. McFiggans, H. Coe, M. Flynn, P. Williams, A. R. Rickard and Z. L. Fleming (2005). "Impact of halogen monoxide chemistry upon boundary layer OH and HO_2 concentrations at a coastal site." Geophysical Research Letters **32**: L06814.

Brauers, T., U. Aschmutat, U. Brandenburger, H. P. Dorn, M. Hausmann, M. Hessling, A. Hofzumahaus, F. Holland, C. PlassDulmer and D. H. Ehhalt (1996). "Intercomparison of tropospheric OH radical measurements by multiple folded long-path laser absorption and laser induced fluorescence." Geophysical Research Letters **23**(18): 2545-2548.

Brune, W. H., D. Tan, I. F. Faloona, L. Jaegle, D. J. Jacob, B. G. Heikes, J. Snow, Y. Kondo, R. Shetter, G. W. Sachse, B. Anderson, G. L. Gregory, S. Vay, H. B. Singh, D. D. Davis, J. H. Crawford and D. R. Blake (1999). "OH and HO2 chemistry in the North Atlantic free troposphere." Geophysical Research Letters **26**(20): 3077-3080.

Butler, T. M., D. Taraborrelli, C. Brühl, H. Fischer, H. Harder, M. Martinez, J. Williams, M. G. Lawrence and J. Lelieveld (2008). "Improved simulation of isoprene oxidation chemistry with the ECHAM5/MESSy chemistry-climate model: lessons from the GABRIEL airborne field campaign." Atmos. Chem. Phys. **8**: 4529-4546.

Cantrell, C. A., R. E. Shetter, J. G. Calvert, F. L. Eisele, E. Williams, K. Baumann, W. H. Brune, P. S. Stevens and J. H. Mather (1997). "Peroxy radicals from photostationary state deviations and steady state calculations during the Tropospheric OH Photochemistry Experiment at Idaho Hill, Colorado, 1993." Journal of Geophysical Research-Atmospheres **102**(D5): 6369-6378.

Commane, R., C. F. A. Floquet, T. Ingham, D. Stone, M. J. Evans and D. E. Heard (2010). "Observations of OH and HO_2 radicals over West Africa." Atmospheric Chemistry and Physics **10**: 8783-8801.

Creasey, D. J., P. A. Halford-Maw, D. E. Heard, M. J. Pilling and B. J. Whitaker (1997). "Implementation and initial deployment of a field instrument for measurement of OH and HO_2 in the troposphere by laser-induced fluorescence." Journal of the Chemical Society-Faraday Transactions **93**(16): 2907-2913.

Creasey, D. J., D. E. Heard and J. D. Lee (2001). "OH and HO2 measurements in a forested region of north-western Greece." Atmospheric Environment **35**(27): 4713-4724.

Crounse, J. D., F. Paulot, H. G. Kjaergaard and P. O. Wennberg (2011). "Peroxy radical isomerization in the oxidation of isoprene." Physical Chemistry Chemical Physics **13**(30): 13607-13613.

Da Silva, G., C. Graham and Z. F. Wang (2010). "Unimolecular beta-Hydroxyperoxy Radical Decomposition with OH Recycling in the Photochemical Oxidation of Isoprene." Environmental Science & Technology **44**(1): 250-256.

Di Carlo, P., W. H. Brune, M. Martinez, H. Harder, R. Lesher, X. Ren, T. Thornberry, M. Carroll, V. Young, P. Shepson, D. Riemer, E. Apel and C. Campbell (2004). "Missing OH reactivity in a forest: Evidence for unknown reactive biogenic VOCs." Science Magazine **304**(5671): 722-725.

Dillon, T. J. and J. N. Crowley (2008). "Direct detection of OH formation in the reactions of HO_2 with $CH_3C(O)O_2$ and other substituted peroxy radicals." Atmospheric Chemistry and Physics **8**: 4877-4889.

Dorn, H. P., U. Brandenburger, T. Brauers, M. Hausmann and D. H. Ehhalt (1996). "In-situ detection of tropospheric OH radicals by folded long-path laser absorption. Results from the POPCORN field campaign in August 1994." Geophysical Research Letters **23**(18): 2537-2540.

Dusanter, S., D. Vimal and P. S. Stevens (2008). "Technical note: Measuring tropospheric OH and HO_2 by laser-induced fluorescence at low pressure. A comparison of calibration techniques." Atmospheric Chemistry and Physics **8**(2): 321-340.

Dusanter, S., D. Vimal, P. S. Stevens, R. Volkamer and L. T. Molina (2009). "Measurements of OH and HO2 concentrations during the MCMA-2006 field campaign - Part 1: Deployment of the Indiana University laser-induced fluorescence instrument." Atmospheric Chemistry and Physics **9**(5): 1665-1685.

Eisele, F., L. Mauldin, C. Cantrell, M. Zondlo, E. Apel, A. Fried, J. Walega, R. Shetter, B. Lefer, F. Flocke, A. Weinheimer, M. Avery, S. Vay, S. G., J. Podolske, G. Diskin, J. D. Barrick, H. B. Singh, W. Brune, H. Harder, M. Martinez, A. Bandy, D. Thornton, B. Heikes, Y. Kondo, D. Riemer, S. Sandholm, D. Tan, R. Talbot and J. Dibb (2003). "Summary of measurement intercomparisons during TRACE-P." J. Geophys. Res. **108**(D20): 8791-8810.

Eisele, F. L., R. L. Mauldin, D. J. Tanner, C. Cantrell, E. Kosciuch, J. B. Nowak, B. Brune, I. Faloona, D. Tan, D. D. Davis, L. Wang and G. Chen (2001). "Relationship between OH measurements on two different NASA aircraft during PEM Tropics B." Journal of Geophysical Research-Atmospheres **106**(D23): 32683-32689.

Eisele, F. L. and D. J. Tanner (1991). "Ion-Assisted Tropospheric OH Measurements." Journal of Geophysical Research-Atmospheres **96**(D5): 9295-9308.

Faloona, I. C., D. Tan, R. L. Lesher, N. L. Hazen, C. L. Frame, J. B. Simpas, H. Harder, M. Martinez, P. Di Carlo, X. R. Ren and W. H. Brune (2004). "A laser-induced fluorescence instrument for detecting tropospheric OH and HO_2: Characteristics and calibration." Journal of Atmospheric Chemistry **47**(2): 139-167.

Fuchs, H., B. Bohn, A. Hofzumahaus, F. Holland, K. D. Lu, S. Nehr, F. Rohrer and A. Wahner (2011). "Detection of HO_2 by laser-induced fluorescence: calibration and interferences from RO_2 radicals." Atmospheric Measurement Techniques **4**(6): 1209-1225.

Fuchs, H., H.-P. Dorn, M. Bachner, B. Bohn, T. Brauers, S. Gomm, A. Hofzumahaus, F. Holland, S. Nehr, F. Rohrer, R. Tillmann and A. Wahner (2012). "Comparison of OH concentration measurements by DOAS and LIF during SAPHIR chamber experiments at high OH reactivity and low NO concentration." Atmospheric Measurement Techniques **5**: 1611-1626.

Glowacki, D. R., A. Goddard, K. Hemavibool, T. L. Malkin, R. Commane, F. Anderson, W. J. Bloss, D. E. Heard, T. Ingham, M. J. Pilling and P. W. Seakins (2007). "Design of and initial results from a Highly Instrumented Reactor for Atmospheric Chemistry (HIRAC)." Atmospheric Chemistry and Physics **7**(20): 5371-5390.

Hard, T. M., L. A. George and R. J. O'Brien (1995). "FAGE Determination of Tropospheric HO and HO_2." Journal of the Atmospheric Sciences **52**(19): 3354-3372.

Hasson, A. S., G. S. Tyndall and J. J. Orlando (2004). "A product yield study of the reaction of HO_2 radicals with ethyl peroxy, acetyl peroxy and acetonyl peroxy radicals." Journal of Physical Chemistry A **108**: 5979-5989.

Hasson, A. S., G. S. Tyndall, J. J. Orlando, S. Singh, S. Q. Hernandez, S. Campbell and Y. Ibarra (2012). "Branching Ratios for the Reaction of Selected Carbonyl-Containing Peroxy Radicals with Hydroperoxy Radicals." Journal of Physical Chemistry A **116**(24): 6264-6281.

Heard, D. E. and M. J. Pilling (2003). "Measurement of OH and HO_2 in the Troposphere." Chemical Reviews **103**: 5163-5198.

Heard, D. E., K. Read, J. Methven , S. Al-Haider, W. J. Bloss, G. P. Johnson, M. J. Pilling, P. W. Seakins, S. C. Smith, R. Sommariva, J. C. Stanton, T. J. Still, B. Brooks, G. De Leeuw, A. V. Jackson, J. B. McQuaid and e. al (2006). "The North Atlantic Marine Boundary Layer Experiment (NAMBLEX). Overview of the campaign held at Mace Head, Ireland, in summer 2002." Atmospheric Chemistry and Physics **6**(8): 2241-2272.

Hewitt, C. N., J. D. Lee, A. R. MacKenzie, M. P. Barkley, N. Carslaw, G. D. Carver, N. A. Chappell, H. Coe, C. Collier, R. Commane, F. Davies, B. Davison, P. Di Carlo, C. F. Di Marco, J. R. Dorsey, P. M. Edwards, M. J. Evans, D. Fowler, K. L. Furneaux, M. Gallagher, A. Guenther, D. E. Heard, C. Helfter, J. Hopkins, T. Ingham, M. Irwin, C. Jones, A. Karunaharan, B. Langford, A. C. Lewis, S. F. Lim, S. M. MacDonald, A. S. Mahajan, S. Malpass, G. McFiggans, G. Mills, P. Misztal, S. Moller, P. S. Monks, E. Nemitz, V. Nicolas-Perea, H. Oetjen, D. E. Oram, P. I. Palmer, G. J. Phillips, R. Pike, J. M. C. Plane, T. Pugh, J. A. Pyle, C. E. Reeves, N. H. Robinson, D. Stewart, D. Stone, L. K. Whalley and X. Yin (2010). "Overview: oxidant and particle photochemical processes above a south-east Asian tropical rainforest (the OP3 project): introduction, rationale, location characteristics and tools." Atmospheric Chemistry and Physics **10**(1): 169-199.

Hofzumahaus, A., T. Brauers, U. Aschmutat, U. Brandenburger, H. P. Dorn, M. Hausmann, M. Heβling, F. Holland, C. Plass-Dulmer, M. Sedlacek, M. Weber and D. H. Ehhalt (1997). "The measurement of tropospheric OH radicals by laser-induced fluorescence spectroscopy during the POPCORN field campaign and Intercomparison of tropospheric OH radical measurements by multiple folded long-path laser absorption and laser induced fluorescence - Reply." Geophysical Research Letters **24**(23): 3039-3040.

Hofzumahaus, A., F. Rohrer, K. D. Lu, B. Bohn, T. Brauers, C. C. Chang, H. Fuchs, F. Holland, K. Kita, Y. Kondo, X. Li, S. R. Lou, M. Shao, L. M. Zeng, A. Wahner and Y. H. Zhang (2009). "Amplified Trace Gas Removal in the Troposphere." Science **324**(5935): 1702-1704.

Ingham, T., A. Goddard, L. K. Whalley, K. L. Furneaux, P. M. Edwards, C. P. Seal, D. E. Self, G. P. Johnson, K. A. Read, J. D. Lee and D. E. Heard (2009). "A flow-tube based laser-induced fluorescence instrument to measure OH reactivity in the troposphere." Atmospheric Measurement Techniques **2**(2): 465-477.

Jenkin, M. E., M. D. Hurley and T. J. Wallington (2007). "Investigation of the radical product channel of the $CH_3C(O)O_2$+HO_2 reaction in the gas phase." Physical Chemistry Chemical Physics **9**(24): 3149-3162.

Jenkin, M. E., M. D. Hurley and T. J. Wallington (2008). "Investigation of the radical product channel of the CH3C(O) CH2O2+HO2 reaction in the gas phase." Physical Chemistry Chemical Physics **10**(29): 4274-4280.

Karl, M., T. Brauers, H. P. Dorn, F. Holland, M. Komenda, D. Poppe, F. Rohrer, L. Rupp, A. Schaub and A. Wahner (2004). "Kinetic Study of the OH-isoprene and O_3-isoprene reaction in the atmosphere simulation chamber, SAPHIR." Geophysical Research Letters **31**(5): L05117.

Kovacs, T. A., W. H. Brune, H. Harder, M. Martinez, J. B. Simpas, G. J. Frost, E. Williams, T. Jobson, C. Stroud, V. Young, A. Fried and B. Wert (2003). "Direct measurements of urban OH reactivity during Nashville SOS in summer 1999." Journal of Environmental Monitoring **5**(1): 68-74.

Kubistin, D., H. Harder, M. Martinez, M. Rudolf, R. Sander, H. Bozem, G. Eerdekens, H. Fischer, C. Gurk, T. KlÃ¼pfel, R. KÃ¶nigstedt, U. Parchatka, C. L. Schiller, A. Stickler, D. Taraborrelli, J. Williams and J. Lelieveld (2008). "Hydroxyl radicals in

the tropical troposphere over the Suriname rainforest: comparison of measurements with the box model MECCA." Atmos. Chem. Phys. Discuss. **8**(4): 15239-15289.

Kubistin, D., H. Harder, M. Martinez, M. Rudolf, R. Sander, H. Bozem, G. Eerdekens, H. Fischer, C. Gurk, T. Kluepfel, R. Koenigstedt, U. Parchatka, C. L. Schiller, A. Stickler, D. Taraborrelli, J. Williams and J. Lelieveld (2010). "Hydroxyl radicals in the tropical troposphere over the Suriname rainforest: comparison of measurements with the box model MECCA." Atmospheric Chemistry and Physics **10**(19): 9705-9728.

Kukui, A., G. Ancellet and G. Le Bras (2008). "Chemical ionisation mass spectrometer for measurements of OH and Peroxy radical concentrations in moderately polluted atmospheres." Journal of Atmospheric Chemistry **61**(2): 133-154.

Lelieveld, J., T. M. Butler, J. N. Crowley, T. J. Dillon, H. Fischer, L. Ganzeveld, H. Harder, M. G. Lawrence, M. Martinez, D. Taraborrelli and J. Williams (2008). "Atmospheric oxidation capacity sustained by a tropical forest." Nature **452**(7188): 737-740.

Malkin, T. L., A. Goddard, D. E. Heard and P. W. Seakins (2010). "Measurements of OH and HO_2 yields from the gas phase ozonolysis of isoprene." Atmospheric Chemistry and Physics **10**(3): 1441-1459.

Mao, J., X. Ren, L. Zhang, D. M. Van Duin, R. C. Cohen, J. H. Park, A. H. Goldstein, F. Paulot, M. R. Beaver, J. D. Crounse, P. O. Wennberg, J. P. DiGangi, S. B. Henry, F. N. Keutsch, C. Park, G. W. Schade, G. M. Wolfe, J. A. Thornton and W. H. Brune (2012). "Insights into hydroxyl measurements and atmospheric oxidation in a California forest." Atmospheric Chemistry and Physics **12**(17): 8009-8020.

Martinez, M., H. Harder, D. Kubistin, M. Rudolf, H. Bozem, G. Eerdekens, H. Fischer, T. Klupfel, C. Gurk, R. Koenigstedt, U. Parchatka, C. L. Schiller, A. Stickler, J. Williams and J. Lelieveld (2010). "Hydroxyl radicals in the tropical troposphere over the Suriname rainforest: airborne measurements." Atmos. Chem. Phys. **10**(8): 3759-3773.

Mauldin, R. L., 3rd, T. Berndt, M. Sipila, P. Paasonen, T. Petaja, S. Kim, T. Kurten, F. Stratmann, V. M. Kerminen and M. Kulmala (2012). "A new atmospherically relevant oxidant of sulphur dioxide." Nature **488**(7410): 193-196.

McKeen, S. A., G. Mount, F. Eisele, E. Williams, J. Harder, P. Goldan, W. Kuster, S. C. Liu, K. Baumann, D. Tanner, A. Fried, S. Sewell, C. Cantrell and R. Shetter (1997). "Photochemical modelling of hydroxyl and its relationship to other species during the Tropospheric OH Photochemistry Experiment." Journal of Geophysical Research **102**(D5): 6467-6493.

MCM. (2014). "Master Chemical Mechanism Version 3.2 (http://mcm.leeds.ac.uk/MCM)."

Mount, G. H. and F. L. Eisele (1992). "An Intercomparison of Tropospheric Oh Measurements at Fritz- Peak-Observatory, Colorado." Science **256**(5060): 1187-1190.

Nguyen, T. L., L. Vereecken and J. Peeters (2010). "HOx Regeneration in the Oxidation of Isoprene III: Theoretical Study of the key Isomerisation of the Z-delta-hydroxy-peroxy Isoprene Radicals." Chemphyschem **11**(18): 3996-4001.

Paulot, F., J. D. Crounse, H. G. Kjaergaard, A. Kurten, J. M. St. Clair, J. H. Seinfeld and P. O. Wennberg (2009). "Unexpected Epoxide Formation in the Gas-Phase Photooxidation of Isoprene." Science **325**: 730-733.

Peeters, J. and J. F. Muller (2010). "HOx radical regeneration in isoprene oxidation via peroxy radical isomerisations. II: experimental evidence and global impact." Physical Chemistry Chemical Physics **12**(42): 14227-14235.

Peeters, J., T. L. Nguyen and L. Vereecken (2009). "HOx radical regeneration in the oxidation of isoprene." Physical Chemistry Chemical Physics **11**(28): 5935-5939.

Plane, J. M. C. and A. Saiz-Lopez (2006). Analytical Techniques for Atmospheric Measurement, Edited by Heard, D. E.: Chapter 3 UV-Visible Differential Optical Absorption Spectroscopy (DOAS), Blackwell.

Ren, X., J. R. Olson, J. H. Crawford, W. H. Brune, J. Mao, R. B. Long, Z. Chen, G. Chen, M. A. Avery, G. W. Sachse, J. D. Barrick, G. S. Diskin, L. G. Huey, A. Fried, R. C. Cohen, B. Heikes, P. O. Wennberg, H. B. Singh, D. R. Blake and R. E. Shetter (2008). "HO_x chemistry during INTEX-A 2004: Observation, model, calculation, and comparison with previous studies." Journal of Geophysical Research **113**(D05310).

Sadanaga, Y., A. Yoshino, K. Shungo and K. Yoshizumi (2005). "Measurements of OH Reactivity and Photochemical Ozone Production in the Urban Atmosphere." Environmental Science & Technology **39**(22): 8847-8852.

Saiz-Lopez, A., J. A. Shillito, H. Coe and J. M. C. Plane (2006). "Measurements and modelling of I-2, IO, OIO, BrO and NO3 in the mid-latitude marine boundary layer." Atmospheric Chemistry and Physics **6**: 1513-1528.

Schlosser, E., T. Brauers, H. P. Dorn, H. Fuchs, R. Haseler, A. Hofzumahaus, F. Holland, A. Wahner, Y. Kanaya, Y. Kajii, K. Miyamoto, S. Nishida, K. Watanabe, A. Yoshino, D. Kubistin, M. Martinez, M. Rudolf, H. Harder, H. Berresheim, T. Elste, C. Plass-Dulmer, G. Stange and U. Schurath (2009). "Technical Note: Formal blind intercomparison of OH measurements: results from the international campaign HOxComp." Atmospheric Chemistry and Physics **9**(20): 7923-7948.

Siese, M., K. H. Becker, K. J. Brockmann, H. Geiger, A. Hofzumahaus, F. Holland, D. Mihelcic and K. Wirtz (2001). "Direct measurement of OH radicals from ozonolysis of selected alkenes: A EUPHORE simulation chamber study." Environmental Science & Technology **35**(23): 4660-4667.

Sinha, V., J. Williams, J. Lelieveld, T. M. Ruuskanen, M. K. Kajos, J. Patokoski, H. Hellen, H. Hakola, D. Mogensen, M. Boy, J. Rinner and M. Kulmala (2010). "OH Reactivity Measurements within a Boreal Forest: Evidence for Unknown Reactive Emissions." Environ. Sci. Technol. **44**: 6614-6620.

Sjostedt, S. J., L. G. Huey, D. J. Tanner, J. Peischl, G. Chen, J. E. Dibb, B. Lefer, M. A. Hutterli, A. J. Beyersdorf, N. J. Blake, D. R. Blake, D. Sueper, T. Ryerson, J.

Burkhart and A. Stohl (2007). "Observations of hydroxyl and the sum of peroxy radicals at Summit, Greenland during summer 2003." Atmospheric Environment **41**(24): 5122-5137.

Smith, S. C., J. D. Lee, W. J. Bloss, G. P. Johnson, T. Ingham and D. E. Heard (2006). "Concentrations of OH and HO2 during NAMBLEX: measurements and steady state analysis." Atmospheric Chemistry and Physics **6**: 1435-1453.

Sommariva, R., W. J. Bloss, N. Brough, N. Carslaw, M. Flynn, A.-L. Haggerstone, D. E. Heard, J. R. Hopkins, J. D. Lee, A. C. Lewis, G. McFiggans, P. S. Monks, S. A. Penkett, M. J. Pilling, J. M. C. Plane, K. A. Read, A. Saiz-Lopez, A. R. Rickard and P. I. Williams (2006a). "OH and HO2 chemistry during NAMBLEX: roles of oxygenates, halogen oxides and heterogeneous uptake." Atmospheric Chemistry and Physics **6**(4): 1135-1153.

Sommariva, R., W. J. Bloss, N. Brough, N. Carslaw, M. Flynn, A. L. Haggerstone, D. E. Heard, J. R. Hopkins, J. D. Lee, A. C. Lewis, G. McFiggans, P. S. Monks, S. A. Penkett, M. J. Pilling, J. M. C. Plane, K. A. Read, A. Saiz-Lopez, A. R. Rickard and P. I. Williams (2006b). "OH and HO2 chemistry during NAMBLEX: roles of oxygenates, halogen oxides and heterogeneous uptake." Atmospheric Chemistry and Physics **6**: 1135-1153.

Sommariva, R., M. J. Pilling, W. J. Bloss, D. E. Heard, J. D. Lee, Z. L. Fleming, P. S. Monks, J. M. C. Plane, A. Saiz-Lopez, S. M. Ball, M. Bitter, R. L. Jones, N. Brough, S. A. Penkett, J. R. Hopkins, A. C. Lewis and K. A. Read (2007). "Night-time radical chemistry during the NAMBLEX campaign." Atmospheric Chemistry and Physics **7**: 587-598.

Stavrakou, T., J. Peeters and J. F. Müller (2010). "Improved global modelling of HOx recycling in isoprene oxidation: evaluation against the GABRIEL and INTEX-A aircraft campaign measurements." Atmospheric Chemistry and Physics **10**(20): 9863-6878.

Stevens, P. S., J. H. Mather and W. H. Brune (1994). "Measurement of Tropospheric OH and HO_2 by Laser-Induced Fluorescence at Low-Pressure." Journal of Geophysical Research-Atmospheres **99**(D2): 3543-3557.

Stevens, P. S., J. H. Mather, W. H. Brune, F. Eisele, D. Tanner, A. Jefferson, C. Cantrell, R. Shetter, S. Sewall, A. Fried, B. Henry, E. Williams, K. Baumann, P. Goldan and W. Kuster (1997). "HO_2/OH and RO_2/HO_2 ratios during the Tropospheric OH Photochemistry Experiment: Measurement and theory." Journal of Geophysical Research **102**(D5): 6379-6391.

Stone, D., M. J. Evans, P. M. Edwards, R. Commane, T. Ingham, A. R. Rickard, D. M. Brookes, J. Hopkins, R. J. Leigh, A. C. Lewis, P. S. Monks, D. Oram, C. E. Reeves, D. Stewart and D. E. Heard (2011). "Isoprene oxidation mechanisms: measurements and modelling of OH and HO_2 over a South-East Asian tropical rainforest during the OP3 field campaign." Atmospheric Chemistry and Physics **11**(13): 6749-6771.

Stone, D., L. K. Whalley and D. E. Heard (2012). "Tropospheric OH and HO2 radicals: field measurements and model comparisons." Chem Soc Rev **41**(19): 6348-6404.

Tan, D., I. Faloona, J. B. Simpas, W. Brune, P. B. Shepson, T. L. Couch, A. L. Sumner, M. A. Carroll, T. Thornberry, E. Apel, D. Riemer and W. Stockwell (2001). "HOx budgets in a deciduous forest: Results from the PROPHET summer 1998 campaign." Journal of Geophysical Research-Atmospheres **106**(D20): 24407-24427.

Taraborrelli, D., M. G. Lawrence, J. N. Crowley, T. J. Dillon, S. Gromov, C. B. M. Gross, L. Vereecken and J. Lelieveld (2012). "Hydroxyl radical buffered by isoprene oxidation over tropical forests." Nature Geoscience **5**(3): 190-193.

Welz, O., J. D. Savee, D. L. Osborn, S. S. Vasu, C. J. Percival, D. E. Shallcross and C. A. Taatjes (2012). "Direct Kinetic Measurements of Criegee Intermediate (CH_2OO) Formed by Reaction of CH_2I with O_2." Science **335**(6065): 204-207.

Whalley, L. K., M. A. Blitz, M. Desservettaz, P. W. Seakins and D. E. Heard (2013). "Reporting the sensitivity of Laser Induced Fluorescence instruments used for HO_2 detection to an interference from RO_2 radicals and introducing a novel approach that enables HO_2 and certain RO_2 types to be selectively measured." Atmospheric Measurement Techniques **6**: 3425-3440.

Whalley, L. K., P. M. Edwards, K. L. Furneaux, A. Goddard, T. Ingham, M. J. Evans, D. Stone, J. R. Hopkins, C. E. Jones, A. Karunaharan, J. D. Lee, A. C. Lewis, P. S. Monks, S. J. Moller and D. E. Heard (2011). "Quantifying the magnitude of a missing hydroxyl radical source in a tropical rainforest." Atmospheric Chemistry and Physics **11**(14): 7223-7233.

Whalley, L. K., K. L. Furneaux, A. Goddard, J. D. Lee, A. Mahajan, H. Oetjen, K. A. Read, N. Kaaden, L. J. Carpenter, A. C. Lewis, J. M. C. Plane, E. S. Saltzman, A. Wiedensohler and D. E. Heard (2010). "The chemistry of OH and HO2 radicals in the boundary layer over the tropical Atlantic Ocean." Atmospheric Chemistry and Physics **10**(4): 1555-1576.

Wolfe, G. M., J. D. Crounse, J. D. Parrish, J. M. St Clair, M. R. Beaver, F. Paulot, T. P. Yoon, P. O. Wennberg and F. N. Keutsch (2012). "Photolysis, OH reactivity and ozone reactivity of a proxy for isoprene-derived hydroperoxyenals (HPALDs)." Physical Chemistry Chemical Physics **14**(20): 7276-7286.

Chapter 2. The Highly Instrumented Reactor for Atmospheric Chemistry

2.1 Introduction

Field campaigns lie at the heart of the comprehension of our atmosphere and the very large number of reactions within it. Atmospheric composition is complex and varied, dependent on parameters such as latitude, altitude, season and anthropogenic emissions and many variables remain unknown. Comparison of global observations with computer driven chemical models powered by reaction databases such as the MCM (MCM, 2014) identify gaps in our knowledge and help to direct further kinetic and mechanistic research. Both small scale kinetic studies and larger chamber based investigations play a key role in developing a more detailed understanding of lesser known processes over a range of atmospheric conditions.

Small scale kinetic laboratory studies investigations commonly rely on flash photolysis experiments where premixed reactants are continuously flowed through small multiport cells and flashed light sources (lamps or high energy pulse lasers) are used to initiate chemistry through photolysis (pulsed laser photolysis, or PLP). Radicals such as OH are easily generated through this technique, and their decay due reaction can be detected through laser induced fluorescence (LIF, described in more detail in Chapter 4). As reactions are typically measured in the microsecond range, wall losses and heterogeneous processes are negligable and the reactors can easily be adapted to operate over a range of temperatures and pressures. However, these experiments are often limited by single species detection, the number of photolytic precursors and the short timescale of the reactions where study of further chemistry of potential atmospheric significance is not practical.

Flow tube type experiments can offer some advantage as reactant/product detection occurs further downstream creating longer effective reaction times (in the ms range), which can also be varied by using movable injectors. Reactive species are often created continuously through chemical reactions, microwave discharge or photolysis lamp source, lending the experiments to detection techniques that require longer averaging times (e.g. absorption based techniques). Products can be viewed at an effective point in time based on the flow rate of gas and position of the movable injector. However, flow tubes are difficult to operate over a wide range of temperatures and pressures as wall

interactions and heterogeneous uptake play a more significant role in this type of reactor.

Chambers offer the advantage of multiple species detection using several detection techniques on longer timescales, bridging the gap between field work and small scale kinetic studies. Conducting experiments in atmospherically relevant gas mixtures (e.g. air, O_3, NOx, H_2O, temperature etc.), chambers are able to control more variables than fieldwork. Typically, an increasing chamber volume reduces the chance of possible heterogeneous wall-surface chemistry, whilst allowing a range of instrumentation to measure several different species simultaneously.

However, chambers are not without disadvantages. Most instrumentation requires examination of trace gas chemistry at concentrations higher than ambient (i.e. detection limits ~10 - 100 ppbv) resulting in atmospherically unrepresentative concentrations used in experiments. This limits the value of the data when comparing experiments to observations in the field where concentrations are significantly more dilute. Using high reagent concentrations results in large quantities of potentially unwanted secondary products (e.g. aerosols) that can hinder the target reaction or interfere with the measurement of a certain species (Dodge, 2000; Carter et al., 2005), something that does not affect small scale kinetics experiments due to short reaction timescales. Heterogeneous surface chemistry is also a problem in chambers where it has the potential not only to remove target species (especially radicals), but create or catalyse the formation of secondary products and this process is often enhanced due to small surface to volume ratios (S/V). These losses, along with those that occur on the sampling lines necessary for *ex situ* based measurement techniques, can be estimated but are hard to thoroughly characterise and quantify as little is known about the chemical processes that drive them. Despite these disadvantages, chambers still offer an excellent platform for atmospheric chemistry research due to their versatility in construction, size, operating conditions and instrumentation.

There are several atmospheric chambers throughout the world differing in geometry, sizes and construction materials dependent on the application, be it gas phase chemistry, aerosol ageing or smog chamber investigations (to name but a few). A detailed review of chambers is beyond the scope of this thesis and readers are referred to Malkin (2010), Seakins and Blitz (2011) and Farrugia (2014) for more information . Chambers are most

commonly constructed from metal (steel/aluminium), glass (or quartz) and Teflon and these materials dictate the size, radiation sources, operating conditions and instrumentation that can be coupled to the chambers. A certain degree of control is offered by artificial radiation sources, i.e. lamps, as emission spectra can be selected depending on the target molecule. Whilst a variety of different lamps are available, the exact replication of solar radiation is currently not possible. Certain radical precursors used in chamber studies (e.g. H_2O_2 for the production of OH), are photolysed using Hg lamps at 254 nm and therefore other photolabile species will unavoidably be photolysed, adding complexity and uncertainty to the system. Using solar radiation directly removes the need to characterise molecular action spectra, but there can still be a inhomogeneous field created by shadow effects, clouds and the dependence on the solar zenith angle (Bohn et al., 2005; Bohn and Zilken, 2005).

Metal chambers, such as those at LISA (Wang et al., 2011) and NCAR (Shetter et al., 1987), offer the most versatility in terms of instrumentation as various ports can be cut and welded onto the chamber surface. Pressure and temperature control is also possible as the chamber walls can withstand low pressures down to vacuum, whilst easily conducting to allow heat exchange (Akimoto et al., 1979; Shetter et al., 1987; Stone, 1990). Metal chambers tend to be small (3 - 2000 litres) to keep construction costs down and are irradiated using actinic lamps through quartz windows, which often leads to an inhomogeneous radiation distribution. Quartz and glass chambers, such as QUAREC (Barnes et al., 1994) and UCPH (Nilsson et al., 2009), are usually of a similar size to their metal counterparts, as the fragility and cost of quartz limits chamber size. Operation over a range of pressures down to < 1 Torr is also possible (Barnes et al., 1983; Wallington and Japar, 1989; Nilsson et al., 2009). Instrumentation and sample lines are typically mounted to metal end flanges, while artificial radiation sources can be shone directly through the chamber walls (Nolting et al., 1988; Wallington and Japar, 1989; Barnes et al., 1994; Doussin et al., 1997). Externally mounted photolysis lamps around chambers such as QUAREC result in a more uniform photolysis field and limit temperature gradients created by internally mounted lamps. Quartz chambers can also be operated over a range of temperatures by enclosing the entire chamber and radiation source in a temperature controlled case (Nilsson et al., 2009).

Due to the small size of both quartz and metal chambers, *in situ* Fourier transform infrared (FTIR) spectrometers coupled to multi-pass White Cell type optics are favoured

for the detection of VOCs and inorganic species. Other low sampling rate (< 1 litre min^{-1}) instruments are also used such as gas chromatography (GC) coupled to flame ionisation detection (FID) or mass spectrometer (MS) detection systems as well mass spectrometers with soft ionisation sources, e.g. chemical ionisation (CIMS) and proton transfer (PTR-MS) used for VOC or aerosol detection.

Teflon chambers, such as SAPHIR (Karl et al., 2004) and EUPHORE (Siese et al., 2001), are the most common chamber type as the material is comparatively cheap and hence a wide variety of chamber sizes exist (1 - 280,000 litres). Smaller Teflon chambers are often used in a similar manner to quartz chambers, where they are encased in a temperature controlled box or room surrounded by photolysis lamps (Thuener et al., 2004; Carter et al., 2005). Larger Teflon chambers have been constructed outside, as with SAPHIR and EUPHORE, taking advantage of the small surface to volume ratio and using solar radiation to initiate chemistry as it is able to penetrate the walls. Dilution is also less of a problem and hence EUPHORE and SAPHIR chambers are able to employ an even larger range of *ex situ* instrumentation such as FAGE for OH radical detection, along with GC-FID, GC-MS and PTR-MS. The larger construction of the SAPHIR chamber recently permitted deployment of instruments inside the chamber (Fuchs et al., 2010; Dorn et al., 2013). Teflon bag systems cannot change their temperature and pressure, and so always conduct experiments under ambient conditions, and outdoor chambers are inherently weak and cannot withstand strong weather patterns. Reactants and products are typically removed from these chambers by dilution, where clean air is continuously flushed into the system; a long process for large chambers. Surface reactions can also be significant on Teflon surfaces, and Schlosser et al. (2007) have observed the slow release HONO into the SAPHIR chamber from the walls.

By carefully considering the current variety of atmospheric simulation chambers around the world, the Highly Instrumented Reactor for Atmospheric Chemistry (HIRAC) was constructed and employed at the University of Leeds. HIRAC is a custom-built metal atmospheric simulation chamber providing the unique ability to simultaneously vary pressure and temperature whilst measuring the short-lived free radical species OH, HO_2 and NO_3. These features make HIRAC ideally suited to the study of the kinetics and mechanisms of atmospherically relevant reactions and the calibration, validation and development of atmospheric measurement instrumentation.

2.2 The HIRAC Chamber

A schematic of HIRAC is displayed in Figure 2.1. The chamber's full description and characterisation studies have been presented in the literature (Glowacki et al., 2007a; Malkin, 2010; Malkin et al., 2010). The chamber was 2.0 m long, 1.2 m in diameter and made of grade 304 stainless steel giving an internal surface area of ~10 m^2 and a volume of ~2.25 m^3. Including all internal surfaces (fans, tubes, mirrors etc.), a low surface to volume ratio (S/V) was maintained (~5.8 m^{-1}) minimising heterogeneous wall interactions which could affect chemistry inside the chamber. The chamber was designed for the investigation of gas phase reaction kinetics and chemical mechanism studies and could operate over a range of temperatures (225 - 345 K) and pressures (10 - 1000 mbar).

Stainless steel was chosen over more commonly used quartz or glass designs as access ports of various sizes could easily be cut into the chamber walls during manufacture. The curved walls were 4 mm thick and the end walls 25 mm thick. Each end panel had a centrally mounted ISO-K500 access port. Two more ISO-K500 ports were positioned on one side of the chamber while the remaining six smaller ISO-K160 ports were positioned two opposite the larger access holes, two on the top and two on the bottom of the chamber. Different flanges were attached to each of these access ports allowing various instruments (commercial gas analysers, gas chromatography etc.) to monitor reactions inside HIRAC. As well as large access holes, HIRAC has eight ISO-KF16 ports (four on each end plate) which allowed the connection of gas inlets, pressure gauges and extra sampling lines.

Gases were mixed inside HIRAC using four circulation fans, two located at each endplate. The 225 mm diameter fans were custom made from aluminium and connected to external motors using ferro-fluidic feedthroughs (Ferrotec SS-250-SLBD). To ensure homogeneous mixing of gases, fans on the same end plate rotated in opposing directions. Damping the motor housings with neoprene and cork combined with a flexible connection between the motor and feedthrough reduced the vibrations transferred to the end plates which is important for the FTIR (section 2.3.1) signal to noise ratio (S/N). The chamber was evacuated to ~0.05 mbar for ~60 mins following each experiment using a rotary pump backed roots blower (Leybold, trivac D40B and ruvac WAU251) to ensure removal of the majority of gas phase reactants/products.

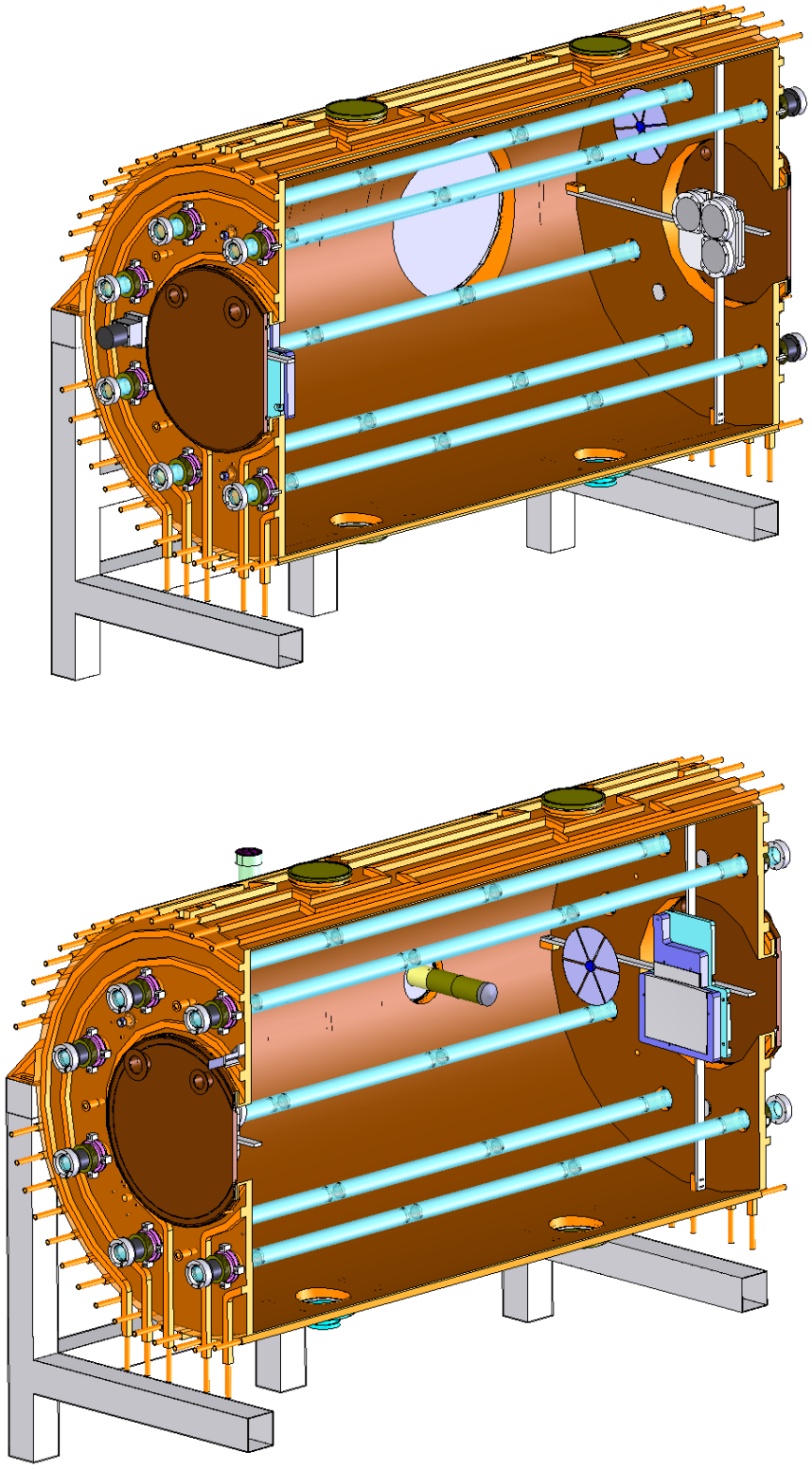

Figure 2.1: Vertical cross-sectional schematics showing the photolysis lamps housed in quartz tubes, mixing fans, ISO-K500 and ISO-K160 port positions, FTIR field (below) and object mirrors (above) and FAGE inlet (below) inside the HIRAC chamber.

Instrumentation used to measure different gas phase species in HIRAC included *in situ* Fourier Transform Infrared Spectroscopy (FTIR) and Gas Chromatography using Flame Ionisation Detection (GC-FID) for VOCs, Fluorescence Assay by Gas Expansion (FAGE) for OH and HO_2 radicals and commercial trace level NOx (NO + NO_2), H_2O vapour, O_3 and CO analysers. These detection techniques are discussed below (section 2.3), with the exception of FAGE, which is described in more detail in Chapter 4.

2.2.1 Temperature control

Recently a new temperature control system was installed which used a Huber Thermostat 690W to flow thermofluid (DW-Therm, operating range = 183 - 543 K) through several steel pipes welded to the outer skin of the HIRAC chamber. In total there were six separate flow circuits around the chamber controlled using a series of taps allowing each circuit to be isolated, a useful tool for future temperature ramping experiments. The main body of the chamber, where possible, was covered in two layers of 20 mm thick neoprene insulation. Tubes connecting the different thermofluid circuits between the chamber and thermostat unit were also insulated with a single layer of 20 mm thick neoprene. Pictures of the thermofluid inlet manifold connected to the insulated chamber are displayed in Figure 2.2. The larger diameter pipes are connected to the end of the quartz tubes housing the lamps and served to extract the N_2 used to purge the lamps. To date the maximum operating range of the chamber was measured as 225 - 345 K, however more extreme temperatures could be reached in the future through using a second thermostat unit, and the inlet manifold was designed for this application. Temperature gradients measured across the diameter of the chamber have been shown to be within 1 K. Small deviations (± 4 K) were observed close to the chamber flanges where there are no thermofluid circuits. As all experiments presented here were conducted at room temperature, readers are referred to Farrugia (2014) for more detailed information.

Figure 2.2: Left: Thermofluid inlet manifold before insulation was installed. Temperature set point = 238 K. Right: Inlet manifold and HIRAC with 2 mm and 4 mm neoprene insulation was used to cover the entire chamber and external tubing.

2.2.2 Gas handling and sample preparation

The design of HIRAC has allowed the connection of dedicated lines for the injection of N_2 and O_2 gases for cylinders (Ultra High Purity (UHP) 99.999 %, BOC Zero Grade) and a laboratory generator supply (Dominick Hunter N_2 generator, MAX116, > 99.995 % purity), O_3 injection from the output of a custom made generator (based on VUV photolysis of O_2) for ozonolysis experiments as well as a connection to the main sample preparation and delivery system. Gas and liquid samples were prepared for injection into HIRAC by expansion into a 1 litre stainless steel delivery vessel through a Pyrex glass vacuum line system. Sample pressures were measured using two Leybold Ceravac CTR90 (0 - 1000 Torr and 0 - 10 Torr) and pushed into the chamber using a 3 bar backing pressure of N_2. Gases were introduced directly from lecture bottles and liquids were subjected to several freeze-pump-thaw cycles to remove any potential impurities. For experiments requiring higher concentrations and for species whose vapour pressure at 298 K were < 1 Torr, samples were injected directly into the chamber through a rubber septum using 100 (±5) and 10 (±0.5) µl syringes.

2.2.3 Data acquisition

HIRAC was equipped with several peripheral devices to monitor temperature and pressure inside the chamber. Type-T thermocouples were selected for monitoring temperatures in the HIRAC chamber due to their linearity over a wide temperature range (-200 - 350 ^{o}C). Six were placed randomly inside the chamber and 8 more were placed one each inside the quartz tubes to monitor the photolysis lamp temperatures. The thermocouples were connected to a data logger (PICO USB TC-08). The total chamber pressure was monitored using a Leybold Ceravac CTR90 (0 - 1000 Torr). Data from the thermocouples, pressure gauges, commercial trace gas analysers (section 2.3) and chamber dilution rate (section 2.3.4) were all simultaneously acquired to a central computer.

2.2.4 Artificial light sources

The photolysis lamps, housed in eight quartz tubes mounted radially inside the reactive volume, were used to initiate photochemistry. Silicon 'o-rings' create an airtight seal around the outside of the quartz without restricting movement to avoid damage when changing temperature and pressure. Plastic collars were attached at either end of each lamp mounting them away from the quartz wall and allowing a flow of N_2 in between. The output of the lamps was temperature dependent outside of a narrow temperature range (~35 - 39 °C) and so the housings were flushed with N_2 to regulate the temperature and remove photolabile species. A photolysis lamp induced chamber temperature increase of ~2 K was seen over the course of a typical experiment (< 40 mins), and was therefore considered negligible compared to the diurnal temperature of the chamber on any given day (289 ± 5 K). The H_2O vapour content in the air used to flush the lamps, was high enough to condense and sometimes freeze inside the quartz tubes when operating at temperatures lower than ambient, hence the lamps were flushed with N_2 instead.

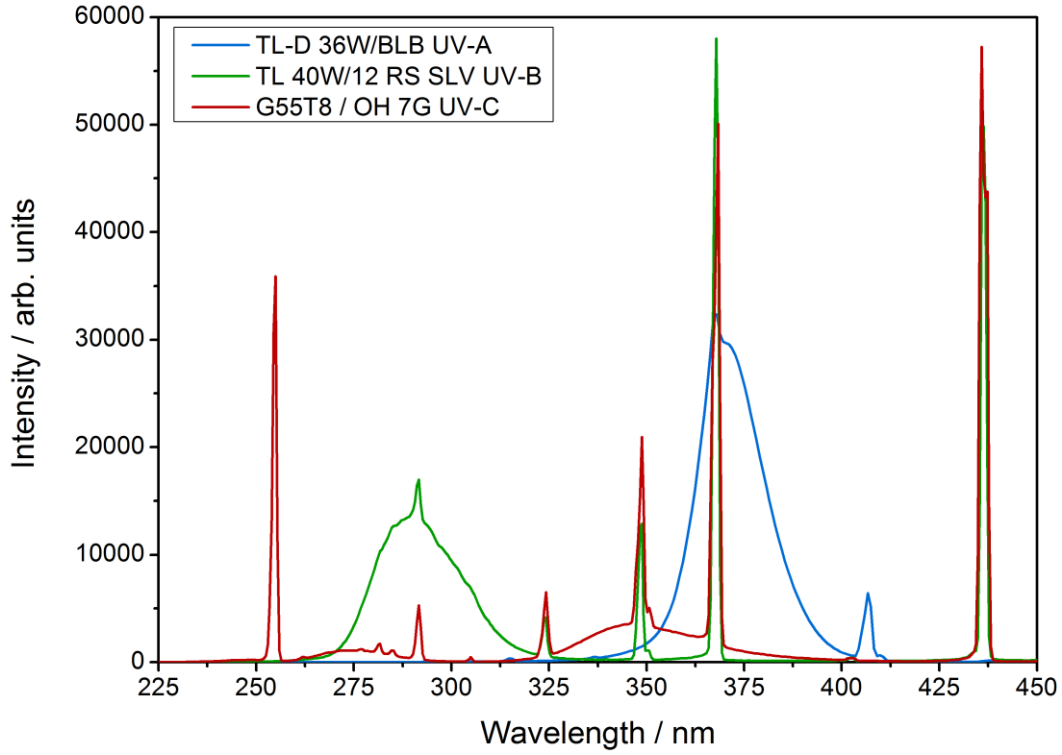

Figure 2.3: Comparison of the emission spectra for the most commonly used HIRAC photolysis lamps measured using the SpecRad instrument (section 2.2.4.1).

Displayed in Figure 2.3 is a comparison of the emission spectra of the most commonly used photolysis lamps in the HIRAC chamber, measured qualitatively using the NCAS spectral radiometer (SpecRad, see section 2.2.4.1): GE G55T8 / OH 7G UV-C (active λ = 254 nm), Philips TL 40W/12 RS SLV UV-B (active λ = 270 - 320 nm) and Philips TL-D 36W/BLB UV-A (active λ = 350 - 400 nm). All lamps were ~ 1 m in length and hence only 8 lamps were introduced into the quartz tubes, with alternate lamps overlapping to provide as homogeneous a radiation profile as possible. As mentioned previously, each photolysis source can be used to photolyse different target molecules; the UV-C lamps have been used in the photolysis of peroxides as a low NOx source of OH, namely *tert*-butylhydroperoxide (Chapter 6 and Farrugia (2014)), while UV-B were used in the photolysis of aldehydes and methyl nitrite (Chapter 6 and Malkin (2010)) and the UV-A were used for the photolysis of Cl_2 in the study of the acetyl peroxy reaction with HO_2 (Chapter 7). As the lamps are external to the chamber, they can be easily interchanged depending on the target molecule.

Even distribution of light throughout the chamber for this lamp arrangement was confirmed through modelling work by Glowacki et al. (2007a). The model was able to predict the NO_2 photolysis rate across the diameter of the chamber, and was in good agreement within 5 % of previous measurements of $j(NO_2)$. Investigation into OH radical gradients across the HIRAC chamber were conducted by Malkin (2010) using direct FAGE measurements of OH produced from both photolytic (methyl nitrite) and non-photolytic (O_3 + *trans*-2-butene) sources using an extended inlet (80 cm) to probe across the chamber diameter. No significant OH radical gradient was observed until the FAGE sampling nozzle was ≤ 20 mm from the walls whereupon a ~15 % decrease was seen when the sampling inlet was flush with the chamber walls. The lack of gradient in OH radicals from both photolytic and non-photolytic sources provides direct evidence of the homogeneity of the lamp radiation profile and efficacy of mixing in the chamber, whilst showing that the standard FAGE inlet (280 mm, Chapter 4) samples well into the homogeneous area.

2.2.4.1 Spectral radiometer measurements inside HIRAC

The Spectral Radiometer (SpecRad) was applied to the chamber for two separate sets of experiments: (i) semi-quantitative measurement of the emission spectra and intensity as a function of time for each set of lamps over a range of temperatures for modelling study constraints (see Chapter 7); (ii) quantitative measurement of lamp emission for the calculation of photolysis rates. Parts (i) and (ii) required different applications of the SpecRad apparatus to the HIRAC chamber which are described below. The SpecRad instrument has been designed for use on field campaigns to provide a direct measurement of solar actinic UV flux for the determination of temporal photolysis frequencies. The instrument used a 2Π quartz diffuser, coupled to a fixed grating spectrometer (Ocean Optics, QE65000Pro) *via* a 10 m fibre optic cable. The spectrometer was calibrated to operate over the 250 - 750 nm range at < 1 nm resolution with light detected on a cooled, fast Fourier transform charge-coupled device (FFT-CCD, Hamamatsu). Figure 2.4a shows a top-down cross section schematic of the experimental setup for the first set of experiments.

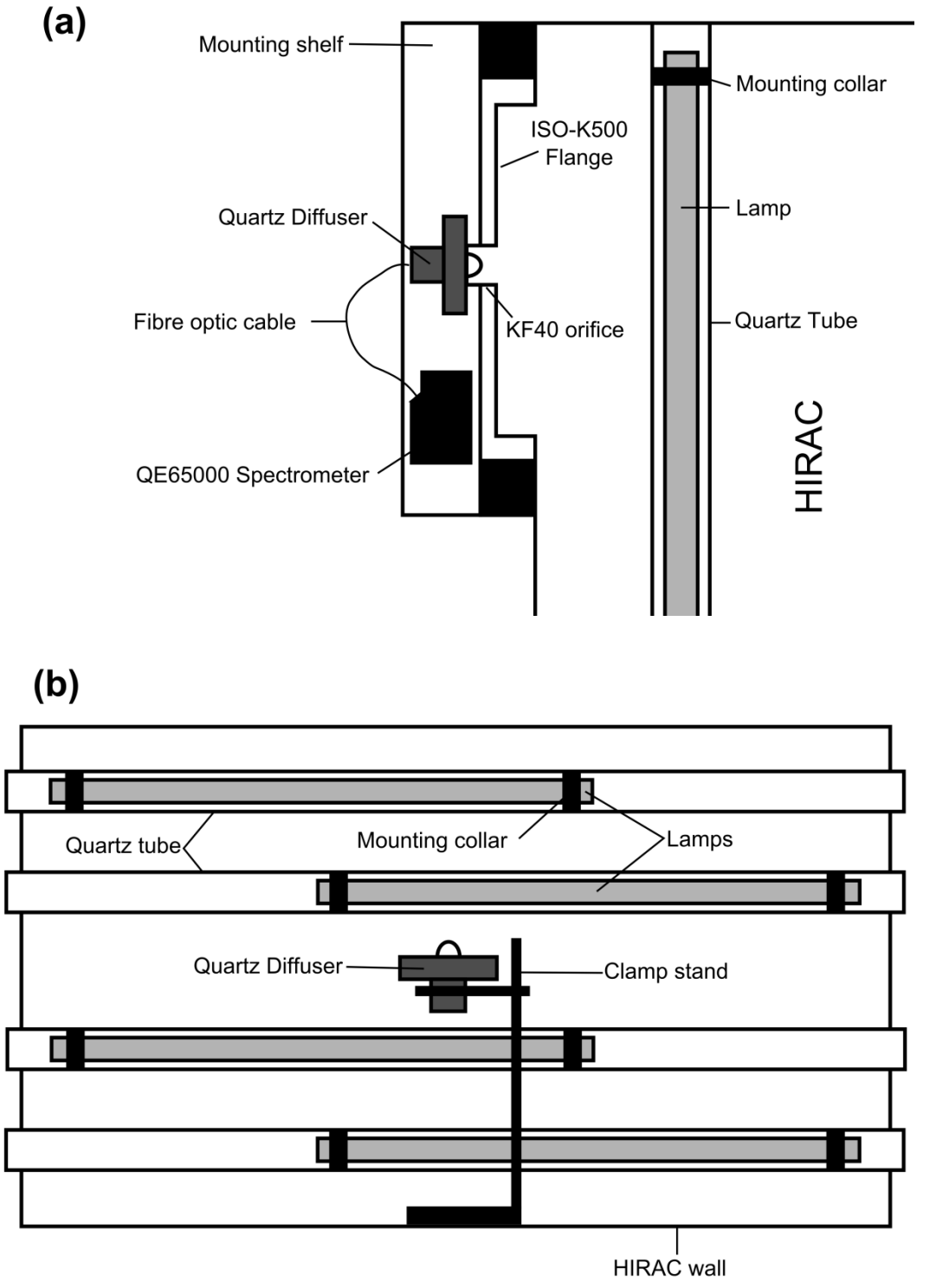

Figure 2.4: (a) Top-down cross section of the HIRAC chamber displaying the experimental setup for the semi-quantitative determination of the lamp intensity as a function of time. Profiles were recorded for all lamp sets (see text) over the 235 - 345 K temperature range in 1000 mbar N_2. (b) Side-on cross section of the HIRAC chamber displaying the placement of the SpecRad quartz diffuser used to quantitatively measure the TL-D 36W/BLB lamp flux in 1000 mbar N_2. The QE65000 was mounted externally.

The SpecRad diffuser dome was introduced into the KF-40 opening of an ISO-500 flange at the side of the chamber. The chamber was over-pressurised with N_2 (laboratory supply), flowing gas out past the SpecRad diffuser which was not vacuum sealed to the chamber. This ensured removal of photolabile species that could potentially interfere with the light intensity measurements. Spectra were integrated over 100 ms and 10 spectra were averaged to achieve a 1 s time resolution using the supplied SpectraSuite software. After initiating data recording, the lamps were switched on and spectra were recorded for ~ 30 minutes. This procedure was repeated for all lamp sets at room temperature and 273, 325 and 345 K for the TL-D 36W/BLB lamps (active λ = 350 - 400 nm).

The room temperature emission spectra were presented in Figure 2.3 and the output intensity as a function of time for the UVA lamps measured between 273 - 342 K are shown in Figure 2.5. The profiles are neither absolute nor relative due to the experimental method and were calculated by integrating the spectrum between the 350 - 400 nm range. As mentioned above, the lamps have a narrow operating temperature range for optimum intensity (~40 ^{o}C) and hence the change in temperature of HIRAC influences the speed at which the optimum is achieved. These profiles were essential in predicting radical concentrations when using chemical modelling simulations, as the majority of radical precursors used in the chamber are photolabile. The profiles can be entered into the Kintecus numerical integrator package (Ianni, 2002) as a constraint for the photolysis rate, allowing accurate modelling of the precursor photolysis at different temperatures. At room temperature (293 K), the lamps were observed to have a warm up period, reaching maximum output at ~150 s, before decreasing at longer times due to the optimum temperature being passed. Observations at 325 and 342 K show a near instantaneous maximum before a general decrease in output as the lamps were already above the optimum temperature before being turned on. At 273 K, a maximum value was not reached in the 600 s measurement window as the lamps were too cold to give a stable output. Not all lamps were initially operational at this temperature and the sudden increase at ~50 s is likely due to a delayed lamp ignition.

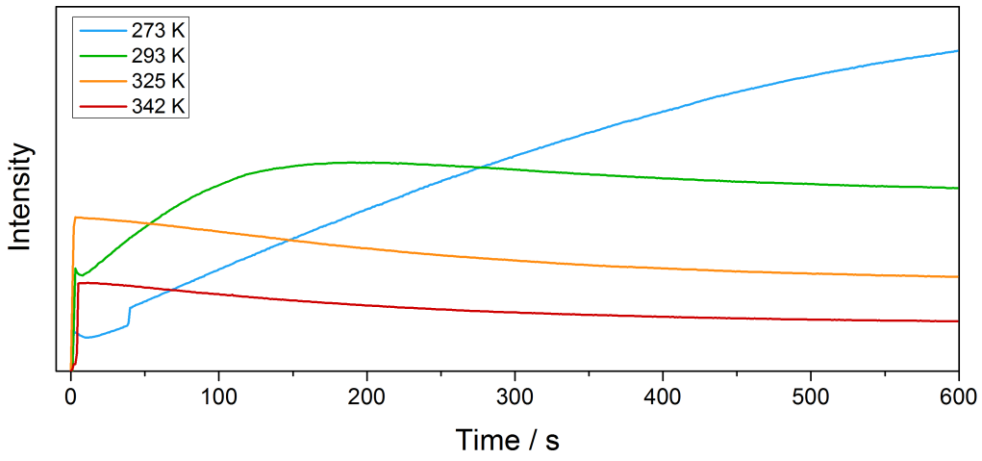

Figure 2.5: Intensity profile for all 8 TL-D 36W/BLB lamps (λ = 350 - 400 nm) as a function of time, measured at four different temperatures using the SpecRad instrument. Intensity is not absolute or relative to other temperatures due to the nature of the experiments. See text for details.

The aim of the second set of experiments was to quantitatively determine the lamp flux for the TL-D 36W/BLB lamps and calculate the photolysis rate for Cl_2, $j(Cl_2)$. The SpecRad diffuser was mounted on a clamp stand in the centre of the chamber, as shown in Figure 2.4b. As the diffuser dome collected light at a 180^o solid angle, $j(Cl_2)$ could be approximated by measuring the emission from all 8 lamps with the SpecRad facing up and down. Spectra were integrated for 50 ms, averaging 20 co-added scans to give a 1 s time resolution. The lamps were left on for > 10 minutes to ensure a stable output relevant to a standard chamber based experiment. Flux concentrations were determined by applying the SpecRad calibration factor across the λ = 300 - 450 nm wavelength range. Using a literature absorption cross section (Tellinghuisen, 2003), $j(Cl_2)$ was calculated at 2.5×10^{-4} s^{-1}. Comparison with the more commonly employed NO_2 actinometric method (described in Malkin (2010) and Glowacki et al. (2007a)) was not completed due to time constraints, however modelling studies conducted in Chapter 7 showed $j(Cl_2) = (5.9 \pm 1.0) \times 10^{-4}$ s^{-1} based on the measured decay of acetaldehyde upon reaction with Cl. These preliminary results show the SpecRad measurement is under-predicting the photolysis rate. It was possible that the position of the SpecRad diffuser was unable to account for the heterogeneous distribution of lamp radiation where photolysis closer to the quartz tubes is increased, as suggested by the photolysis profile modelling work by Glowacki et al. (2007a). Clearly more work is required to make a quantitative measure of flux for these lamps through the study of NO_2 photolysis and to

determine a method for the SpecRad to provide an accurate measurement of other lamp fluxes.

2.3 Instrumentation

All instrumentation connected to the HIRAC chamber that was used in this project are discussed in this chapter, except FAGE, for which the principles, design and characterisation are discussed in Chapter 4. Instrumentation is discussed briefly here as more in depth characterisations are presented elsewhere. For detailed information on cavity ring down spectroscopy readers are directed to Malkin (2010), GCs to Farrugia (2014) and FTIR to Glowacki et al. (2007a) and Glowacki et al. (2007b).

2.3.1 FTIR

Infrared theory and measurement analysis are covered in detail in the following Chapter 3 and so only instrumental and experimental detail will be given here. A Bruker IFS/66 FTIR spectrometer was coupled to a multipass optical cell designed by Glowacki et al. (2007b) inside HIRAC allowing the measurements to take place *in situ*, an advantage over sampling methods such as GC-FID. The infrared light was passed into the chamber *via* a set of feedthrough optics housed in a N_2 purged Perspex box. Two KBr windows (8.7 millirad wedged, 75 mm diameter, 5 mm thick) mounted into one of the ISO-K500 end flanges separated the purge box from the chamber. Infrared light exiting the multipass arrangement was then focused onto a mid-band mercury-cadmium-telluride detector (MCT, 12000 - 600 cm^{-1}) which was also mounted inside the purged box.

The collection optics were a modified multipass matrix system (MMS) Chernin type cell which is shown in Figure 2.6 with the spot pattern for 36 images (72 passes) used throughout the experiments described here. Three objective mirrors (O1, O2 and O3) and two field mirrors (F1 and F2) were used in the design. All had the same radius of curvature, obeying the White Rule, and hence defined the length of the cell (~1.785 m). The centre of curvature of the larger field mirror, F1, was located in between objective mirrors O1 and O2, while the smaller field mirror, F2, had centre of curvature aligned

between O1 and O3. Unlike the original modified MMS (Chernin and Barskaya, 1991; Chernin, 2002), the input and output apertures were located on opposite sides of the F2 mirror. Light entered the cell to the right of F2, (image 0 in Figure 2.6), and hitting O3. The light was then reflected onto the far left of F2 reflecting the light towards O1, in turn reflecting the light back onto F1 (image 2 in Figure 2.6). The light was then passed between O1 and O2 until image 12 where the light was passed back to O3 and the cycle was repeated until the light exited the cell at image 36.

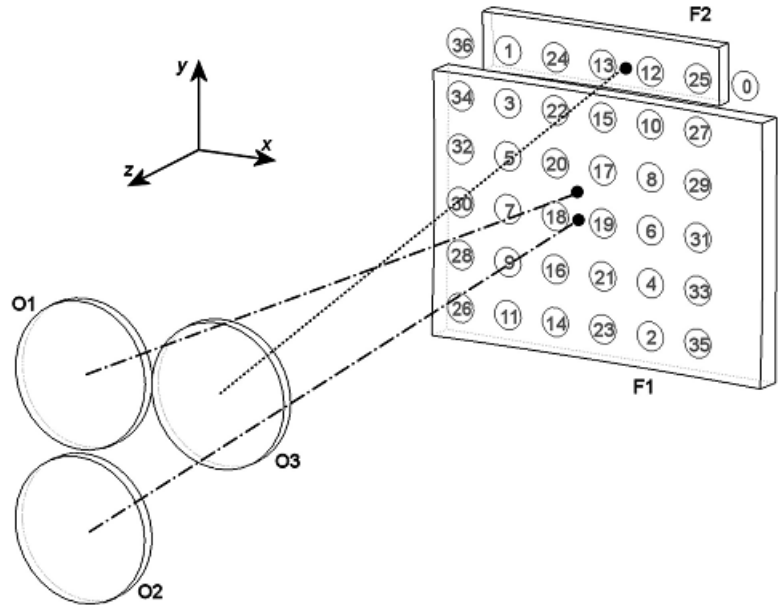

Figure 2.6: Schematic showing the arrangement of the 3 objective mirrors (O1 – O3) and the 2 field mirrors (F1 and F2) in HIRAC. The centre of curvature alignments (illustrated with dotted lines) for the 3 objective mirrors and the image locations for a 72 pass arrangement used through this thesis are also shown. Figure reproduced from Glowacki et al. (2007b).

The modified MMS cell was chosen over more traditional White Cell designs as it conserves optical through-put over a range of matrix arrangements, is easy to align and has shown very good stability to vibrations (Glowacki et al., 2007a; Glowacki et al., 2007b). The mirrors were constructed from Zerodur which was polished to a high accuracy, coated easily and has a very small thermal expansion coefficient. The mirrors inside HIRAC were mounted on aluminium crosses attached to the cylindrical skin ~10 cm from the end flanges (Figure 2.1). This setup helped (i) to prevent the vibrations from mixing fans affecting the signal to noise ratio (S/N) and (ii) to maintain a stable

alignment as mounting on the end walls of the chamber would have subjected the optics to pressure gradient bowing during experiments. Tests in HIRAC have shown that the alignment of the modified MMS is stable at pressures from 10 - 1000 mbar and temperatures from 223 - 323 K.

The mirrors are mounted on specially designed spring loaded aluminium supports shown in Figure 2.7 and are easily aligned by 80-pitch per inch adjustment screws which allow total travel of 50 mm. The mounts permitted adjustment of each mirror in the cell individually as well as having an adjustable common back plate for objective mirrors O1 and O2 which enabled movement of the two mirrors without changing their relative alignment. The 50 mm travel enables the system to be used with mirrors of differing thickness.

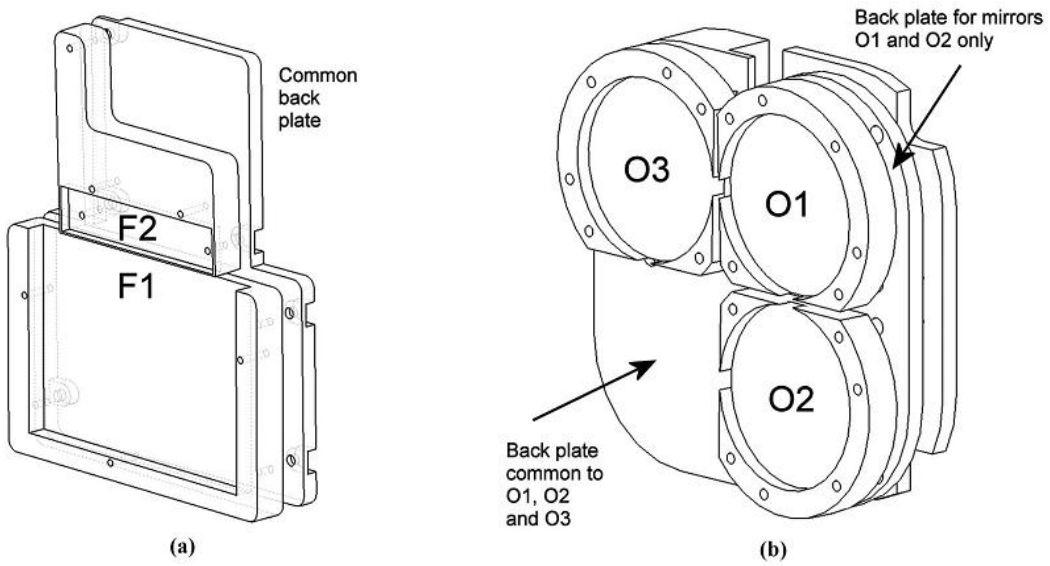

Figure 2.7: Schematic showing the mount designed for (a) the 2 field mirrors and (b) the 3 objective mirrors reproduced from Glowacki et al. (2007b).

2.3.2 GC-FID

Two calibrated gas chromatography instruments with flame ionisation detector (GC-FID, Agilent Technologies, 6890N) were used for the online detection of reactants. Gas samples were injected onto the column and species were separated based on their physical properties (boiling point, polarity etc.) before entering the detector. The FID is designed to respond to ions created through burning VOCs in a hydrogen flame,

attracting them onto the detector using an electric current. As different compounds elute from the column, a rise in signal from the FID is measured to a maxima, before returning to background levels. These are known at chromatographic peaks and their integral is proportional to concentration. Signals were produced of varying intensities dependent on the VOC functionality and hence calibration was necessary (see below).

For the experiments conducted herein the GCs were fitted with two different columns to aid the separation of polar and non-polar species in experiments. The first was fitted with a CP-SIL-5 column (50 m, 0.32 mm, 5 μm), a non-polar column ideal for separating C_2 - C_6 hydrocarbons (both saturated and unsaturated) due to the length. The second column used was a DB-WAX (15 m, 0.32 mm, 0.25 μm) suited for the detection of highly polar molecules. Both GCs used He carrier gas and a constant oven temperature (40 - 75 ^{o}C dependent on the hydrocarbon being detected, more detail is given in chapters 6 and 7).

Displayed in Figure 2.8 is a schematic showing the online gas sampling system for the GC; this was recently adapted to allow sampling for two GCs, however the principle is the same. Gas samples were collected for injection using two independent 5 ml evacuated sampling loops into which gas from the chamber was expanded. Samples were injected onto the GC column through a 2-position 6-way multiport valve controlled by the GC which pushed He carrier gas through the sample loop towards the injector when the valve was switched.

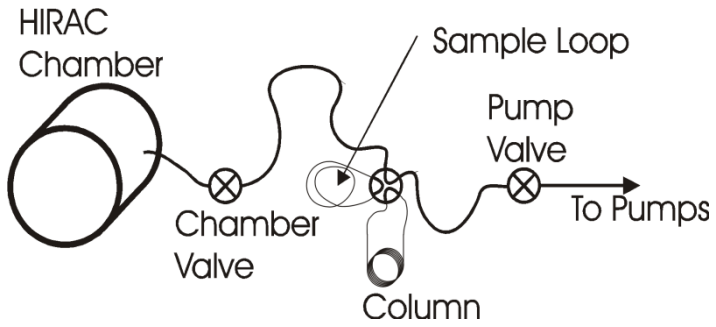

Figure 2.8: Diagram of the GC sampling system used in conjunction with HIRAC. Reproduced from Glowacki et al. (2007a).

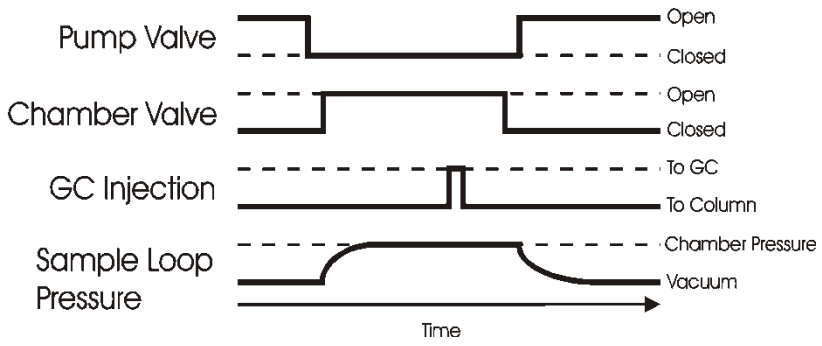

Figure 2.9: Timeline of the GC sampling process showing the control of sampling system. Reproduced from Glowacki et al. (2007a).

A rotary pump (Leybold 4B) was used to evacuate the sample line and sample loop when the chamber valve is closed. The GC injection timeline is then activated (Figure 2.9). Before an injection takes place, the pump valve was closed and the chamber valve opened, allowing the sample loop to fill up at the current chamber pressure. The GC switched the 6-way valve after ~25 s, pushing the sample gas onto the column. The 25 s wait allowed pressure to stabilise in the sample loop before injection. The valves were then reset to their initial positions to evacuate the system. The time taken for this cycle can be adjusted to increase the measurement time resolution, depending on the elution times of the species being measured. Heating the column will increase the speed of the elution, but peaks for different compounds may overlap and make integration impractical.

The GC-FID systems were typically calibrated by expanding known concentrations of VOCs into HIRAC using the gas delivery system or direct liquid injection. All calibrations were completed at the relevant experimental chamber pressures using the departmental generated N_2 supply. The linearity of the FID signal to concentration was tested by repeat injections and dilution of the chamber. Dilutions were completed quickly by evacuating a portion of the chamber gas using the vacuum pump set and refilling with N_2. Calibrations would typically consist of two dilutions and four injections. Good signal to concentration linearity and reproducibility was observed. The GC precision was calculated at ~4 % (2σ).

2.3.3 Commercial trace-level gas analysers

Measurements of O_3 and NOx were conducted using commercial trace-level gas analysers connected to HIRAC using ¼" Teflon tubing. Both analysers were connected to a common sample line which was inserted ~30 cm into the top of the chamber through an ISO-350 flange. This ensured gas was sampled from a well mixed area of the chamber.

Ozone concentrations were measured using a UV photometric O_3 analyzer (TEC Model 49C) which has a detection limit = 1.0 ppb over a 30 s averaging time and 20 s response time. The O_3 analyser was calibrated using a commercial ozone primary standard (Thermo Electron Corporation 49i-PS) and an intercomparison with the FTIR was linear (Glowacki et al., 2007a; Malkin, 2010). A trace level chemiluminescence NO_x box (TEC Model 42C) was used to detect NOx at a limit of 50 pptv over a 30 s averaging time and 40 s response time. The NOx box was calibrated for NO using an NO standard (450 ppb in N2, BOC) in a flow of N_2, whilst NO_2 was generated by introducing an excess of O_3 into the flow. All flows were accurately controlled using Brooks mass flow controllers.

2.3.4 Dilution compensation system

All instrumentation apart from the FTIR (section 2.3.1) and the previously used cavity ring down spectroscopy system (Malkin, 2010; Farrugia, 2014) were required to draw a sample from the chamber. The GCs (sampling rate = 0.05 slm (standard litres min^{-1})) and commercial analysers (~1.5 slm combined) do not have a significant impact on the dilution of species in the chamber with a total dilution rate of $< 1 \times 10^{-4}$ s^{-1}. However, the sampling rate for the FAGE system (see chapter 4) was much larger at ~8 slm, leading to a total dilution rate of 5.6×10^{-4} s^{-1} measured using the average of several experimental determinations of hydrocarbon dilution using GC-FID. An example of the difference between the effects of dilution for the O_3 analyser and FAGE is shown in Figure 2.10. Over the course of a typical 30 minute experiment the chamber was diluted by ~12 % and the dilution rate coul become competitive with the rate of decay of

reactants due to radical reactions (based on typical operating conditions of [OH] ≈ 10^7 molecule cm^{-3} and $k_{OH} \approx 10^{-11}$ molecule^{-1} cm^3 s^{-1}).

As the volume of the chamber is fixed, pressures were maintained manually using a rotameter controlled flush of laboratory grade N_2. Recently, a new automated dilution control system was developed and installed that was able to monitor the change in temperature and pressure of the chamber, adjusting the flow of both N_2 and O_2 through two mass flow controllers (MFCs, Brooks). The software was developed using LabView and was designed to integrate with the current software tool that was used to log the data from all the chamber peripherals (section 2.2.3). Pressures were seen to fluctuate ~2 % about the desired pressure, based on initial guesses from the user, improving the level of control over the pressure in HIRAC. This system was used during all of the experiments presented here.

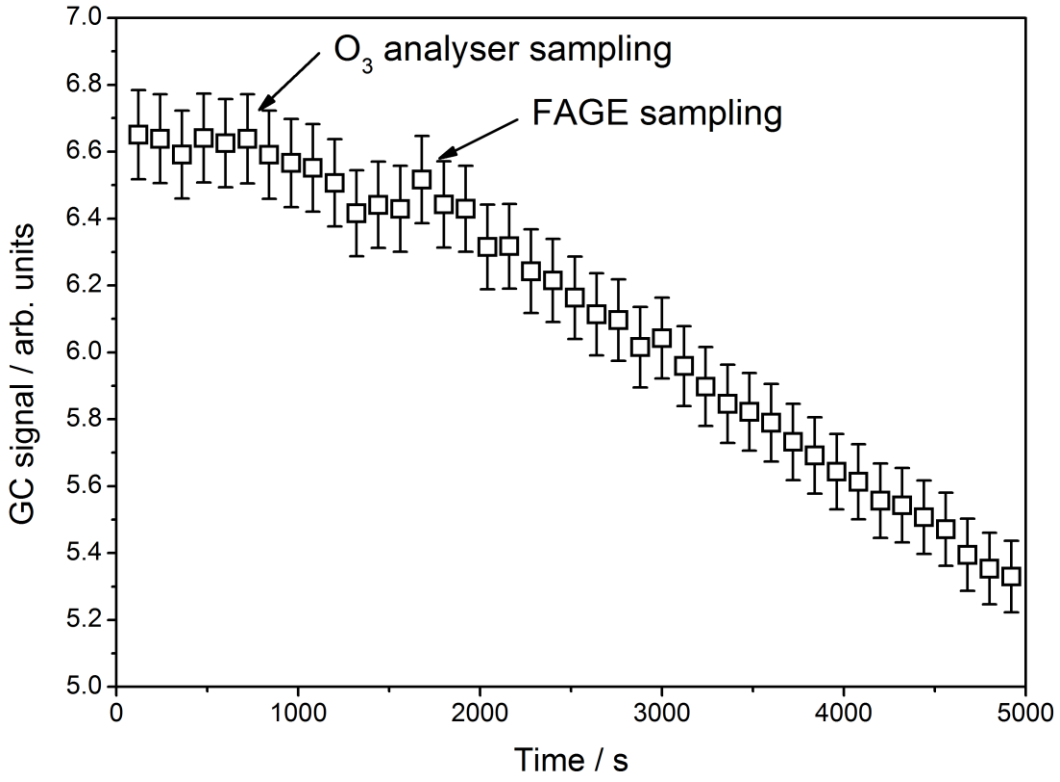

Figure 2.10: Example of chamber dilution rate based on the decay of *trans*-2-butene measured using GC-FID. Dilution commences at ~800 s with the O_3 analyser, followed at ~1800 s with the FAGE instrument. Error bars are representative of the precision of the GC-FID technique to 1σ.

2.4 References

Akimoto, H., M. Hoshino, G. Inoue, F. Sakamaki, N. Washida and M.Okuda (1979). "Design and characterization of the evacuable and bankable photochemical smog chamber " Environmental science and technology **13**(4): 471.

Barnes, I., K. H. Becker, E. H. Fink, A. Reimer, F. Zabel and H. Niki (1983). "Rate constant and products of the reaction CS_2 + OH in the presence of O_2." International journal of chemical kinetics **15**: 631-645.

Barnes, I., K. H. Becker and N. Mihalopoulos (1994). "An FTIR product study of the photooxidation of dimethyl disulphide." Journal of atmospheric chemistry **18**: 267-289.

Bohn, B., F. Rohrer, T. Brauers and A. Wahner (2005). "Actinometric measurements of NO2 photolysis frequencies in the atmosphere simulation chamber SAPHIR." Atmospheric Chemistry and Physics **5**: 493-503.

Bohn, B. and H. Zilken (2005). "Model-aided radiometric determination of photolysis frequencies in a sunlit atmosphere simulation chamber." Atmos. Chem. Phys., **5**: 191-206.

Carter, W. P. L., D. R. Cocker(III), D. R. Fitz, I. L. Malkina, K. Bumiller, C. G. Sauer, J. T. Pisano, C. Bufalino and C.Song (2005). "A new environmental chamber for evaluation of gas-phase chemical mechanisms and secondary aerosol formation." Atmospheric Environment **39**: 7768–7788.

Chernin, S. (2002). "Promising Version of the three-objective multipass matrix system." Optics Express **10**: 104-107.

Chernin, S. M. and E. G. Barskaya (1991). "Optical multipass matrix systems." Applied Optics **30**(1): 51-58.

Dodge, M. C. (2000). "Chemical Oxidant Mechanisms for Air Quality Modeling: A critical review." Atmospheric Environment **34**: 2103-2130.

Dorn, H. P., R. L. Apodaca, S. M. Ball, T. Brauers, S. S. Brown, J. N. Crowley, W. P. Dube, H. Fuchs, R. Haeseler, U. Heitmann, R. L. Jones, A. Kiendler-Scharr, I. Labazan, J. M. Langridge, J. Meinen, T. F. Mentel, U. Platt, D. Poehler, F. Rohrer, A. A. Ruth, E. Schlosser, G. Schuster, A. J. L. Shillings, W. R. Simpson, J. Thieser, R. Tillmann, R. Varma, D. S. Venables and A. Wahner (2013). "Intercomparison of NO_3 radical detection instruments in the atmosphere simulation chamber SAPHIR." Atmospheric Measurement Techniques **6**(5): 1111-1140.

Doussin, J. F., D. Ritz, R. DurandJolibois, A. Monod and P. Carlier (1997). "Design of an environmental chamber for the study of atmospheric chemistry: New developments in the analytical device." Analusis **25**(7): 236-242.

Farrugia, L. (2014). Kinetics and mechanistic studies in the HIRAC chamber. PhD, University of Leeds.

Fuchs, H., T. Brauers, H. P. Dorn, H. Harder, R. Haseler, A. Hofzumahaus, F. Holland, Y. Kanaya, Y. Kajii, D. Kubistin, S. Lou, M. Martinez, K. Miyamoto, S. Nishida, M. Rudolf, E. Schlosser, A. Wahner, A. Yoshino and U. Schurath (2010). "Technical Note: Formal blind intercomparison of HO_2 measurements in the atmosphere simulation chamber SAPHIR during the HOxComp campaign." Atmospheric Chemistry and Physics **10**(24): 12233-12250.

Glowacki, D. R., A. Goddard, K. Hemavibool, T. L. Malkin, R. Commane, F. Anderson, W. J. Bloss, D. E. Heard, T. Ingham, M. J. Pilling and P. W. Seakins (2007a). "Design of and initial results from a Highly Instrumented Reactor for Atmospheric Chemistry (HIRAC)." Atmospheric Chemistry and Physics **7**(20): 5371-5390.

Glowacki, D. R., A. Goddard and P. W. Seakins (2007b). "Design and performance of a throughput-matched, zero-geometric-loss, modified three objective multipass matrix system for FTIR spectrometry." Applied Optics **46**(32): 7872-7883.

Ianni, J. C. (2002). "Kintecus, Windows Version 2.80, www.kintecus.com." from www.kintecus.com.

Karl, M., T. Brauers, H.-P. Dorn, F. Holland, M. Komenda, D. Poppe, F. Rohrer, L. Rupp, A. Schaub and A. Wahner (2004). "Kinetic Study of the OH-isoprene and O_3-isoprene reaction in the atmosphere simulation chamber, SAPHIR." Geophysical Research Letters **31**: L05117.

Malkin, T. L. (2010). Detection of free-radicals and other species to investigate atmospheric chemistry in the HIRAC chamber Thesis (Ph D), University of Leeds (School of Chemistry), 2010.

Malkin, T. L., A. Goddard, D. E. Heard and P. W. Seakins (2010). "Measurements of OH and HO_2 yields from the gas phase ozonolysis of isoprene." Atmospheric Chemistry and Physics **10**(3): 1441-1459.

MCM. (2014). "Master Chemical Mechanism Version 3.2 (http://mcm.leeds.ac.uk/MCM)."

Nilsson, E. J. K., C. Eskebjerg and M. S. Johnson (2009). "A photochemical reactor for studies of atmospheric chemistry." Atmospheric Environment **43**(18): 3029-3033.

Nolting, F., W. Behnke and C. Zetzsch (1988). "A Smog Chamber for Studies of the Reactions of Terpenes and Alkanes with Ozone and OH." Journal of Atmospheric Chemistry **6**(1-2): 47-59.

Schlosser, E., B. Bohn, T. Brauers, H. P. Dorn, H. Fuchs, R. Haseler, A. Hofzumahaus, F. Holland, F. Rohrer, L. O. Rupp, M. Siese, R. Tillmann and A. Wahner (2007). "Intercomparison of two hydroxyl radical measurement techniques at the atmosphere simulation chamber SAPHIR." Journal of Atmospheric Chemistry **56**(2): 187-205.

Seakins, P. W. and M. A. Blitz (2011). Developments in Laboratory Studies of Gas-Phase Reactions for Atmospheric Chemistry with Applications to Isoprene Oxidation and Carbonyl Chemistry. Annual Review of Physical Chemistry, Vol 62.

S. R. Leone, P. S. Cremer, J. T. Groves and M. A. Johnson. Palo Alto, Annual Reviews. **62:** 351-373.

Shetter, R. E., J. A. Davidson, C. A. Cantrell and J. G. Calvert (1987). "Temperature Variable Long Path Cell for Absorption-Measurements." Review of Scientific Instruments **58**(8): 1427-1428.

Siese, M., K. H. Becker, K. J. Brockmann, H. Geiger, A. Hofzumahaus, F. Holland, D. Mihelcic and K. Wirtz (2001). "Direct measurement of OH radicals from ozonolysis of selected alkenes: A EUPHORE simulation chamber study." Environmental Science & Technology **35**(23): 4660-4667.

Stone, D. A. (1990). "A Controlled-Environment Chamber for Atmospheric Chemistry Studies Using FT-IR Spectroscopy." Applied Spectroscopy **44**(6): 945-950.

Tellinghuisen, J. (2003). "Precise equilibrium constants from spectrophotometric data: BrCl in Br_2/Cl_2." Journal of Physical Chemistry A **107**: 753-757.

Thuener, L. P., P. Bardini, G. J. Rea and J. C. Wenger (2004). "Kinetics of the Gas-Phase Reactions of OH and NO_3 Radicals with Dimethylphenols." Journal of Physical Chemistry A **108**: 11019 - 11025.

Wallington, T. J. and S. M. Japar (1989). "Fourier Transform Infrared Kinetic Studies of the Reaction of HONO with HNO_3, NO_3 and N_2O at 295 K." Journal of Atmospheric Chemistry **9**: 399-409.

Wang, J., J. F. Doussin, S. Perrier, E. Perraudin, Y. Katrib, E. Pangui and B. Picquet-Varrault (2011). "Design of a new multi-phase atmospheric simulation chamber for atmospheric photosmog, aerosol and cloud chemistry research." Atmospheric Measurement Techniques **4**: 2465-2494.

Chapter 3. Quantitative FTIR Analysis Techniques

3.1 Introduction

Infrared spectra are possible due to transitions between quantised vibrational energy levels, V_υ, which for diatomic molecules can be given by E 3.1, using the harmonic oscillator approximation:

$$V_\upsilon = h\nu\left(\upsilon + \frac{1}{2}\right) \qquad \text{E 3.1}$$

where υ is the vibrational quantum number, h is Planck's constant and ν is the classical vibrational frequency. Vibrations involve displacement of the atoms in a molecule from their equilibrium positions and these vibrations occur at specific frequencies, ν_i. In IR spectroscopy, molecules that undergo an overall change in dipole moment, μ, across a bond upon vibration exhibit an IR absorption at a frequency, ν_i, specific to the nature of the vibrating bond, determined by the force constant, k, and the reduced mass of the two vibrators, μ_m:

$$\nu_i = \frac{1}{2\pi}\left(\frac{k}{\mu_m}\right)^{\frac{1}{2}} \qquad \text{E 3.2}$$

The force constant is a measure of the strength of the bond, thought of classically as two balls connected *via* a spring, and is a combination of nuclear-electronic repulsions and attractions. For an allowed vibrational transition, i.e., $\Delta\upsilon = \pm 1$, there must also be a rotational transition $\Delta J = \pm 1$ (where J is the rotational quantum number). For gaseous diatomic molecules, vibrational bands consist of a series of lines where changes in J correspond to the P branch ($\Delta J = -1$) and R branch ($\Delta J = +1$). For polyatomic molecules, the spacing of lines in vibrational bands decreases and spectra become more complex as the number of vibrational modes increases ($3N - 6$ for a polyatomic molecule compared to one for diatomic molecules). Transitions of $\Delta J = 0$ (Q branch) are permitted for polyatomic molecules when a mode of symmetry within the molecule is lost (e.g., the ν_2 bend in CO_2) and in diatomic molecules which possess electronic angular momentum in the ground state, such as NO. As the ro-vibrational transitions are specific to the nature of the bond being vibrated (atoms involved, surrounding functional groups etc.), each molecule that exhibits an IR absorption has a unique spectrum that can be assigned.

FTIR spectrometers use an interferometer, which is based on the widely known and historical Michelson interferometer (see Figure 3.1). A light source is divided into two separate beams using a beam-splitter. After reflection from two distinct mirrors, one fixed and one movable, the beams are recombined at the same beam-splitter and sent to a detector. When the mirrors are equidistant from the beam-splitter (i.e., MO = FO in Figure 3.1), also known as the zero-path-difference point (ZPD), the two beams travel the same distance before reaching the detector. Altering the distance between the movable mirror and the beam-splitter results in a change in total distance travelled to the detector for one of the beams. This additional distance is called the retardation.

For a monochromatic light source, movement of the mirror would result in easily visible constructive and destructive interference at the beam-splitter, as the two beams are moved in and out of phase. With a broadband source the process is similar, and can be where multiple wavelengths of light are all interfering with each other, weighted to their relative spectral intensity. At the ZPD, constructive interference is at a maximum, and as retardation increases, the intensity of the beam at the detector decreases as a function of the multiple convolved frequencies. The detected intensity of the beam that reaches the detector is measured as a function of retardation and this is known as the interferogram. Computing the cosine Fourier transform of the interferogram allows the conversion of measured signals from the time (or distance) domain to the frequency domain, where the intensity of the light can be displayed as a function of wavenumber (cm^{-1}).

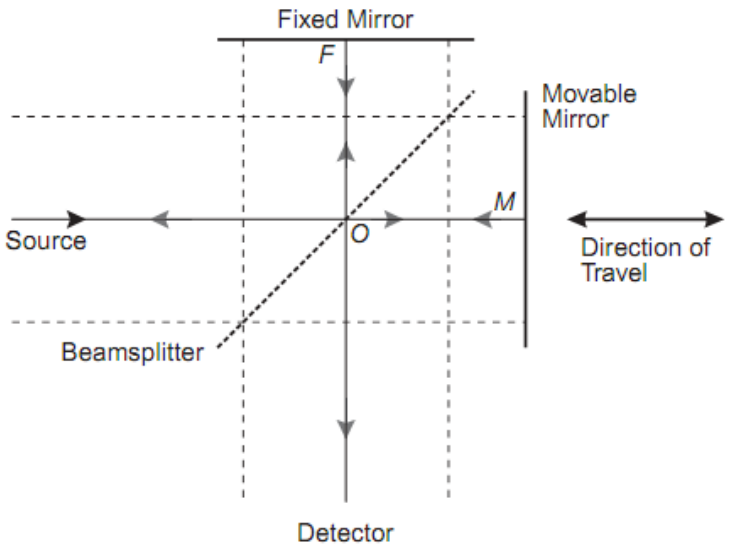

Figure 3.1: Example of a simple Michelson interferometer, reproduced from Griffiths and de Haseth (2007).

The above discussion relates to FTIR in its simplest form, however in reality a series of mathematical algorithms are applied to the interferogram before the Fourier transform takes place. Imperfections in the instrument, such as mirror misalignment, can lead to erroneous readings from phase or time delays, which are compensated by phase corrections. The interferogram can only be measured over a finite retardation range, and its truncation leads to spectral leakage: the creation of artificial spectral features due to the Fourier transform of a sudden transition to zero. Spectral leakage, or the spectral "feet", is minimised by applying an apodisation function that ensures the interferogram intensity smoothly decreases to zero over a given retardation, the distance which defines the resolution of the resultant spectrum (as the two are inversely related). These factors define the instrument line shape (ILS) which is applied to all spectra taken and can be modified by the user, depending on their requirements.

Gas phase Fourier transform infrared spectroscopy is a fast and robust measurement technique that has enjoyed success in many kinetic chambers (Akimoto et al., 1979; Barnes et al., 1983; Shetter et al., 1987; Wallington and Japar, 1989; Barnes et al., 1994; Bloss et al., 2004; Thuner et al., 2004; Bardini et al., 2005). Enhanced by the inclusion of multipass optics to create longer pathlength cells (see chapter 2 for a description of the HIRAC multipass system), atmospheric chambers can reach detection limits down to ~10 ppbv (cross-section dependent). Spectral calculators and databases exist with

collections of hundreds of spectra, and many allow calculation of or give cross-sections for quantitative analysis (Chu et al., 1999; Jacquinet-Husson et al., 2004; Sharpe et al., 2004; Rothman et al., 2009; SpectraCalc, 2011).

Quantitative analysis is an easy task; in principle. Beer's law shows that for a given species at a given wavelength, absorption, *Abs*, and concentration, [*c*], are directly proportional (*Abs* ∝ [*c*]), assuming a constant path length, *l*, and absorption cross-section, σ:

$$Abs = \log_{10}\left(\frac{I_0}{I}\right) = \sigma\,[c]\,l \qquad \text{E 3.3}$$

where I and I_0 are the light intensity before and after the sample respectively. Therefore, with an accurate measurement of l and σ, this linear relationship can be used to quantitatively analyse IR spectra.

The simplest form of quantitative analysis is integration (section 3.1.1). The area or height of a specific absorption band can be calculated to determine the concentration using a known cross-section. Ideally, this method relies on an isolated absorption band (univariate); a rare phenomenon in complex chamber studies. When two or more spectral features from separate compounds overlap (a multivariate system), integration for quantitative analysis is harder and can be subject to large uncertainties from potential changes in absorption from secondary species. For binary or tertiary systems, a simple spectral subtraction can isolate a single peak (section 3.1.2). This method relies on reference spectra for subtraction, and hence can provide a direct route to determine a concentration through the multiplication factor of a given reference. This is most effective when the species forming the convolved spectrum are known and can be easily identified.

Where more than three known compounds are present in a system there are linear regression techniques that can estimate the concentration of the separate components, instead of manual subtraction. This process forms part of a field of Chemometrics. Figure 3.2 shows a flow diagram depicting the decision making process for various matrix-math based multivariate analysis techniques. The most common is the Classic Least Squares (CLS) or K-matrix method which finds the best fit of the supplied reference spectra to the sample spectrum (section 3.1.3). However, the system cannot be accurately analysed if there are unknown components of the sample spectra.

Methods that do not require all species in the multivariate system to be known are grouped under Inverse Least Squares (ILS) or P-matrix analysis (right hand side of Figure 3.2). Based closely on CLS, only the sample spectrum of interest is required. Due to the matrix mathematics involved, the wavelength range for ILS analysis cannot exceed the number of samples; i.e., if there are 15 samples fitted to a multivariate peak, then only 15 wavelengths can be analysed. Therefore, if the number of components to be analysed is small then Multiple Linear Regression (MLR) can be used (section 3.1.4).

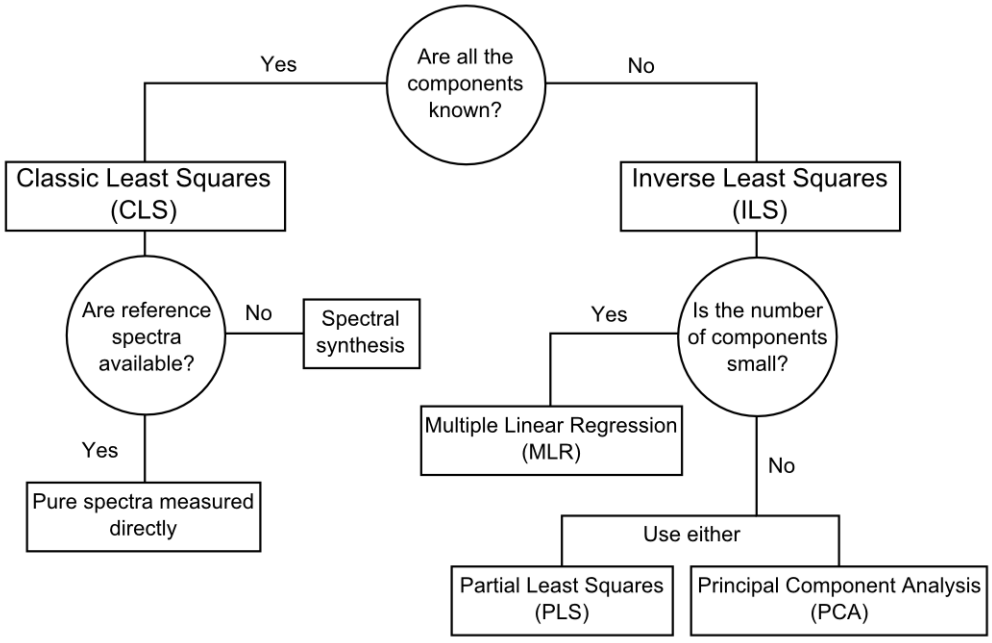

Figure 3.2: Flow diagram showing the decision process for the best multivariate FTIR spectra analysis method based on whether all components of the convolved spectrum are known.

For a larger multivariate system, Principal Component Analysis (PCA) offers a solution (section 3.1.5). Factor analysis reduces the dimensionality of the spectrum, optimising the Principal Component Regression (PCR, a form of ILS) performed afterwards. The intricacies of PCA and PCR are beyond the scope of this chapter and are therefore only

discussed briefly here. Further details can be found in Kramer (1998) and Griffiths and de Haseth (2007).

Section 3.3 outlines the development of a new quantitative spectral analysis tool using LabVIEW. The software uses CLS and non-linear least squares (NLLSQ) methods of fitting to analyse convoluted spectra and this program has been applied, so far, to two experimental systems. Firstly in a proof-of-concept system in collaboration with Farrugia (2014), where the rate coefficient of *n*-butane and *iso*-butane upon reaction with Cl atoms was investigated using the relative rate method as a function of temperature (section 3.4.1), followed by application to the product detection from the reaction of acetylperoxy and HO_2 radicals (section 3.4.2 and chapter 7). Whilst the CLS fitting method was the driving force of the software, uncertainties and non-positive concentrations led to the development of the NLLSQ method (section 3.3.1). This method formed part of a continuing project to develop the software to fit spectral stretch and shift parameters based on spectral parameters as a function of pressure and temperature. This would eventually allow the calculation of "synthetic" spectra from line parameter databases such as HITRAN.

Much care was taken with selection and construction of reference spectra. Any imperfections (baseline drift, for example) or impurities can lead to improper assignment or quantification. This will be discussed further in section 3.2. All spectra displayed here were taken using a Bruker IFS/66 spectrometer coupled to the Chernin style multipass optics inside the HIRAC chamber (see chapter 2 for full instrumental description).

3.1.1 Peak area/height analysis

Peak area or height analysis required the identification of an absorption peak that belonged uniquely to one species and this was only possible: (i) for simple systems that contained very few reactants and products (e.g., binary reactions), (ii) analysing regions of the spectrum where absorptions are limited (e.g., 2000 - 2500 cm^{-1}), or (iii) by analysing absorptions from diatomics which are very well resolved in the IR. Problems arose when species containing similar functional groups were present (C=O or C-H bonds); common for a typical VOC oxidation experiment in HIRAC. If an absorption peak was isolated, area and height measurements were taken with Opus 5.5 from Bruker. Various integration methods exist and were used to account for several experimental systematic changes in the recorded IR spectra (e.g., baseline shift). Integration of the peak allowed quantitative analysis using an integrated cross section from a reference spectrum over the same wavenumber range. Reference spectra were taken as per the instructions in section 3.2.

Figure 3.3a shows the integration of the C-H stretch of iso-butene, used as a chemical tracer in the newly developed determination of FAGE instrument sensitivity to OH using HIRAC (chapter 6). Using an absorption cross-section measured in HIRAC, integration of this peak was used to calculate the [*iso*-butene] over time and was compared to that from GC-FID, shown in Figure 3.3b. Good agreement was observed between both instruments, well within the uncertainty associated with the GC measurements (~2 - 5%). A larger precisional variation in [*iso*-butene] measured by FTIR spectroscopy was observed due to integration of the C-H stretch close to the detection limit (~2×10^{-3} Absorbance units).

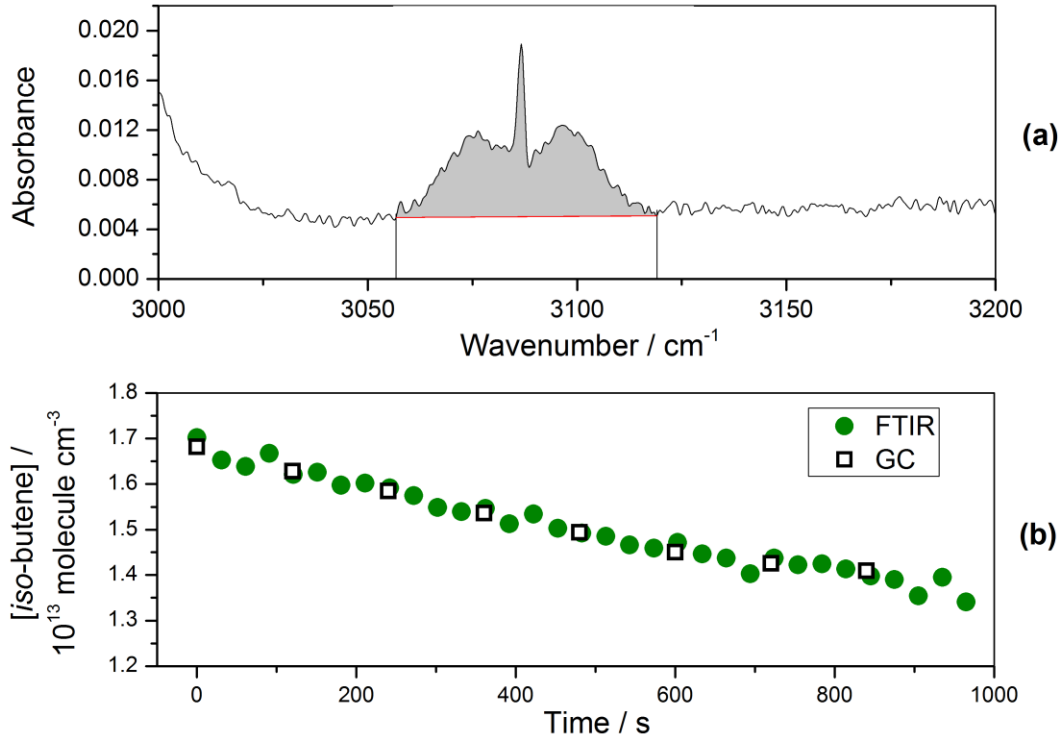

Figure 3.3: Using integration in IR spectra quantitative analysis. (a) Integration for C-H stretch of *iso*-butene where the grey shaded area shows integration using 2-point interpolated baseline, in red. Due to the integration method used, the spectrum was not corrected for the non-zero baseline offset. Spectrum taken at 1000 mbar, 293 K with 40 averaged scans at 1 cm^{-1} resolution using the Happ-Genzel apodisation. (b) Comparison of the quantification of [*iso*-butene] using FTIR, with the integration method described in the text, and GC-FID. False origin used to highlight agreement between measurement techniques.

3.1.2 Spectral subtraction

Subtraction was used to separate multivariate spectra, determining multiplication factors of reference spectra as an alternative to integration. A univariate system where $A_0(\nu)$ was the absorbance of compound A at time = 0 and $A_t(\nu)$ at time = t, both for a given wavenumber, ν, $A_0(\nu)$ was scaled linearly using a factor, γ, determining the change in absorbance over time. This was evaluated using equation E 3.4:

$$A_t(\nu) - \gamma A_0(\nu) = R(\nu) \qquad \text{E 3.4}$$

where $R(\nu)$ was the residual, and should equal zero. If the concentration of the initial sample was known then the concentration at time t was also scaled with the same factor

γ. The subtraction was not restricted to the initial absorbance measurement as a well characterised reference spectrum could be used (discussed further in section 3.2). This method was also applicable to absorbance measurements over a range of wavenumbers, where the residual becomes important as an indication of the quality and success of the subtraction. This method was also applied to multivariate systems, where compounding absorbances were considered a mixture of different absorbers, $M(\nu)$:

$$M(\nu) = A_1(\nu) + A_2(\nu) + A_3(\nu) \ldots + A_i(\nu) \qquad \text{E 3.5}$$

The subtraction of a common element, e.g., A_1, could simplify this system, depending on the total number of component spectra, i:

$$M(\nu) - A_1(\nu) = A_2(\nu) + A_3(\nu) \ldots + A_i(\nu) \qquad \text{E 3.6}$$

Subsequent subtractions proved difficult or useless as the accuracy of quantitative analysis on highly convolved spectra decreased with each subtraction. As systematic errors accumulated, the residual became non-zero and distorted, with remaining components unidentifiable in the residual. When using spectral subtraction, much care must be taken into the quality of reference and sample spectra used, as well as considering the quantity of sample components.

A simple example is shown in Figure 3.4 where the $2\nu_8$ overtone band of methanol, CH_3OH, overlapped with CO between 1980 and 2140 cm^{-1}. A CH_3OH reference spectrum was used for subtraction, leaving the residual displayed in Figure 3.4b. The advantage of having one very well resolved component, in this case the CO, in a two species problem can clearly be seen from the quality of the subtraction. The multiplication factor used to scale the CH_3OH absorption was also a quantitative measure as the reference concentration was already known.

Manual subtraction becomes more limited for a complex multivariate system and section 3.4 compares manual subtraction of increasingly complex systems to the automated least squares regression fitting procedure described in the following section.

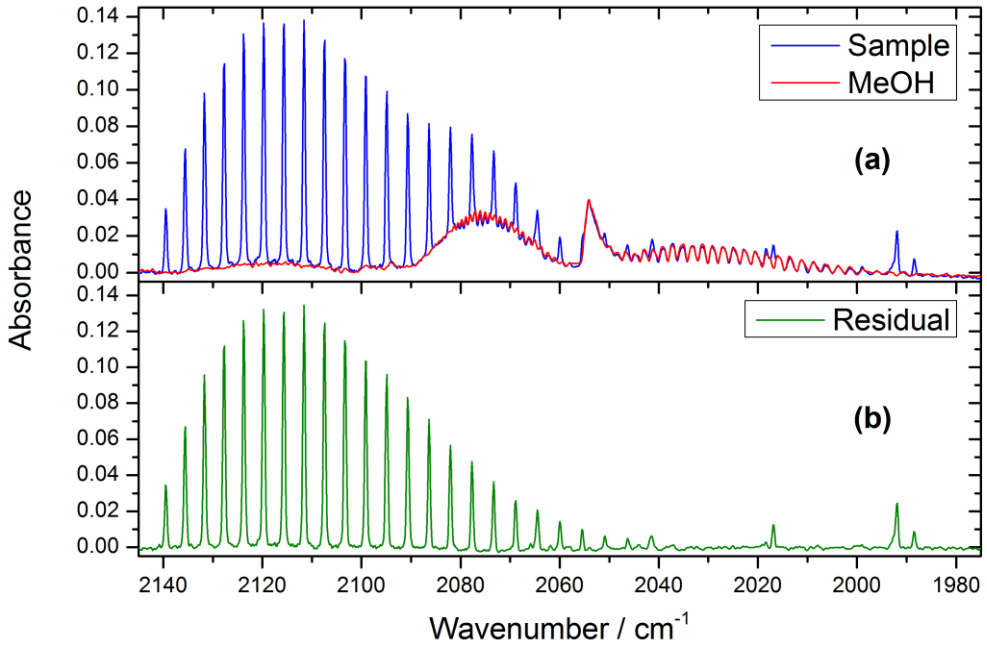

Figure 3.4: (a) The convoluted well-structured R branch of CO with the overtone $2\nu_8$ band of CH_3OH (blue) and the CH_3OH reference spectrum to be subtracted (red). (b) The residual plot resulting from spectral subtraction. All spectra taken at 1000 mbar in air at 293 K and 0.5 cm^{-1} resolution.

3.1.3 Classic Least Squares (CLS)

The CLS method used a linear least squares approximation based on the proportionality of absorbance and concentration, and has been applied to multivariate spectral analysis with up to six components. The total absorbance, $A(\nu_i)$ (the sample), can be expressed in terms of the sum of a set of absorbances (reference spectra), $a_{j,\nu i}$:

$$A(\nu_i) = \sum_{j=1}^{i} a_{j,\nu_i}\,\gamma_j \qquad \text{E 3.7}$$

Each $a_{j,\nu j}$ has its own unique scaling factor, γ_j, that is unknown. Assuming the total absorption of a sample was due to two references at two discrete wavenumbers, ν_1 and ν_2, the following simultaneous equations were solved for $\gamma_{x,\nu i}$:

$$A(\nu_1) = a_{1,\nu_1}\ \gamma_1 + a_{2,\nu_1}\,\gamma_2 \qquad \text{E 3.8}$$

$$A(\nu_2) = a_{1,\nu_2}\ \gamma_1 + a_{2,\nu_2}\,\gamma_2 \qquad \text{E 3.9}$$

This model was not applicable to an FTIR sample spectrum taken over a wide range of wavenumbers as simultaneous equations would have to be tediously written to the i^{th} wavenumber. Matrix notation shortened the process. Equations E 3.8 and E 3.9 became:

$$\mathbf{a} = \mathbf{A}\ \mathbf{k}_{\mathbf{unk}} \qquad \text{E 3.10}$$

where **a** and $\mathbf{k}_{\mathbf{unk}}$ are the column vectors containing the sample absorbance data and the unknown scaling factors, and **A** is the matrix containing the absorbance data of the reference components. As **A** was unlikely to be a square matrix (i.e., there were as many reference components as absorption points), solving for $\mathbf{k}_{\mathbf{unk}}$ involved multiplication of both sides of equation E 3.10 by the transpose of **A**, $\mathbf{A}^{\mathbf{T}}$:

$$\mathbf{A}^{\mathbf{T}}\ \mathbf{a} = \mathbf{A}^{\mathbf{T}}\ \mathbf{A}\ \mathbf{k}_{\mathbf{unk}} \qquad \text{E 3.11}$$

As **A** is singular (i.e. a non-square matrix) and therefore has no inverse. Multiplying E 3.11 by the inverse matrix $\mathbf{[A^T\ A]^{-1}}$ produces the pseudo inverse of matrix **A**, $\mathbf{[A^T\ A]^{-1}\ A^T}$ (E 3.12), which, when left multiplied by the parent matrix, **A**, produces the identity matrix (i.e. unity), simplifying E 3.12 to E 3.13:

$$\mathbf{[A^T\ A]^{-1}\ A^T\ a} = \mathbf{[A^T\ A]^{-1}\ A^T\ A\ k_{unk}} \qquad \text{E 3.12}$$

$$\mathbf{[A^T\ A]^{-1}\ A^T\ a} = \mathbf{k_{unk}} \qquad \text{E 3.13}$$

Therefore, the vectors of reference spectra scaling factors, $\mathbf{k}_{\mathbf{unk}}$, was calculated for a given sample spectrum and set of reference spectra. Assuming that the sample spectrum contained no unknowns left this method vulnerable to large uncertainties and miscalculations of multiplication factors. As the algorithm looked for the best linear fit to a sample spectrum based on given component spectra, it will over or under fit component spectra if an unknown is absorber is present. Error analysis and careful study of the residual can often identify the presence of an unknown.

There are adaptations of CLS to help with the quantification of unknowns, such as the non-zero intercept method (Beebe et al., 1998), but they will not be discussed here as there is a non-CLS alternative that is more versatile with respect to unknowns; the Inverse Least Squares method. The following methods are discussed briefly here but have not been implemented for analysis of FTIR data from the HIRAC chamber.

3.1.4 Inverse Least Squares (ILS): the Multiple Linear Regression method (MLR)

Using similar matrix manipulation to the CLS method, the Inverse Least Squares regression allows the calculation of the vector of unknown scaling factors, $\mathbf{k_{unk}}$, for an unknown vector of the sample spectrum, $\mathbf{a_{unk}}$. This requires the **P** matrix (E 3.15), which contains the necessary coefficients to evaluate the vector, $\mathbf{k_{unk}}$, of reference spectra multiplication factors. First, **P** is calculated from the matrix containing all the reference spectra, **A** (not the sample spectrum), and the vector of their relative scaling factors, **k** (E 3.14 and E 3.15). The **k** vector has one entry for each reference, while **A** is a square matrix that has one row for each component and one column for each wavenumber.

$$\mathbf{k} = \mathbf{P}\ \mathbf{A} \qquad \text{E 3.14}$$

Equation E 3.14 is rearranged for **P**:

$$\mathbf{P} = \mathbf{k}\ \mathbf{A}^{\mathbf{T}}\ [\mathbf{A}\ \mathbf{A}^{\mathbf{T}}]^{-1} \qquad \text{E 3.15}$$

The **P** matrix is then used for the determination of unknown scaling factors, $\mathbf{k_{unk}}$, from the desired sample spectra, $\mathbf{a_{unk}}$:

$$\mathbf{k_{unk}} = \mathbf{P}\ \mathbf{a_{unk}} \qquad \text{E 3.16}$$

The ILS method has one major advantage over CLS as it does not require the spectra of all the components of $\mathbf{a_{unk}}$ to evaluate a single reference spectrum multiplication factor, γ. However, unlike the CLS method where the number of absorbances could essentially be increased without limit as they are the dependent variable, in ILS the absorbances become the independent variable and the matrix algebra requires that the columns in **A** cannot exceed the number of rows (as the inverse of $\mathbf{[A\ A^T]}$ would be impossible). Therefore, the number of absorbances cannot exceed the number of calibration spectra.

Selecting the best absorbances for each species is difficult and can require complex algorithms. By averaging the data over a set number of bins, equal to the number of component spectra to be used, the dimensionality of the data is reduced and can be analysed using ILS. This process loses spectral information and the averaged bins may not contain significant spectral features of analysed components. The optimization of data that is required for ILS creates a more challenging analysis technique. Principal

Component Analysis (PCA) and Partial Least Squares (PLS) are two methods that are able to reduce the dimensionality of the spectra without averaging the data into bins.

3.1.5 PCA and PLS

The PCA and PLS methods are more robust than the CLS when unknown components are present in samples. PCA uses factor space to separate the sample spectra into orthogonal components sorted according to variance (not the same as the component spectra) where the dimensionality can be optimally reduced without degrading the quality of data. Using a calibration matrix of reference compounds, as in the calculation of the **P** matrix (section 3.1.4, E 3.15), the components calculated in the PCA analysis are applied to the calibration set to determine the **k** vector of scaling factors. This method is limited, however, as the factors that are identified will contain features of multiple IR absorption spectra, and will not directly relate to one unknown.

Taking the PCA a step further is PLS, which calculates factors for both absorption and concentration. This enhances the noise removal capabilities of PCA, however the reference spectra required are much more complicated. Instead of having individual component reference spectra, mixtures of the required components must be made and measured. These cannot be linear mixtures (i.e., several dilutions of a concentrated mixture) and must contain varying concentrations of each component. This is time consuming, especially if there are a large number of samples to be analysed.

3.1.6 Spectral synthesis for quantitative analysis

Synthetic calibration spectra generated from line parameter sets have long been a practice of FTIR spectroscopists who are unable to take reference spectra for sample quantification, such as solar FTIR (Griffith, 1996). Synthesising component spectra is difficult, as the line set databases do not account for environmental (pressure, temperature etc.) and instrumental parameters (line shape, resolution, wavelength shift etc.). Previous methods used line parameters sets, such as HITRAN (Rothman et al., 2009), in conjunction with an iterative non-linear least squares (NLLSQ) fitting method,

varying environmental parameters to best fit the components to the sample. However, this process was very computer intensive and not very time efficient.

A program, MALT (Multiple Atmospheric Layer Transmission), was developed at the University of Wollongong (Griffith, 1996) which calculates reference spectra from line parameter sets such as HITRAN. Spectral lines are a combination of Gaussian and Lorentzian line shapes from well-defined environmental and instrumental properties. The line parameters are therefore corrected for temperature, pressure, wavelength shift, instrument line shape and the resolution of the measured sample spectrum, to produce a "synthetic" reference spectrum. This set of synthetic data is then used in a quantitative CLS calculation, which is faster and of comparable precision to traditional methods.

3.2 Reference Spectra - Guidelines

The wrong choice of reference spectra could lead to inaccurate quantitative analysis of a sample spectrum. Several factors must be considered before using the reference spectrum as it depends on both environmental and instrumental parameters. When a spectrum is taken from a database, or another source, all relevant data must be included so that the spectra can be corrected for pressure, temperature and instrument line shape, if needed. This can often result in degradation of the spectrum and should be avoided, if possible.

Reference spectra for experiments described in this thesis were taken using HIRAC at a 0.5 cm^{-1} resolution in a bath gas of N_2 at 293 K. Species were injected into the chamber *via* the gas delivery line or direct liquid injection (depending on the vapour pressure, see chapter 2). Conducting the reference spectra measurements in HIRAC removed the need for cross-section calculations from small cell measurements (l = 10 cm) and later application to absorption measurements in the chamber; a procedure that could induce extra error in quantitative measurements. Griffiths and de Haseth (2007) investigated various apodisation functions and their effects on the linearity of Beer's law with increasing absorbance. One of the best functions to show linear behaviour up to Abs = 2 was the Happ-Genzel apodisation and this was adopted for the work discussed here.

3.3 Software Development

The following sections outline the development and implementation of a new IR spectral analysis tool. Quant2 used the CLS method of spectral analysis (section 3.1.3), as well as an adapted NLLSQ algorithm, to fit multivariate sample spectra taken in HIRAC with a set of known reference spectra, determining their concentrations. The NLLSQ fitting procedure was developed with the scope of automatically fitting any spectral shift and lineshape "stretching" due to temperature and pressure effects inside HIRAC, as described in section 3.1. However, due to time constraints this was not possible and so the initial implementation will be discussed in section 3.3.1. Commercial chemometric software alternatives are available and were considered, however the high price of the software and technical support was a deterrent. Often commercial software can act like a "black box", where a degree of control over the data manipulation is lost. By developing the software, the exact data handling procedure is known and understood, adding confidence to the end result.

The software was written in LabVIEW which has its roots in data acquisition and real-time display, as well as containing a suite of matrix manipulation modules which facilitated the analysis procedure. A comprehensive user interface was constructed which was used to evaluate the fitting quality in "real-time", allowing the user to improve fitting parameters before committing the data to memory. Figure 3.5 shows the graphical user interface (GUI) for Quant2. The main window was divided into two halves: the top displayed plots of the sample, fitted and residual spectra, while the bottom display contained tabulated data relating to each loaded sample (e.g., file time, time etc.). Whilst it is not yet possible to view the contributions of individual spectra in the software, examples of this are shown in section 3.4.2.

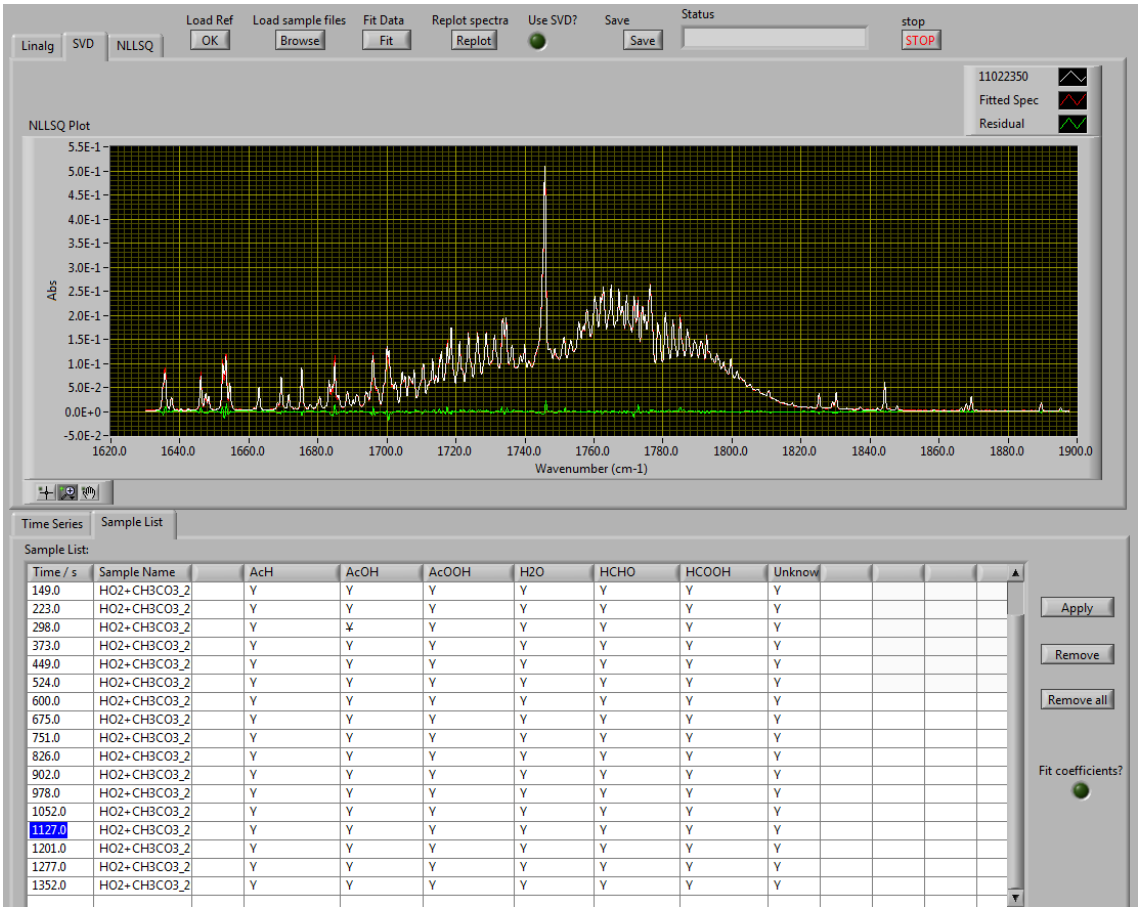

Time / s	Sample Name	AcH	AcOH	AcOOH	H2O	HCHO	HCOOH	Unknow
149.0	HO2+CH3CO3_2	Y	Y	Y	Y	Y	Y	Y
223.0	HO2+CH3CO3_2	Y	Y	Y	Y	Y	Y	Y
298.0	HO2+CH3CO3_2	Y	¥	Y	Y	Y	Y	Y
373.0	HO2+CH3CO3_2	Y	Y	Y	Y	Y	Y	Y
449.0	HO2+CH3CO3_2	Y	Y	Y	Y	Y	Y	Y
524.0	HO2+CH3CO3_2	Y	Y	Y	Y	Y	Y	Y
600.0	HO2+CH3CO3_2	Y	Y	Y	Y	Y	Y	Y
675.0	HO2+CH3CO3_2	Y	Y	Y	Y	Y	Y	Y
751.0	HO2+CH3CO3_2	Y	Y	Y	Y	Y	Y	Y
826.0	HO2+CH3CO3_2	Y	Y	Y	Y	Y	Y	Y
902.0	HO2+CH3CO3_2	Y	Y	Y	Y	Y	Y	Y
978.0	HO2+CH3CO3_2	Y	Y	Y	Y	Y	Y	Y
1052.0	HO2+CH3CO3_2	Y	Y	Y	Y	Y	Y	Y
1127.0	HO2+CH3CO3_2	Y	Y	Y	Y	Y	Y	Y
1201.0	HO2+CH3CO3_2	Y	Y	Y	Y	Y	Y	Y
1277.0	HO2+CH3CO3_2	Y	Y	Y	Y	Y	Y	Y
1352.0	HO2+CH3CO3_2	Y	Y	Y	Y	Y	Y	Y

Figure 3.5: GUI for the Quant2 program developed in LabVIEW. Buttons to control the loading of sample and reference spectra and saving of files are located at the top along with a plot displaying the sample spectrum (white), fitted spectrum (red) and the residual (green). Below is the table which displays the time, name and reference spectra used in the analysis for each sample.

The table was used to identify the active fit components in the analysis of the respective sample file. Buttons to the top of the graph control the loading of sample and reference spectra as well as saving the fitting output and quitting, whereas buttons around the table controlled the addition or removal of reference spectra from the fitting routine. A time dependent reaction profile was displayed in a separate tab with the table in the lower half of the GUI, shown here in Figure 3.6. The graphical display tools offered by LabVIEW were invaluable in this regard, making sure each sample spectrum, data fit and residual was clearly displayed.

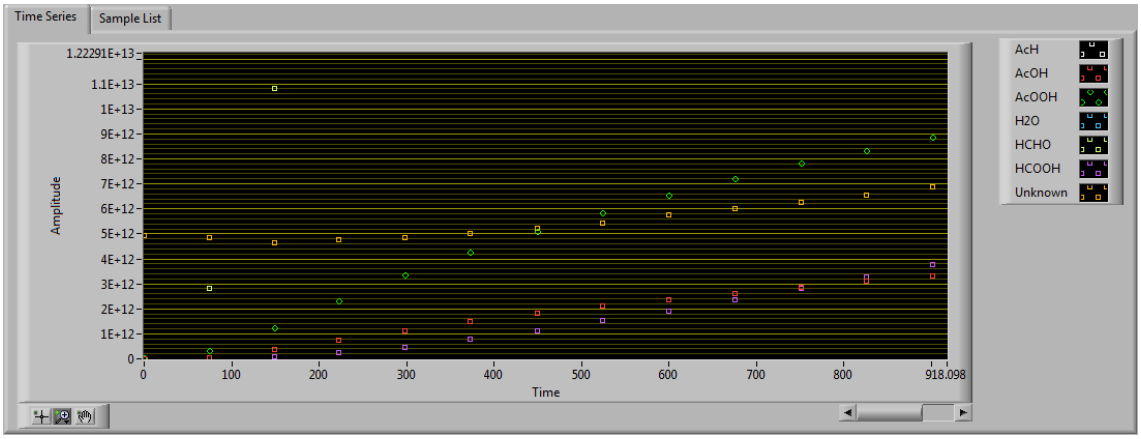

Figure 3.6: Time series window if the Quant2 program displaying the time dependent concentration information for each reference spectrum.

Figure 3.7 shows a flow chart of the software's general procedure. The references and sample spectra were loaded into Quant2, at which time the fitting procedure was initiated and output was subsequently displayed on the GUI. If any further manipulations were required (such as adding or removing a reference compound) then the fitting procedure is run again (path (a)), until the user stops the program or saves the data (path (b)). In the current software revision, this process is linear and every time an experimental data set is analysed, the software must be stopped and all the reference spectra re-loaded.

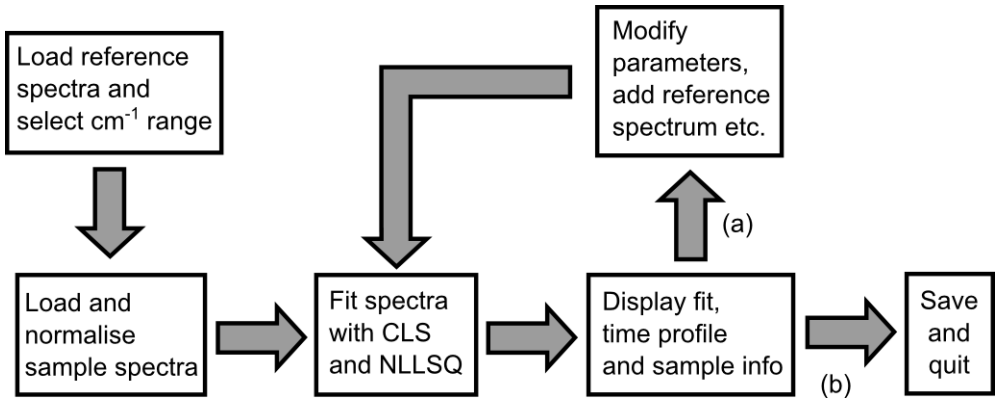

Figure 3.7: Flow diagram representing the operational procedure of the Quant2 software. Options (a) and (b) are dependent on the user judged quality of the fitting procedure, where (a) is a poor fit and (b) is a satisfactory fit.

Reference spectra were chosen from a database of species, taken *in situ* using the HIRAC FTIR system. References were prepared using the OPUS software to correct any baseline shift and zero correction, and exported using a custom-made macro in text format. The text file contained both the spectrum and additional information such as concentration, date, resolution etc., which was interpreted by the LabVIEW code in order to calculate concentrations after the fitting procedure. The entire spectrum was not fitted however, and so at this stage the user was prompted to select the desired wavenumber range, using the reference spectra as a guide. Figure 3.8 shows the reference spectrum load window, in which the wavenumber range is chosen by using two sliders to clearly mark the desired region of the spectrum. Sample spectra were prepared using OPUS and loaded into LabVIEW, automatically initiating the fitting procedure using both the CLS and NLLSQ algorithms.

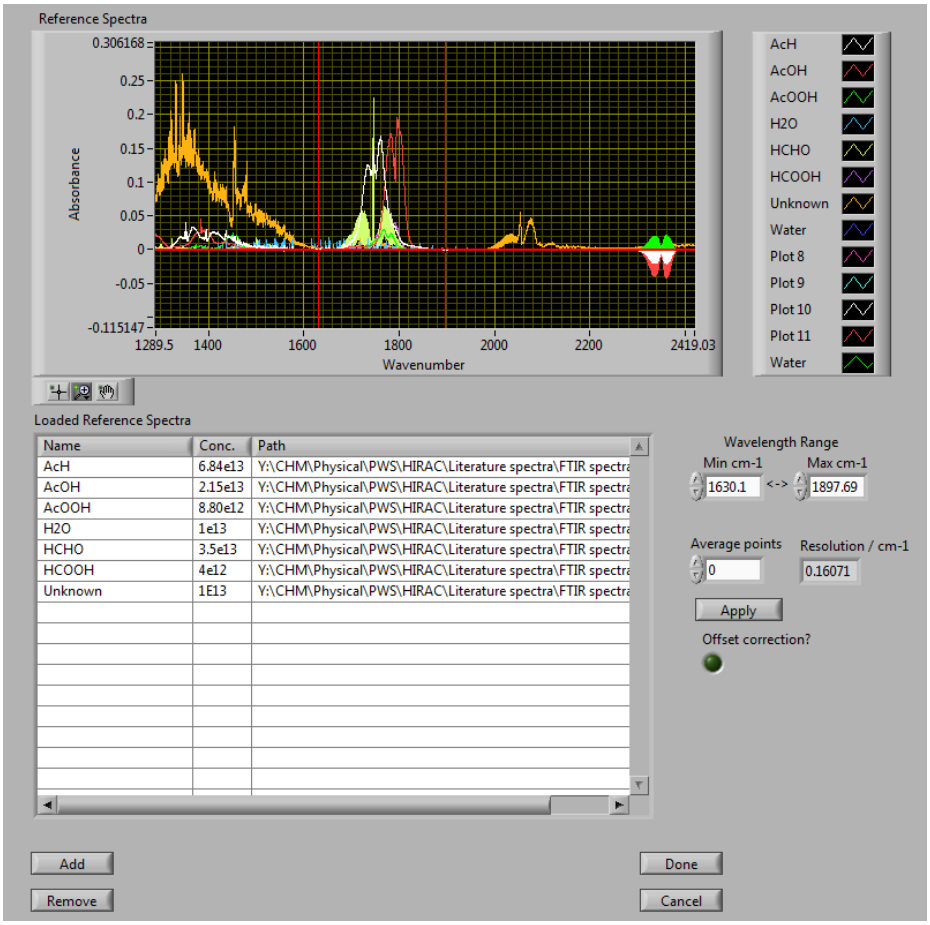

Figure 3.8: Load screen for reference spectra in Quant2. Vertical red lines show the desired wavenumber range for analysis.

The saved output file contains the sample name, time and reference compound concentrations in TAB delimited format that can be easily loaded into any data analysis tool, such as MS Excel.

3.3.1 Non-linear least-squares fitting algorithm

Figure 3.9 pictorially represents the NLLSQ fitting process in flow chart form. The sample spectra were loaded and fit with the desired reference spectra using an initial estimate (user input) of the multiplication factors, γ, for the respective references. A Levenberg-Marquardt (LVM) fitting method was used, which aimed to minimise the χ^2 parameter by determining the next best estimate of the multiplication factors. This process was repeated until the convergence criterion was satisfied ($\Delta\chi^2 < 1 \times 10^{-6}\%$), and the sample, fit and residual were displayed along with the time profile for each species.

The NLLSQ fitting procedure has one major advantage over the previously used CLS method. Linear fitting methods will determine the best set of multiplication factors, irrespective of whether these factors are negative. Whilst there is potential for there to be a negative absorption due to a decrease in a background component, it is rare to see this in anything other than H_2O vapour and CO_2 (the decrease was from change in composition of laboratory N_2 purging the spectrometer and optical coupling box (see chapter 2)). The LVM algorithm has been modified to only accept best estimates of multiplication factors that are positive, constraining and improving the accuracy of the fits.

This method also outputs various statistics that can be useful for uncertainty analysis such as the χ^2 parameter, judging the goodness of fit. No measure is given for the equivalent CLS. Uncertainty analysis is discussed more in section 3.5.

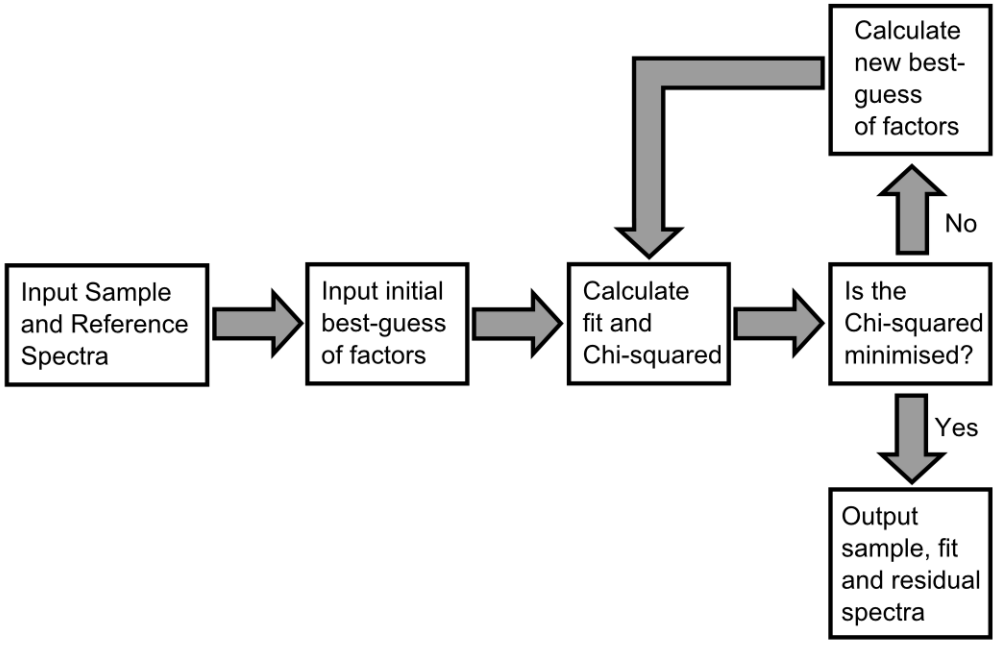

Figure 3.9: Flow diagram of the iterative NLLSQ fitting procedure.

3.4 Results and discussion

Results discussed in section 3.4.1 are from recent experiments into the rate of reaction of *n*-butane, *iso*-butane, *n*-pentane and *iso*-pentane with Cl atoms conducted in HIRAC by Farrugia (2014). Firstly, hydrogen abstraction rate constants were determined by monitoring the decay of the chosen hydrocarbon relative to ethane (relative rate method) as a function of temperature. Secondly, the study focussed on the site specific hydrogen abstraction products in N_2, determining the branching ratios. The results measured using GC-FID and FTIR are compared and discussed. Experimental details and results are discussed here briefly, and more detail and the success of the study can be found in Farrugia (2014). A second section (3.4.2) discusses the fitting quality compared to manual subtraction from the investigation into the acetylperoxy radical reaction with HO_2 in chapter 7.

3.4.1 Reaction of Cl atoms with butane isomers

Farrugia (2014) recently completed an investigation into the rate of reaction of Cl atoms with butane and pentane isomers as a function of temperature. Chlorine atoms were generated by constant photolysis (central λ = 360 nm) of Cl_2 and all experiments were conducted in 1000 mbar of N_2 which promoted radical chain propagation through alkyl radical reactions with molecular chlorine producing halogenated alkanes (R 3.1 - R 3.3).

$$Cl_2 + h\nu \rightarrow 2Cl \qquad \text{R 3.1}$$

$$R\text{-}H + Cl \rightarrow R + HCl \qquad \text{R 3.2}$$

$$R + Cl_2 \rightarrow R\text{-}Cl + Cl \qquad \text{R 3.3}$$

The hydrocarbons used were *n*-butane and *iso*-butane. Reactants and products were quantified using both calibrated GC-FID and FTIR instruments. Sample IR spectra were recorded as the average of 100 scans (~70 s per sample) at 1 cm^{-1} resolution and reference spectra were taken of the pure compounds at 0.5 cm^{-1} in the HIRAC chamber for continuity by Farrugia (2014). Spectra were recorded for *n*-butane, 1-chlorobutane, 2-chlorobutane, *iso*-butane, 1-chloro-2-methylpropane, 2-chloro-2-methylpropane, ethane, chloroethane and methane. Concentrations were determined from FTIR spectra

by fitting with the Quant2 package in the C-H stretch region of the IR spectrum between 2800 - 3100 cm^{-1}.

Good fits were observed for data from the butane isomers due to the limited isomers of primary halogenated products and the availability of the reference spectra. The rates of reaction for *n*-butane and *iso*-butane were determined using the relative rate method, with ethane as a reference. The relative rate method is described briefly in chapter 6. Good agreement between GC-FID and FTIR was observed for all datasets and the relative rate plot for *n*-butane conducted at 292 ± 2 K is shown in Figure 3.10a as an example. Also shown in Figure 3.10a are the two linear regression fits to the FTIR and GC-FID data used to determine the rate coefficient for *n*-butane. Relative rate ratios calculated using the GC-FID data and FTIR data were in good agreement and were determined as (3.1 ± 0.1) and (3.05 ± 0.03) respectively.

Secondly, Farrugia (2014) looked at the site specific hydrogen abstraction from the butane isomers in reaction with Cl atoms. As the fitting process required reference spectra for each chlorinated product of the reaction as well as the reactants, branching ratio information was easily obtained from the Quant2 package. The branching ratios determined using Quant2 were compared to the data from the GC-FID and were found to be in excellent agreement across all temperatures. Figure 3.10b shows a comparison of results taken from Farrugia (2014), where the decay of *iso*-butane and growth of 1-chloro-2-methylpropane (α_1) and 2-chloro-2-methylpropane (α_2) were monitored using GC-FID and FTIR at 1000 mbar and 292 K. Branching ratios for α_1 = (0.62 ± 0.03) and (0.63 ± 0.02) and α_2 = (0.36 ± 0.03) and (0.37 ± 0.02) were reported for the GC-FID and FTIR techniques respectively.

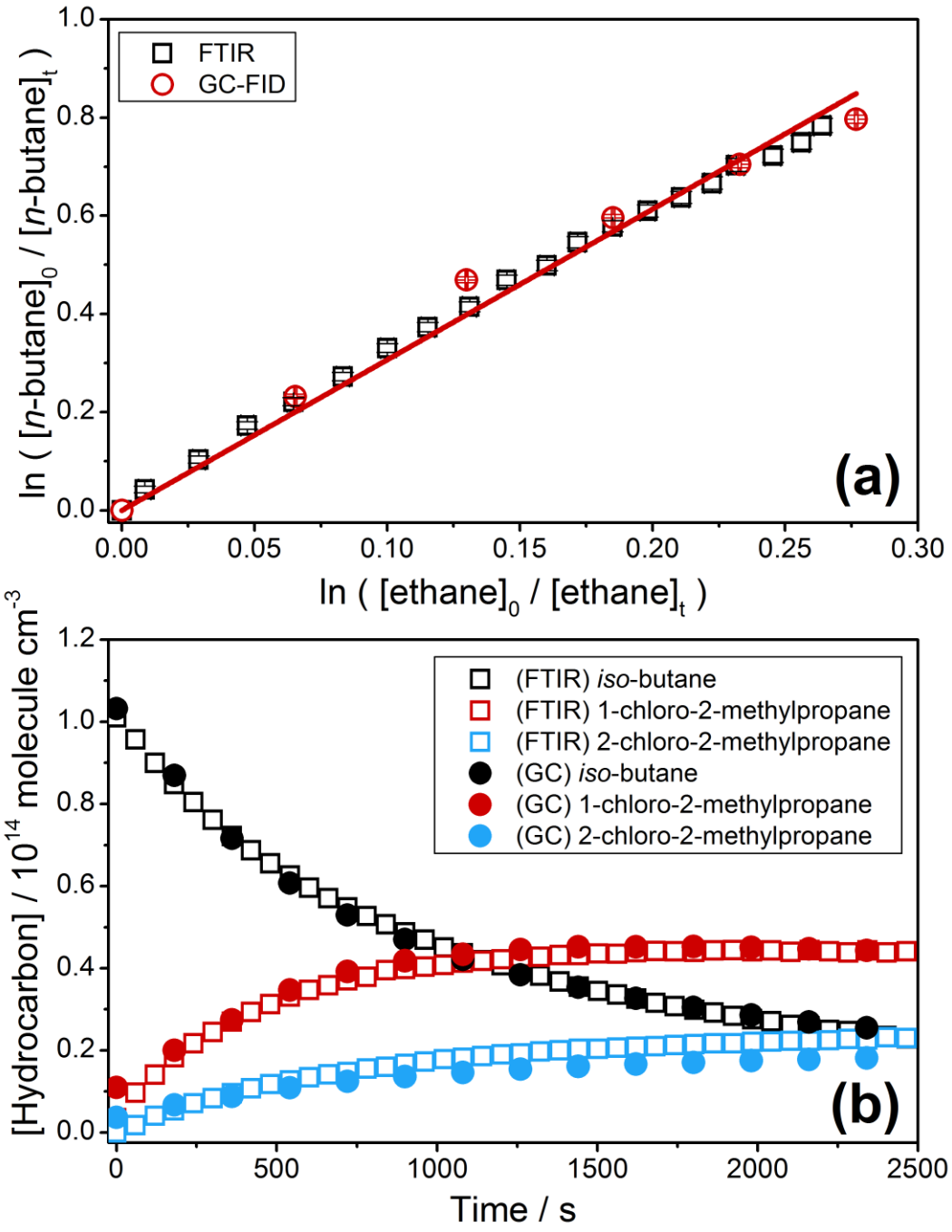

Figure 3.10: (a) Decay of *n*-butane displayed as a function of decay of ethane for the relative rate measurement of Cl + *n*-butane conducted at (292 ± 2) K and 1000 mbar. k_{Cl}(FTIR) = 1.73 × 10^{-10} molecule^{-1} cm^3 s^{-1} (GC-FID) = 1.73 × 10^{-10} molecule^{-1} cm^3 s^{-1} (b) Comparison of measurements taken using GC-FID and FTIR during the reaction of *iso*-butane with Cl at 1000 mbar and 320 K. Decay of *iso*-butane reactant displayed along with products formed from reactions (R 3.1 - R 3.3). Measurements from FTIR and GC instruments are shown as a comparison. FTIR concentrations were determined using the Quant2 package analysing the C-H stretch region of the IR spectrum between 2800 - 3100 cm^{-1}. Experimental data taken by Farrugia (2014).

3.4.2 Application to HO_2 + $CH_3C(O)O_2$

The data analysis for the study of stable products and reactants from the reaction of HO_2 with acetylperoxy was conducted using Quant2. Chapter 7 details the results and implications of the study, and here only the comparison between automated and manual analysis is discussed. Reference spectra used were acetaldehyde, CH_3CHO, acetic acid, $CH_3C(O)OH$, peractic acid, $CH_3C(O)OOH$, formic acid, HCOOH, formaldehyde, HCHO, water and methanol, CH_3OH, and all were measured at 0.5 cm^{-1} in the HIRAC chamber (more details in chapter 7). Sample spectra were analysed using Quant2 in the 1650 - 1850 cm^{-1} range for carbonyl containing species and 2000 - 2200 cm^{-1} for methanol (as in Figure 3.4). Manual subtraction was conducted in the 1000 - 1600 cm^{-1} range as several prominent absorption features for peracetic and acetic acid are observed around 1200 cm^{-1} which aids manual subtraction. This is the method used for analysis of product yields in the previous chamber studies into the same reaction by Hasson et al. (2004). Shown in Figure 3.11 are the stacked spectra sample, fit (generated with Quant2) and residual spectra taken from an experiment conducted at 1000 mbar and 293 K. The residual showed signs of spectral mismatch, where sharper lines were unable to be accurately fit using Quant2, most likely from H_2O vapour and the Q-branch of the HCHO carbonyl feature. Due to the scale of the residual (×20), it is unlikely that this impacted significantly on the calculated concentrations of the constituent reference spectra.

Figure 3.12 displays the concentration determined using Quant2 as a function of manually determined concentrations *via* subtraction for all species. Excellent agreement was observed for the majority of species, with $R^2 \sim 1$. For methanol, the R^2 was close to unity indicating an excellent proportionality between the two datasets, however the observed slope showed the Quant2 package was predicting systematically ~10% lower [CH_3OH] over the measured range. As the analysis involved the manipulation of spectra over small absorption unit ranges (10^{-2} - 10^{-3}) to determine the multiplication factors, it is likely that a systematic uncertainty in the manual subtraction occurred as the goodness of fit is judged visually. Acetic acid was under predicted at early times by the Quant2 software, and this was explained by analysis of spectra close to the detection limit for acetic acid (~5×10^{11} molecule cm^{-3}), incurring large uncertainties.

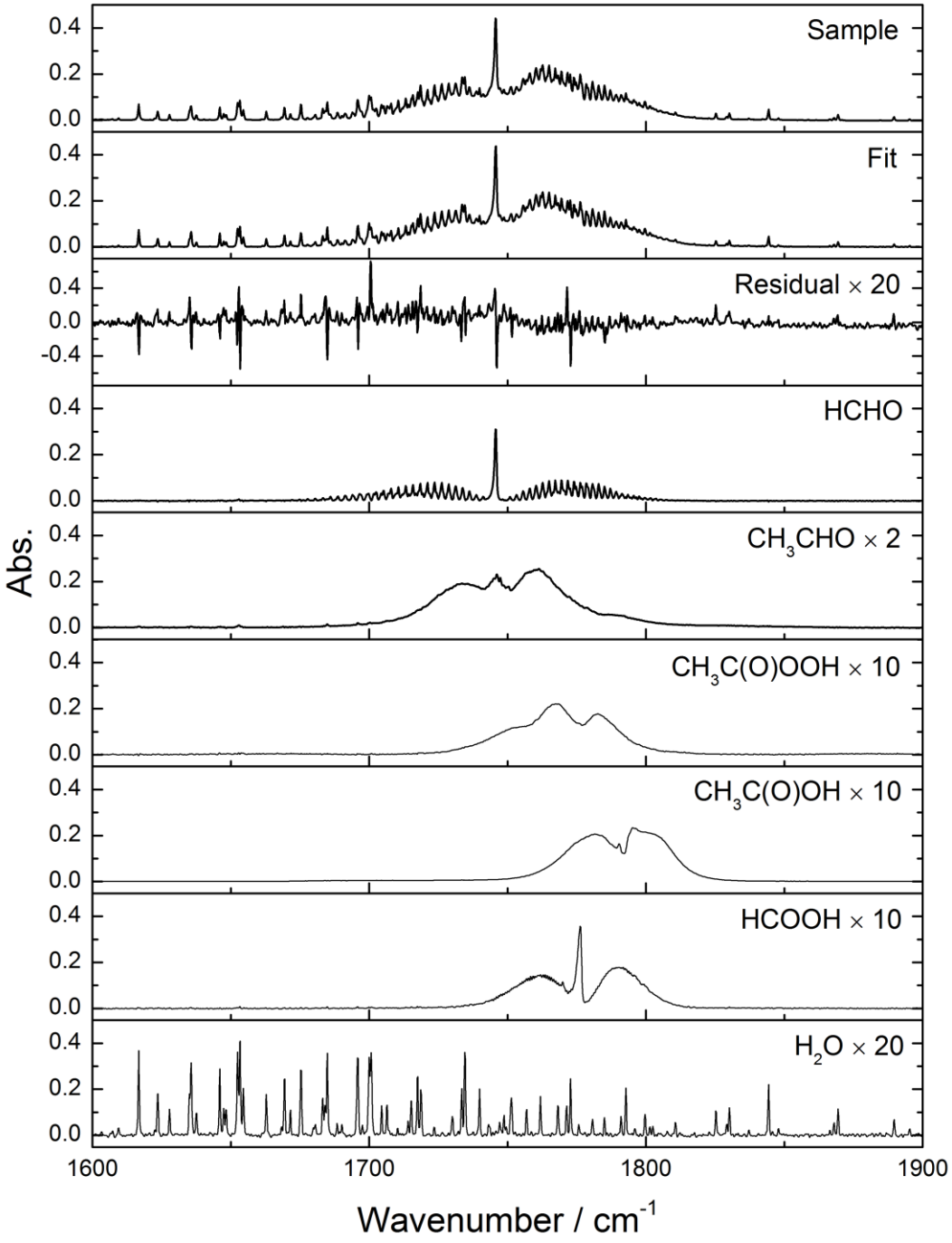

Figure 3.11: Sample spectrum taken from the reaction of acetylperoxy with HO_2 conducted at 1000 mbar and 293 K stacked on top of the fit spectrum calculated using the Quant2 package and the residual spectrum. Underneath are the six reference spectra used in the fitting routine, scaled to match the y-axis from the sample spectrum. Spectra recorded at 0.5 cm^{-1}.

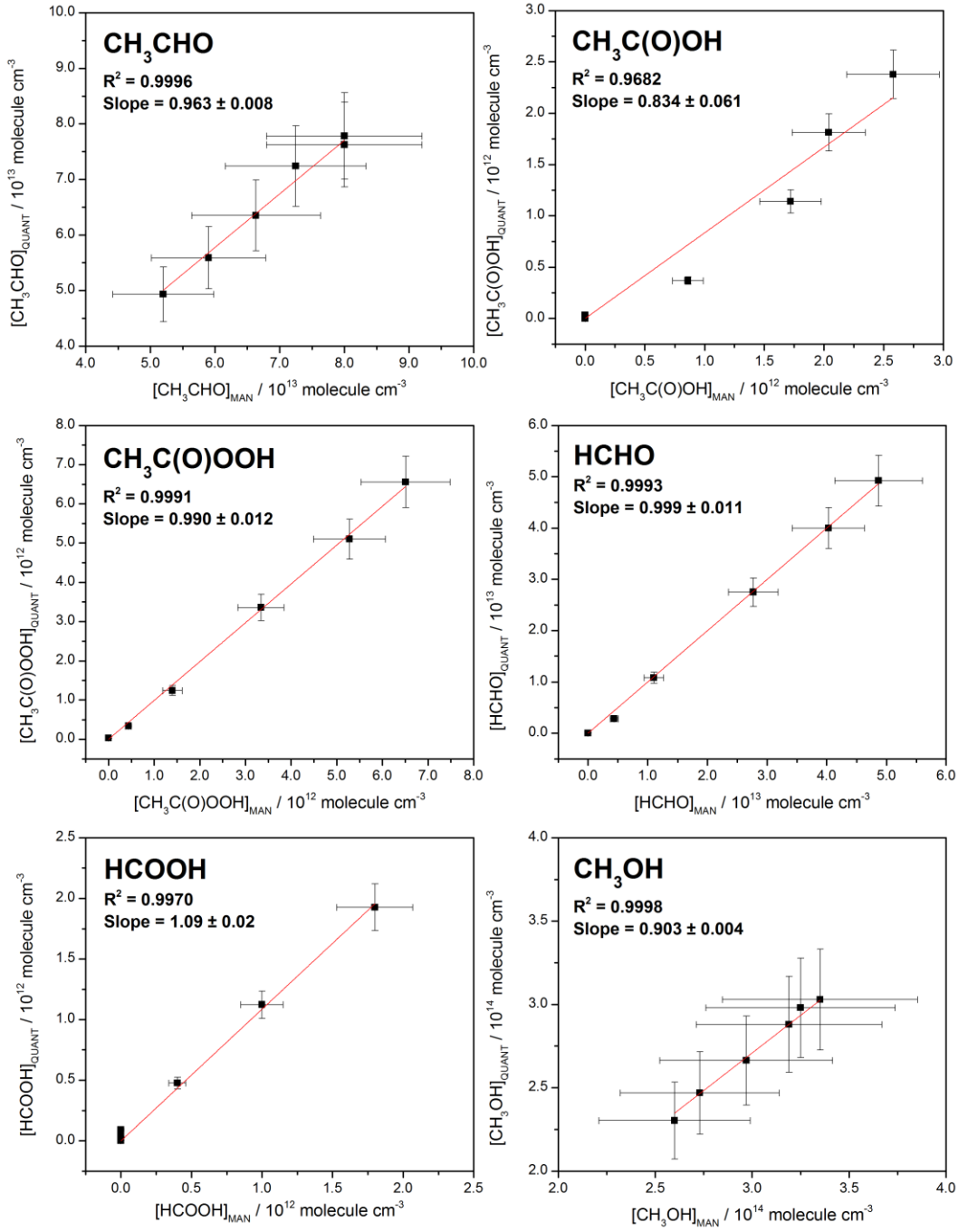

Figure 3.12: Comparison of FTIR quantitative analysis techniques. Automated fitting using Quant2 is displayed against manual subtraction. The linear regression was weighted to uncertainties in both axes (±1σ), with a fixed intercept at (0,0).

3.5 Uncertainty analysis

3.5.1 Manual subtraction

Uncertainties for the manual subtraction method of analysis were the sum in quadrature of the multiplication factor and the error in calibration of the respective reference spectra. Uncertainties in the multiplication factors were estimated manually by determining upper and lower limits around the judged best fit for a given reference spectrum. Errors in calibration incorporated the uncertainties associated with measurement and introduction of species into the chamber (*via* the vacuum line or liquid injection) through a linear regression of a multipoint calibration as described in section 3.2.

3.5.2 Quant2

Uncertainties in calculated concentrations were taken as the sum in quadrature of the error associated with the fit and the systematic error associated with the calibration of each species. The uncertainty for the NLLSQ procedure was determined from the fit parameter uncertainties combined with the root mean squared error of the residual. These uncertainties were often very small (< 2 %), even if the fit was judged visually to be bad, and herein lies the greatest disadvantage of the automated fitting software. Figure 3.13 shows the fit from the well defined C=O stretch region for the reaction of acetylperoxy with HO_2.

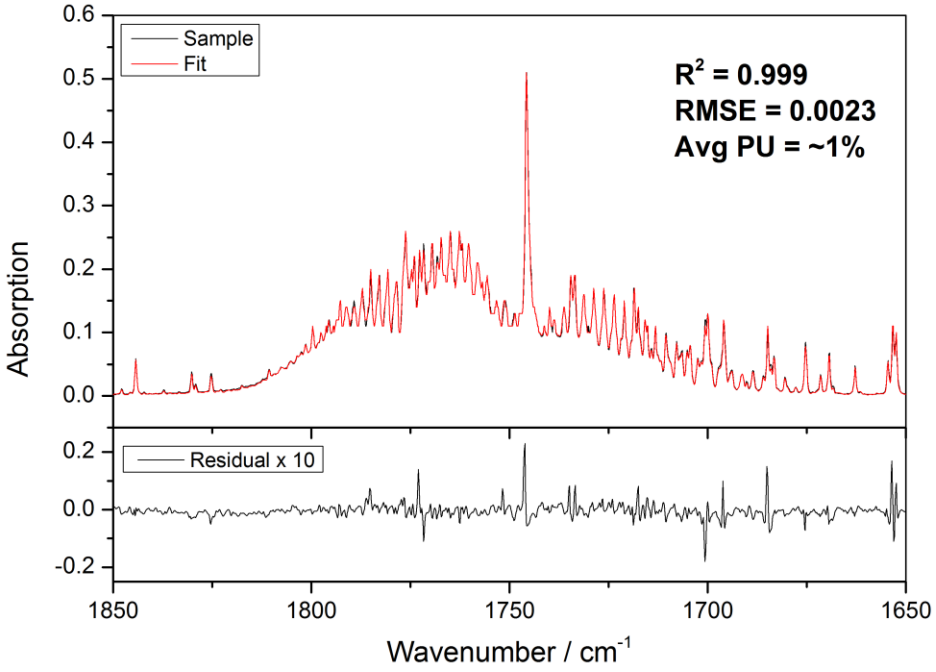

Figure 3.13: Infrared spectrum, in black, taken during the product study of the acetyl peroxy with HO_2 reaction in the C=O stretch region between 1650 – 1850 cm^{-1}. The fit, in red, was calculated using Quant2 with reference spectra for acetaldehyde, acetic acid, peracetic acid, formic acid, HCHO and H_2O. Underneath is the amplified residual (×10) from the fitting procedure. In bold are the R^2, Root Mean Squared Error (RMSE, 1σ) of the residual and the average parameter uncertainty (i.e., the uncertainty in each multiplication factor) used to judge the goodness of fit.

As all the component reference spectra are known, the standard deviation of the reference spectrum and the fit parameters is small, and the calculated R^2 = 0.999. Removing the HCHO reference spectrum from the fitting procedure creates a visually bad fit, looking at the residual in Figure 3.14. However, the uncertainty in the fitted parameters was ~10 % and the R^2 = 0.873. This stressed the importance of examination of the residual over reliance on the R^2 statistical output as unknown spectra will not always be obvious as in the example shown here. More indicative of fitting quality was the root mean squared error (RMSE, 1σ) of the residual, which was observed to increase by a factor of ~10 with the HCHO spectrum removal. However, this is at best a relative tool that can be used to assess the quality of fit based on changing parameters (e.g., reference spectra used). More work is required into the overall uncertainty from the fitting routine. The total uncertainty in the Quant2 procedure was therefore estimated at ~10%, depending on the uncertainty in calibration of the respective reference spectra used.

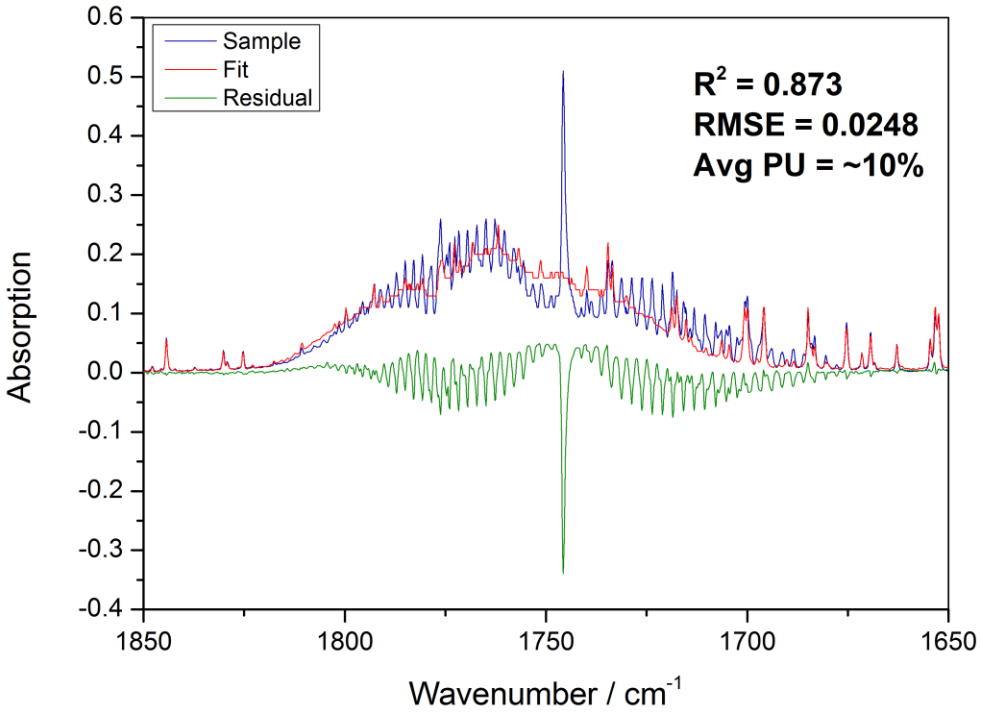

Figure 3.14: The infrared spectrum, in blue, as in Figure 3.13, taken in the C=O stretch region between 1650 – 1850 cm^{-1}. The fit, in red, was calculated using Quant2 with reference spectra for acetaldehyde, acetic acid, peracetic acid, formic acid and H_2O. The HCHO reference was omitted to exaggerate the effect of fitting with an unknown component and the disadvantages therein. The residual from the fitting procedure is in green and plotted to scale. In bold are the R^2, RMSE (1σ) of the residual and the average parameter uncertainty used to judge the goodness of fit.

3.6 Conclusions and further work

A quantitative analysis program based on a NLLSQ fitting routine has been written to efficiently quantify different species through FTIR absorption measurements. The automated software allows the fast analysis of multiple well-defined multivariate spectra using accurately measured reference spectra for the respective components of the system being studied. The software has been shown to perform well and was tested in systems of varying complexity including the determination of rate coefficients for the reaction of butane isomers with Cl atoms. The software was able to separate the overlapping reactant and product spectra used to give information about the hydrogen abstraction sites and were compared to measurements made using GC-FID, which were in good agreement. The validation of the new software was reinforced through the rapid evaluation and accurate determination of product and reactant concentrations for an

important and topical reaction (acetylperoxy + HO_2). The software performed well against manual subtraction techniques for the same reaction and an overall uncertainty in measurements was found to be weighted heavily on the accurate measurement of the reference spectra used. An estimated uncertainty in the fitting procedure has been given at ~10 %, however this requires further investigation. Through further experiments and analysis of different systems, a guide on statistical parameters (e.g., R^2) and their significance will be constructed.

Further work needs to be conducted into the development and implementation of this software to enhance its efficiency and efficacy. Implementation of a spectral line stretching and shifting algorithm, based on the instrument line shape, will enable implementation of synthetic spectra from the HITRAN database. Such a technique may also offer the ability to fit sample spectra at different temperatures from a reference spectrum measured at 298 K, something that would be especially useful for compounds which exhibit enhanced wall loss coefficients at $T < 298$ K, making reference spectra measurements difficult (such as organic acids and peracids). Application of the software to more chemical systems inside HIRAC, and perhaps elsewhere, will also help to identify the limitations and capabilities of the fitting routine. For example, the software has the potential to be adapted to other spectroscopic techniques that require analysis of convolved spectra, such as broadband cavity enhanced absorption. Use by more people in the HIRAC group and further afield will allow any other problems to be identified and corrected.

3.7 References

Akimoto, H., M. Hoshino, G. Inoue, F. Sakamaki, N. Washida and M.Okuda (1979). "Design and characterization of the evacuable and bankable photochemical smog chamber " Environmental science and technology 13(4): 471.

Bardini, P., G. M. Clifford, R. M. Healy, G. J. Rea, B. Temime-Roussel, L. P. Thuener and J. C. Wenger (2005). "Kinetic and mechanistic studies on the atmospheric degradation of dimethylphenols and tolualdehydes " Geophysical Research Abstracts 7: 06946.

Barnes, I., K. H. Becker, E. H. Fink, A. Reimer, F. Zabel and H. Niki (1983). "Rate constant and products of the reaction CS2 + OH in the presence of O2." International journal of chemical kinetics 15: 631-645.

Barnes, I., K. H. Becker and N. Mihalopoulos (1994). "An FTIR product study of the photooxidation of dimethyl disulphide." Journal of atmospheric chemistry 18: 267-289.

Beebe, K. R., R. J. Pell and M. B. Seasholtz (1998). Chemometrics: A Practical Guide, Wiley-Interscience.

Bloss, W. J., J. D. Lee, C. Bloss, D. E. Heard, M. J. Pilling, K. Wirtz, M. Martin-Reviejo and M. Siese (2004). "Validation of the calibration of a laser-induced fluorescence instrument for the measurement of OH radicals in the atmosphere." Atmospheric Chemistry and Physics 4: 571-583.

Chu, P. M., F. R. Guenther, G. C. Rhoderick and W. J. Lafferty (1999). "The NIST Quantitative Infrared Database." J. Res. Natl. Inst. Stand. Technol. 104(59).

Farrugia, L. (2014). Kinetics and mechanistic studies in the HIRAC chamber. PhD, University of Leeds.

Griffith, D. W. T. (1996). "Synthetic Calibration and Quantitative Analysis of Gas-Phase FT-IR Spectra." Applied Spectroscopy 50(1): 59-70.

Griffiths, P. R. and J. A. de Haseth (2007). Fourier Transform Infrared Spectroscopy - Second Edition, Wiley Interscience.

Hasson, A. S., G. S. Tyndall and J. J. Orlando (2004). "A product yield study of the reaction of HO2 radicals with ethyl peroxy, acetyl peroxy and acetonyl peroxy radicals." Journal of Physical Chemistry A 108: 5979-5989.

Jacquinet-Husson, N., N. A. Scott, A. Chédin and A. A. Chursin (2004). "The GEISA Spectroscopic Database System Revisited For IASI Direct Radiative Transfer Modelling." Atmospheric and Oceanic Optics 16(3): 256-261.

Kramer, R. (1998). Chemometric Techniques for Quantitative Analysis.

Rothman, L. S., I. E. Gordon, A. Barbe, D. C. Benner, P. F. Bernath, M. Birk, V. Boudon, L. R. Brown, A. Campargue, J.-P. Champion, K. Chance, L. H. Coudert, V. Dana, V. M. Devi, S. Fally, J.-M. Flaud, R. R. Gamache, A. Goldman, D.

Jacquemart, I. Kleiner, N. Lacome, W. J. Lafferty, J.-Y. Mandin, S. T. Massie, S. N. Mikhailenko, C. E. Miller, N. Moazzen-Ahmadi, O. V. Naumenko, A. V. Nikitin, J. Orphal, V. I. Perevalov, A. Perrin, A. Predoi-Cross, C. P. Rinsland, M. Rotger, M. Simeckova, M. A. H. Smith, K. Sung, S. A. Tashkun, J. Tennyson, R. A. Toth, A. C. Vandaele and J. V. Auwera (2009). "The HITRAN 2008 molecular spectroscopic database." Journal of Quantitative Spectroscopy & Radiative Transfer 110: 533-572.

Sharpe, S. W., T. J. Johnson, R. L. Sams, P. M. Chu, G. C. Rhoderick and P. A. Johnson (2004). "Gas-Phase Databases for Quantitative Infrared Spectroscopy." Applied Spectroscopy 58(12): 1452-1461.

Shetter, R. E., J. A. Davidson, C. A. Cantrall and J. G. Calvert (1987). "Temperature variable long path cell for absorption measurements." Review of scientific instrument 58(8).

SpectraCalc. (2011). "Spectral Calc: High Resolution Spectral Modelling." from http://www.spectralcalc.com.

Thuner, L. P., P. Bardini, G. J. Rea and J. C. Wenger (2004). "Kinetics of the gas-phase reactions of OH and NO_3 radicals with dimethylphenols." Journal Of Physical Chemistry A 108(50): 11019-11025.

Wallington, T. J. and S. M. Japar (1989). "Fourier Transform Infrared Kinetic Studies of the Reaction of HONO with HNO_3, NO_3 and N_2O at 295 K." Journal of Atmospheric Chemistry 9: 399-409.

Chapter 4. HOx instrumentation

4.1 Introduction

As discussed in chapter 1, the high reactivity of the OH radical results in low ambient steady state concentrations (~10^6 molecule cm^{-3}) and a short tropospheric lifetime of ≤ 1 s. Due to the short lifetime, HOx concentrations are uninfluenced by transport, requiring measurement techniques to be highly sensitive and *in situ*. The majority of field measurements have been made using laser induced fluorescence (LIF) spectroscopy at low pressure (the fluorescence assay by gas expansion technique (FAGE)). The FAGE technique has enjoyed success on several field campaigns (more recent references include: (Holland et al., 2003; Faloona et al., 2004; Kubistin et al., 2008; Dusanter et al., 2009; Commane et al., 2010; Whalley et al., 2011)), and is used in both SAPHIR and EUPHORE reactions chambers (Siese et al., 2001; Karl et al., 2004). FAGE is able to detect both OH and HO_2 radicals, through conversion of HO_2 to OH *via* reaction with NO (section 4.2). Measurement of HOx radicals is challenging as ambient OH concentrations are low. Potential interferences have also been suggested (Fuchs et al., 2011; Mao et al., 2012; Whalley et al., 2013) and CIMS and LIF are not absolute and hence require calibration, increasing the uncertainty in measured concentrations. However, as discussed in chapter 1, intercomparisons exist which validate the different techniques in both chamber (Schlosser et al., 2007; Schlosser et al., 2009; Fuchs et al., 2012) and field environments (Eisele et al., 2001; Eisele et al., 2003).

This chapter will focus on the description of the LIF based FAGE technique (section 4.2), with a brief discussion of the principles and current instruments in circulation (section 4.3). One of the unique features of the HIRAC chamber is the ability to detect HOx radicals using a dedicated FAGE instrument, as discussed previously by Glowacki et al. (2007) and Malkin (2010), however several modifications to the instrument design have been made and these are described in detail here in section 4.4. The instrument relies on a laser light source, and has been calibrated (chapters 5 and 6) using both a new medium pulse repetition frequency laser (PRF) at 200 Hz, and a more commonly used high PRF system at 5 kHz (section 4.4.1). The medium PRF system was purchased as a cheaper alternative to the higher PRF systems, and the instrumental details are discussed here. Further details on instrument sensitivity to HOx are discussed in chapter 5.

4.2 The FAGE technique

Fluorescence Assay by Gas Expansion, FAGE, is a low pressure LIF technique commonly used for the detection of OH and HO_2 radicals (Heard (2006) and references therein). LIF uses laser light to excite specific molecular rovibrational energy levels from the ground state to an electronically excited state. For OH, there are two pathways for an excited radical to relax to the ground state: (i) collisional quenching and (ii) fluorescence, resulting in a photon being emitted which can be detected. Originally, LIF for FAGE was attempted by exciting OH to the first vibrational level in the *A* state at 282 nm ($A^2\Sigma^+$ (v'=1) ← $X^2\Pi_i$ (v''=0), Figure 4.1a), whereby vibrational relaxation to the $A^2\Sigma^+$ (v'=0) level occurs. Off-resonance fluorescence was then observed at ~308 nm using an interference filter to help discriminate against scattered laser radiation (Davis et al., 1976). Fluorescence from (v'=1) to (v''=1) also occurs at 311 nm and is detected in the same way. Although off-resonant LIF has been successful in stratospheric applications (Wennberg et al., 1994), in the troposphere 282 nm photolysis of ozone generates an unacceptably high interfering OH signal, through the reaction of $O(^1D)$ with higher ambient H_2O vapour concentrations.

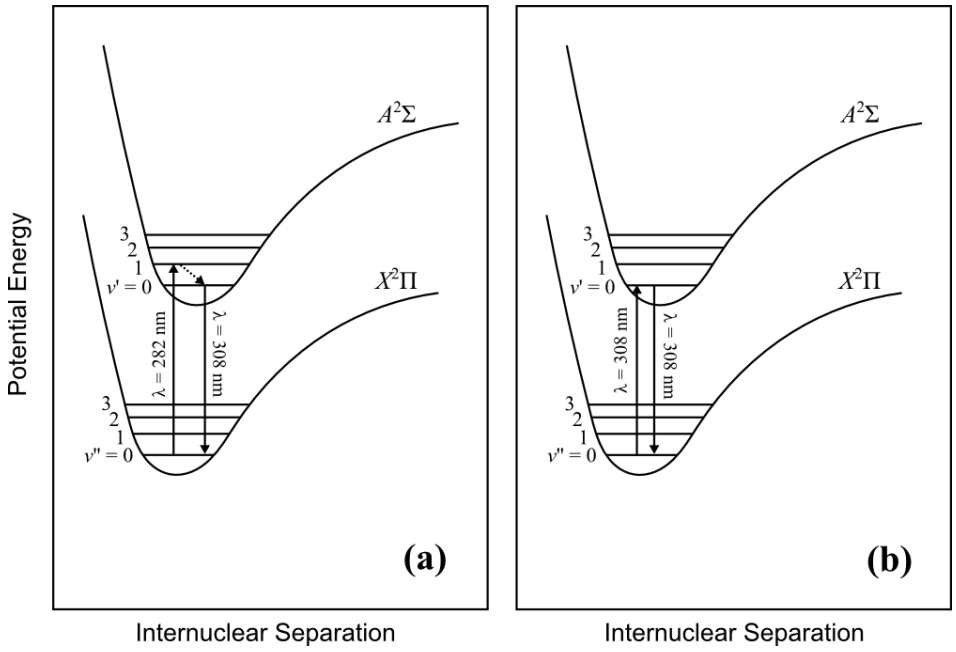

Figure 4.1: The electronic transitions of OH for excitation at (a) 282 nm ($A^2\Sigma^+$ (v'=1) ← $X^2\Pi_i$ (v''=0)) and (b) 308 nm ($A^2\Sigma^+$ (v'=0) ← $X^2\Pi_i$ (v''=0)). Vibrational relaxation of the $A^2\Sigma^+$ (v'=1) → $A^2\Sigma^+$ (v'=0) represented by the dotted arrow. Fluorescence of OH occurs in both cases ~308 nm. Relaxation of OH due to collisional quenching and higher vibrational energy levels are not shown for clarity.

Currently, all FAGE instruments employ "on-resonance" fluorescence detection of OH. A 308 nm excitation pulse ($A^2\Sigma^+$ (v'=0) ← $X^2\Pi_i$ (v''=0), Figure 4.1b) is used and fluorescence is collected at the same wavelength. Excitation at 308 nm proved beneficial for two reasons: (i) the O_3 absorption cross section is ~23 times smaller at this wavelength and (ii) the OH absorption cross section for the (0,0) band is ~4 times greater than the (1,0) band at 282 nm. High PRF lasers (~5 kHz) with low pulse energies (typically ~8 μJ pulse^{-1}) were employed to avoid saturation of the OH (0,0) band (σ ~10^{-16} cm^2 molecule^{-1}), which in turn further reduced the laser generated OH interference from O_3 photolysis. Injection of an OH scavenger (e.g., C_3F_6) allows quantification of any laser generated OH interference (Mao et al., 2012), which is useful in the characterisation of the FAGE technique. A similar system has been developed for the HIRAC based FAGE instrument, and is described in section 4.4, and the operation is described in chapter 6. The work by Mao et al. (2012) was discussed in chapter 1.

Expanding the sample through a pinhole (typically ~ 1.0 mm) to a low pressure cell (~1 - 2 Torr) increases the fluorescence lifetime of the *A* state beyond the laser scattered light, allowing for temporal discrimination against the resonant 308 nm excitation pulse. The lower number density inside the cell, when operating at reduced pressures, also decreases the effects of Mie and Rayleigh scattering of laser light (Stevens et al., 1994). HO_2 radicals can also be measured using FAGE systems after titration with added NO:

$$HO_2 + NO \rightarrow OH + NO_2 \qquad \text{R 4.1}$$

and the resultant OH is detected in the same way.

LIF is a very sensitive, but non-absolute detection method and therefore each channel of the instrument needs to be calibrated. Calibration and characterisation of the HIRAC FAGE instrument has been conducted using the H_2O vapour photolysis technique which is discussed in chapter 5. Two alternative calibration techniques have also been developed using the HIRAC chamber and these are discussed in chapter 6.

4.3 FAGE instrumentation

There are currently eight field work based FAGE instruments in operation around the world, deployed by six institutions and these have been compared in terms of detection limit and uncertainty in chapter 1. Abbreviations for each institution are used where appropriate and are listed here with relevant references: Penn State University, USA (PSU, Faloona et al. (2004)), Max Plank Institute für Chemie, Germany (MPI, Martinez et al. (2008)), Forschungzentrum Jülich Germany (FZJ, Holland et al. (2003); Karl et al. (2004) and Karl et al. (2004b)) University of Leeds (UoL airborne, Commane et al. (2010) and UoL ground-based Whalley et al. (2011)), Indiana University, USA (IU, Dusanter et al. (2009)) and Frontier Research for Global Change, Japan (FRCGC, Kanaya et al. (2001a)).

The fluorescence detection cells used for FAGE instruments are all constructed differently. Generally, a metal cell is maintained at low pressure using a high capacity pump set. Gas is sampled through a pinhole drilled into an inlet, the design of which differs depending on the cell application. These are discussed in more detail below. Wider cell designs combined with short inlets (~20 mm) allow the supersonic jet expansion of gas after the pinhole to be probed by the laser before the jet interacts with internal surfaces of the cell (Creasey et al., 1997). Minimising heterogeneous uptake of radicals to the cell walls, which impacts negatively on instrument sensitivity to OH, is an advantage; however these cells are large and require a large pumping capacity to maintain the cell pressure and the free jet expansion. Therefore, these cells are employed in ground based field measurements at UoL (Smith et al., 2006; Whalley et al., 2010; Whalley et al., 2011).

Airborne FAGE instruments are required to sample gas external to the fuselage of the aircraft as radical losses prevent the use of sample lines. Longer, narrower, cylindrical cells were designed with longer sampling inlets (UoL, MPI, PSU). For example, the airborne FAGE instrument uses a 50 mm diameter cell with a ~350 mm inlet length (more details in section 4.5). The heterogeneous uptake of radicals onto the walls of the long inlet used with the UoL airborne FAGE instrument have been characterised by Commane (2009) and were found to reduce the instrument sensitivity by ~30 % compared to measurements directly behind the inlet pinhole.

Instruments used at MPI and PSU have employed a multipass White cell optic arrangement inside the LIF detection axis. For the same laser power entering the cell, multipass arrangements are more sensitive than their single pass counterparts. However, maintenance of the multipass system alignment is more difficult and time consuming, and due to the several passes, scattered laser light signals due to reflections from internal surfaces of the cell are much higher than single pass systems.

Detection of OH and HO_2 can be achieved either simultaneously or in series using the same LIF detection cell (measurements in series, (Creasey et al., 2003; Fuchs et al., 2011; Nehr et al., 2012)), with two separate LIF axes within the same cell (simultaneous, (Stevens et al., 1994)) or with two separate detection cells (simultaneous, (Whalley et al., 2010)). Depending on the application of the instrument, measurements using the same cell can save space and money. Simultaneous measurements of HOx radicals with two LIF axes in the same cell benefit from sampling from the same air mass, of particular importance in mid-size chamber and airborne measurements. In all current instruments of this design, the OH LIF axis is first and closest to the inlet pinhole, with some separation, which allows the injection of NO before the HO_2 detection axis. Reduced pumping capacity is required compared to two separate detection cells, however, back diffusion of NO into the OH detection axis has been reported for cell designs of this type (Kanaya et al., 2001b; Faloona et al., 2004). Careful control of the injection of NO can reduce this effect. Twin LIF detection cells avoid the contamination of the OH cell with NO, however special separation of the cells (~700 mm for the UoL ground based instrument (Smith et al., 2006)) has the potential for air of different composition to be sampled.

Atop the FAGE inlet is a nozzle, into which the inlet pinhole is accurately drilled. Nozzle designs differ between groups, however the majority use a conical design aimed to reduce the surface area in contact with a given gas sample (PSU, MPI, FZJ, UoL airborne), whereupon the potential heterogeneous loss of radicals could occur. Smith (2007) showed, however, that for the UoL ground-based FAGE, better sensitivities to OH and HO_2 were achieved using a flat nozzle.

As mentioned in section 4.2, high PRF lasers (3 - 8 kHz) are used currently by all FAGE groups. The high PRF results in low laser pulse energies that reduce laser generated OH, scattered laser light and saturation of the OH transition. Lasers are also

chosen with short laser pulse durations (~12 ns) and narrow spectral bandwidths matched to the OH lineshape (~0.1 cm^{-1} at 300 K). Diode pumped Neodymium-ion doped Yttrium Aluminium Garnet ($Y_3Al_5O_{12}$, Nd:YAG) are used to produce 532 nm radiation, which is used to pump either tunable dye (PSU, FZJ, FRCGC, MPI) or solid state Ti:Sapphire (Ti:Al_2O_3) lasers (UoL, both instruments). Using a mixture of dyes, the red shifted output of the dye laser is centred around 616 nm, which can be frequency doubled *via* secondary harmonic generation (SHG) to produce 308 nm. Output from the pumped Ti:Sapphire crystal undergoes several conversion stages to create 308 nm radiation, which are discussed in section 4.5 along with the aircraft FAGE instrument. Wavelength tuning is enabled using either an intracavity etalon (PSU and FZJ) or a diffraction grating (UoL ground-based and airborne instruments). Dye lasers benefit from the use of the intracavity etalons as a more stable spectral bandwidth results, however the bandwidth of emission from the Ti:Sapphire system is already sufficiently narrow. Laser radiation is delivered to the fluorescence cells *via* fibre optic cables.

The majority of groups use channeltron photomultiplier tubes (CPM) for the collection of OH fluorescence. The CPMs superseded the use of photomultiplier tubes (PMT) as the gating requirements are much simpler; fast switching of high-voltage power supplies at kHz frequencies causes significantly less after-pulsing and a shorter recovery time to full gain after gating. The gating and data acquisition processes are described in section 4.4.3. The FZJ and PSU instruments use microchannel plate (MCP) detectors which are not subject to after-pulsing, only require low switching voltages for gating, have a fast recovery time to full gain and are directional (i.e., they are not as susceptible to the collection of scattered laser light). However, MCPs have lower sensitivity and are very expensive (Heard, 2006).

A FAGE instrument was designed with these considerations in mind for the application to the study of HOx radical chemistry in the HIRAC chamber (Glowacki et al., 2007; Malkin, 2010; Malkin et al., 2010) and this is discussed in the following section.

4.4 FAGE instrument for HOx radical detection in the HIRAC chamber

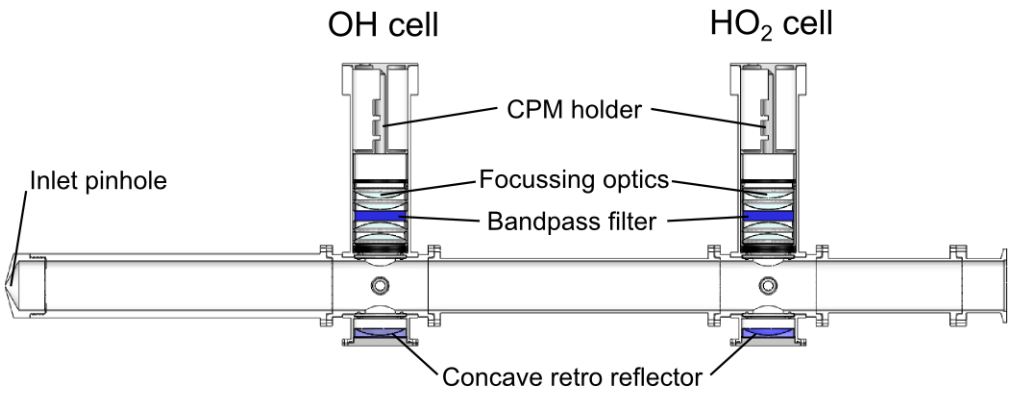

Figure 4.2: Side on vertical cross section schematic of the HIRAC FAGE apparatus showing the instrument inlet pinhole, OH and HO_2 fluorescence cells arranged in series. Channeltron PhotoMultiplier tubes (CPM) are not shown, however holders are included.

Figure 4.2 shows the cross sectional schematic of the HIRAC FAGE instrument. The cells were constructed of black anodised aluminium cylinders (internal diameter = 50 mm), in a design similar to the University of Leeds airborne FAGE instrument (section 4.5 and Commane et al. (2010)). The inlet pinhole was drilled into the apex of a conical nozzle and mounted at the end of the inlet flow tube, ~280 mm from the OH fluorescence cell. It was essential that the distance between sampling and detection was kept to a minimum as HOx radicals are easily lost to metal surfaces *via* heterogeneous uptake (Faloona et al., 2004). However, when sampling from HIRAC, radical losses became significant (~20 %) close to the chamber walls (see chapter 2 and Malkin (2010)) and hence a longer inlet was used. The inlet was designed with a screw thread, allowing conical nozzles with different diameter pinholes to be easily interchanged (chapter 5) and inlet extension sections (~150 mm) to be attached. Also, internally mounted lamps can lead to a heterogeneous radiation field, and the inlet extensions have been used previously to probe this intensity distribution (see chapter 2 for more details). The HIRAC chamber has the unique ability to investigate kinetics and reaction mechanisms over a range of temperatures and pressures with direct HOx

radical detection. The FAGE instrument was coupled to the HIRAC chamber using a custom made ISO-K160 Cajon-type fitting.

Under typical operating conditions, gas was sampled at ~6 slm, through a 1.0 mm diameter pinhole, and was passed down the inlet into the OH detection axis. A high capacity rotary-backed roots blower pumping system (Leybold, trivac D40B and ruvac WAU251) was used to maintain the cells at low pressure (~3.85 mbar). Concentrations of HO_2 were measured simultaneously in a second detection axis ~300 mm downstream of the OH detection axis (in series). High purity NO (BOC, N2.5 Nitric Oxide) was added ~2 cm before the HO_2 detection axis into the centre of flow through 1/8" stainless steel tubing at a rate of 5 sccm (Brooks 5850S) converting HO_2 to OH. The NO injector was positioned in the centre of the flowtube facing in the same direction as the gas flow. Recently published material on the conversion of certain RO_2 radicals to OH upon reaction with NO in FAGE detections cells (Fuchs et al., 2011; Whalley et al., 2013) have shown a significant enhancement of the HO_2 signal in the presence of certain peroxy radicals, RO_2. Preliminary RO_2 conversion efficiency results for the HIRAC FAGE instrument are discussed briefly in chapter 5 using a range of different hydrocarbons.

Laser light (λ = 308 nm) was introduced into the cell perpendicular to the gas flow, as in Figure 4.3. The laser entrance and exit arms contained baffles (small aluminium rings) which reduced reflections from internal cell surfaces which can contribute to the measured background signal (section 4.4.3). Fluctuations in laser power were accounted for using a linear response UV sensitive photodiode (UDT-555UV, Laser Components, UK) at the exit arm of the detection axes to normalise the LIF signal. Both laser systems provided between 5 - 10 and 2 - 5 mW of 308 nm light to the OH and HO_2 detection axes respectively. Maintaining a narrow range of laser powers minimized the experimentally determined inverse dependence of instrument sensitivity with respect to laser power (see chapter 5).

OH fluorescence was detected perpendicular to both the laser beam and gas flow, and was collimated by two lenses (plano-convex 50 mm diameter, 100 mm focal length) passed through a 308 nm bandpass filter (Barr associates, 308.75 nm central wavelength, 5.0 nm bandwidth, 50% transmission) and refocused onto the CPM. The use of a concave back reflector below the detection axis approximately doubled the

fluorescence collected by the detector. All optics were coated with a 308 nm anti-reflective coating. To avoid detector saturation, the CPM was gated (i.e., switched off) for the duration of the laser pulse using a custom made gating unit. The gating process is discussed in more detail in section 4.4.3.

A new OH scavenger system was installed to help discriminate between OH sampled from the chamber and laser generated OH in the fluorescence cells due to the higher pulse energies associated with the 200 Hz PRF laser system (1×10^{14} compared to 5×10^{12} photons pulse^{-1} cm^{-2} at 5 kHz for laser power = 8 mW). A mixture of *iso*-butane (20% in N_2) was injected ~40 mm inside the inlet pinhole in to the central flow, through a 3 mm stainless steel pipe at a rate of ~20 sccm (Brooks MFC), reacting with the sampled OH before it reaches the detection axis. The laser generated OH is probed within the same laser pulse (12 ns) and hence is not suppressed by the scavenger injection. Neither a pressure increase nor attenuation of UV light was detected during the scavenger injection process at this flow rate and dilution. The system was automated using a solenoid and adapting the currently existing FAGE instrument control software (section 4.4.3). This system was used primarily in the alternative OH calibration method, and example data and the correction process are described in chapter 6.

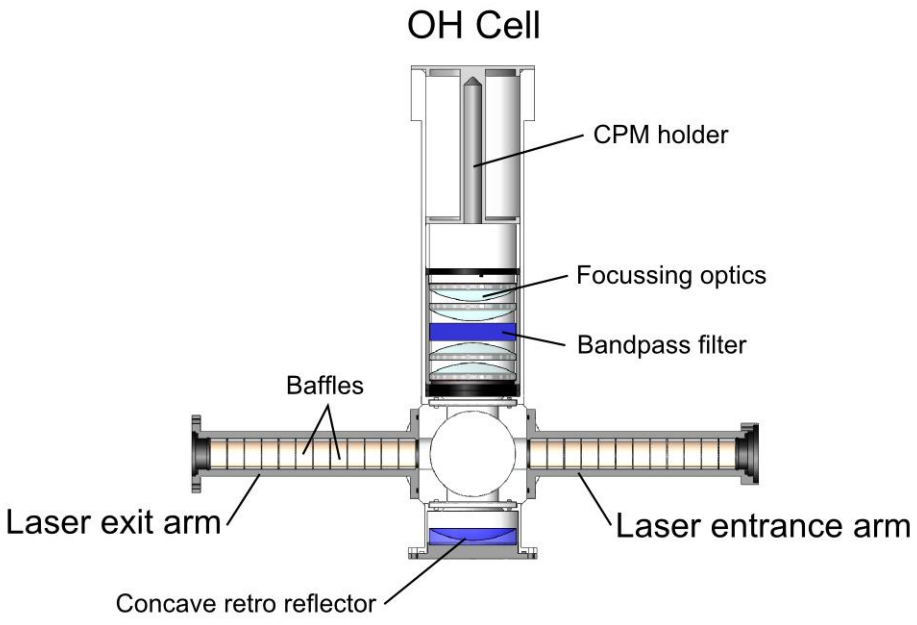

Figure 4.3: Cross section of the OH cell, showing the laser entrance and exit arms, with baffles used to reduce laser scattering from the surfaces of the cell arms. Channeltron PhotoMultiplier tubes (CPM) not shown here. The gas flow direction is into the page.

4.4.1 Laser systems and light delivery

Laser light for the on-resonance detection of OH fluorescence at 308 nm in the HIRAC FAGE instrument was generated using two Nd:YAG pumped dye laser systems operating at different PRFs. The first consisted of a diode pumped Nd:YAG laser (JDSU Q201-HD) which was Q-switched and intracavity frequency-doubled (lithium triborate crystal (LBO)) to give $\lambda = 532$ nm with a laser pulse duration of ~10 ns at a 5 kHz PRF. The 532 nm light was used to pump a tunable single stage dye laser (SIRAH Cobra stretch), using a mixture of 0.2 g l^{-1} Rhodamine B and 0.05 g l^{-1} of Rhodamine 101 in methanol. The maxima of the red shifted output was centred ~616 nm, which in turn was frequency-doubled using a potassium dihydrogen phosphate (KPO) crystal to $\lambda = 308$ nm, with a linewidth of (0.097 ± 0.010) cm^{-1} (Malkin, 2010). The UV light was separated from the fundamental using four Pellin-Broca prisms and typical power output was ~40 mW (= 8 μJ $pulse^{-1}$). Light was transferred to the fluorescence cells using two fibre optic cables (Oz Optics, angled ended, 308 nm AR coated, 200 μm core diameter), one for each cell, using sequential beamsplitters of 90 and 80% reflectivity at 45^o for the OH and HO_2 cells respectively. The remaining light exiting the second beamsplitter was aligned through the OH reference cell (section 4.4.2).

The second system used a Q-switched, flash-lamp pumped Nd:YAG (Litron, NANO-TRL-50-250) laser operating at 200 Hz PRF with ~12 ns pulse duration. The fundamental ($\lambda = 1064$ nm) was frequency-doubled after exiting the laser using an LBO crystal to give $\lambda = 532$ nm which was aligned into a two stage, tunable, Lambda Physik dye laser (LPD3000). The dye mixture and 308 nm light were prepared using the same method as described above. UV light was generated at ~20 mW (= 100 μJ $pulse^{-1}$) with a linewidth of (0.29 ± 0.05) cm^{-1} (Lee, 2000). The higher energy per pulse at 200 Hz was found to burn the ends of the optical fibres, and hence direct light delivery using mirrors was used, as shown in the top-down schematic of the modified HIRAC FAGE instrument displayed in Figure 4.4.

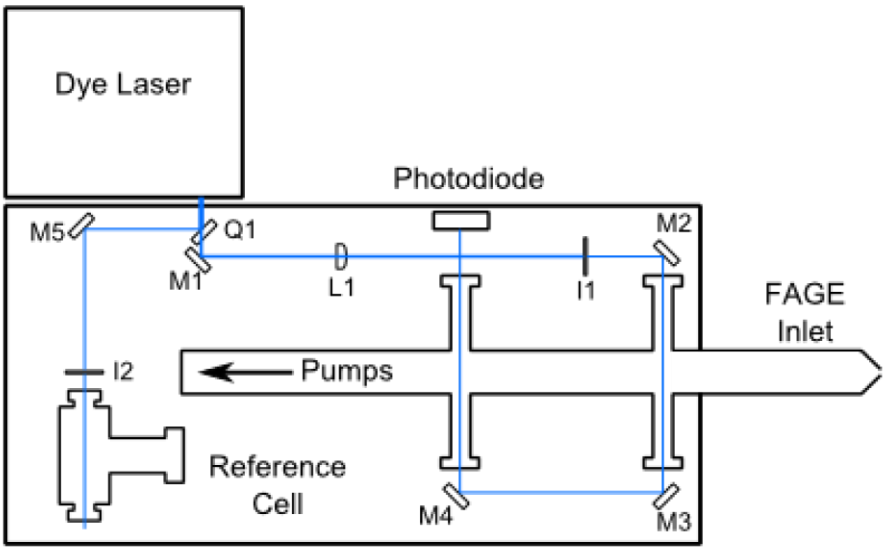

Figure 4.4: Top-down schematic of the FAGE instrument showing the laser beam path (blue line) through the OH and HO_2 detection cells, and the reference cell using the LITRON/LPD3000, 200 Hz PRF laser source. Q = quartz flat, M = mirror, I = iris and L = lens. The FAGE inlet was extended past the edge of the mounting table for insertion into the HIRAC chamber. The calibrated photodiode was used to normalise the fluorescence signals to fluctuations in laser power.

The UV light exiting the dye laser was split with a quartz flat (Q1) to direct ~5% of the laser light towards the reference cell (see following section). The remaining light was aligned through the OH and HO_2 cells sequentially using a series of 308 nm centred turning optics (M1 – M4, CVI Laser Optics, Melles Griot). Fluctuations in laser power were accounted for using a linear response UV sensitive photodiode (UDT-555UV, Laser Components, UK) at the exit arm of the HO_2 detection axis to normalise the LIF signal. Both laser systems provided between 5 - 7 and 2 - 3 mW of 308 nm light to the OH and HO_2 detection axes respectively. Maintaining a narrow range of laser powers minimized the experimentally determined inverse dependence of instrument sensitivity with respect to laser power (~18 % mW^{-1}, see chapter 5).

4.4.2 Reference cell

The reference cell enabled precise tuning of the laser wavelength to the absorption maxima of the OH $Q_1(2)$ line (within 98 %). The cell was maintained at a low pressure (< 4 mbar) and OH was generated continuously from a hot wire filament (80:20 Nickel:Chrome) in water saturated air. Approximately 5% of the total UV laser light output was passed through the reference cell, exciting the OH radicals and collecting the fluorescence on an un-gated CPM perpendicular to the laser beam. Laser power through the cell was sufficiently low (< 1 mW) that saturation of the detector did not occur and [OH] was sufficiently high that the OH fluorescence was observed.

4.4.3 Data acquisition

As mentioned in section 4.2 and 4.4.1, current FAGE instruments rely on the on-resonance fluorescence measurements of OH radicals, where the excitation and fluorescence wavelengths are identical. At low pressure, the fluorescence lifetime was extended past the duration of the laser pulse, and fast electronic gating of the CPMs was used to acquire the fluorescence. Custom made gating boxes switched the CPMs between low (off) and high (on) gain states as required using a TTL pulse (transistor-transistor logic). When a photon was detected by the CPM, an electron pulse was generated and the signal was interpreted by photon counting cards (Becker and Hickl PMS-400A) which collect discrete pulses into 1 μs width bins.

The delay timings and setups were different depending on the laser light source and so the timings for the 5 kHz PRF system are described first. The Nd:YAG control unit (JDSU) was used as the master clock to trigger all subsequent events. A delay generator (DG535, Stanford Research Systems Inc.) was synchronized to the master trigger from the JDSU and was used to trigger the photon counting cards and CPM gating as shown in Figure 4.5.

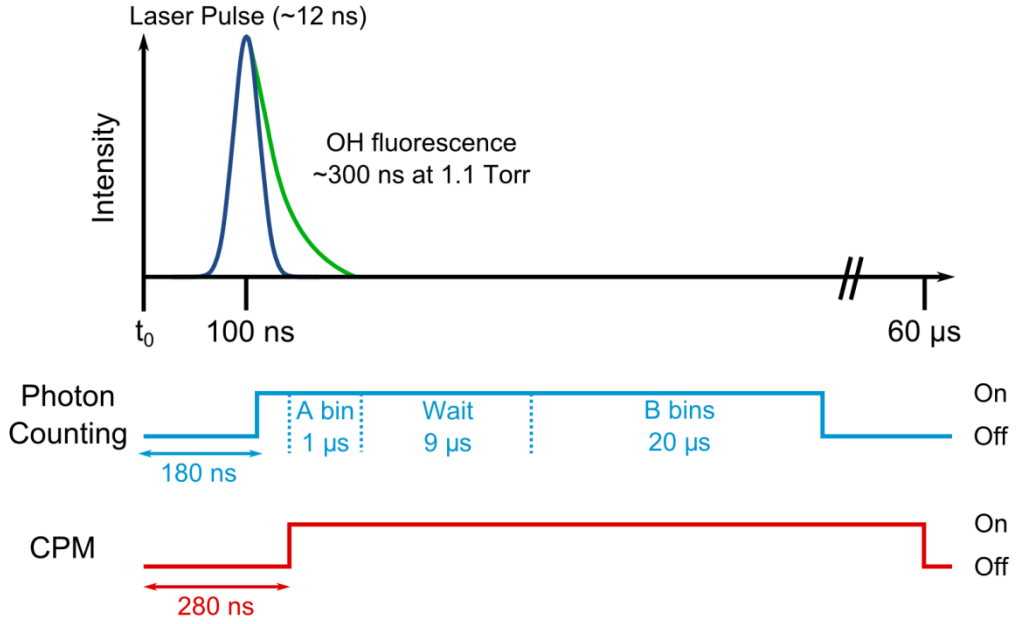

Figure 4.5: Schematic showing the gating and photon counting card timings for the 5 kHz laser system using the JDSU Nd:YAG as the master clock used to trigger the CPM gain state and photon counting cards. Not to scale.

In Figure 4.5, t_0 denotes the master clock trigger signal given by the JDSU Nd:YAG control unit. At t_0 + 100 ns the laser pulse is generated and the photon counting card and detector (CPM) are off (high gain state). After the laser pulse, the delay generator triggered the photon counting card to start the collection cycle at t = 180 ns. The CPM was switched to the low gain state (on) at t = 280 ns, immediately after the laser pulse. At t_0 + 60 µs the CPM is switched off and the sequence started again.

For the 200 Hz PRF system, the LITRON Nd:YAG laser was triggered externally using a Becker and Hickl (BH, DDG120) delay generator PCI card as the master clock. The flash lamp and Q-switch were triggered at t = 10 µs and t = 482 µs with a 1 µs width TTL pulse (Figure 4.6) and the laser pulse was generated at t = 482.5 µs. Here the CPM was kept in the high gain state (on) until ~5 µs before the laser pulse which enabled a better recovery time of the CPM to the low gain state after the laser pulse, improving the collection efficiency. The photon counting cards, after being triggered, were operated identically to the method described above for the 5 kHz PRF laser system.

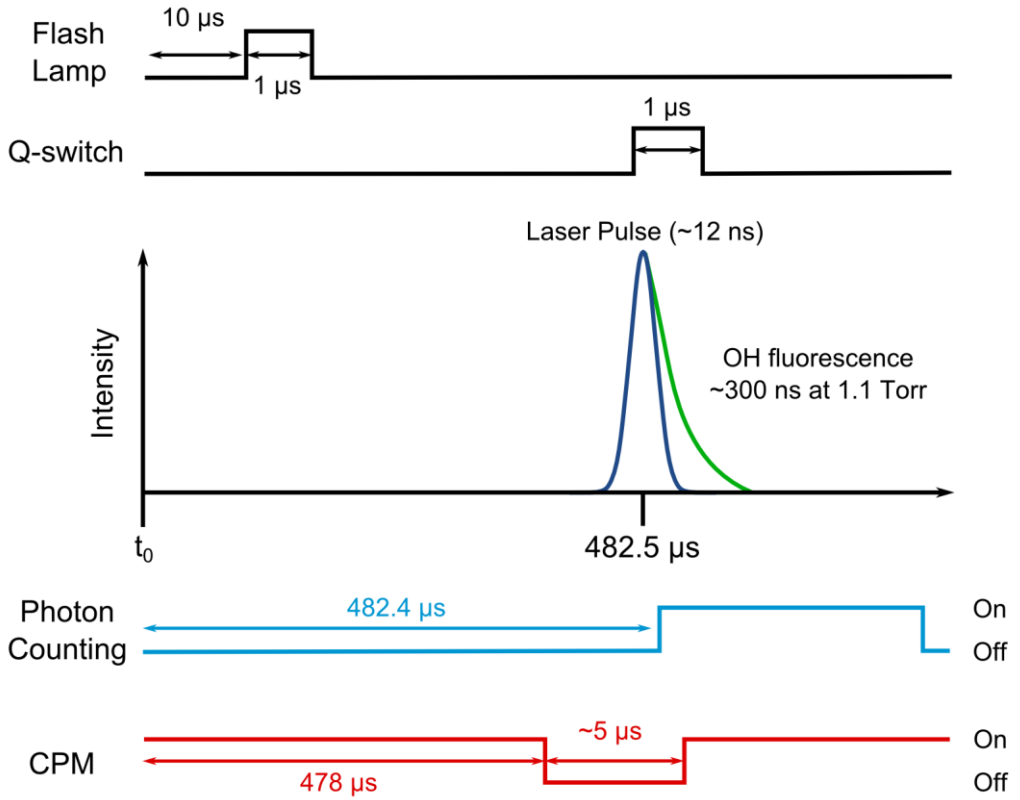

Figure 4.6: Schematic showing the laser flash lamp and Q-switch triggers for the LITRON Nd:YAG system operating at 200 Hz. The BH-DDG120 delay generator was used as the master clock and also triggered the CPM gain state and photon counting card. Photon counting bins not shown, but are identical to Figure 4.5. Not to scale.

The photon counting card measurement cycle was ~26 µs long (26 bin widths) with a ~100 ns start up delay (hence the cycle is started before the CPM is switched on). The OH fluorescence was collected for the first 1 µs (A bin) followed by a 5 µs wait. The final 20 µs (B bin) was used to collect any background signal due to dark counts or scattered light entering the instrument; (typically 1 - 2 counts s^{-1}). The counted signals are integrated over 1 second and the OH fluorescence signal, corrected for scattered light, is calculated using X:

$$\text{OHSignal} = Sig(\text{A bin}) - \frac{Sig(\text{B bins})}{x} \qquad \text{E 4.1}$$

where *Sig*(A bin) and *Sig*(B bins) are the cumulative counted photons collected in the A and B bins shown in Figure 4.5, and *x* is the ratio of the A and B bin widths (i.e. 1:20,

therefore $x = 20$). The integrated signal for the HO_2 fluorescence signal was calculated in the same way.

The dye lasers, pressure, photodiode signal and CPM signal are all monitored using a rack mounted computer system. The CPM signal is process by a photon counting card (Becker and Hickl PMS-400A), the SIRAH dye laser controlled using an RS232 connection and the LPD3000 dye laser *via* GPIB (General Purpose Interface Bus, National Instruments). Signals from the Baratrons (MKS, 10 Torr) and the photodiode (New Focus, 2032) are converted from analogue to digital signal using an analogue/digital (A/D) card (Measurement Computing, PCI-DAC1200). All of these inputs were analysed by custom written LabVIEW software which allows control of the dye lasers whilst monitoring the OH fluorescence, internal cell pressure and fluctuations in laser power (*via* the photodiode voltage).

Figure 4.7 shows a reference cell signal trace, which has been corrected for background counts caused by the laser pulse (see section 4.4.2), for a typical FAGE experiment conducted over ~2000 s. The data acquisition process was initialised and the laser wavelength was stepped at a resolution of 0.005 nm over the Q1(2) line (inlay plot, Figure 4.7). The maxima value and position is logged by the instrument software before the scan is restarted. When the S_{Ref} reaches > 98% of the maximum of the previous scan, the laser wavelength scan is stopped, and the online position is reached. The time online was user defined. Background laser signals from sources other than OH (e.g., scattered laser light) are accounted for by stepping the laser wavelength 0.02 nm from the online position, and this is called the offline position. This is indicated by a sharp decrease in S_{Ref} to near zero (Figure 4.7).

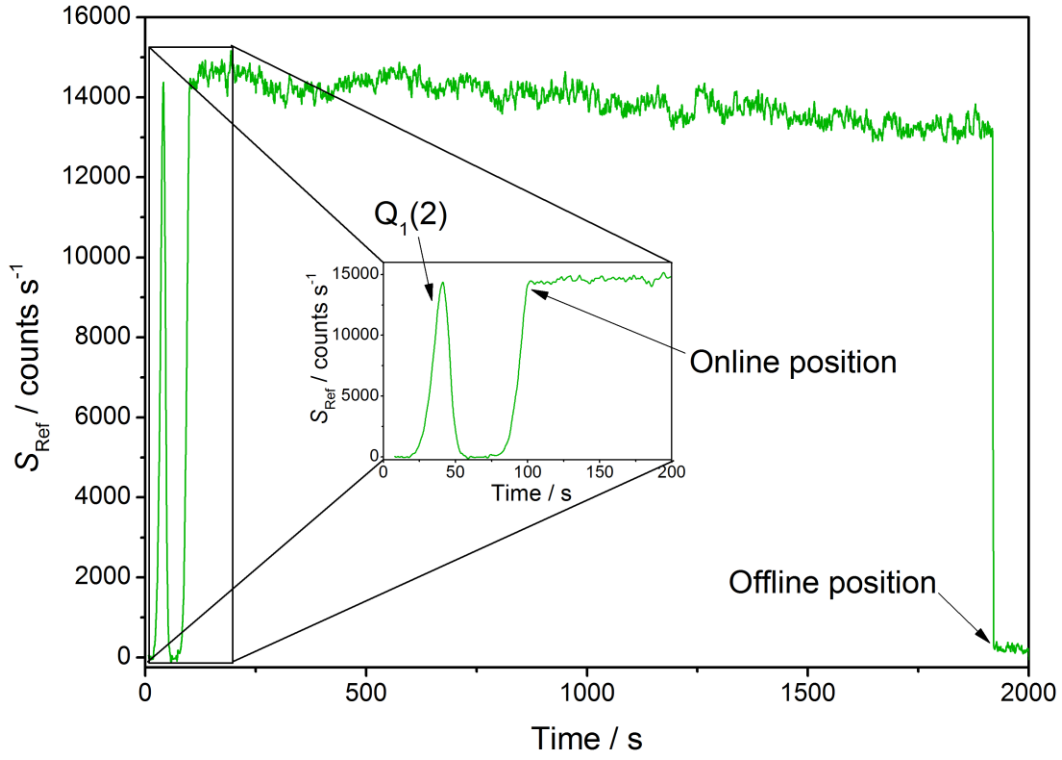

Figure 4.7: Reference cell signal, S_{Ref}, as a function of time measured using the 5 kHz PRF laser system. Background signals due to the ungated CPM measurement of the laser pulse (~11000 counts s^{-1}) have been subtracted for clarity. Plot inlay shows the tunable dye laser scan (0.004 nm step size) over the Q1(2) OH line, before reinitiating the scan to find the online position at > 98% of the first measured maxima. Reasonable stability in the online position was observed over the ~1800 s time period. Deviations from the maxima were due to the instability of the dye laser stepper motor over long time periods. The laser wavelength was stepped 0.02 nm < λ_{online} to the offline position.

4.5 Aircraft instrument

The airborne FAGE instrument used at the University of Leeds has been used in the newly developed alternative HO_2 calibration method (chapter 6) used to validate the standard H_2O vapour photolysis method (chapter 5). The instrument has been described in several theses (Floquet, 2006; Commane, 2009; Edwards, 2011; Walker, 2013) and in the literature (Commane et al., 2010) and hence will only be discussed briefly here. The reference cell, detectors, gating procedure and data acquisition cycle were all identical to the procedures described in the previous section and hence will not be repeated.

The instrument was designed around the strict requirements of FAAM (Faculty for Airborne Atmospheric Measurements), the organization that runs the BAe-146 G-LUXE research aircraft and hence the detection cells, pumpset, laser and additional electronics were designed to be compact and portable. A SolidWorks diagram of the detection cells, inlet pinhole and Eisele inlet are shown in Figure 4.8. The instrument was positioned so that all components except the inlet were inside the fuselage, and the instrument sampled from the retarded air flow created by the Eisele inlet (Eisele et al. (1997), designed for the BAe-146 by Jack Fox: formerly of NCAR, Boulder).

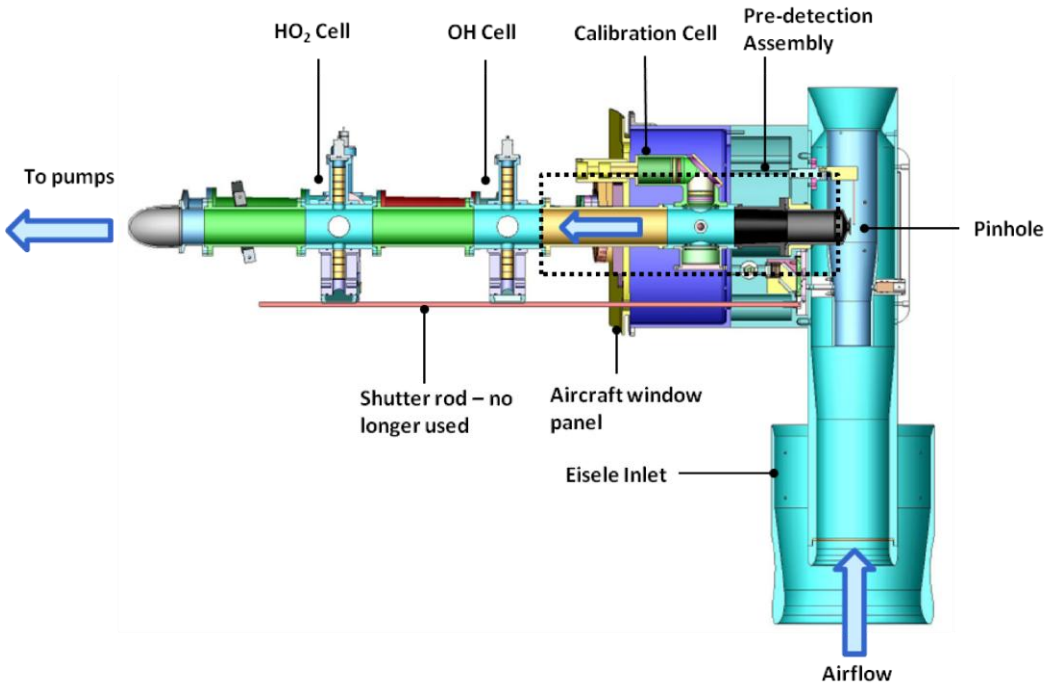

Figure 4.8: SolidWorks drawing of the airborne FAGE instrument employed by the University of Leeds on the BAe-146 aircraft. Reproduced from Walker (2013).

The FAGE inlet pinhole measured 0.7 mm in diameter, mounted in the centre of a conical nozzle and gas was expanded towards the OH detection axis, 50 cm from the pinhole. The OH and HO_2 detection axes were mounted in series, ~24 cm apart, and are almost identical in design to the HIRAC FAGE cells described above. NO was injected directly before the HO_2 detection axis using an MFC (Brooks) at 10 sccm, converting HO_2 to detectable OH radicals. The RO_2 conversion efficiency has recently been measured for ethene derived RO_2 only and $\alpha_{RO2} = S_{RO2}/S_{HO2} = \sim 0.40$, where S_{RO2} and S_{HO2} are the normalised fluorescence signals due to RO_2 and HO_2 in counts s^{-1} mW^{-1}. Walker (2013) showed that, using a modelling study based on the MCM v3.2 (MCM, 2014), the average model predicted RO_2 conversion during the most recent field campaign was small ($\alpha_{RO2} \approx 0.15$).

Laser light was collimated through baffled side arms to the fluorescence cell where OH is excited at 308 nm (see below for laser description) and the fluorescence was collected orthogonal to the direction of gas flow using electronically gated CPMs. Photodiodes were placed at the OH and HO_2 cell exit arms to normalise fluorescence signals to fluctuations in laser power. A diagram of the laser system used is shown in Figure 4.9. Laser radiation at 532 nm was generated using a diode pumped, Q-switched Nd:YAG laser (Photonics Industries, DS-532-10) with intracavity second harmonic generation operating at a 5kHz PRF. The 532 nm output was polarised and used to pump a solid-state, tunable Ti:Sapphire laser (Photonics Industries, TU-UV-308nm). Infrared light is emitted from the Ti:Sapphire at λ ~924 nm, which was tuned using a diffraction grating mounted to a computer controlled stepper motor. The target λ = 308 nm was generated by sum-frequency mixing of the first and second harmonics of the incident IR radiation using LBO and beta barium borate, BBO crystals. The pulse width of the light generated is ~35 ns with a linewdith ~0.06 cm^{-1} (λ = 308 nm), narrower than the dye lasers used by the HIRAC FAGE instrument (section 4.4.1).

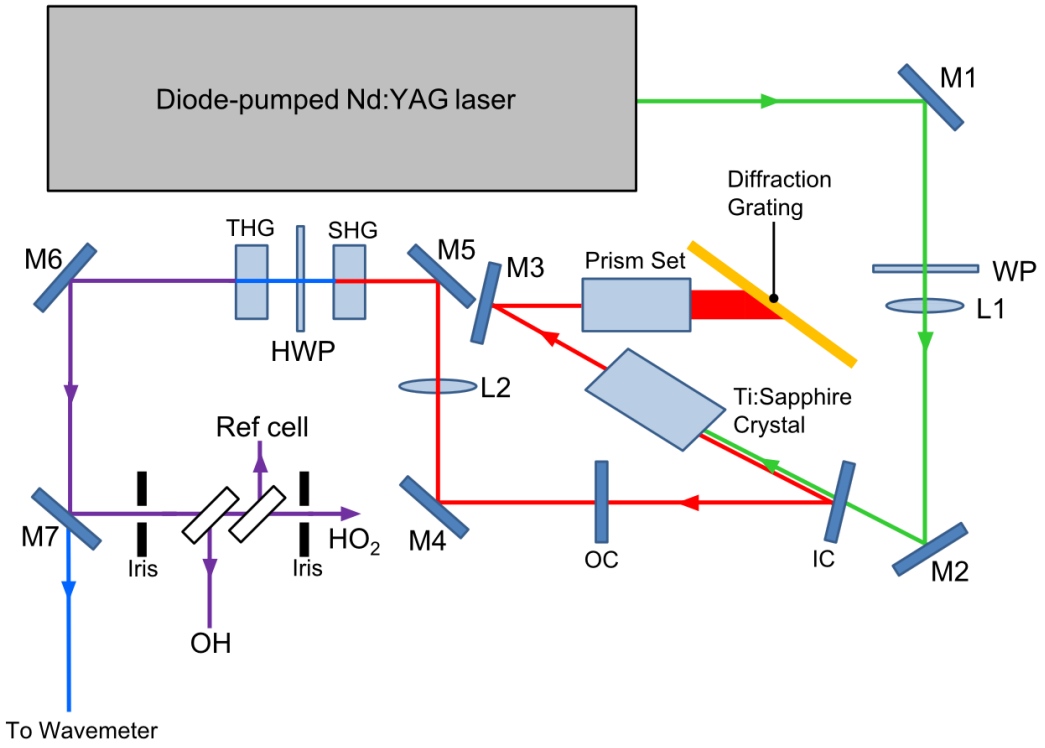

Figure 4.9: Schematic of the Nd:YAG pumped Ti:Sapphire laser used in conjunction with the University of Leeds aircraft instrument. M = mirror, WP = waveplate, L = lens, IC = input coupler, OC = output coupler, SHG = second harmonic generation, HWP = half wave plate, THG = third harmonic generation. Reproduced from Walker (2013).

4.6 Summary

The methodology and construction of the FAGE instrument used for HOx radical detection in the HIRAC chamber has been described here in detail. The instrument has been operated using two laser light sources for excitation of OH radicals at ~308 nm. The dependency of laser light source on the characterisation of the instrument is discussed in the following chapter. Using the 200 Hz PRF laser system, two new alternative calibration methods have been developed for the OH and HO_2 fluorescence detection cells (discussed in chapter 6). During the final stages of the alternative OH calibration process, a significant laser generated OH signal was observed from the photolysis of the OH precursor used, due to the high laser pulse energies from the 200 Hz system (see chapter 6 for details). Whilst this was corrected for in the relatively simple chemical systems used in chapter 6, the laser system was deemed unsuitable for

sensitive OH product detection studies in more chemically complex systems. Hence, the 5 kHz laser light source was used to conduct an investigation into the direct OH detection from the reaction of acetylperoxy with HO_2 (detailed in chapter 7).

The University of Leeds airborne FAGE instrument has been described briefly. Whilst no direct comparisons were drawn with the HIRAC based instrument in the calibration and characterisation process, the airborne FAGE cells were successfully calibrated using the new alternative HO_2 calibration method.

4.7 References

Commane, R. (2009). Understanding Radical Chemistry Throughout the Troposphere using Laser-Induced Fluorescence Spectroscopy. PhD, University of Leeds.

Commane, R., C. F. A. Floquet, T. Ingham, D. Stone, M. J. Evans and D. E. Heard (2010). "Observations of OH and HO_2 radicals over West Africa." Atmospheric Chemistry and Physics **10**: 8783-8801.

Creasey, D. J., G. E. Evans, D. E. Heard and J. D. Lee (2003). "Measurements of OH and HO2 concentrations in the Southern Ocean marine boundary layer." Journal of Geophysical Research-Atmospheres **108**(D15): -.

Creasey, D. J., D. E. Heard, M. J. Pilling, B. J. Whitaker, M. Berzins and R. Fairlie (1997). "Visualisation of a supersonic free-jet expansion using laser- induced fluorescence spectroscopy: Application to the measurement of rate constants at ultralow temperatures." Applied Physics B-Lasers and Optics **65**(3): 375-391.

Davis, D. D., W. Heaps and T. McGee (1976). "Direct Measurements of Natural Tropospheric Levels of OH *via* an Aircraft Borne Tunable Dye-Laser." Geophysical Research Letters **3**: 331.

Dusanter, S., D. Vimal, P. S. Stevens, R. Volkamer and L. T. Molina (2009). "Measurements of OH and HO_2 concentrations during the MCMA-2006 field campaign - Part 1: Deployment of the Indiana University laser-induced fluorescence instrument." Atmospheric Chemistry and Physics **9**(5): 1665-1685.

Edwards, P. M. (2011). Tropospheric oxidation from the Tropics to the Poles. PhD, Universirt of Leeds.

Eisele, F., L. Mauldin, C. Cantrell, M. Zondlo, E. Apel, A. Fried, J. Walega, R. Shetter, B. Lefer, F. Flocke, A. Weinheimer, M. Avery, S. Vay, S. G., J. Podolske, G. Diskin, J. D. Barrick, H. B. Singh, W. Brune, H. Harder, M. Martinez, A. Bandy, D. Thornton, B. Heikes, Y. Kondo, D. Riemer, S. Sandholm, D. Tan, R. Talbot and J. Dibb (2003). "Summary of measurement intercomparisons during TRACE-P." J. Geophys. Res. **108**(D20): 8791-8810.

Eisele, F. L., R. L. Mauldin, D. J. Tanner, C. Cantrell, E. Kosciuch, J. B. Nowak, B. Brune, I. Faloona, D. Tan, D. D. Davis, L. Wang and G. Chen (2001). "Relationship between OH measurements on two different NASA aircraft during PEM Tropics B." Journal of Geophysical Research-Atmospheres **106**(D23): 32683-32689.

Eisele, F. L., R. L. Mauldin, D. J. Tanner, J. R. Fox, T. Mouch and T. Scully (1997). "An inlet/sampling duct for airborne OH and sulfuric acid measurements." Journal of Geophysical Research-Atmospheres **102**(D23): 27993-28001.

Faloona, I. C., D. Tan, R. L. Lesher, N. L. Hazen, C. L. Frame, J. B. Simpas, H. Harder, M. Martinez, P. Di Carlo, X. R. Ren and W. H. Brune (2004). "A laser-induced fluorescence instrument for detecting tropospheric OH and HO_2: Characteristics and calibration." Journal of Atmospheric Chemistry **47**(2): 139-167.

Floquet, C. F. (2006). Airborne Measurements of Hydroxyl Radicals by Fluorescence Assay by Gas Expansion. PhD, University of Leeds.

Fuchs, H., B. Bohn, A. Hofzumahaus, F. Holland, K. D. Lu, S. Nehr, F. Rohrer and A. Wahner (2011). "Detection of HO_2 by laser-induced fluorescence: calibration and interferences from RO_2 radicals." Atmospheric Measurement Techniques **4**(6): 1209-1225.

Fuchs, H., H.-P. Dorn, M. Bachner, B. Bohn, T. Brauers, S. Gomm, A. Hofzumahaus, F. Holland, S. Nehr, F. Rohrer, R. Tillmann and A. Wahner (2012). "Comparison of OH concentration measurements by DOAS and LIF during SAPHIR chamber experiments at high OH reactivity and low NO concentration." Atmospheric Measurement Techniques **5**: 1611-1626.

Glowacki, D. R., A. Goddard, K. Hemavibool, T. L. Malkin, R. Commane, F. Anderson, W. J. Bloss, D. E. Heard, T. Ingham, M. J. Pilling and P. W. Seakins (2007). "Design of and initial results from a Highly Instrumented Reactor for Atmospheric Chemistry (HIRAC)." Atmospheric Chemistry and Physics **7**(20): 5371-5390.

Heard, D. E. (2006). Analytical techniques for atmospheric measurement. Oxford, Blackwell Pub.

Holland, F., A. Hofzumahaus, R. Schafer, A. Kraus and H. W. Patz (2003). "Measurements of OH and HO_2 radical concentrations and photolysis frequencies during BERLIOZ." Journal of Geophysical Research **108**(D4).

Kanaya, Y., J. Matsumoto, S. Kato and H. Akimoto (2001a). "Behavior of OH and HO2 radicals during the Observations at a Remote Island of Okinawa (ORION99) field campaign 2. Comparison between observations and calculations." Journal of Geophysical Research-Atmospheres **106**(D20): 24209-24223.

Kanaya, Y., Y. Sadanaga, J. Hirokawa, Y. Kajii and H. Akimoto (2001b). "Development of a ground-based LIF instrument for measuring HOx radicals: Instrumentation and calibrations." Journal of Atmospheric Chemistry **38**(1): 73-110.

Karl, M., T. Brauers, H. P. Dorn, F. Holland, M. Komenda, D. Poppe, F. Rohrer, L. Rupp, A. Schaub and A. Wahner (2004). "Kinetic Study of the OH-isoprene and O_3-isoprene reaction in the atmosphere simulation chamber, SAPHIR." Geophysical Research Letters **31**(5): L05117.

Kubistin, D., H. Harder, M. Martinez, M. Rudolf, R. Sander, H. Bozem, G. Eerdekens, H. Fischer, C. Gurk, T. KlÃ¼pfel, R. KÃ¶nigstedt, U. Parchatka, C. L. Schiller, A. Stickler, D. Taraborrelli, J. Williams and J. Lelieveld (2008). "Hydroxyl radicals in the tropical troposphere over the Suriname rainforest: comparison of measurements with the box model MECCA." Atmos. Chem. Phys. Discuss. **8**(4): 15239-15289.

Lee, J. D. (2000). University of Leeds.

Malkin, T. L. (2010). Detection of free-radicals and other species to investigate atmospheric chemistry in the HIRAC chamber Thesis (Ph D), University of Leeds (School of Chemistry), 2010.

Malkin, T. L., A. Goddard, D. E. Heard and P. W. Seakins (2010). "Measurements of OH and HO_2 yields from the gas phase ozonolysis of isoprene." Atmospheric Chemistry and Physics **10**(3): 1441-1459.

Mao, J., X. Ren, L. Zhang, D. M. Van Duin, R. C. Cohen, J. H. Park, A. H. Goldstein, F. Paulot, M. R. Beaver, J. D. Crounse, P. O. Wennberg, J. P. DiGangi, S. B. Henry, F. N. Keutsch, C. Park, G. W. Schade, G. M. Wolfe, J. A. Thornton and W. H. Brune (2012). "Insights into hydroxyl measurements and atmospheric oxidation in a California forest." Atmospheric Chemistry and Physics **12**(17): 8009-8020.

Martinez, M., H. Harder, D. Kubistin, M. Rudolf, H. Bozem, G. Eerdekens, H. Fischer, C. Gurk, T. Klupfel, R. Konigstedt, U. Parchatka, C. L. Schiller, A. Stickler, J. Williams and J. Lelieveld (2008). "Hydroxyl radicals in the tropical troposphere over the Suriname rainforest: airborne measurements." Atmospheric Chemistry and Physics **10**(4): 3759-3773.

MCM. (2014). "Master Chemical Mechanism Version 3.2 (http://mcm.leeds.ac.uk/MCM)."

Nehr, S., B. Bohn and A. Wahner (2012). "Prompt HO_2 Formation Following the Reaction of OH with Aromatic Compounds under Atmospheric Conditions." Journal of Physical Chemistry A **116**(24): 6015-6026.

Schlosser, E., T. Brauers, H.-P. Dorn, H. Fuchs, A.Hofzumahaus, F. Holland and A.Wahner (2007). "Intercomparison of Two Hydroxyl Radical Measurement Techniques at the Atmosphere Simulation Chamber SAPHIR." Journal of Atmospheric Chemistry **56**: 187-205.

Schlosser, E., T. Brauers, H. P. Dorn, H. Fuchs, R. Haseler, A. Hofzumahaus, F. Holland, A. Wahner, Y. Kanaya, Y. Kajii, K. Miyamoto, S. Nishida, K. Watanabe, A. Yoshino, D. Kubistin, M. Martinez, M. Rudolf, H. Harder, H. Berresheim, T. Elste, C. Plass-Dulmer, G. Stange and U. Schurath (2009). "Technical Note: Formal blind intercomparison of OH measurements: results from the international campaign HOxComp." Atmospheric Chemistry and Physics **9**(20): 7923-7948.

Siese, M., K. H. Becker, K. J. Brockmann, H. Geiger, A. Hofzumahaus, F. Holland, D. Mihelcic and K. Wirtz (2001). "Direct measurement of OH radicals from ozonolysis of selected alkenes: A EUPHORE simulation chamber study." Environmental Science & Technology **35**(23): 4660-4667.

Smith, S. C. (2007). Atmospheric Measurements of OH and HO2 using the FAGE technique: Instrument development and data analysis, University of Leeds.

Smith, S. C., J. D. Lee, W. J. Bloss, G. P. Johnson, T. Ingham and D. E. Heard (2006). "Concentrations of OH and HO2 radicals during NAMBLEX: measurements and steady state analysis." Atmospheric Chemistry and Physics **6**: 1435-1453.

Stevens, P. S., J. H. Mather and W. H. Brune (1994). "Measurement of Tropospheric OH and HO_2 by Laser-Induced Fluorescence at Low-Pressure." Journal of Geophysical Research-Atmospheres **99**(D2): 3543-3557.

Walker, H. M. (2013). Field Measurements and Analysis of Reactive Tropospheric species Using the FAGE Technique. PhD., Leeds.

Wennberg, P. O., R. C. Cohen, N. L. Hazen, L. B. Lapson, N. T. Allen, T. F. Hanisco, J. F. Oliver, N. W. Lanham, J. N. Demusz and J. G. Anderson (1994). "Aircraft-Borne, Laser-Induced Fluorescence Instrument for the in-Situ Detection of Hydroxyl and Hydroperoxyl Radicals." Review of Scientific Instruments **65**(6): 1858-1876.

Whalley, L. K., M. A. Blitz, M. Desservettaz, P. W. Seakins and D. E. Heard (2013). "Reporting the sensitivity of Laser Induced Fluorescence instruments used for HO_2 detection to an interference from RO_2 radicals and introducing a novel approach that enables HO_2 and certain RO_2 types to be selectively measured." Atmospheric Measurement Techniques **6**: 3425-3440.

Whalley, L. K., P. M. Edwards, K. L. Furneaux, A. Goddard, T. Ingham, M. J. Evans, D. Stone, J. R. Hopkins, C. E. Jones, A. Karunaharan, J. D. Lee, A. C. Lewis, P. S. Monks, S. J. Moller and D. E. Heard (2011). "Quantifying the magnitude of a missing hydroxyl radical source in a tropical rainforest." Atmospheric Chemistry and Physics **11**(14): 7223-7233.

Whalley, L. K., K. L. Furneaux, A. Goddard, J. D. Lee, A. Mahajan, H. Oetjen, K. A. Read, N. Kaaden, L. J. Carpenter, A. C. Lewis, J. M. C. Plane, E. S. Saltzman, A. Wiedensohler and D. E. Heard (2010). "The chemistry of OH and HO_2 radicals in the boundary layer over the tropical Atlantic Ocean." Atmospheric Chemistry and Physics **10**(4): 1555-1576.

Chapter 5. FAGE Instrument Calibration and Characterisation

5.1 Introduction

All methods of OH detection, with the exception of DOAS (Heard and Pilling, 2003) require a rigorous calibration technique to make accurate OH and HO_2 measurements in both the field and the laboratory. The FAGE instrument sensitivity to OH is defined *via* the relationship:

$$S_{OH} = C_{OH}\,[OH] \qquad \text{E 5.1}$$

where S_{OH} is the FAGE instrument signal normalised for laser power (counts s^{-1} mW^{-1}), C_{OH} the sensitivity or calibration factor (counts cm^3 $molecule^{-1}$ s^{-1} mW^{-1}) and [OH] the known concentration of OH produced (molecule cm^{-3}).

As E 5.1 shows, the instrument sensitivity to OH is dependent on the number of fluorescence photons counted, which is determined by several experimental parameters (Creasey et al., 1997a; Faloona et al., 2004). The laser light source defines the number of photons that excite the OH molecule, and so the OH absorption cross section, laser line width, beam area and laser power are important. The collection of the fluorescence after excitation is defined by the electronic gate time, the quantum yield of the channeltron photomultiplier tube (CPM) and the alignment of the detection optics. The OH fluorescence quantum yield is dependent on the cell pressure and composition of sample gas, as the OH excited state can be relaxed *via* collision. The fluorescence cell pressure defines the OH number density and the OH fluorescence quantum yield (i.e., the fluorescence lifetime), which is dependent on the concentration and composition of sample gas (as different gases have different quenching coefficients, (Creasey et al., 1997b)). These parameters can vary over time and can also depend on environmental or experimental conditions.

It is therefore important to regularly determine the instrument sensitivity experimentally, accounting for the most commonly varying parameters through generation and detection of OH (and HO_2) radicals. The current FAGE calibration method uses the vacuum ultra-violet (VUV) photolysis of H_2O vapour (Creasey et al., 2003) to produce quantifiable concentrations of OH and HO_2. As the calibration source determines the overall uncertainty of radical detection it must be carefully characterised (section 5.3).

It is important to be able to compensate and characterise any possible change in instrument sensitivity to OH and HO_2 when studying chamber based kinetics or field measurements. Specifically, and central to the work contained herein, changes in pressure (external to the instrument) and temperature are part of kinetics and airborne FAGE measurements alike. Using the H_2O vapour photolysis technique, changes in external pressure are accounted for by varying the FAGE inlet pinhole diameter (section 5.2.2.3), which induces a change in the fluorescence cell pressure. The dependence of instrument sensitivity to OH and HO_2 as a function of laser power (section 5.2.2.1), the OH excited state quenching efficiency of H_2O vapour (section 5.2.2.2), and inlet temperature (section 5.2.2.4) are also investigated here.

Characterisation and calibration of the HIRAC FAGE instrument was completed using two different laser light sources: the JDSU Nd:YAG (Photonic Solutions) pumped Sirah Cobra Stretch system (pulse repetition frequency (PRF) = 5 kHz) and the Litron pumped LPD3000 system (PRF = 200 Hz). Certain calibrations shown here were also conducted using the University of Leeds aircraft instrument (Commane, 2009; Commane et al., 2010; Walker, 2013), which was used as part of the newly developed alternative calibration techniques discussed in Chapter 6. Comparisons between results obtained using the two laser sources and instruments are drawn in the text where appropriate.

The final section of this chapter discusses the preliminary results into the on-going investigation of the conversion efficiency of certain RO_2 radicals to OH upon reaction with NO in the HIRAC FAGE detections cells (section 5.4). Previous reports have shown a significant enhancement of the HO_2 signal in the presence of certain hydrocarbons (Fuchs et al., 2011; Whalley et al., 2013). These effects are in the process of being thoroughly studied using a range of different hydrocarbons for the HIRAC FAGE apparatus, and hence only the preliminary results are discussed, along with the future aims for the project in section 5.5.

5.2 Water vapour photolysis

Laser induced fluorescence is a very sensitive, but non-absolute detection method and therefore each channel of the instrument needs to be calibrated. The VUV photolysis of H_2O vapour was originally developed for the calibration of HO_x measurement instruments in the 1990s (Aschmutat et al., 1994; Schultz et al., 1995; Heard and Pilling, 2003). Since then the methodology has become the HO_x measurement community standard (Stone et al., 2012), as shown in chapter 1. Upon the photolysis of a known H_2O vapour concentration (in synthetic air at atmospheric pressure) by a mercury pen-ray lamp at 184.9 nm, OH and HO_2 are produced in unity ratio (Fuchs et al., 2011) *via* reactions R 1.16 and R 1.17 (Schultz et al., 1995):

$$H_2O + h\nu \rightarrow OH + H \qquad \text{R 5.1}$$

$$H + O_2 + M \rightarrow HO_2 + M \qquad \text{R 5.2}$$

The radicals are then sampled by the HO_x instrument at atmospheric pressure; the concentrations of OH and HO_2 produced can be determined using equation E 1.2:

$$[OH] = [HO_2] = [H_2O]_{vap}\, \sigma_{H2O}\, \Phi_{OH}\, F_{184.9\,nm}\, \Delta t \qquad \text{E 5.2}$$

where $[H_2O]_{vap}$ is the water vapour concentration, σ_{H2O} is the known absorption cross-section of H_2O vapour at 184.9 nm ($(7.22 \pm 0.22) \times 10^{-20}$ molecule^{-1} cm^2 (Cantrell et al., 1997; Creasey et al., 2000), Φ_{OH} (= Φ_{HO2} = 1) is the photodissociation quantum yield of OH and HO_2 from water photolysis (Fuchs et al., 2011), $F_{184.9\,nm}$ is the photon flux of 184.9 nm light and Δt is the exposure time of the air to the Hg lamp output. There are two main methodologies used for obtaining the product $F_{184.9\,nm}\,\Delta t$ in equation E 1.2. In the first, $F_{184.9\,nm}$ can be measured using a calibrated phototube and Δt calculated using knowledge of the volumetric flowrate and geometric parameters of the flowtube (Stevens et al., 1994). In the second, a chemical actinometer can be used to obtain the product directly, with either O_2 or N_2O photolysis at 184.9 nm to generate either O_3 or NO respectively, both of which can be subsequently detected with reasonable sensitivity (Creasey et al., 1997a; Hofzumahaus et al., 1997; Heard and Pilling, 2003; Faloona et al., 2004). Both N_2O and O_2 chemical actinometers have been used in the current study, and are discussed in sections 5.3.1 and 5.3.2 respectively.

There are two main methods for delivery of the OH radicals to the FAGE inlet at atmospheric pressure. A laminar flow-tube, for which there was a radial gradient in the OH concentration which has to be quantified (Holland et al., 1995; Creasey et al., 1997a), or a turbulent flow-tube (referred to in this work as the "wand"). In the latter, the radial OH concentration is constant except very close to the walls. The HIRAC FAGE calibration source used the turbulent flow method and is discussed in more detail in section 5.2.1 and Malkin (2010).

5.2.1 Experimental

A detailed description of the HIRAC FAGE calibration source design and experimental procedure has been given by Malkin (2010) and so only relevant details and changes will be discussed here. The H_2O vapour photolysis calibration source, also known as the "wand" (Potter and Dumbledore, 2000), consisted of a square cross section flow tube (12.7 × 12.7 × 300 mm) through which 40 slm of humidified air (BOC, BTCA 178) was passed resulting in a turbulent flow regime (Reynolds number ≥ 4000). Figure 5.1 shows a schematic of the experimental apparatus used. The air was humidified by passing a fraction of the total air flow through a deionised water bubbler using three taps and the $[H_2O]_{vap}$ was measured using a dew-point hygrometer (CR4, Buck Research Instruments) prior to the "wand". The collimated 184.9 nm output of a mercury pen-ray lamp (LOT-Oriel, Hg-Ar) was introduced to the end of the main flow tube, photolysing H_2O (R 1.16 and R 1.17). The Hg lamp was positioned close to the end of the flow-tube to reduce the loss of OH to the internal surfaces of the "wand" and through reactions with impurities in the air prior to entering the FAGE inlet (Faloona et al., 2004). Thermocouples positioned at the opening of the flowtube and next to the lamp monitor the temperatures of the gases and lamp respectively, ensuring a greater degree of control over lamp and "wand" output.

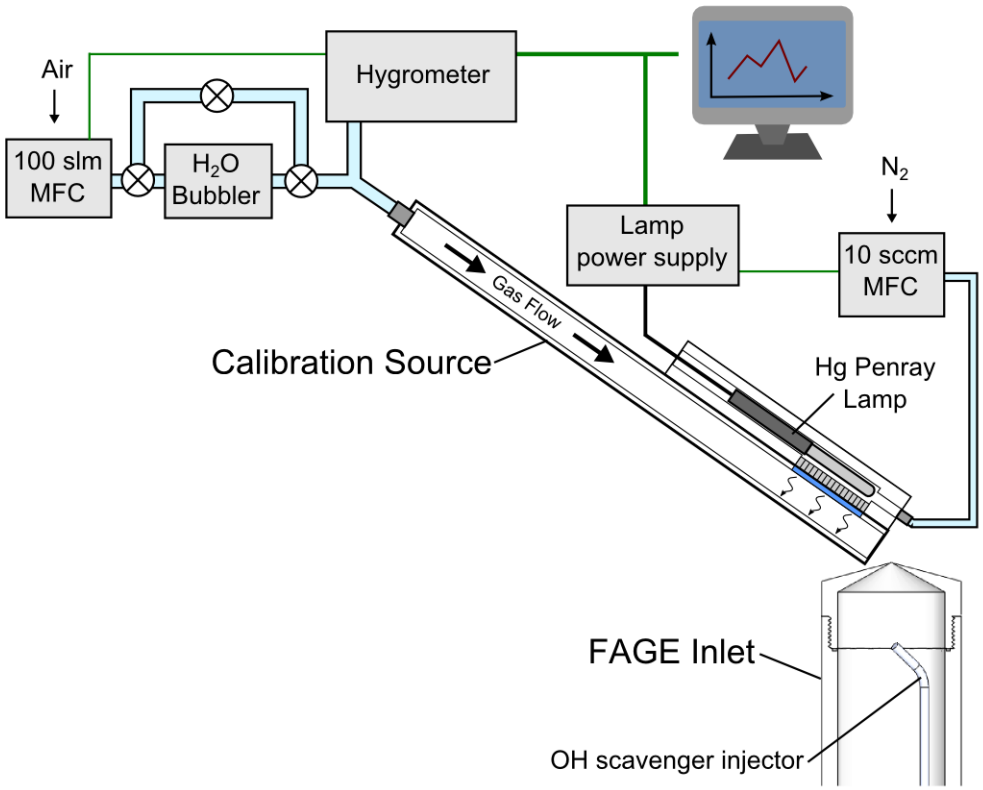

Figure 5.1: Schematic of the H_2O vapour photolysis setup used in the calibration of FAGE. Scavenger injection system is discussed in chapters 4 and 6.

The gas output from the "wand" was directed towards the FAGE sampling inlet and a range of HOx concentrations (~10^8 - 10^9 molecule cm^{-3}) were produced by changing the mercury lamp photon flux through changes in lamp current (as the two are proportional, see section 5.3) whilst maintaining a constant [H_2O]. Data were acquired and stored from the mass flow controllers (MFCs), lamp power supply and hygrometer to calculate the [HOx] produced from the "wand" continuously throughout the calibration. The time resolution of this process was ~5 s. After setting a chosen lamp current and ensuring that the [HOx] output was stable (±5%), the FAGE data acquisition process was initiated (for a more detailed description see chapter 4). Data from FAGE were recorded at a 1 s time resolution for a total of 60 s online and 30 s offline. After ~120 s (including finding the online position: see previous chapter), the FAGE software automatically restarted the cycle and the lamp current was manually changed to determine a new [HOx]. The measurements were repeated 5 - 6 times including a measurement at [HOx] = 0. For the OH cell the 60 s online period was averaged and plotted as a function of the 60 s averaged calibration data (i.e. S_{OH} vs. [HOx]) producing a

multipoint calibration plot. For HO_2, signals due to OH alone were measured in the HO_2 fluorescence cell for 30 s ($S_{OH(HO2)}$). After which the NO was injected into the cell for the final 30 s online, measuring the combined signals due to HO_2 and OH, S_{HOx}. Measurement of the OH signal in the HO_2 cell allowed the calculation of the fluorescence signal due to HO_2, S_{HO2} (= S_{HOx} - $S_{OH(HO2)}$). The linear regression, weighted to the uncertainties in both axes, was used to determine the calibration factors, or instrument sensitivities, C_{OH} and C_{HO2}.

The laser power entering the FAGE cells was altered by using a combination of different neutral density filters (0.2, 0.3 and 0.6 O.D., ThorLabs) at the dye laser exit aperture. Laser powers between 2.0 - 10 mW were achieved by attenuating the UV light in this manner, which span the operating range of the FAGE instrument (5 - 9 mW, see chapter 4). By altering the fractional flow of air through the water bubbler *via* a series of bypass valves, different H_2O vapour concentrations were passed to the calibrator (25 - 6000 ppmv). Different internal detection cell pressures (1.8 – 3.8 mbar) were achieved by changing the diameter of the FAGE inlet pinhole between 0.5 – 1.0 mm. The aircraft FAGE instrument sensitivity was determined as a function of fluorescence cell pressure only, using the HIRAC calibration source and inlet pinhole diameters between 0.5 - 0.75 mm.

Whilst the listed dependencies have been extensively covered before in the literature, to date there exists only one reported study into the effect of inlet temperature on instrument sensitivity (Regelin et al., 2013). To investigate this, the FAGE inlet was wrapped with ¼" copper tubing and covered in aluminum foil, to aid thermal contact, and an outer layer of 10 mm thick neoprene, to aid insulation. A Huber temperature control unit (Huber Unistat 360, 3.2 l) was used to flow a specially formulated fluid (Huber DW-THERM, -90 - 200 ^{o}C) through the ¼" copper tubing. Calibrations were conducted at five inlet temperatures between 263 - 343 K, representative of the active temperature range of the HIRAC chamber (Farrugia, 2014).

5.2.2 Results

All uncertainties displayed are quoted to ±2σ and all regressions shown are empirical, unless otherwise stated.

Figure 5.2 shows a typical plot for the HIRAC FAGE OH fluorescence cell instrument sensitivity, C_{OH}, using the H_2O photolysis method. Several [OH] concentrations were generated by varying the $F_{184.9\ nm}$ Hg pen-ray lamp output at a constant $[H_2O]_{vap}$. The typical $[H_2O]_{vap}$ and lamp current range for the calibration process are 3500 - 4500 ppmv and 0.8 - 3.0 mA respectively. The uncertainties shown are calculated as the standard deviation in the S_{OH} and [OH] measurements to 1σ and the linear regression displayed was weighted to the uncertainties in both the *x* and *y* axes. The calibration factor shown was determined for the most commonly used FAGE inlet pinhole (1.0 mm) for the HIRAC FAGE instrument using the 200 Hz PRF laser system: $C_{OH} = (2.62 \pm 0.92) \times 10^{-8}$ counts cm^3 $molecule^{-1}$ mW^{-1} s^{-1} for $[H_2O]_{vap}$ = 4500 ppmv, fluorescence cell pressure = 3.85 mbar and laser power = 5 mW. Calibration uncertainties were calculated at ~34 % and are described in detail in section 5.2.3. Using the 5 kHz PRF system at the same cell pressure and laser power at $[H_2O]$ = 3500 ppmv, $C_{OH} = (4.64 \pm 1.68) \times 10^{-8}$ counts cm^3 $molecule^{-1}$ mW^{-1} s^{-1}. The increase in sensitivity of ~77% was hypothesized as the narrower laser line width of the 5 kHz system compared to that of the 200 Hz PRF system: (0.097 ± 0.010) cm^{-1} compared to (0.29 ± 0.05) cm^{-1}, measured by Malkin (2010) and Lee (2000), respectively (±1σ). The ~1000 ppmv discrepancy between the calibration datasets was discounted as the instrument sensitivity due to $[H_2O]_{vap}$ over that range was considered negligible, and this is demonstrated in section 5.2.2.2.

The average range of $[HO_x]$ produced was 10^8 - 10^9 molecule cm^{-3}, ~10 times higher than the maximum concentration seen in a typical chamber experiment (~10^7 molecule cm^{-3}, see chapters 6 and 7 for experimental data). As fewer points are measured close to the limit of detection for the instrument (5.8×10^6 molecule cm^{-3} using the 5 kHz laser system, calculated in section 5.2.4), calculation of [HOx] relies heavily on the extrapolation of the instrumental sensitivities. This could likely introduce uncertainty into measurements at low [HOx] concentrations that has not been accounted for by the current uncertainty analysis (section 5.2.3).

Generation of [HOx] < 5 × 10^8 molecule cm^{-3} was difficult due to limitations of the calibration source. The instability of the Hg lamp output at lower currents (< 1 mA) and $[H_2O]_{vap}$ measurements < 1000 ppmv close to the detection limit of the hygrometer (100 ppmv) restricted the production of HOx below 10^8 molecule cm^{-3}. Calibration of the OH cell at ~200 ppmv was completed, however lamp currents > 3.0 mA had to be used to generate a stable [HOx]. As the lamp flux has not been determined at lamp currents > 2.7 mA, the added uncertainty in a lower [HOx] measurement increased the overall calibration uncertainty for the FAGE instrument to ~25%.

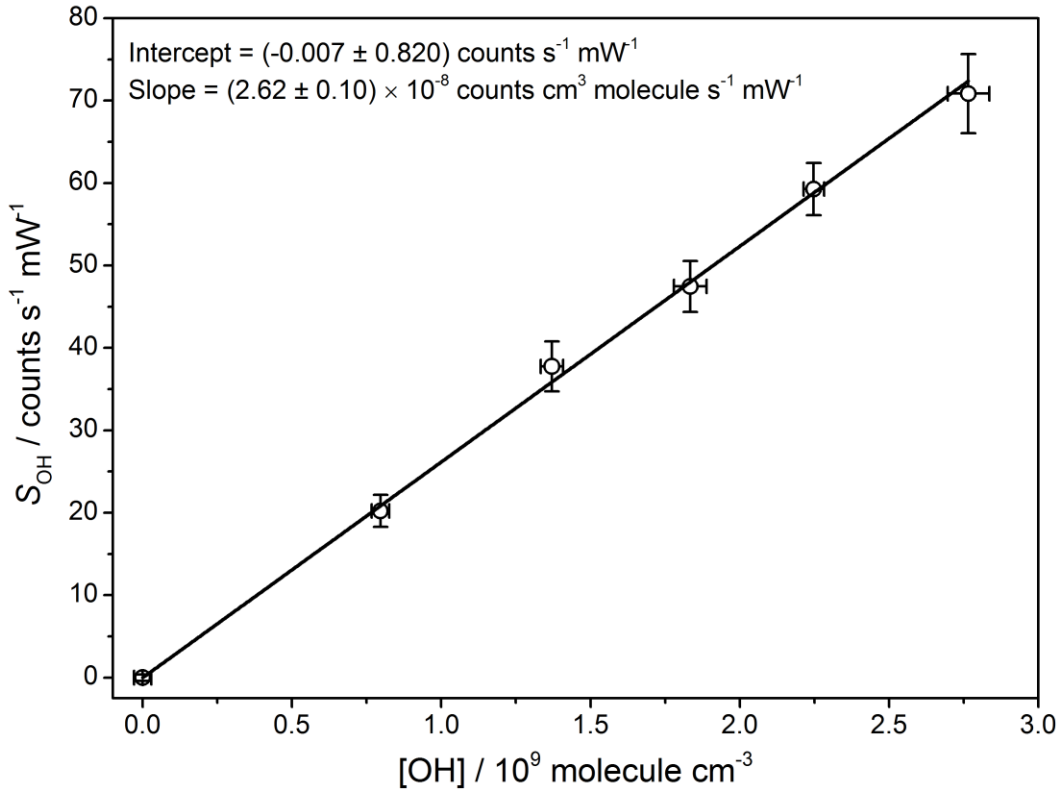

Figure 5.2: Detected OH signal normalized for laser power (S_{OH}) as a function of calculated [OH] determined in the OH fluorescence cell calibration procedure. Error bars and regression uncertainties are indicative of standard deviation to 1σ of data over the 60 s online measurement period. Linear regression, weighted to *x* and *y* errors, gives calibration factor (including systematic uncertainties), C_{OH} = (2.62 ± 0.92) × 10^{-8} counts cm^3 $molecule^{-1}$ mW^{-1} s^{-1} at cell pressure = 3.82 mbar, inlet pinhole diameter = 1.0 mm, $[H_2O]_{vap}$ = 4500 ppmv and laser power = 5 mW using the 200 Hz PRF laser system. The uncertainty in C_{OH} is a function of linear regression standard error and systematic errors associated with the calibration process (section 5.2.3).

5.2.2.1 Instrument sensitivity as a function of laser power

The instrument sensitivity to OH was evaluated as a function of laser power over an extended operating laser power range (3 - 10 mW). The values of C_{OH} for both 200 Hz and 5 kHz PRF laser systems are compared in Figure 5.3(a) and (b), relative to the C_{OH} at 7 mW (the modal operating laser power). All calibrations conducted at constant $[H_2O]_{vap}$ (Figure 5.3(a) 3300 ± 500 ppmv, (b) 2100 ± 100 ppmv) and internal cell pressure (Figure 5.3(a) 3.84 ± 0.03 mbar, (b) 3.96 ± 0.04 mbar) with error bars representative of the overall error associated with the calibration process (1σ). Using a linear regression as an empirical measure, a decrease in C_{OH} was observed, with ΔC_{OH} = -20% mW^{-1} at 200 Hz PRF (Figure 5.3a) and $\Delta C_{OH} \approx$ -3% mW^{-1} at 5 kHz PRF (Figure 5.3b).

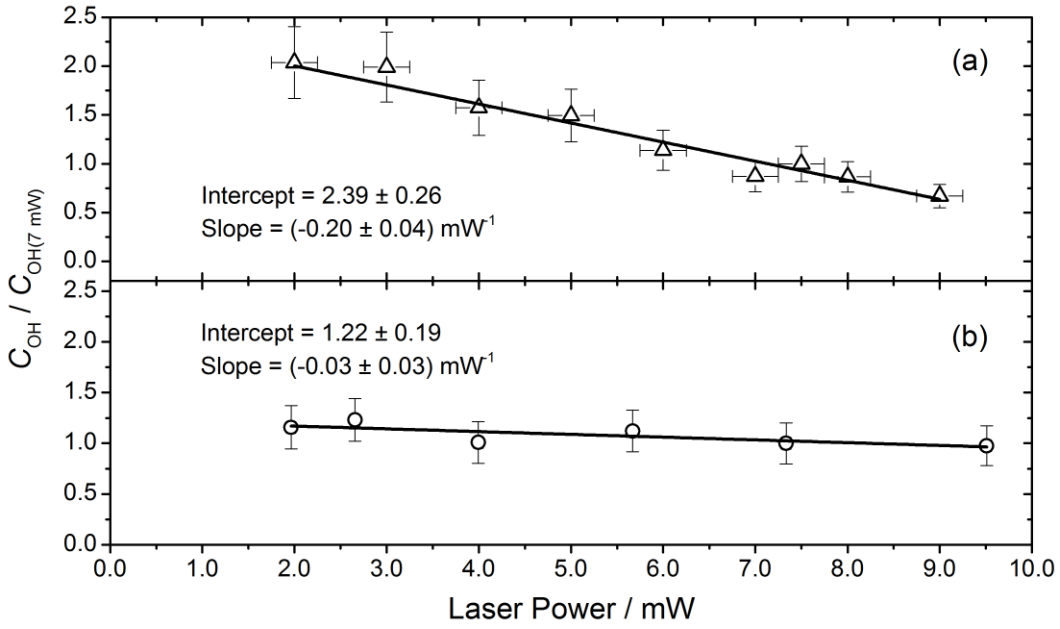

Figure 5.3: HIRAC FAGE instrumental sensitivity to OH, C_{OH}, relative to C_{OH} at 7 ± 1 mW as a function of laser power entering the OH fluorescence cell for the 200 Hz (a) and 5 kHz (b) Nd:YAG pumped dye laser systems using the H_2O photolysis calibration method. All calibrations conducted at constant $[H_2O]_{vap}$ ((a) 3300 ± 500 ppmv, (b) 2100 ± 100 ppmv) and internal cell pressure ((a) 3.84 ± 0.03 mbar, (b) 3.96 ± 0.04 mbar); uncertainties quoted to ±1σ.

The small decrease in sensitivity to OH as a function of laser power for the 5 kHz PRF laser source was likely due to an increased background S_{OH} measurement from increased laser light reflections from surfaces inside the cell combined with increased Rayleigh scattering, decreasing the overall S/N ratio. However a more marked decrease was observed in the instrumental sensitivity for the 200 Hz PRF laser system. Upon examination of the $Q_1(2)$ and $Q_{21}(2)$ OH rotational transitions of the OH $A^2\Sigma^+$ (v'=0) ← $X^2\Pi_i$ (v''=0) transition near 308 nm measured OH emission bands measured using the 200 Hz PRF laser at (5.0 ± 0.5) and (24.0 ± 0.5) mW (Figure 5.4a and b respectively), a broadening of the lines was observed at higher laser powers.

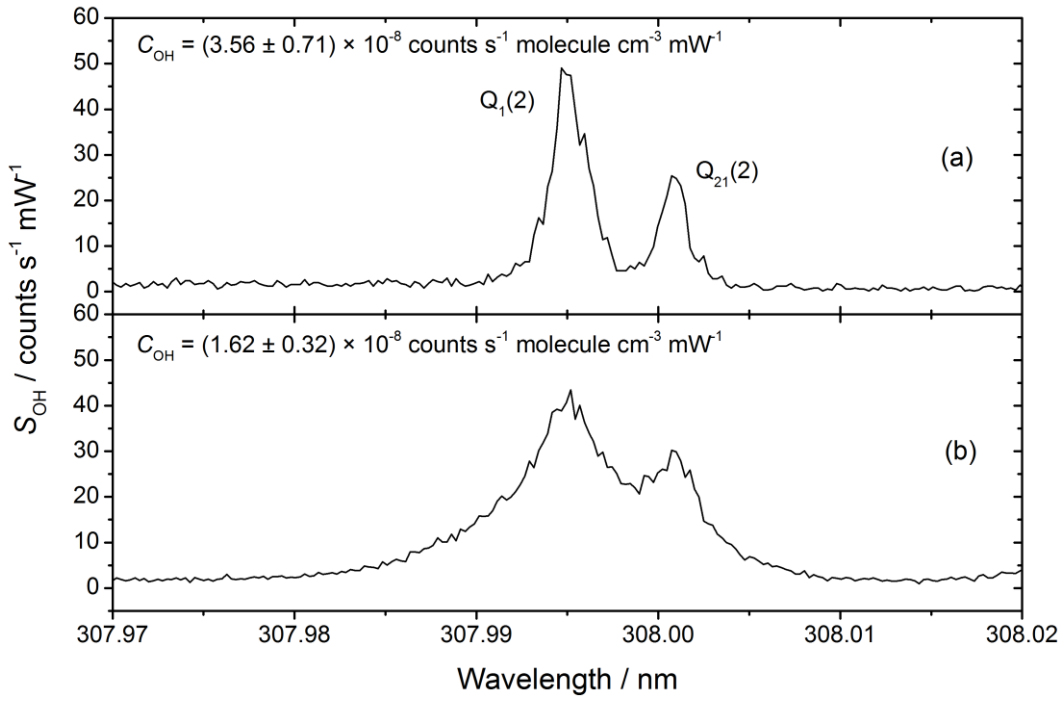

Figure 5.4. Comparison of the laser excitation spectra for the $Q_1(2)$ and $Q_{21}(2)$ rotational transitions of the OH $A^2\Sigma^+$ (v'=0) ← $X^2\Pi_i$ (v''=0) transition near 308 nm measured using the LITRON pumped dye laser (200 Hz PRF) at 5.0 ± 0.5 mW (a) and 24.0 ± 0.5 mW (b) laser power respectively. The spectrum was recorded at a 0.004 nm grating resolution with 1 second averaging in the OH detection cell maintained at 3.81 mbar (1.0 mm diameter pinhole). Calibration factors, C_{OH}, quoted to demonstrate reduction in sensitivity to OH at higher laser powers due to power broadening of the OH LIF line.

Photolysis of a species that could create an excited state OH(v'=0,1) radical upon dissociation could explain the phenomenon. However, as high purity air was used and no species other that H_2O vapour were introduced into the airflow of the calibration source, this seems unlikely. Laser power broadening of the OH emission is also possible. The increased pulse energy of the 200 Hz PRF laser system (25 μJ pulse^{-1}) causes stimulated emission (Rabi flopping), effectively broadening the measured OH emission bands. No further quantitative analysis was performed, however, and during operation of the instrument laser powers were maintained at (7 ± 1) mW to minimize the effects on HOx radical measurements.

5.2.2.2 Instrument sensitivity as a function of $[H_2O]_{vap}$

Figure 5.5 shows the instrument sensitivity to OH as a function of $[H_2O]_{vap}$ relative to the C_{OH} measured at 2900 ppmv determined using the conventional flow tube calibration method. Calibrations were conducted at a constant laser power ((7 ± 1) mW) and internal cell pressure (3.85 mbar) using the 1.0 mm diameter inlet pinhole and the 200 Hz PRF laser system. The instrument sensitivity was found to decrease with increasing $[H_2O]_{vap}$ ($\Delta C_{OH} \approx$ -4% (1000 ppmv)$^{-1}$, calculated using the empirical linear regression to the data weighted to the uncertainties in the x and y axes). The linear regression is purely empirical, and helps to clarify that from the standard operating $[H_2O]_{vap}$ (2000 - 4000 ppmv), any change in C_{OH} falls well within the experimental uncertainty associated with the calibration (section 5.2.3).

The observed decrease in C_{OH} could be explained by the increased collisional quenching of the OH excited state ($A^2\Sigma^+$ (v'=0)) at higher $[H_2O]_{vap}$ (Copeland and Crosley, 1986; Bailey et al., 1999), which reduces the OH fluorescence quantum yield, ϕ_{fl}, and the total measurable fluorescence, f_{gate}. As mentioned in the main text (section 5.1.1), the OH fluorescence quantum yield is defined as $\phi_{fl} = A / (A+k_q[M])$, where A is the inverse of the radiative lifetime, and k_q is the rate coefficient for quenching of the excited OH. As $[H_2O]_{vap}$ increases, so does k_q, which in turn decreases ϕ_{fl}, f_{gate} and therfore C_{OH}. Displayed in Figure 5.5 is the predicted decrease in C_{OH} with increasing $[H_2O]_{vap}$ calculated relative to the C_{OH} at 200 ppmv (0.86 ± 0.15), which falls well within the calculated uncertainty of the calibration over the experimental range of $[H_2O]$, ~18% to 1σ.

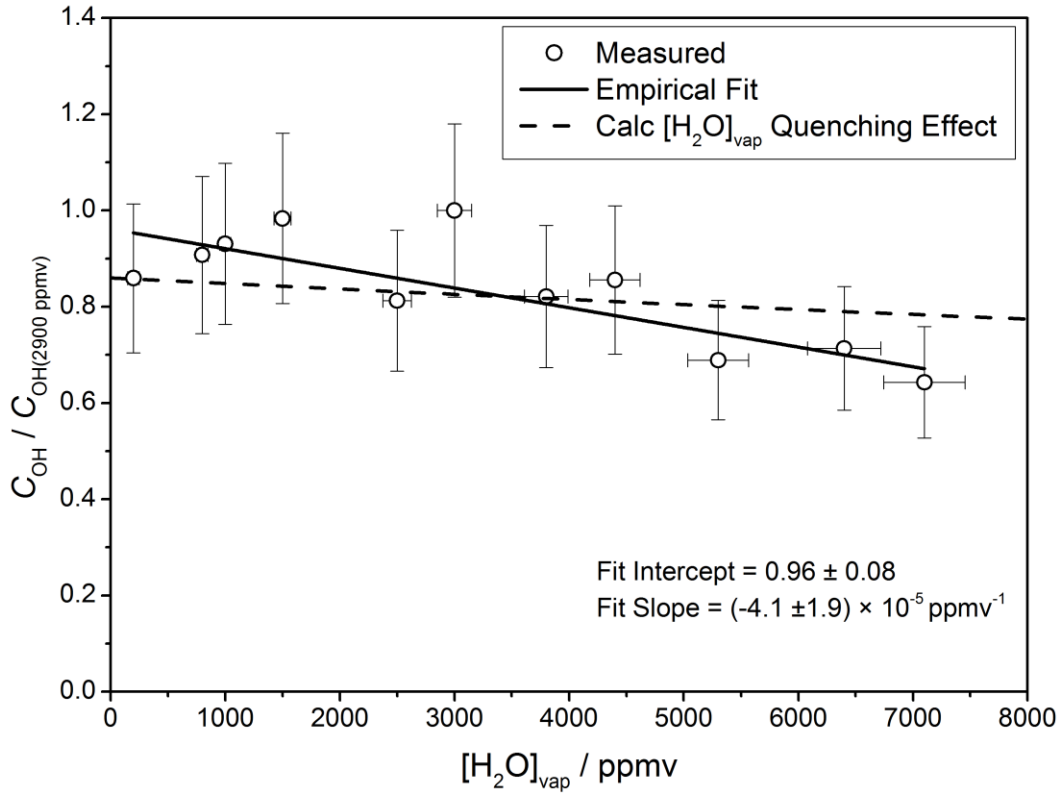

Figure 5.5: HIRAC FAGE instrument sensitivity to OH, C_{OH}, as a function of $[H_2O]_{vap}$ relative to C_{OH} at 2900 ppmv using the LITRON Nd:YAG pumped dye laser system at 200 Hz PRF. All calibrations conducted at constant laser power (7 ± 1 mW) and fluorescence cell pressure (3.84 ± 0.03 mbar) using the 1.0 mm diameter pinhole. Solid line shows the empirical linear regression of the data weighted to the uncertainties in the *x* and *y* axes. Dashed line represents the theoretical effect on the quenching of the OH excited state ($A^2\Sigma^+$ (v'=0)) due to the change in $[H_2O]_{vap}$, displayed relative to the C_{OH} at 200 ppmv (0.86 ± 0.15). Error bars represent the total uncertainty in the calibration procedure quoted to ±1σ.

5.2.2.3 Instrument sensitivity as a function of fluorescence cell pressure

The FAGE instrument sensitivity to OH and HO_2 (Figure 5.6) was determined as a function of pressure over the inlet pressure range between 1.8 - 3.8 mbar using the 0.5, 0.7, 0.8, 0.9, 0.95 and 1.0 mm diameter pinholes and the error bars are representative of the total uncertainty (±1σ) in the calibration (section 5.2.3). Constant laser power ((8 ± 1) and (4 ± 1) mW for the OH and HO_2 cells respectively) and $[H_2O]_{vap}$ (4500 ± 600 ppmv) were maintained throughout the calibration process. In both the OH and HO_2 cells an increase in sensitivity as a function of pressure was observed and was described empirically using a linear regression weighted to the uncertainties in the *y* axis.

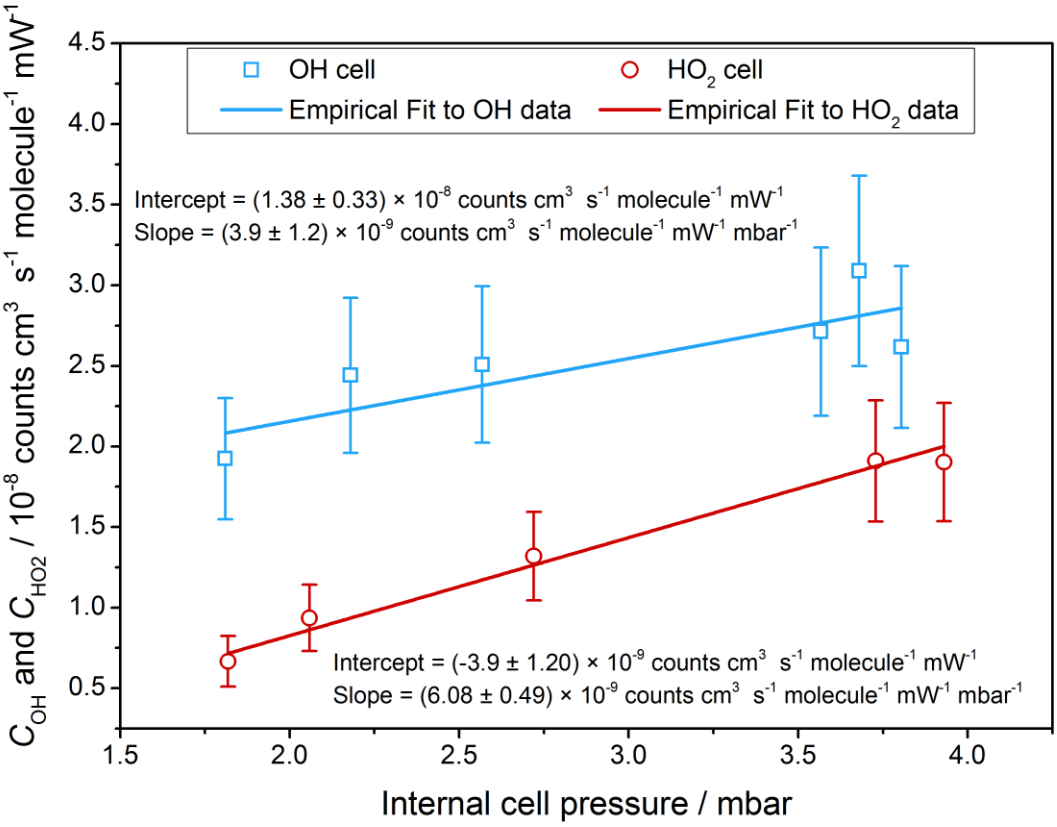

Figure 5.6: Instrument sensitivity to OH and HO_2 as a function of internal cell pressure for the HIRAC FAGE instrument using the 200 Hz PRF laser system. Error bars are representative of total uncertainty in C_{OH} and C_{HO2} (section 5.2.3). Constant laser power ((8 ± 1) and (4 ± 1) mW for the OH and HO_2 cells respectively) and $[H_2O]_{vap}$ (4500 ± 600 ppmv) were maintained throughout the calibration process.

The empirical linear regressions were used to describe the sensitivity as a function of fluorescence cell pressure for experiments conducted in HIRAC, and are a valid description of the data inside the 1.8 - 3.8 mbar pressure range only. The C_{OH} and C_{HO2} datasets shown here were not conducted at the same time, but 6 months apart. This was due to the chronological order of the development of the alternative calibration techniques discussed in chapter 6, during which time the FAGE pump-set was serviced, increasing the pumping capacity and generally lowering the fluorescence cell pressures for each pinhole in the C_{OH} determination.

The increase in C_{HO2} as function of pressure was observed to be sharper compared to C_{OH}, where ΔC_{OH} = (17.3 ± 10.6) % and ΔC_{HO_2} = (31.6 ± 4.4) % increase between 1.3 - 3.8 mbar. Altering the pinhole diameter could change the flow dynamics inside the instrument reducing NO mixing efficiency, and therefore HO_2 conversion efficiency, before the HO_2 cell. This empirical decrease has been reproduced in a more recent calibration of the HO_2 cell using the 5 kHz PRF laser source (slope = (5.14 ± 0.46) × 10^{-9} counts cm^3 $molecule^{-1}$ s^{-1} mW^{-1} $mbar^{-1}$), suggesting the process was not affected by changes in laser pulse energy.

The experimental parameters controlling the instrument sensitivity, C_{OH}, which are dependent upon pressure, are the OH concentration in the laser-excitation region, $[OH]_{cell}$, the fluorescence quantum yield following laser excitation to the OH $A^2\Sigma^+$ (v′=0) excited state, ϕ_{fl}, and the fraction of the fluorescence decay which falls within the integrating gate of the photon counter, f_{gate}(Creasey et al., 1997b; Faloona et al., 2004).

The OH concentration in the cell held at total density [M] is given by $[OH]_{cell} = \chi[M]$, where χ is the mixing ratio of OH impinging at the pinhole (assuming no losses at the pinhole), and $\phi_{fl} = A / (A+k_q[M])$, where A is the inverse of the radiative lifetime, and k_q is the rate coefficient for quenching of the excited $A^2\Sigma^+$ (v′=0) (averaged appropriately over all quenching species). Assuming that f_{gate} = 1, then $[OH]_{cell} \times \phi_{fl} = \chi[M]\, A / (A+k_q[M])$. At the limit of [M]→0, the product becomes χ[M] and C_{OH} is directly proportional to pressure ([M]), whereas at higher pressures when $k_q[M] >> A$ (at 14 Torr the ratio is ~ 10) the product becomes $\sim\chi\, A / k_q$ and C_{OH} is independent of [M], and thus depends only on the mixing ratio of OH. Hence the observation that C_{OH} increased non-linearly over pressures between 1.3 - 3.8 mbar in

this study is consistent with the expected behaviour based purely on the balance between OH number density and rate of quenching.

The pressure dependence of the aircraft instrument sensitivity to OH and HO_2 are presented in Figure 5.7 for comparison. All calibrations were conducted at constant laser power (15 ± 2 and 10 ± 2 mW, for OH and HO_2 respectively) and [H_2O] (6700 ± 500 ppmv). As with the HIRAC FAGE instrument, the C_{HO2} was observed to increase as a function of pressure. However, the C_{OH} appears to show no pressure dependence, although there is variability of ~2.5 between at 1.4 and 1.9 mbar. This is unusual as both the HO_2 and OH calibrations at respective pressures are performed simultaneously under the same conditions (laser power, [H_2O] etc.). Commane (2009) has recently investigated the instrument sensitivity as a function of fluorescence cell pressure and did not observe the same variability in C_{OH}. As only the accurate measurement of C_{HO2} was required for comparison with the newly developed alternative HO_2 calibration method (chapter 6), the C_{OH} was ignored.

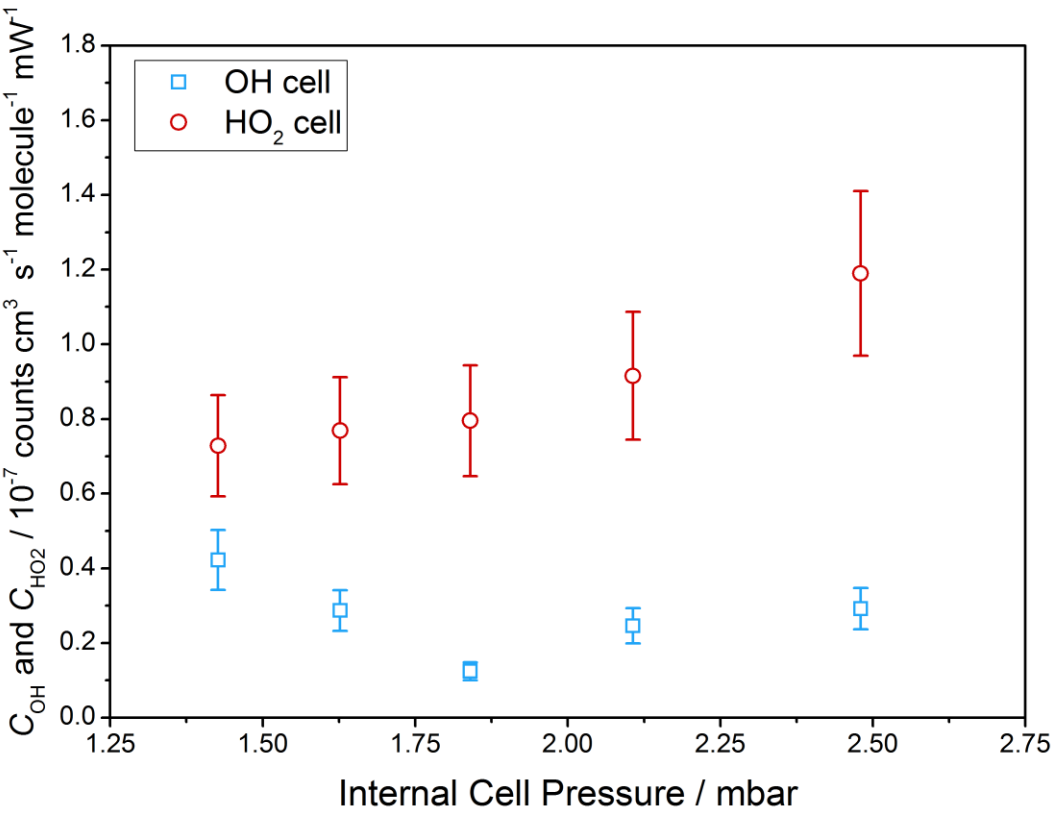

Figure 5.7: Instrument sensitivity to OH (C_{OH}, blue) and HO_2 (C_{HO2}, red) as a function of internal cell pressure for the aircraft FAGE instrument. Error bars are representative of total uncertainty in C_{OH} and C_{HO2} (section 5.2.3). All calibrations were conducted at constant laser power (15 ± 2 and 10 ± 2 mW, for OH and HO_2 respectively) and $[H_2O]_{vap}$ (6700 ± 500 ppmv).

5.2.2.4 External Inlet Temperature

Figure 5.8 displays the instrument sensitivity to OH and HO_2 as a function of external inlet temperature between 266 - 343 K, relative to the calibration at room temperature. The inlet temperature was controlled as described in section 5.2.1 and all instrument sensitivities were measured using the conventional calibration method. Temperature profile measurements were conducted in the FAGE instrument prior to calibration and gas temperatures in the OH and HO_2 fluorescence cells were observed between 280 - 318 K and 288 - 301 K respectively over the external inlet temperature range. The corresponding internal gas temperatures are displayed on the upper *x*-axes of Figure 5.8. All calibrations were conducted using the 1.0 mm pinhole (internal cell pressure = (3.81 ± 0.02) mbar), while maintaining a constant [H_2O] (2000 ± 300 ppmv) and laser power ((7.0 ± 1.0) and (3.5 ± 1.0) mW for the OH and HO_2 cells respectively), using the 5 kHz PRF laser system. An line of best fit, weighted to the total calibration uncertainties in the *y*-axes (see section 5.2.3 for details), displayed a small linear dependence in sensitivity for both the OH and HO_2 cells, equating to ΔC_{OH} = (0.18 ± 0.22) % and ΔC_{HO2} = (0.29 ± 0.42) % increase per Kelvin.

The small measured increase in C_{OH} and C_{HO2} with temperature was well within the total uncertainty of the conventional calibration process (~34%, see section 5.2.3 for details), hence the effect of temperature was considered insignificant over the 266 - 343 K temperature range examined. Investigation using the alternative calibration methods (described in chapter 6) over a range of chamber temperatures could provide more information and validation of the negligible temperature dependence observed here.

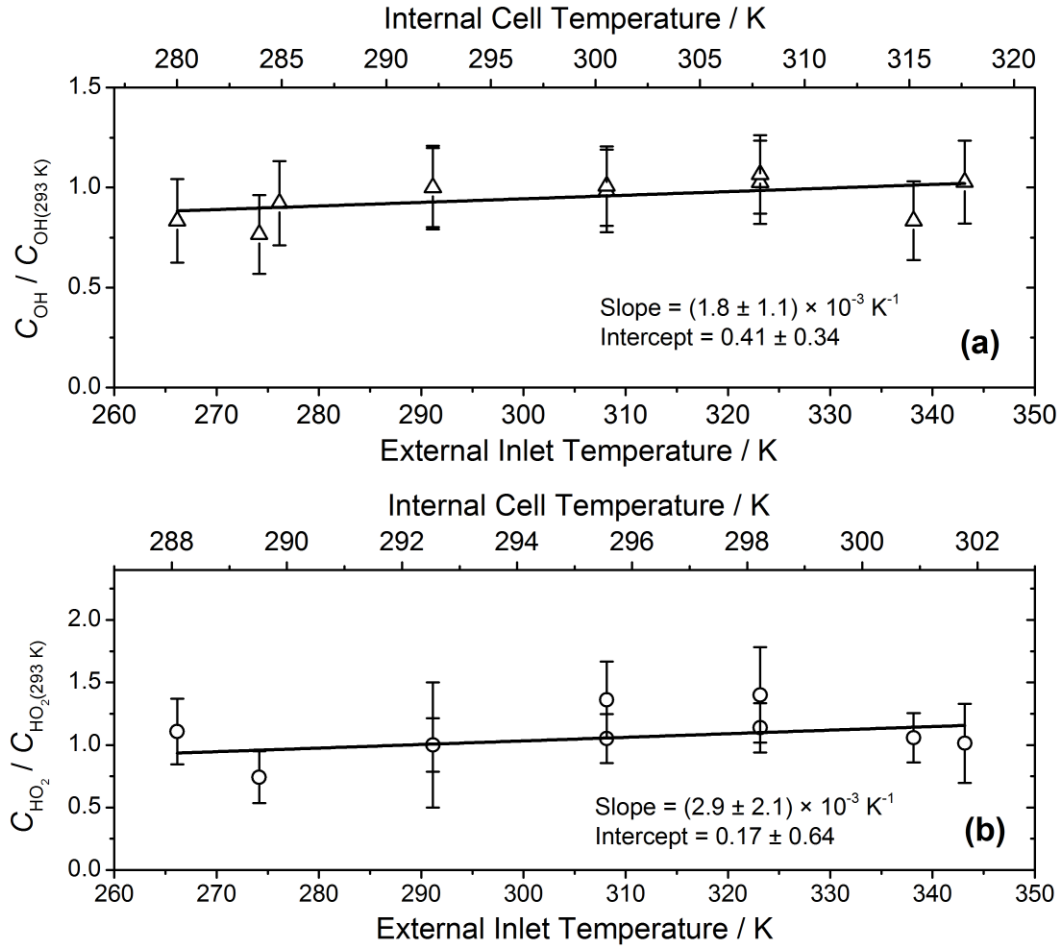

Figure 5.8: The FAGE instrument sensitivity to OH (a) and HO_2 (b) as a function of external inlet temperature for a constant internal cell pressure ((3.81 ± 0.02) mbar) and [H_2O] (2000 ± 300 ppmv) determined using the conventional calibration method. Sensitivity ratios calculated relative to the calibration at 293 K. Error bars represent the total error in the calibration procedure to ±1σ, and uncertainties in the slope and intercept represent the precision of the regression to ±1σ. An empirical linear least-squares fit to data is shown to quantify sensitivity as a function of temperature. Internal cell temperatures shown on the top *x*-axes, which were determined in a temperature profile experiment prior to calibration.

5.2.3 Uncertainty analysis

Parameters considered in the calculation of uncertainty are displayed in Table 5.1. The total uncertainty was estimated at ~34 %, calculated from the sum in quadrature of the precision and accuracy of the calibration process. The accuracy was defined by the uncertainty associated with each term of equation E 1.2 in the determination of [HOx]. The largest uncertainty occurred in the N_2O actinometric determination of the calibration source flux, $F_{184.9\ nm}$ (equation E 1.2), which relied on the evaluation using four rate constants with ~20% uncertainty and the detection of trace levels of NO (see section 5.3.3). The irradiation time, Δt, uncertainty was a function of the mass flow controllers used (~2 %), σ_{H2O} was taken from Cantrell et al. (1997) who reported a total error of ±6%, $[H_2O]$ was taken from the hygrometer instrumental uncertainty (± 10%) whilst laser power was defined by the laser power meter (Molectron Powermax 500A, ±0.25 mW). The online position uncertainty was defined by the threshold used to judge the laser wavelength position, typically 98 %, hence 4 % uncertainty to 2σ.

Parameter	**Uncertainty (2σ)**
$F_{184.9nm}$ / photons cm^{-2} s^{-1}	32%
t / s	2%
$[H_2O]$ / molecule cm^{-3}	10%
σ_{H2O} / cm^2 $molecule^{-1}$	6%
Laser power / mW	5%
Online position	4%
C_{OH} / cts s^{-1} $molecule^{-1}$ cm^3 mW^{-1}	**34%**

Table 5.1: The overall accuracy in the OH and HO_2 fluorescence cell sensitivity calculated from the sum in quadrature of the systematic uncertainties associated with the calibration procedure.

The precision was typically small for the "wand" calibration process (4 - 10%) and was taken from the standard error in the error weighted fit of the calibration plot (Figure 5.2). The errors were representative of the standard deviation in the S_{OH} and [HOx] for the *x* and *y* axes respectively. The flux output of the calibration source, hygrometer and CPM measurements were observed to have good point-to-point stability and therefore low standard deviation.

5.2.4 Limit of Detection

The limit of detection of the HIRAC FAGE instrument was defined by the instrumental sensitivity to OH (or HO_2) and the standard deviation of the background signal, calculated by using the following equation:

$$[OH]_{min} = \frac{S/N}{C_{OH} P} \sqrt{\left(\frac{1}{m} + \frac{1}{n}\right)} \sigma_b \qquad \text{E 5.3}$$

where S/N is the signal to noise ratio, C_{OH} is the sensitivity of the instrument to OH, P is the laser power (in mW), m is the number of online data points, n is the number of offline data points and σ_b is the sample standard deviation of the background signal. As the photon counting signal is subject to Poisson statistics (Stevens et al., 1994; Holland et al., 1995; Faloona et al., 2004), σ_b becomes:

$$\sigma_b = \sqrt{\frac{1}{t}(S_{lb} + S_{sb} + S_{db})} \qquad \text{E 5.4}$$

where t (s) is the averaging time for each data point and S_{lb}, S_{sb} and S_{db} (counts s^{-1}) are the background signals due to laser scatter, solar scatter and the CPM dark counts respectively. In HIRAC, solar scatter is negligible, even when the photolysis lamps are switched on, and so S_{sb} = 0. For a typical 60 s averaged signal, S/N = 1, P = 7 mW, C_{OH} = 2.62 (or 4.64 at 5 kHz) × 10^{-8} counts s^{-1} molecule cm^{-3} mW^{-1}, t = 1 s, m = 60, n = 60 and σ_b = 2.5 giving a limit of detection of 1.57 × 10^6 molecule cm^{-3} using the 200 Hz pulse repetition frequency laser and 8.89 × 10^5 molecule cm^{-3} for the 5 kHz PRF laser system.

5.3 Calibration source characterization, $F_{184.9\text{nm}}$

The flux of 184.9 nm light, $F_{184.9\ \text{nm}}$, was varied by altering the lamp supply current and was dependent on the specific mercury lamp employed along with the lamp temperature and orientation (Hofzumahaus et al., 1997; Dusanter et al., 2008). To this end, determinations of the flux from the specific mercury lamp used in the calibrations described in this work were made *in situ* for lamp supply currents between 0.2 and 3.0 mA using the N_2O (Edwards et al., 2003; Heard and Pilling, 2003; Faloona et al., 2004; Glowacki et al., 2007; Whalley et al., 2007) and O_2 actinometry (Faloona et al., 2004; Smith et al., 2006), described in sections 5.3.1 and 5.3.2. Faloona et al. (2004) reported good agreement between both actinometric methods and a separate absolute flux determination method using a calibrated photodiode. Both actinometric methods rely on an easily detectable photolysis product that can be related to the flux output of the Hg pen-ray lamp *via* a general equation based on E 1.2:

$$[X] = [Y]\ \sigma_{Y,184.9\ \text{nm}}\ \Phi_X\ F_{184.9\ \text{nm}}\ \Delta t \qquad \text{E 5.5}$$

where X = O_3 or NO and Y = O_2 or N_2O. Both the absorption cross section and photolysis quantum yield are typically taken from literature (as is the case for N_2O), however σ_{O2} must be determined for each calibration source as it is known to depend on lamp specification, orientation and $[O_2]$ (Lanzendorf et al., 1997; Dusanter et al., 2008). Both N_2O and O_2 actinometry were conducted using the HIRAC FAGE calibration source and are presented here (sections 5.3.1 and 5.3.2 respectively) along with an experimental determination of the O_2 absorption cross section (section 5.3.4). As these procedures have been covered extensively by other members of the Leeds FAGE group and in the literature (see references above), only the key points will be discussed here.

5.3.1 N_2O actinometry

A known concentration of N_2O is photolysed (λ = 184.9 nm) in the "wand" producing $O(^1D)$ ($\Phi_{O(1D)}$ = 1), which rapidly reacts with N_2O to produce two NO molecules (R 5.8). However, $O(^1D)$ is also removed by a suite of other reactions in the flow tube (R 5.3 - R 5.9) which impacts the total yield of NO.

$$N_2O + h\nu \rightarrow N_2 + O(^1D) \quad \text{R 5.3}$$

$$O(^1D) + O_2 \rightarrow O(^3P) + O_2 \quad \text{R 5.4}$$

$$O(^1D) + N_2 \rightarrow O(^3P) + N_2 \quad \text{R 5.5}$$

$$O(^1D) + N_2O \rightarrow O(^3P) + N_2O \quad \text{R 5.6}$$

$$O(^3P) + O_2 + M \rightarrow O_3 + M \quad \text{R 5.7}$$

$$O(^1D) + N_2O \rightarrow 2NO \quad \text{R 5.8}$$

$$O(^1D) + N_2O \rightarrow N_2 + O_2 \quad \text{R 5.9}$$

Calculating the fraction of NO produced from the total $O(^1D)$ loss following reactions R 5.3 - R 5.9, based on literature rate constants allowed the $F_{184.9\ nm}\ \Delta t$ product to be calculated from the rearrangement of E 5.5:

$$F_{184.9\ nm}\ \Delta t = \frac{(k_{R\ 5.4}\ [O_2] + k_{R\ 5.5}\ [N_2] + (k_{R\ 5.6} + k_{R\ 5.8})\ [N_2O])\ [NO]}{2(k_{R\ 5.8}\sigma_{N2O}\Phi_{NO}[N_2O]^2)} \quad \text{E 5.6}$$

where $k_{R\ 5.4} = 4.05 \times 10^{-11}$ molecule^{-1} cm^3 s^{-1}, $k_{R\ 5.5} = 2.60 \times 10^{-11}$ molecule^{-1} cm^3 s^{-1}, k_{R} 5.6 = 4.90×10^{-11} molecule^{-1} cm^3 s^{-1}, $k_{R\ 5.8} = 6.70 \times 10^{-11}$ molecule^{-1} cm^3 s^{-1} and $\sigma_{N2O} = (1.43 \pm 0.02) \times 10^{-19}$ cm^2 molecule^{-1} (Creasey et al., 2000). All rate coefficients were taken from Sander et al. (2011):. The Δt was calculated as a function of the flow rates used and the length of the photolysis region of the "wand", typically ~8.3×10^{-3} s at 40 slm. Possible loss of NO through reaction with O_3 (produced in R 5.7 and O_2 photolysis at 184.9 nm) has been shown to be negligible at the high flow rates and low N_2O concentrations used (Commane, 2009); repeating the procedure with pure nitrogen instead of synthetic air has been shown to not significantly affect results when using the structurally identical aircraft calibration source (Floquet, 2006).

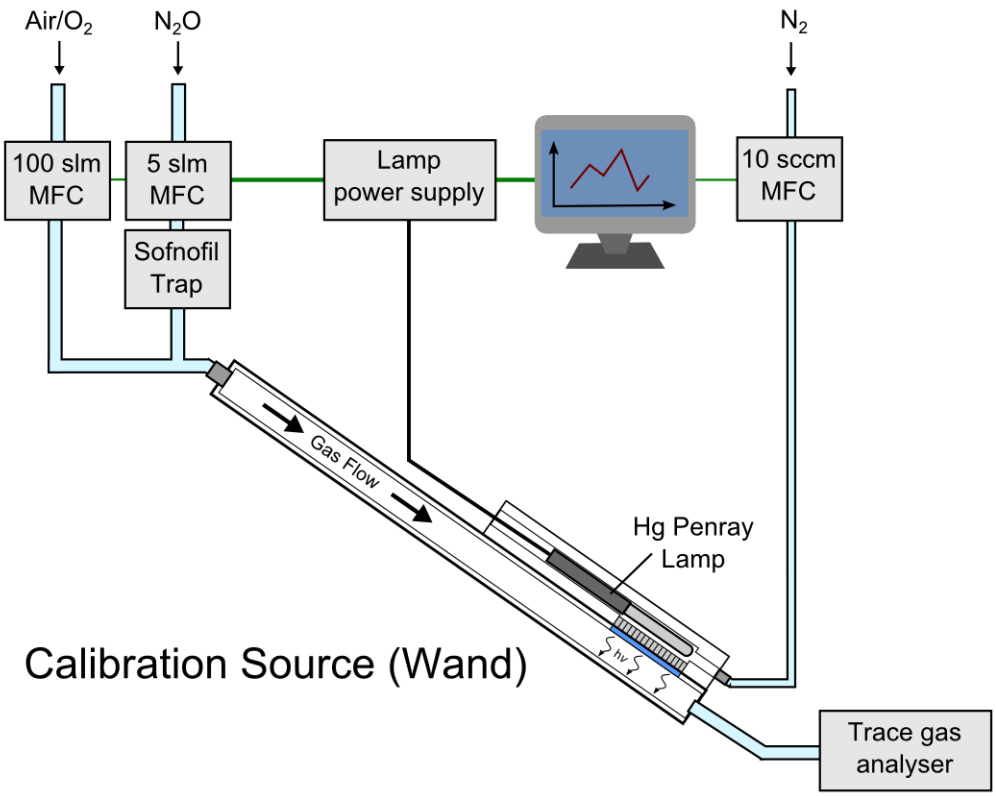

Figure 5.9: Schematic of the HIRAC calibration source apparatus used in the actinometric determination of the Hg lamp flux, $F_{184.9\ nm}$. A mixture of N_2O in air (40 slm total flow) or pure O_2 (30 slm) were flowed into the calibration source and NO or O_3 were detected using the appropriate gas analyser for the N_2O and O_2 actinometry methods respectively (sections 5.3.1 and 5.3.2).

Displayed in Figure 5.9 is the experimental apparatus used interchangeably in the N_2O and O_2 actinometry procedures (section 5.3.2). Pure N_2O (BOC medical grade), regulated using a 5 slm MFC, was passed through a Sofnofil gas trap to oxidise any $NO_{x/y}$ impurities and added to a flow of high purity air (BOC BTCA-178) before the gas mixture enters the "wand" at a total flow of 40 slm. The photolytically produced NO was detected using a calibrated chemiluminescence trace gas analyser (TEC 42C, LOD = 25 pptv) sampling at ~250 sccm through a 1/4" PTFE tube placed at the exit orifice of the calibration source. In the analyser, NO was titrated with excess O_3 to produce an excited state NO_2 molecule. Relaxation of the NO_2 to the ground state occurred *via* either collisional quenching or radiative decay, resulting in the emission of an infrared photon which was detected. As N_2O is a more efficient quencher of NO_2 than air, fractional concentrations > 0.01 had a measurable negative effect on the analyser calibration factor. This was accounted for by completing a set of calibrations

with N_2O present in the calibration flow over a range of N_2O fractions representative of those used in the actinometry (0.00 - 0.10). The 10 sccm N_2 flow is used as in section 5.2.1; to remove impurities from around the lamp which could absorb at 184.9 nm and to help maintain a constant lamp temperature.

The Hg lamp flux, $F_{184.9\ nm}$, was determined as a function of lamp current (in mA), shown here in Figure 5.10. A range of [NO] (0.5 – 3 ppb) were produced across three N_2O fractions in air (0.05, 0.07 and 0.10). Measurements of NO were corrected for the N_2O quenching effect and $F_{184.9\ nm}$ was observed to be independent of [N_2O]. The [NO] produced were close to the LOD of the NOx analyser and the uncertainties associated with this measurement are accounted for in section 5.3.3. The linear regression of the data displayed in Figure 5.10, weighted to the uncertainties in the *x* and *y* axes ($(1.57 \pm 0.03) \times 10^{13}$ photons cm^{-2} s^{-1} mA^{-1}), was used in the FAGE HOx calibration process to calculate $F_{184.9\ nm}$ for a given lamp current.

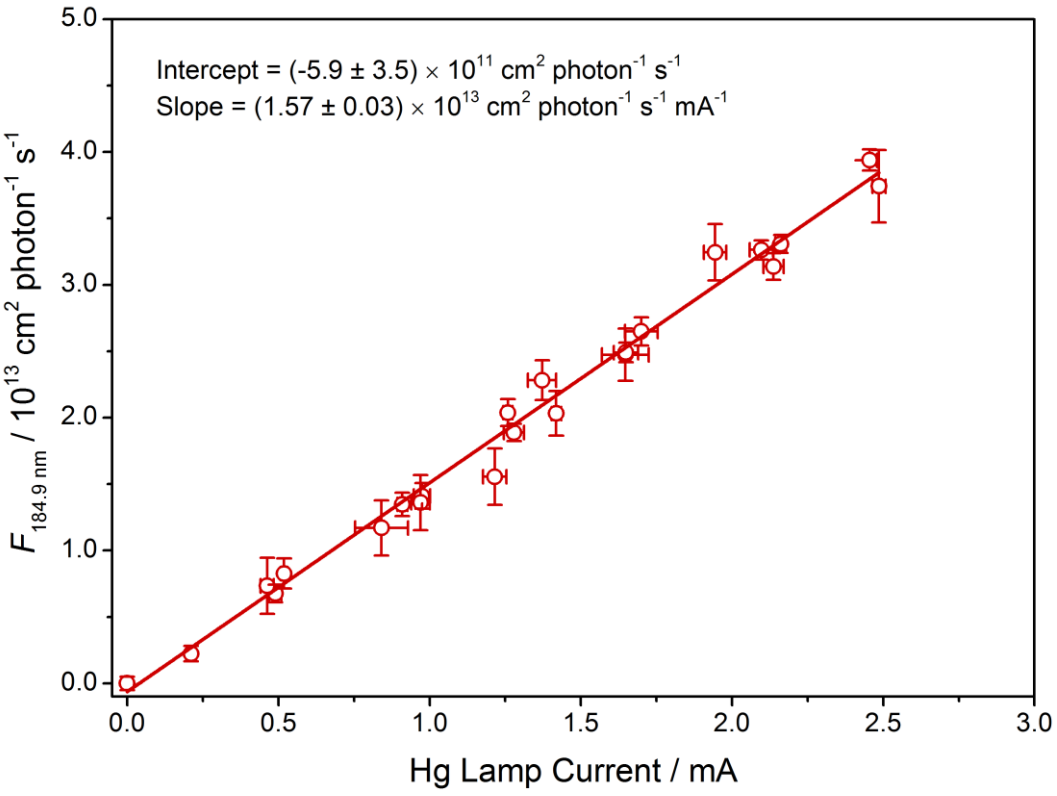

Figure 5.10: The Hg lamp flux, $F_{184.9\ nm}$, as a function of lamp current determined using the N_2O actinometry method. Parameters from the linear regression were used to calculate $F_{184.9\ nm}$ for a given lamp current during the FAGE HOx calibration process (section 5.2.1). Error bars represent the standard deviation in the measurements and uncertainties quoted to 1σ.

5.3.2 O_2 actinometry

An alternative method of determining $F_{184.9\ nm}$ is O_2 actinometry. When molecular oxygen is photolysed (R 5.10), it produces two oxygen atoms, which react with two O_2 molecules to form two O_3 molecules (R 5.11) which are easily measured with a commercial ozone analyser.

$$O_2 + h\nu \rightarrow 2O(^3P) \qquad \text{R 5.10}$$

$$2O(^3P) + 2O_2 \rightarrow 2O_3 \qquad \text{R 5.11}$$

Using the general equation E 5.5, knowledge of the absorption cross section, quantum yield ($\Phi_{O3} = 2$) and $[O_3]$ allow the $F_{184.9\ nm}\Delta t$ product to be calculated. Unlike the N_2O actinometry where σ_{N2O} is taken from literature, σ_{O2} must be measured experimentally because of an Hg pen-ray lamp dependent variation in the emission spectrum and the structured nature of the O_2 absorption around 184.9 nm (discussed in detail in section 5.3.4). Δt was calculated as a function of the flow rates used and the length of the photolysis region of the "wand", as in the N_2O actinometry procedure.

Previously, O_2 has been used as a chemical actinometer to calibrate FAGE without the necessity for the calculation of $F_{184.9\ nm}\Delta t$. This process was used for the ground based FAGE group at the University of Leeds using a long cylindrical calibration source, different in design to the HIRAC "wand" apparatus (Lee, 2000; Smith, 2007; Furneaux, 2009). This modified calibration technique measured both the H_2O and O_3 (from photolysis of O_2) in a humidified air flow, allowing the HO_x to be calculated (E 5.7) *via* substitution of E 1.2.

$$[HO_x] = \frac{[O_3]\,[H_2O]\,\sigma_{H_2O(184.9\ nm)}}{[O_2]\,\sigma_{O_2(184.9\ nm)}\,\Phi_{O_3(184.9\ nm)}} \qquad \text{E 5.7}$$

However, the technique required much slower flow-rates as the $[O_3]$ generated from O_2 photolysis in air (20% $[O_2]$) was below the detection limit of the O_3 box used (0.5 ppb). This led to laminar flow conditions inside the calibration source flowtube that were difficult to characterise. As the FAGE inlet was positioned at the centre of the flow tube, a second O_3 analyser was used to measure the O_3 inside the FAGE inlet, $[O_3]_{inlet}$, where concentrations were at a maximum, creating a correction factor, *P*, that could be used to correct the $[O_3]_{excess}$, measured from the flow tube (E 5.8).

$$P = \frac{[O_3]_{excess}}{[O_3]_{inlet}} \qquad \text{E 5.8}$$

Due to the increased uncertainty in using a laminar flow system and the absence of any modified inlets for attachment of a second O_3 analyser, a turbulent flow ($R_e > 4000$) O_2 actinometry method was developed. Using high purity O_2 and the existing "wand" at flow-rates of ~30 slm, levels of O_3 < 0.5 ppb were detected using the TEI 49C commercial O_3 analyser (apparatus shown in Figure 5.9).

High purity O_2 (BOC standard, zero-grade, 99.99%) was flowed at 30 slm (Brooks 5851S MFC) into the calibration "wand", where it was photolysed by the Hg pen-ray lamp to produce O_3. As with the NO, varying the current supplied to the lamp allows various $[O_3]$ to be measured. The O_3 was sampled from the centre of the calibration flowtube opening using a ¼" PTFE tube connected to the commercial UV-photometric O_3 analyser (TEC 49C). The $[O_3]$ measured during this calibration was sufficient (1 - 10 ppbv) to be measured accurately and reliably without using the converted trace gas NO_x analyser. The lamp was continuously purged using N_2 (BOC standard, zero grade, 99.99%) flowed at 10 sccm to remove any gases that may attenuate the flux at 184.9 nm and to help maintain a steady operating temperature.

The linear relationship between the $F_{184.9\ nm}$ and Hg lamp current for the O_2 actinometry is seen in Figure 5.11 ($(1.31 \pm 0.26) \times 10^{13}$ photons s^{-1} cm^{-2} mA^{-1}) compared to $F_{184.9\ nm}$ determined using the N_2O actinometry. Good agreement in the determination of $F_{184.9\ nm}$ was observed using the two methods up to ~2.5 mA Hg lamp current. This investigation has shown that the O_2 actinometry is a reliable and comparable method for the determination of $F_{184.9\ nm}$. However, due to the larger uncertainties (~40 % compared to 32 %, 2σ) and a flow-rate that was slower than the 40 slm flow used in the calibration process (section 5.2.1), the N_2O actinometry was used for the HOx calibration method discussed earlier in the chapter.

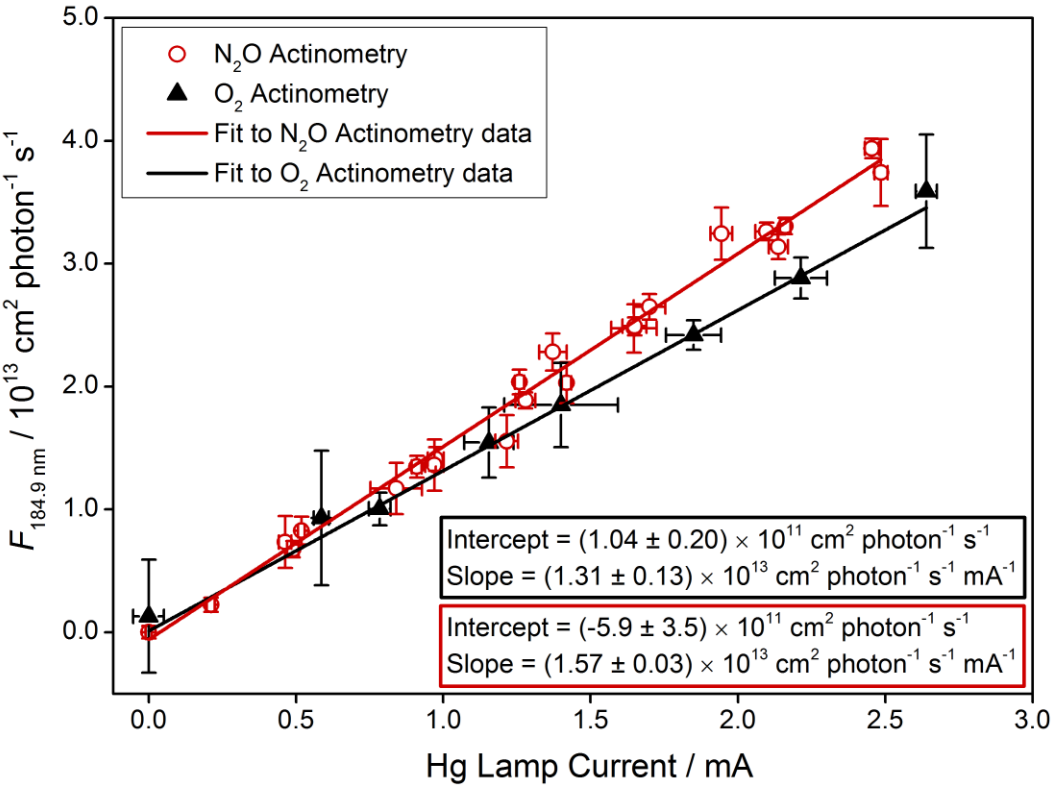

Figure 5.11: Comparison of the determination of $F_{184.9\ nm}$ as a function of Hg lamp current using the O_2 and N_2O actinometry methods. Error bars represent the standard deviation to 1σ in the averaged data. Linear regressions were weighted to uncertainties in both the *x* and *y* axes.

5.3.3 Uncertainty analysis

Accurate determination of the Hg lamp flux at 184.9 nm is essential for the accurate calibration of the FAGE instrument as the largest uncertainty associated with the H_2O photolysis based calibration method is in $F_{184.9\ nm}$. The total uncertainty in the N_2O and O_2 actinometry were calculated at 32% and 44% to 2σ respectively. The total uncertainty in $F_{184.9\ nm}$ is defined as the sum in quadrature of the overall precision and accuracy:

$$\delta_F = \sqrt{(\delta_{F,acc})^2 + (\delta_{F,prec})^2} \qquad \text{E 5.9}$$

The precision is determined from the standard error in the linear regression of the $F_{184.9\ nm}$ data as a function of lamp current (Figure 5.11) and the accuracy is defined as the sum in quadrature of the systematic uncertainties in the mass flow controllers

(δ_{MFC} = 1%), absorption cross sections for both N_2O, $\delta_{\sigma N2O}$ (= 2%), and O_2, $\delta_{\sigma O2}$ (= 24%), and commercial analysers used (δ_{O3} = 0.5 ppbv ≈ 30%, δ_{NO} = 0.05 ppbv ≈ 20%, over the range of [O_3] and [NO] measured (sections 5.3.1 and 5.3.2)). For the N_2O actinometry, extra systematic uncertainties were taken into account for the N_2O quenching effect on the NO_2 excited state detection efficiency, δ_{NO2} (= 14%), and the combined uncertainty in the rate coefficients used in the calculation of the rate of production of NO through reaction of $O(^1D)$ with N_2O ($k_{R\ 5.4}$, $k_{R\ 5.5}$, $k_{R\ 5.6}$ and k_{R} 5.8), $\delta_{O(1D)}$ (= 20%, taken from Sander et al. (2011)).

5.3.4 O_2 cross section

The Beer-Lambert law relates the absorption, Abs, to the absorption cross section of a given species, in this case O_2, σ_{O2}, the concentration of the species, [O_2], and the path length of the system, l (equation E 5.10). If [O_2], l and Abs are known then the absorption cross section can be calculated. The product of concentration and path length known as the O_2 column (molecule cm^{-2}) for the remainder of this work.

$$\text{Abs} = \log_{10}\left(\frac{I}{I_0}\right) = \sigma_{O2}\,[O_2]\;l \qquad \text{E 5.10}$$

For most spectroscopic applications (section 5.3.1) a literature value for σ_{O2} can be used, but oxygen is a special case that is dependent on the experimental conditions (Creasey et al., 2000). This is due to the Hg lamps used for the O_2 photolysis and the very structured absorption spectrum for O_2 (Schumann-Runge bands, (Yoshino et al., 1983)). As the Hg lamp is not a line source and is known to have an asymmetric emission spectrum broadening towards the red, Hofzumahaus et al. (1997) have shown the measured σ_{O2} for seven different lamps to vary by as much as 26%; an effect also reported by Creasey et al. (2000). Lanzendorf et al. (1997) found a ~30% change in spectral output depending on side or end-on orientation as well as a 2% σ_{O2} dependence on lamp current. It is important, due to the number of variables, that the determination of σ_{O2} is conducted using the same operating conditions as in the calibration procedure.

Due to the structured absorption of O_2 and the broad emission of the Hg lamp, there is a strong non-linear relationship between σ_{O2} and O_2 column (Figure 5.12 from Furneaux (2009)). The dashed red line in Figure 5.12 represents the O_2 column at the back wall of

the calibration "wand" (opposite the Hg lamp). Over a small range of O_2 columns where the rate of change of $\sigma_{184.9\ nm}$ is great, the relationship can be considered linear.

To correct the σ_{O2} for the dependence on O_2 column, the effective absorption cross section, σ_{eff}, can be calculated from the experimentally observed absorption cross section, σ_{obs}, for the O_2 column, C, observed at the centre of the calibration "wand" (E 5.11).

$$\sigma_{eff}(C) = \sigma_{obs}(C) + C\,[d\,\sigma_{obs}(C) / dC] \qquad \text{E 5.11}$$

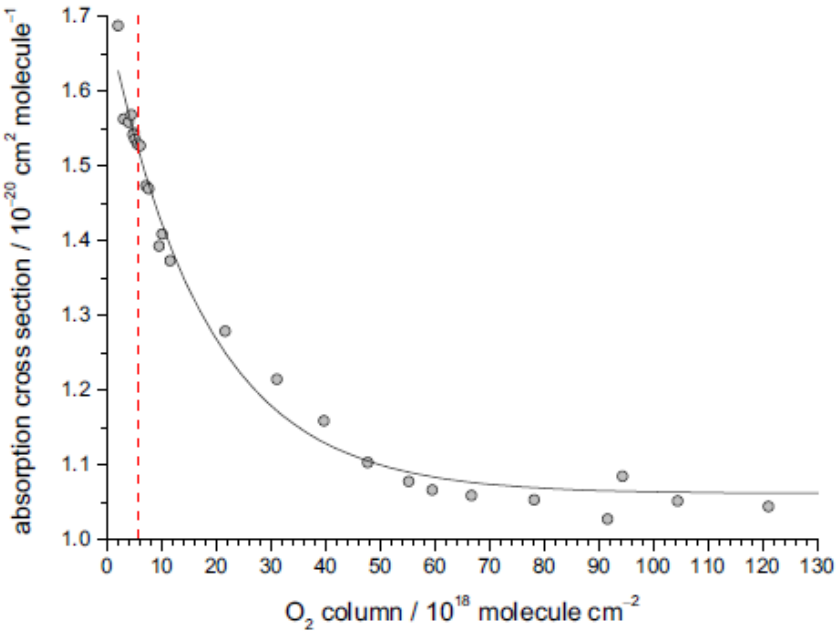

Figure 5.12: Non-linear decrease in absorption cross section with respect to a wide range of O_2 columns. The dashed red line represents the O_2 column at the back wall of the "wand", opposite the Hg lamp. Reproduced from Furneaux (2009).

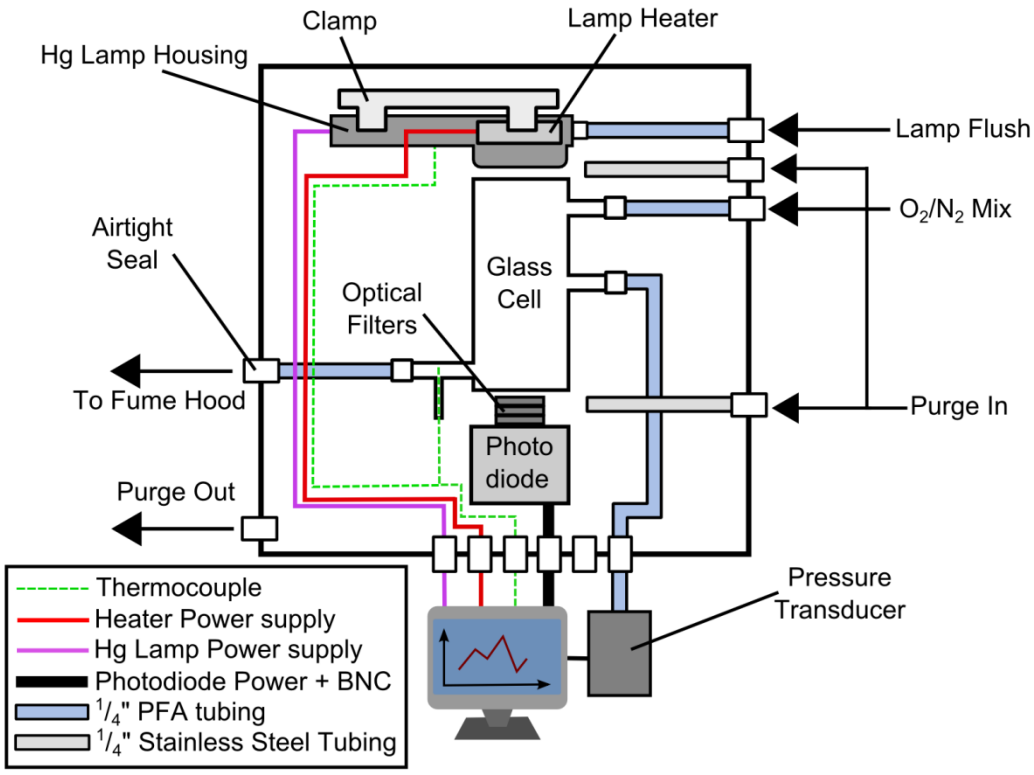

Figure 5.13: Schematic of the modified absorption cross section apparatus modified from the original design by Furneaux (2009).

An instrument has been designed at the University of Leeds that is able to measure absorption cross sections at 184.9 nm using Hg pen-ray lamps (Furneaux, 2009). Figure 5.13 shows the modified airtight box which houses a four port, 10.00 cm length, 3.00 cm inner diameter glass absorption cell with two Spectrosil B windows at either end. The four ports allows the connection of gas input and output as well as a pressure transducer (MKS 870B, range = 0 - 1000 Torr) and thermocouple (RS, K-type, 270 - 400 K).

As the original lamp housing placed at one end of the cell was designed to mimic the housing used in the ground based FAGE O_2 actinometry (Furneaux, 2009), it was replaced with a stand that incorporated the HIRAC calibration "wand", which is of a different design. A photodiode (Hamamatsu SI225-44BQ, Si, 190 - 1000 nm, with some sensitivity < 190 nm) was used to measure light intensity at 184.9 nm. Three 184.9 nm centred UV bandpass filters (Glen spectra, XB32-185NB20) were mounted before the photodiode to exclude any interference from the stronger 254 nm lamp emission. The

box was continuously purged with dry N_2 (laboratory supply) to avoid absorption from any impurities outside of the cell.

A range of O_2 columns (0.8 - 2.2 molecule cm^{-2}) were measured at a constant flow of 3 slm through the cell using various ratios of N_2 (BOC, OFN grade) and O_2 (BOC, zero grade, 99.97%). The O_2 and N_2 were mixed approximately 1 m before entering the cell to prevent heterogeneous mixing. The pressure, temperature and photodiode voltages were measured by computer at a rate of 1 Hz, measuring each chosen O_2 column for approximately 60 s. The lamp was operated at a constant current (2.5 mA), continuously purged and heated to maintain a stable output. As the path length, O_2 column and absorption were known, the σ_{O2} can be calculated for a given O_2 column. Correcting for σ_{eff} (Equation E 5.11) the linear relationship between effective cross section as a function of O_2 column is seen in Figure 5.14, showing the importance of measuring the σ_{O2}.

The error bars in Figure 5.14 are representative of the standard deviation in the photodiode measurements. The σ_{eff} was calculated at $(1.72 \pm 0.40) \times 10^{-20}$ $molecule^{-1}$ cm^2, with a total uncertainty of ~24% (2σ) calculated from the sum in quadrature of the standard error in the linear regression of Figure 5.4 and the systematic errors associated with the MFC, photodiode and lamp current.

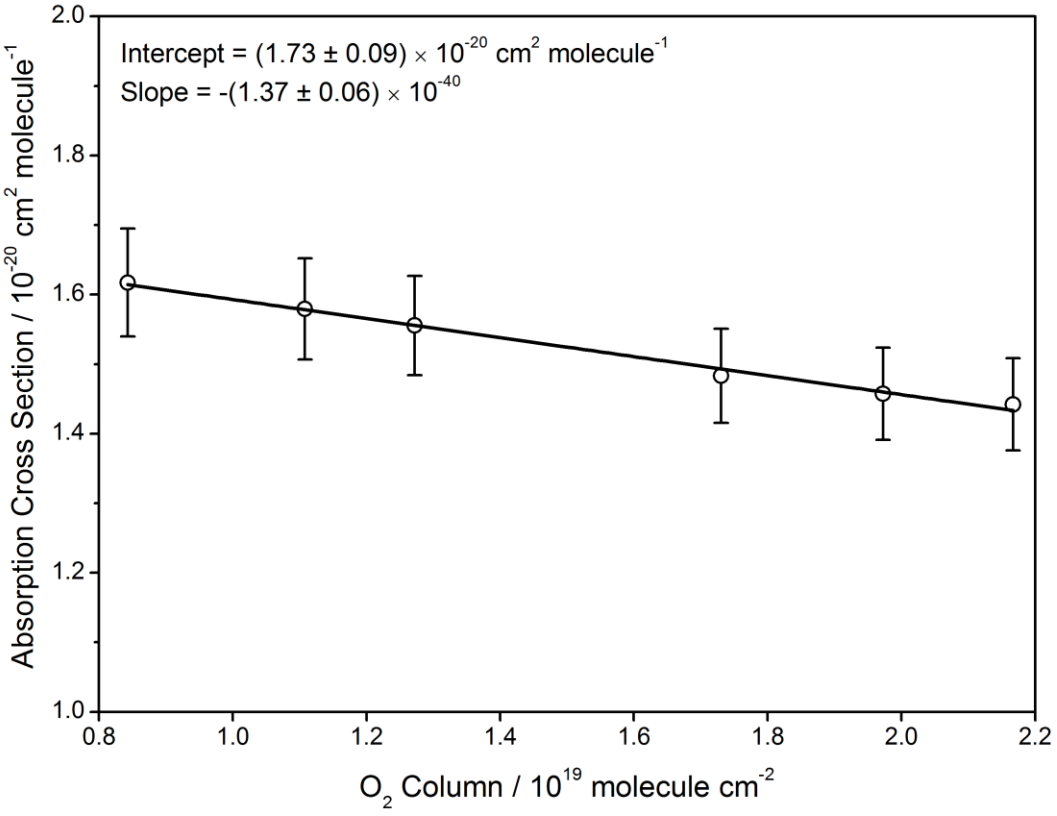

Figure 5.14: Effective O_2 absorption cross section (cm^2 $molecule^{-1}$) as a function of O_2 column (molecule cm^{-2}) measured using the Hg lamp used in both O_2 and N_2O actinometry. All measurements were conducted at 1000 mbar and 293 K at Hg lamp current = 2.5 mA. Errors in the *y* axis are a function of the uncertainty in the gas concentrations and photodiode measurements and uncertainties in regression parameters quoted to 1σ.

5.4 RO_2 interference in HO_2 measurements

Recently published material on the conversion of certain peroxy radicals (RO_2) to OH upon reaction with NO in FAGE detections cells (Fuchs et al., 2011; Whalley et al., 2013) have shown a significant enhancement of the HO_2 signal in the presence of RO_2 derived from certain hydrocarbons. Peroxy radicals are produced in the troposphere from the oxidation of VOCs. In the case of OH, oxidation of saturated VOCs proceeds *via* a hydrogen abstraction step, and reaction with O_2 results in a peroxy radical (R 5.12):

$$R\text{-}H + OH\ (+O_2) \rightarrow RO_2 + H_2O \qquad \text{R 5.12}$$

$$RO_2 + NO \rightarrow RO + NO_2 \qquad \text{R 5.13a}$$

$$\rightarrow RONO_2 \qquad \text{R 5.13b}$$

$$RO_2 + HO_2 \rightarrow ROOH + O_2 \qquad \text{R 5.14}$$

$$RO + O_2 \rightarrow R'CHO + HO_2 \qquad \text{R 5.15}$$

$$RO + NO \rightarrow RONO \qquad \text{R 5.16}$$

Peroxy radicals undergo reaction with NO (R 5.13a and b) or HO_2 (R 5.14). Reaction with NO is dominated by the production of NO_2 and an alkoxy radical, RO, (R 5.13a) and further reaction with O_2 eventually produces HO_2 through a slow O_2-hydrogen extraction step (~12 s^{-1} for CH_3O at 0.20 partial pressure O_2 at 298 K). In the FAGE cell, NO is introduced directly before the cell, resulting in a short residence time for NO, and hence previous studies had observed no RO_2 conversion to HO_2 for small chain alkanes < C_4 (Hard et al., 1984; Mather et al., 1997; Kanaya et al., 2001; Ren et al., 2004). Assumptions made based on short chain alkanes were extrapolated for all general RO_2, and conversion yields for alkenes and aromatics were not investigated.

Alkoxy radicals are not only limited to reaction with O_2 or NO however, and can isomerise to form hydroxyperoxy radicals, HO-RO_2, in the presence of O_2, a process which is competitive inside the FAGE cell. This process is possible only for alkoxy radicals > C_4, produced from oxidation of alkanes, as the isomerisation takes place exclusively *via* a six-memebered ring (or greater). Subsequent reaction of HO-RO_2 with NO yields a hydroxyalkoxy radical, HO-RO, which can isomerise and react with O_2 to produce an aldehyde and HO_2. Several reaction steps are required to reach the HO-RO

radical, and hence it is likely that an HO_2 interference from unsaturated VOC created RO_2 will be minimal.

The OH initiated oxidation of unsaturated VOCs, however, occurs *via* addition to the C=C double bond, creating a β-hydroxyperoxy radical in the presence of O_2. The β-hydroxyperoxy radicals have been shown to predominantly decompose at room temperature (Atkinson and Arey, 2003) to produce an hydroxyalkyl radical, HO-R, which reacts rapidly ($k = 9.6 \times 10^{-12}$ cm^3 molecule^{-1} s^{-1} for CH_2OH) with O_2 to form a carbonyl and HO_2 (Atkinson, 1997; Orlando et al., 2003). Fuchs et al. (2011) showed that the fast decomposition of βHO-RO radicals generated from alkenes and aromatics resulted in an RO_2 sensitivity of 80% relative to the HO_2 sensitivity. Whalley et al. (2013) considered the effect of instrument design and NO injection method on the RO_2 conversion, observing higher α_{RO2} for a smaller diameter cell similar to those employed for airborne measurements and in the HIRAC chamber.

To date, only two other groups have investigated RO_2 conversion efficiencies: Mao et al. (2012) reported an overall RO_2 sensitivity of ~60% relative to the HO_2 sensitivity of the Penn State airborne FAGE instrument, and Vaughan et al. (2012) have derived the sensitivity to RO_2 radicals from ethene at ~40% for the airborne FAGE instrument used at the University of Leeds (Commane et al., 2010). Reported here are the preliminary results of an ongoing investigation into the RO_2 conversion efficiency for the HIRAC FAGE instrument. Further objectives for this study are discussed below.

Using a method similar to those described in Fuchs et al. (2011) and Whalley et al. (2013), VOC precursors were introduced into the main flow of the calibration source, where reaction with OH in the presence of O_2 produced RO_2 radicals. Enough hydrocarbon was introduced to completely scavenge OH, so that $[RO_2] \approx [HO_2]$. The [NO] was kept constant at 1.14×10^{14} molecule cm^{-3} (= 5 sccm of pure NO), identical to the concentration used under standard operating conditions. Experiments were conducted with the 5 kHz PRF laser system and signals due to RO_2 were measured relative to those from HO_2, calculating the RO_2 conversion efficiency, $\alpha_{RO2} = S_{RO2}/S_{HO2}$. The α_{RO2} was measured for *iso*-butane (-0.01 ± 0.02), 1-butene (1.04 ± 0.05), ethene (0.63 ± 0.04) and isoprene (0.83 ± 0.02).

Further work is planned to investigate the dependence of the RO_2 conversion efficiency on temperature of the FAGE inlet (as in section 5.2.2.4). As the HO_2 detection cell is

located ~200 mm from the inlet which would be exposed to changing temperature, determination of the temperature profile inside the FAGE instrument when the inlet is heated or cooled will highlight whether the α_{RO2} is likely to change. The results obtained could be modelled using the Master Chemical Mechanism, MCM v3.2 (Jenkin et al., 2003; Saunders et al., 2003) to determine an average α_{RO2} for all RO_2 species contained in the MCM. This would allow a full assessment of the α_{RO2} for potential interferences over a range of chamber and instrumental operating conditions.

5.5 Conclusions and future work

The HIRAC FAGE instrument has been successfully calibrated for OH and HO_2 using the H_2O vapour photolysis based calibration source. A number of different parameters known to affect instrument sensitivity were tested and accounted for. Linear regressions were used to describe the changes in C_{OH} and C_{HO2} due to [H_2O], laser power, pressure and temperature, which can be applied to the experimental data analysis procedure for radicals detected in the HIRAC chamber. Characterising C_{OH} and C_{HO2} as a function of pressure and temperature was essential for potential experiments to be conducted in the HIRAC chamber over a range of atmospheric conditions. Calculations have estimated a total calibration uncertainty ~34% (2σ) for both the OH and HO_2 fluorescence cells, which is comparable to values in the literature (Bloss et al., 2004; Faloona et al., 2004) and other FAGE groups at the University of Leeds (Smith, 2007; Malkin, 2010; Walker, 2013).

Accurate determination of [HOx] from the calibration source was essential, and this relied heavily on the measurement of the Hg lamp flux using a chemical actinometer. This study has shown that the O_2 actinometry has successfully validated the more frequently used N_2O actinometry method. A larger uncertainty was associated with the O_2 actinometry due to the lamp dependent σ_{O2} measurement (section 5.3.4) and accuracy of the O_3 analyser. However, unlike the N_2O actinometry, the calculation of $F_{184.9\ nm}$ did not rely on four rate constants (E 5.6), as O_3 is the direct product from the photolysis of O_2 (R 5.10 and R 5.11). Further investigation into the reproducibility of the N_2O actinometry over the coming years is essential to better understand the precision of the technique.

Preliminary results from the investigation into the efficiency of RO_2 conversion to HO_2, has shown that α_{RO2} for alkene derived RO_2 radicals is significant under the current operating conditions of the instrument. Further work is required to enable the instrument to preferentially convert HO_2 over RO_2, which could be achieved by reducing the mixing time (e.g., by moving the NO injection point closer to the HO_2 cell) or by reducing the [NO] introduced. Reducing the [NO] will result in a decrease in C_{HO2}, however measured [HO_2] in HIRAC have typically been ~10^{10} - 10^{11} molecule cm^{-3}, and therefore a dilution of NO introduced would not hamper HO_2 detection at these levels.

5.6 References

Aschmutat, U., M. Hessling, F. Holland and A. Hofzumahaus (1994). A tunable source of Hydroxyl (OH) and Hydroperoxy (HO2) radicals: in the range between 106 and 109 cm-3. Physico-Chemical Behaviour of Atmospheric Pollutants. G. A. a. G. Restelli, European Comission, Brussels: 811-816.

Atkinson, R. (1997). "Atmospheric Reactions of Alkoxy and β-Hydroxyalkoxy Radicals." International Journal of Chemical Kinetics 29: 99-111.

Atkinson, R. and J. Arey (2003). "Atmospheric Degradation of Volatile Organic Compounds." Chemical Reviews 103: 4605-4638.

Bailey, A. E., D. E. Heard, D. A. Henderson and P. H. Paul (1999). "Collisional quenching of OH(A2S+, u'=0) by H2O between 211 and 294 K and the development of a unified model for quenching." Chemical Physics Letters 302(1-2): 132-138.

Bloss, W. J., J. D. Lee, C. Bloss, D. E. Heard, M. J. Pilling, K. Wirtz, M. Martin-Reviejo and M. Siese (2004). "Validation of the calibration of a laser-induced fluorescence instrument for the measurement of OH radicals in the atmosphere." Atmospheric Chemistry and Physics 4: 571-583.

Cantrell, C. A., G. Tyndall and A. Zimmer (1997). "Absorption cross sections for water vapour from 183 to 193 nm." Geophysical Research Letters 24: 2195-2198.

Commane, R. (2009). Understanding Radical Chemistry Throughout the Troposphere using Laser-Induced Fluorescence Spectroscopy. PhD, University of Leeds.

Commane, R., C. F. A. Floquet, T. Ingham, D. Stone, M. J. Evans and D. E. Heard (2010). "Observations of OH and HO2 radicals over West Africa." Atmospheric Chemistry and Physics 10: 8783-8801.

Copeland, R. A. and D. Crosley (1986). "Temperature dependent electronic quenching of OH A2S, v'=0 between 230 and 310 K." Journal of Chemical Physics 84: 3099-3105.

Creasey, D. J., G. E. Evans, D. E. Heard and J. D. Lee (2003). "Measurements of OH and HO2 concentrations in the Southern Ocean marine boundary layer." Journal of Geophysical Research-Atmospheres 108(D15): -.

Creasey, D. J., P. A. Halford-Maw, D. E. Heard, M. J. Pilling and B. J. Whitaker (1997a). "Implementation and initial deployment of a field instrument for measurement of OH and HO2 in the troposphere by laser-induced fluorescence." Journal of the Chemical Society-Faraday Transactions 93(16): 2907-2913.

Creasey, D. J., D. E. Heard and J. D. Lee (2000). "Absorption cross-section measurements of water vapour and oxygen at 185 nm. Implications for the calibration of field instruments to measure OH, HO2 and RO2 radicals." Geophysical Research Letters 27(11): 1651-1654.

Creasey, D. J., D. E. Heard, M. J. Pilling, B. J. Whitaker, M. Berzins and R. Fairlie (1997b). "Visualisation of a supersonic free-jet expansion using laser- induced fluorescence spectroscopy: Application to the measurement of rate constants at ultralow temperatures." Applied Physics B-Lasers and Optics 65(3): 375-391.

Dusanter, S., D. Vimal and P. S. Stevens (2008). "Technical note: Measuring tropospheric OH and HO2 by laser-induced fluorescence at low pressure. A comparison of calibration techniques." Atmospheric Chemistry and Physics 8(2): 321-340.

Edwards, G. D., C. Cantrell, S. Stephens, B. Hill, O. Goyea, R. Shetter, R. L. Mauldin, E. Kosciuch, D. Tanner and F. Eisele (2003). "Chemical Ionization Mass Spectrometer Instrument for the Measurement of Tropospheric HO2 and RO2." Analytical Chemistry 75: 5317-5327.

Faloona, I. C., D. Tan, R. L. Lesher, N. L. Hazen, C. L. Frame, J. B. Simpas, H. Harder, M. Martinez, P. Di Carlo, X. R. Ren and W. H. Brune (2004). "A laser-induced fluorescence instrument for detecting tropospheric OH and HO2: Characteristics and calibration." Journal of Atmospheric Chemistry 47(2): 139-167.

Farrugia, L. (2014). Kinetics and mechanistic studies in the HIRAC chamber. PhD, University of Leeds.

Floquet, C. F. (2006). Airborne Measurements of Hydroxyl Radicals by Fluorescence Assay by Gas Expansion. PhD, University of Leeds.

Fuchs, H., B. Bohn, A. Hofzumahaus, F. Holland, K. D. Lu, S. Nehr, F. Rohrer and A. Wahner (2011). "Detection of HO2 by laser-induced fluorescence: calibration and interferences from RO2 radicals." Atmospheric Measurement Techniques 4(6): 1209-1225.

Furneaux, K. L. (2009). "Field Studies of the Chemistry of Free-Radicals in the Troposphere using Laser Induced Fluorescence Spectroscopy." PhD thesis.

Glowacki, D. R., A. Goddard, K. Hemavibool, T. L. Malkin, R. Commane, F. Anderson, W. J. Bloss, D. E. Heard, T. Ingham, M. J. Pilling and P. W. Seakins (2007). "Design of and initial results from a Highly Instrumented Reactor for Atmospheric Chemistry (HIRAC)." Atmospheric Chemistry and Physics 7(20): 5371-5390.

Hard, T. M., R. J. O'Brien, C. Y. Chan and A. A. Mehrabzadeh (1984). "Tropospheric Free-radical determination by FAGE." Environmental Science & Technology 18(10): 768-777.

Heard, D. E. and M. J. Pilling (2003). "Measurement of OH and HO2 in the Troposphere." Chemical Reviews 103: 5163-5198.

Hofzumahaus, A., T. Brauers, U. Aschmutat, U. Brandenburger, H. P. Dorn, M. Hausmann, M. Heβling, F. Holland, C. Plass-Dulmer, M. Sedlacek, M. Weber and D. H. Ehhalt (1997). "The measurement of tropospheric OH radicals by laser-induced fluorescence spectroscopy during the POPCORN field campaign and Intercomparison of tropospheric OH radical measurements by multiple folded long-

path laser absorption and laser induced fluorescence - Reply." Geophysical Research Letters 24(23): 3039-3040.

Holland, F., M. Hessling and A. Hofzumahaus (1995). "In-Situ Measurement of Tropospheric OH Radicals by Laser- Induced Fluorescence - a Description of the KFA Instrument." Journal of the Atmospheric Sciences 52(19): 3393-3401.

Jenkin, M. E., S. M. Saunders, V. Wagner and M. J. Pilling (2003). "Protocol for the development of the Master Chemical Mechanism, MCM v3 (Part B): tropospheric degradation of aromatic volatile organic compounds." Atmospheric Chemistry and Physics 3: 181-193.

Kanaya, Y., Y. Sadanaga, J. Hirokawa, Y. Kajii and H. Akimoto (2001). "Development of a ground-based LIF instrument for measuring HOx radicals: Instrumentation and calibrations." Journal of Atmospheric Chemistry 38(1): 73-110.

Lanzendorf, E. J., T. F. Hanisco, N. M. Donahue and P. O. Wennberg (1997). "The measurement of tropospheric OH radicals by laser-induced fluorescence spectroscopy during the POPCORN field campaign and Inntercomparison of tropospheric OH radical measurements by multiple folded long-path laser absorption and laser induced fluorescence - Comment." Geophysical Research Letters 24(23): 3037-3038.

Lee, J. D. (2000). University of Leeds.

Malkin, T. L. (2010). Detection of free-radicals and other species to investigate atmospheric chemistry in the HIRAC chamber Thesis (Ph D), University of Leeds (School of Chemistry), 2010.

Mao, J., X. Ren, L. Zhang, D. M. Van Duin, R. C. Cohen, J. H. Park, A. H. Goldstein, F. Paulot, M. R. Beaver, J. D. Crounse, P. O. Wennberg, J. P. DiGangi, S. B. Henry, F. N. Keutsch, C. Park, G. W. Schade, G. M. Wolfe, J. A. Thornton and W. H. Brune (2012). "Insights into hydroxyl measurements and atmospheric oxidation in a California forest." Atmospheric Chemistry and Physics 12(17): 8009-8020.

Mather, J. H., P. S. Stevens and W. H. Brune (1997). "OH and HO2 measurements using laser-induced fluorescence." Journal of Geophysical Research-Atmospheres 102(D5): 6427-6436.

Orlando, J. J., G. S. Tyndall and T. J. Wallington (2003). "The atmospheric chemistry of alkoxy radicals." Chemical Reviews 103(12): 4657-4689.

Potter, H. and A. Dumbledore (2000). Wand Calibration Methods. Review of Magical Instrumentation. L. Vodemort. Diagon Alley, London, Hogwarts Press.

Regelin, E., H. Harder, M. Martinez, D. Kubistin, C. T. Ernest, H. Bozem, T. Klippel, Z. Hosaynali-Beygi, H. Fischer, R. Sander, P. Jöckel, R. Königstedt and J. Lelieveld (2013). "HOx measurements in the summertime upper troposphere over Europe: a comparison of observations to a box model and a 3-D model." Atmospheric Chemistry and Physics 12: 30619-30660.

Ren, X. R., H. Harder, M. Martinez, I. C. Faloona, D. Tan, R. L. Lesher, P. Di Carlo, J. B. Simpas and W. H. Brune (2004). "Interference testing for atmospheric HOx

measurements by laser-induced fluorescence." Journal of Atmospheric Chemistry 47(2): 169-190.

Sander, S. P., R. R. Friedl, J. P. D. Abbatt, J. Barker, D. M. Golden, C. E. Kolb, M. J. Kurylo, G. K. Moortgat, P. H. Wine, R. E. Huie and V. L. Orkin (2011). Chemical kinetics and photochemical data for use in atmospheric studies - Evaluation 17. Pasadena CA, Jet Propulsion Laboratory. 17.

Saunders, S., M. Jenkin, R. Derwent and M. Pilling (2003). "Protocol for the development of the Master Chemical Mechanism, MCM v3 (Part A): tropospheric degradation of non-aromatic volatile organic compounds." Atmos. Chem. Phys. 3: 161–180.

Schultz, M., M. Heitlinger, D. Mihelcic and A. Volzthomas (1995). "Calibration source for peroxy-radicals with built-in actinometry using H2O and O2 photolysis at 185 nm." Journal of Geophysical Research-Atmospheres 100(D9): 18811-18816.

Smith, S. C. (2007). Atmospheric Measurements of OH and HO2 using the FAGE technique: Instrument development and data analysis, University of Leeds.

Smith, S. C., J. D. Lee, W. J. Bloss, G. P. Johnson, T. Ingham and D. E. Heard (2006). "Concentrations of OH and HO2 radicals during NAMBLEX: measurements and steady state analysis." Atmospheric Chemistry and Physics 6: 1435-1453.

Stevens, P. S., J. H. Mather and W. H. Brune (1994). "Measurement of Tropospheric OH and HO2 by Laser-Induced Fluorescence at Low-Pressure." Journal of Geophysical Research-Atmospheres 99(D2): 3543-3557.

Stone, D., L. K. Whalley and D. E. Heard (2012). "Tropospheric OH and HO2 radicals: field measurements and model comparisons." Chem Soc Rev 41(19): 6348-6404.

Vaughan, S., T. Ingham, L. K. Whalley, D. Stone, M. J. Evans, K. A. Read, J. D. Lee, S. J. Moller, L. J. Carpenter, A. C. Lewis, Z. L. Fleming and D. E. Heard (2012). "Seasonal observations of OH and HO2 in the remote tropical marine boundary layer." Atmospheric Chemistry and Physics 12(4): 2149-2172.

Walker, H. M. (2013). Field Measurements and Analysis of Reactive Tropospheric species Using the FAGE Technique. PhD., Leeds.

Whalley, L. K., M. A. Blitz, M. Desservettaz, P. W. Seakins and D. E. Heard (2013). "Reporting the sensitivity of Laser Induced Fluorescence instruments used for HO2 detection to an interference from RO2 radicals and introducing a novel approach that enables HO2 and certain RO2 types to be selectively measured." Atmospheric Measurement Techniques 6: 3425-3440.

Whalley, L. K., K. L. Furneaux, T. J. Gravestock, H. M. Atkinson, C. S. E. Bale, T. Ingham, W. J. Bloss and D. E. Heard (2007). "Detection of iodine monoxide radicals in the marine boundary layer using laser induced fluorescence spectroscopy." Journal of Atmospheric Chemistry 58: 19-39.

Yoshino, K., D. E. Freeman, J. R. Esmond and W. H. Parkinson (1983). "High resolution absorption cross section measurements and band oscillator strengths of

the (1, 0)-(12, 0) Schumann-Runge bands of O2." Planetary and Space Science 31(3): 339-353.

Chapter 6. Alternative FAGE calibration methods

6.1 Introduction

Discrepancies between measured and modelled HOx from field campaigns have been thoroughly discussed in chapter 1. Campaigns such as HOxCOMP (Schlosser et al., 2009; Fuchs et al., 2010) have helped in identifying potential interferences, or the lack thereof, in FAGE measurements originating from certain atmospherically significant VOCs (such as isoprene). However, alternative FAGE calibration methods to the more widely used H_2O vapour photolysis method (chapter 5), would help further validate measured HOx using the FAGE technique.

The OH yield of alkene ozonolysis reactions has been extensively studied for a wide variety of unsaturated hydrocarbons (Calvert et al., 2000) and has been used as a photolysis free source of OH for the calibration of HOx instrumentation at both Portland and Indiana State universities (Hard et al., 2002; Dusanter et al., 2008). Dark reactions offer one main advantage over the H_2O vapour photolysis method: no determination of the photolysis lamp flux, $F_{184.9nm}$, which is the most uncertain part of the calibration procedure (see chapter 5). The [OH] from the reaction of O_3 + *trans*-2-butene was calculated with the knowledge of the rate coefficient and yield of OH production as well as the competing losses due to reaction with the alkene and walls of the calibration flowtube source. Hard et al. (2002) reported good agreement, within the experimental errors (~37 %), between the ozonolysis and a continuously stirred tank reactor (CSTR) based hydrocarbon decay method (described below). Dusanter et al. (2008) compared the ozonolysis method to H_2O photolysis calibration directly showing agreement with the errors of the two methods (44 % and 17 % respectively to 1σ). However, it should be noted that the ozonolysis calibration technique predicted an instrument sensitivity consistently ~40 % less than the H_2O photolysis method. These discrepancies were assigned to the uncertainty associated with the *trans*-2-butene ozonolysis rate constant and OH yields (IUPAC, 2007; Sander et al., 2011).

Another alternative FAGE calibration method that has enjoyed some success was [OH] steady state inferred from the decay of a hydrocarbon tracer (Hard et al., 1995; George et al., 1999; Hard et al., 2002; Bloss et al., 2004). By choosing a hydrocarbon which has a well characterised rate coefficient, accurate measurement of the hydrocarbon allowed the assignment of [OH] to the detected fluorescence signal of the sampling FAGE

instrument. Portland State University (Hard et al., 1995; George et al., 1999; Hard et al., 2002) used a UV-irradiated continuously stirred tank reactor (CSTR) made from PTFE into which a mixture of humidified air, NO and 1,3,5-trimethylbenzene (TMB) were flowed. Various OH sources were used and the TMB decay due to reaction with OH was measured using a GC with photoionisation detection. The calibration method was found to be within error (~36 %, 1σ) of a steady state calculation from the ozonolysis of *trans*-2-butene. No comparison to the H_2O photolysis method was made and Heard and Pilling (2003) drew attention to several shortcomings of the method including the lack of consideration for radical gradients inside the CSTR.

The second study, conducted at the EUPHORE chamber, took place over nine consecutive days (Bloss et al., 2004). The OH was produced *via* the sunlight driven photolysis of O_3 in the presence of H_2O vapour. The decay of nine hydrocarbons was measured, using HPLC, FTIR and GC-FID. Unlike the Portland State study, Bloss et al. (2004) sought to validate the H_2O photolysis calibration method and reported good correlation between the measured and inferred [OH] for most hydrocarbons ($R = [OH]_{FAGE}/[OH]_{INF} = 1.15 \pm 0.13$). Discrepancies up to R = 3 were seen for the experiment conducted with TMB and R = 1.5 for *p*-xylene. It was thought that several factors may have affected the results including the uncertainty in rate constants and incorrect quantification of the hydrocarbons using FTIR at longer times due to products of the complicated oxidation mechanism. However, this should not detract from the overall correlation and agreement between the two datasets.

For HO_2, no alternative calibration method has been reported.

The deployment of the FAGE technique for aircraft-based measurements (Commane et al., 2010) exposes the FAGE cell to varying pressures as the aircraft changes altitude, altering the instrumental sensitivity (Commane et al., 2010; Martinez et al., 2010). It is possible that the varying pressure differential could change other parameters, for example, the nature of the initial expansion into the FAGE apparatus, something that has not been investigated using an H_2O photolysis calibration source. The current design of wand is limited to delivering the calibrated [OH] at atmospheric pressure, however, by using different nozzle pinhole diameters (typically 0.2 – 1.0 mm) it is possible to alter the pressure in the FAGE cell over the range typically encountered during a flight. This is also an important process for potential HOx measurements inside

HIRAC at different pressures, for which the chamber was initially designed (Glowacki et al., 2007).

Reliance on a single calibration method is potentially problematic and the systematic uncertainties around the application of atmospheric calibrations to HOx data obtained at low pressures highlight the need to obtain calibrations at relevant pressures. Reported here is the intercomparison of HOx calibrations based on the 'flowtube' methodology using different inlet nozzle diameters to vary the internal FAGE cell pressure (chapter 5) compared to hydrocarbon decays for OH, and the kinetics of HO_2 decay by self reaction following the photolysis of formaldehyde for HO_2, both conducted in HIRAC. The ability to simultaneously vary pressure and temperature, coupled with HOx radical detection, make HIRAC ideally suited to the validation and development of atmospheric measurement instrumentation.

6.2 Experimental

6.2.1 General HIRAC preparation and instrumentation

Alternative calibration studies were conducted in the HIRAC chamber. The reader is referred to chapter 2 for a detailed description of the chamber and instrumentation used.

Calibration experiments were conducted over a pressure range of 440 – 1000 mbar in an Ultra-High Purity (UHP) 1:4 synthetic air mix of O_2 (BOC, zero-grade, > 99.999%) and N_2 (BOC, zero-grade, > 99.998%) to match the range of pressures from the pinhole calibration method (chapter 5). The UHP gases helped to maintain low H_2O (< 10 ppm), NO_x (< 1 ppb) and non-methane hydrocarbons (< 1 ppb) during experimental runs. The alternative calibration methods discussed here were photolysis driven and hence the lamps with primary emissions centred at 254 and 300 nm (GE Optica, GE55T8/HO and Philips, TL40W/12 RS, see chapter 2 for emission spectra), were used for the alternative OH and HO_2 calibration methods respectively (sections 6.2.2 and 6.2.3).

Ozone was monitored using the UV photometric O_3 analyser (Thermo Electron Corporation 49C, detection limit (d.l.) = 1.0 ppbv, 30 s averaging). The chemiluminescence NO_x analyser (TEC 42C, d.l. = 50 pptv, 30 s averaging) was used to

determine that levels of NO_x were characteristically below the detection limit of the apparatus during the calibration runs. The calibrated GC-FID (Agilent Technologies, 6890N) was used for the online detection of reactants (chapter 2), fitted with the CP-SIL-5 column (50 m, 0.32 mm, 5 μm) using He carrier gas and a constant oven temperature (40 - 75 ^{o}C dependent on the hydrocarbon being detected). and was able to provide hydrocarbon measurements on a 2 - 6 minute time resolution. Supporting measurements of *iso*-butene and TBHP were made via a long path FTIR absorption facility. The FTIR spectrometer was used as described in chapter 2 and spectral resolution was maintained at 1 cm^{-1} across all experiments, using 32 co-added spectra for a 30 s time resolution.

A combined sampling rate of ~9 slm from the chamber required a counter flow of synthetic air maintaining the desired pressure and diluting the reactants ($(4.5 \pm 0.2) \times 10^{-5}$ s^{-1}). This was regulated using two Brooks mass flow controllers (N_2 and O_2) as described in chapter 2. Known concentrations of precursors were introduced to the chamber in the vapour phase through a 0.97 L stainless steel delivery vessel. Thorough mixing of reaction mixtures was assured by repeated stability measurements prior to photolysis. The chamber was evacuated to ~0.05 mbar for ~60 mins following each experiment using a rotary pump backed roots blower (Leybold, trivac D40B and ruvac WAU251) to aid removal of all reactants/products.

6.2.2 Hydrocarbon decay calibration

Hydrocarbons ($0.5 – 2.0 \times 10^{13}$ molecule cm^{-3}) and OH precursor, *tert*-butylhydroperoxide (TBHP, Sigma Aldrich ~40 % in H_2O, 2.0×10^{13} molecule cm^{-3}) were introduced to the chamber before the lamps were switched on initiating the decay experiment. OH was produced directly from the photolysis of TBHP at $\lambda \approx 254$ nm and is, as far as we are aware, the first chamber experiment to use TBHP photolysis as a low NOx source of OH. Upon illumination of the chamber, rapid photolysis led to peak [OH] ~ 10^7 molecule cm^{-3} instantaneously before OH decayed away over ~30 mins as the TBHP is removed by photolysis and reaction with OH ($k_{OH}(296\ K) = (3.58 \pm 0.54) \times 10^{-12}$ cm^3 $molecule^{-1}$ s^{-1} from Baasandorj et al. (2010)).

Cyclohexane (> 99 %, Fisher Scientific), *n*-pentane (> 99 %, Fisher Scientific) and *iso*-butene (99 %, Sigma Aldrich), were employed as the hydrocarbons in this study due to their sufficiently fast rates of reaction with OH to provide a quantifiable decay compared to chamber dilution. The rate coefficient for OH with *iso*-butene has been evaluated by IUPAC as k_{OH} = (51.0 ± 11.8) × 10^{-12} cm^3 $molecule^{-1}$ s^{-1} (IUPAC, 2007), and cyclohexane and *n*-pentane have been reviewed by Calvert et al. (2008) as k_{OH} = (6.97 ± 1.39) and (3.96 ± 0.76) × 10^{-12} cm^3 $molecule^{-1}$ s^{-1} respectively. Uncertainties are quoted to the respective evaluation limit. Alkanes are known to have a rate coefficient for reaction with OH that is independent of pressure. However, the reactions of OH with alkenes occur predominantly by addition, a process which is pressure dependent, with the rate coefficient increasing with pressure up to the high pressure limit where the addition of OH is the rate determining step (Pilling and Seakins, 1995). A study by Atkinson and Pitts (Atkinson and Pitts, 1975) into the reaction of various small chain alkenes showed no pressure dependence for propene over 25 - 100 Torr of argon, therefore the reaction of OH with the larger *iso*-butene molecule is presumed to be pressure independent above 100 Torr (Atkinson, 1986; IUPAC, 2007).

To confirm this, a relative rate study in air was conducted in HIRAC over the 250 - 1000 mbar pressure range using isoprene as a reference (k_{OH} = (1.00 ± 0.14) × 10^{-10} cm^3 $molecule^{-1}$ s^{-1} (IUPAC, 2007)). Both direct and relative rate studies have shown that the reaction of isoprene and OH is at the high pressure limit above 100 Torr (Campuzano-Jost et al., 2004; Park et al., 2004; Singh and Li, 2007), making it a suitable reference. The relative rate method relies on the simultaneous measurement of the rate of removal of the target species, *iso*-butene, and a reference compound, isoprene, due to reaction with a common reactive species, OH:

iso-butene + OH → products $$-\frac{d[A]}{dt} = k_A[A][OH]$$ E 6.1

isoprene + OH → products $$-\frac{d[B]}{dt} = k_B[B][OH]$$ E 6.2

Rearranging for [OH] and combining E 6.1 and E 6.2:

$$\frac{d[B]}{[B]}\ \frac{1}{k_B} = \frac{d[A]}{[A]}\ \frac{1}{k_A} \qquad \text{E 6.3}$$

Integrating E 6.3 from $t = 0$ to t:

$$\ln\left(\frac{[A]_0}{[A]_t}\right) = \frac{k_A}{k_B}\ln\left(\frac{[B]_0}{[B]_t}\right) \qquad \text{E 6.4}$$

Therefore, if the rate coefficient for B + OH is known, in this case isoprene, then it follows that k_A ($k_{iso\text{-butene}}$) can be determined from the linear regression of a $\ln([A]_0/[A]_t)$ as a function of $\ln([B]_0/[B]_t)$.

The HIRAC chamber was filled with a high purity air mixture (see section 6.2.1) to the desired pressure (Table 6.1). The *iso*-butene, isoprene (> 99 %, Sigma Aldrich) and TBHP were introduced in the vapour phase through the gas delivery system at concentrations ~2.5×10^{13} molecule cm^{-3} (1 ppm at 1000 mbar). Photolysis was initiated after ~240 s mixing time and the decays of *iso*-butene and isoprene were monitored using the GC-FID instrument (as in 6.2.1). Figure 6.1 shows $\ln([iso\text{-butene}]_0/[iso\text{-butene}]_t)$ as a function of $\ln([isoprene]_0/[isoprene]_t)$ used in the determination of the rate coefficient of *iso*-butene + OH at 400 mbar and 293 K. The linear regression gives $k_{iso\text{-butene}} / k_{isoprene}$ (= 0.49 ± 0.01), and hence $k_{iso\text{-butene}} = (4.90 \pm 0.15) \times 10^{-11}$ molecule cm^{-3}. Uncertainty in the relative rate ratio was taken from the systematic uncertainty in the GC measurements and the standard error in the linear regression to 2σ. The relative rate ratios and respective $k_{iso\text{-butene}}$ are shown as a function of pressure in Table 6.1 where uncertainties were propagated as a function of the standard error in the relative rate ratio and the quoted uncertainty in $k_{isoprene}$ (IUPAC, 2007) to 2σ.

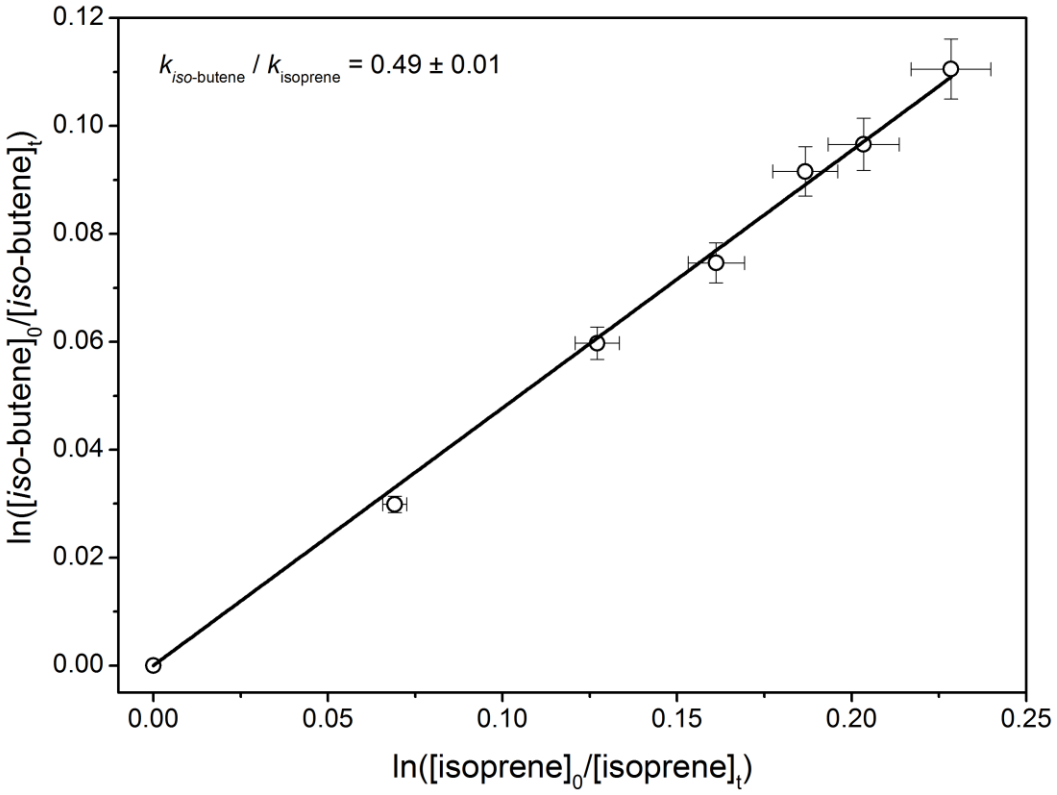

Figure 6.1: ln([*iso*-butene]$_0$/[*iso*-butene]$_t$) as a function of ln([isoprene]$_0$/[isoprene]$_t$) used in the relative rate determination of the rate coefficient for OH + *iso*-butene. The experiment was conducted at 400 mbar and 293 K and TBHP photolysis (λ ≈ 254 nm) was used as an OH source. Error bars represent the precision in the GC-FID measurement to 1σ, and quoted RR ratio uncertainty quoted to 2σ.

Pressure / mbar	$k_{iso\text{-butene}} / k_{isoprene}$	$k_{iso\text{-butene}}$ / 10^{-11} molecule^{-1} cm^3 s^{-1}
1000	0.51 ± 0.05	5.12 ± 0.85
750	0.44 ± 0.02	4.37 ± 0.66
550	0.49 ± 0.03	4.85 ± 0.73
400	0.49 ± 0.03	4.87 ± 0.69
250	0.51 ± 0.05	5.12 ± 0.88
Average =	0.49 ± 0.09	4.87 ± 0.83

Table 6.1: Ratios of $k_{iso\text{-butene}} / k_{isoprene}$ and the corresponding $k_{iso\text{-butene}}$ determined using the relative rate method with isoprene as a reference. Experiments were conducted in high purity air mixtures at the displayed chamber pressures. Uncertainties (2σ) calculated as the combined uncertainty in the ratio and $k_{isoprene}$ from literature (see text for details).

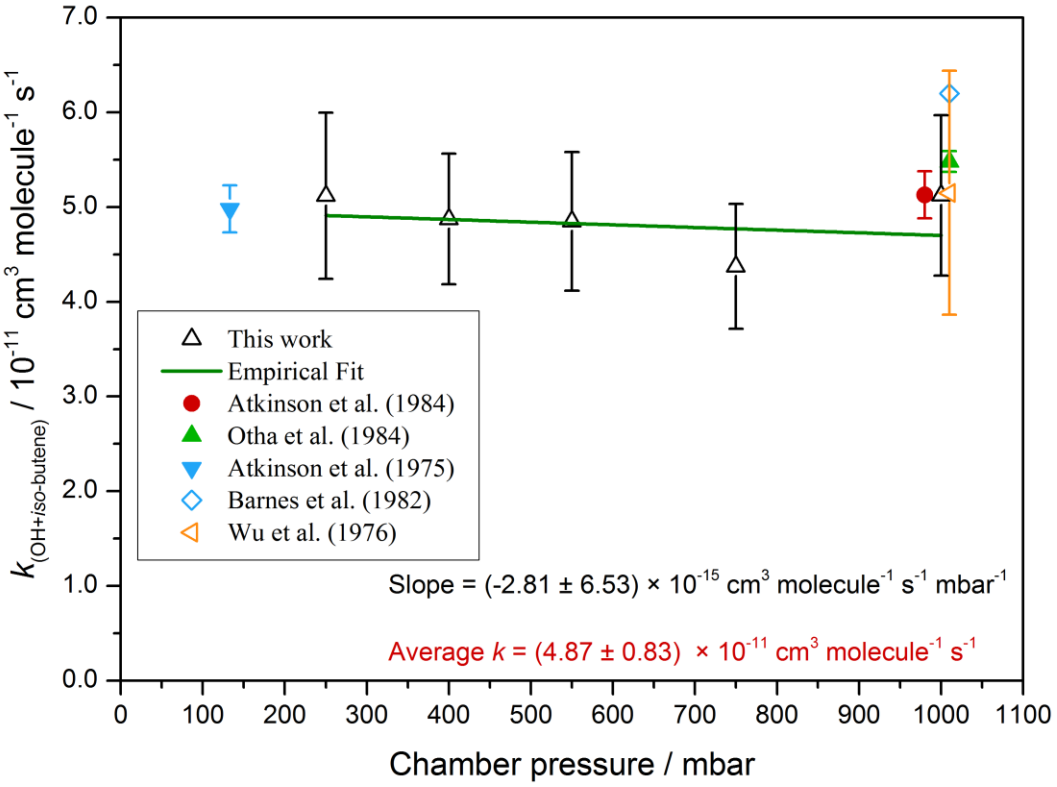

Figure 6.2. Rate constant, *k*, for *iso*-butene + OH over the 250 - 1000 mbar pressure range measured relative to an isoprene reference in the HIRAC chamber. An empirical fit to the data is shown to a emphasise lack of observed pressure dependence in the measured rate constant. Error bars represent the standard error (±2σ) in the associated relative rate determination of *k* (see text) and linear regression is weighted to account for this. Average *k* shown for comparison and uncertainties quoted to 2σ.

Displayed in Figure 6.2 and Table 6.1 are data No significant pressure dependence in *k* for OH + *iso*-butene over the 250 – 1000 mbar pressure range was observed, within the uncertainty of the experiment (1σ). The average measured rate coefficient, k_{OH} = (4.87 ± 0.76) × 10^{-11} cm^3 $molecule^{-1}$ s^{-1}, is in good agreement with the literature (Atkinson, 2003; IUPAC, 2007).

When using the 200 Hz PRF probe laser, an increase in OH detection cell signal was observed upon addition of TBHP to the dark chamber due to the laser generated OH produced from the photolysis of TBHP in the FAGE instrument. The OH interference during the hydrocarbon decay experiments was characterized using the newly developed OH scavenger system in the HIRAC FAGE instrument (chapter 2). *Iso*-butane (20 % in N_2) was injected ~40 mm inside the inlet pinhole in to the central flow, through a 3 mm stainless steel pipe at a rate of ~20 sccm, reacting with the

sampled OH before it reaches the detection axis. The laser generated OH is probed within the same laser pulse (~12 ns) and hence is not suppressed by the scavenger injection. Neither a pressure increase nor attenuation of UV light was detected during the scavenger injection process at this flow rate and dilution. The scavenger was injected for a 60 s period approximately five times during the course of an experiment. The mean measured OH signal for each injection was then plotted as a function of time and a linear regression was used to empirically describe the data, and subtract the interference signal from the measurement data.

The hydrocarbon decay method relied on the loss of hydrocarbon solely due to OH and hence the effects of O_3 and NO_3 must be considered as both are important in the oxidation of alkenes (Atkinson, 1994). Before photolysis, O_3 and NO_x were measured around the instrumental detection limit (1.25 and 0.06 × 10^{10} molecule cm^{-3} respectively) using commercial analysers. Upon photolysis a slow increase in O_3 and NO_2 was observed, to a maximum of ~1 and ~0.5 × 10^{11} molecule cm^{-3} respectively. The [NO_3] upper limit was estimated at ~8 × 10^6 molecule cm^{-3} using a simple steady-state approximation, where NO_3 production was controlled purely by $O_3 + NO_2 \rightarrow NO_3$ (Atkinson et al., 2004) and loss by photolysis. Under these conditions it was estimated that > 98% of the loss of *iso*-butene would be due to OH and not O_3 or NO_3 where $k_{O_3} = (1.13 \pm 0.33) \times 10^{-17}\ cm^3\ molecule^{-1}\ s^{-1}$ and $k_{NO_3} = (3.4 \pm 1.0) \times 10^{-13}\ cm^3\ molecule^{-1}\ s^{-1}$ (Calvert et al., 2000).

6.2.3 Formaldehyde photolysis

Formaldehyde was produced by direct heating of *para*-formaldehyde powder (Sigma Aldrich, 99%) and was introduced into the chamber at concentrations ~2 × 10^{13} molecule cm^{-3}. The chamber was irradiated (λ = 275 - 325 nm) resulting in an almost instantaneous HO_2 signal. Once an approximately steady state HO_2 concentration was achieved the photolysis lamps were turned off and the decay of HO_2 was monitored by FAGE for ~120 sec until near background signals levels were reached. The measurement of HO_2 decays was repeated up to five times before the laser was scanned to the offline position (**Error! Reference source not found.** shows an example). Therefore five individual C_{HO2} determinations could be achieved from one

chamber fill with the limiting factor being the increased complexity of the reaction mixture after repeated photolysis cycles. The absence of OH in these experiments was confirmed by simultaneous measurement of OH.

Formaldehyde concentrations were kept low (< 3×10^{13} molecule cm^{-3}) to avoid removal of HO_2 via reaction with HCHO ($k = (7.9 \pm 5.9) \times 10^{-14}$ molecule cm^{-3} s^{-1} (Atkinson et al., 2004)), ensuring that the loss of HO_2 occurs predominately via self-reaction and wall loss (section 6.3.2).

6.3 Data analysis procedure

6.3.1 Hydrocarbon decay

OH can react with hydrocarbons to give several products:

$$OH + HC \rightarrow \text{Products} \qquad \text{R 6.1}$$

The rate of this reaction depends on both the concentration of the hydrocarbon and of the OH radical, giving a second order reaction.

$$-\frac{d[HC]}{dt} = k_{OH+HC}[OH][HC] \qquad \text{E 6.5}$$

where $-d[HC]/dt$ is the rate of removal of the hydrocarbon and k_{OH+HC} is the rate constant for the removal. The [HC] was measured using GC-FID (and FTIR for *iso*-butene) and Figure 6.3 shows a hydrocarbon decay for *iso*-butene at 750 mbar and 293 K. Using the Guggenheim method (Guggenheim, 1926; Bloss et al., 2004) the pseudo-first-order rate coefficient (k') for the hydrocarbon removal was calculated using E 6.6:

$$k' = \frac{\ln([HC]_1/[HC]_2)}{(t_2 - t_1)} \qquad \text{E 6.6}$$

where $[HC]_1$ and $[HC]_2$ are the concentrations of the hydrocarbon at time t_1 and t_2 respectively.

The mean [OH] between t_1 and t_2, was calculated using E 6.7:

$$[OH] = \frac{(k' - k_{dil})}{k_{OH+HC}} \qquad \text{E 6.7}$$

where k_{dil} is the dilution rate of the measured [HC] due to FAGE and GC sampling. Bloss et al. (2004) found the Guggenheim method to be most effective when smoothing the inferred [OH] over five [HC] measurements (i.e. consider ten measurements taken at times t_1 - t_{10}. [OH] at t_5 would take $[HC]_1$ and $[HC]_5$, t_6: $[HC]_2$ and $[HC]_6$ etc.). Due to the short experiment time (20 - 30 min) and the 2 - 6 min time resolution on GC-FID measurements, this smoothing was not possible. For *iso*-butene, FTIR measurements were taken every 30 s, and these were typically found to be in excellent agreement with the GC-FID measured HC decays, as shown in Figure 6.3. However, measurement of small changes in the [HC], due to low steady state [OH] in the chamber (~5×10^6 molecule cm^{-3}), led to large point-to-point variation in the inferred [OH], even after the smoothing was applied. A solution was found by fitting the hydrocarbon decay data with an empirical exponential function of the form $y = A \times e^{(-x/t1)} + y_0$ as shown in Figure 6.3 which allowed the accurate calculation of [HC] at the same time resolution as the FAGE instrument (20 s averaged). A negligible difference between inferred [OH] determined using the FTIR or GC-FID data was observed and hence only GC-FID measured hydrocarbon decays were used for direct comparison with *n*-pentane and cyclohexane.

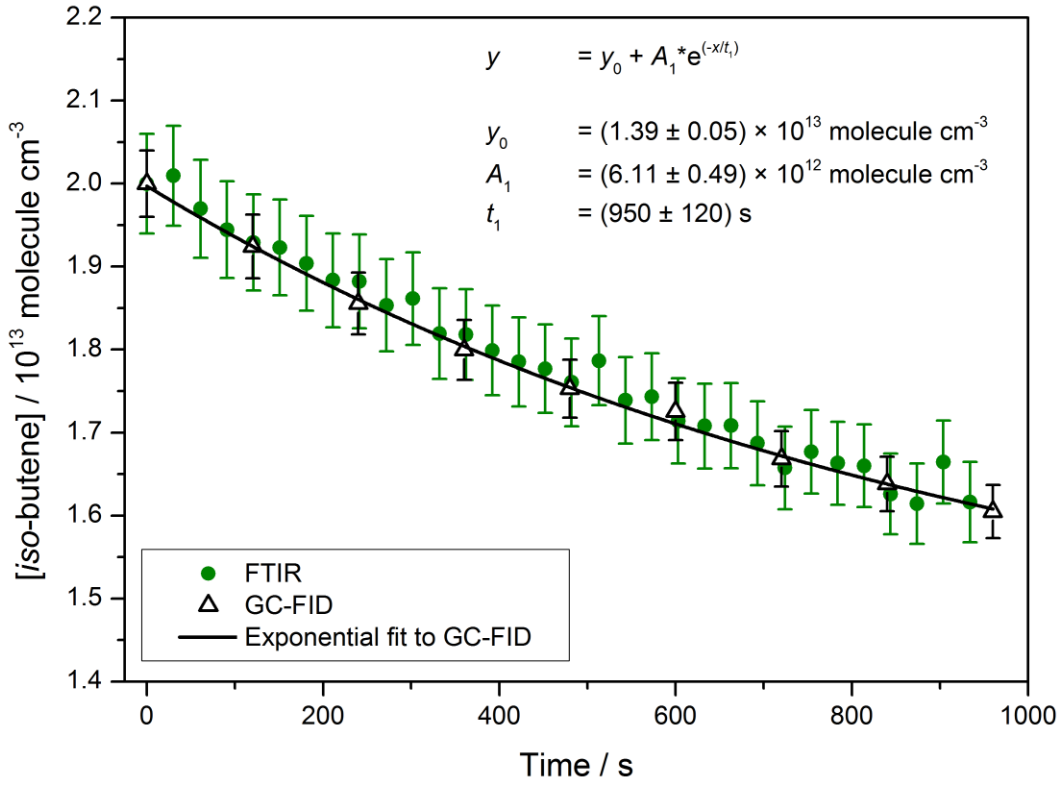

Figure 6.3. Decay of *iso*-butene as a function of time through reaction with OH in HIRAC (750 mbar, 294 K), measured using GC-FID on a 2 min time resolution, and FTIR on a ~20 s time resolution. The data are fitted with a first order exponential decay (purely empirical) to allow calculation of [HC] on the same time scale as the 60 s averaged FAGE data. Time = 0 s indicates photolysis lamp turn-on time and uncertainties are quoted to ±1σ. Error bars are representative of the precision in the GC-FID (~2%) and FTIR (~3%) measurements to 1σ.

When using the 200 Hz PRF probe laser, an increase in OH detection cell signal was detected upon addition of TBHP to a dark chamber due to the laser generated OH produced from the photolysis of TBHP in the FAGE instrument. Displayed in Figure 6.4 is a typical [OH] profile for the photo-oxidation of *n*-pentane (2.1×10^{13} molecule cm^{-3}) in HIRAC at 1000 mbar and 293 K where photolysis of TBHP was used to produce ~1.3×10^{7} molecule cm^{-3} OH at t = 0. The OH was measured directly using the LITRON Nd:YAG pumped dye laser light source, operating at 200 Hz PRF. Upon introduction of TBHP (3.2×10^{13} molecule cm^{-3}) to the dark chamber at t ≈ −500 s, an OH signal equivalent to ~2.5×10^{6} molecule cm^{-3} was observed, and was typically < 25% of the total detected OH signal following lamp photolysis. The measured OH fluorescence signal was observed to increase

quadratically with laser power, suggesting a two photon photolysis-probe process from the OH probe laser at 308 nm, as described by reactions R 6.2 - R 6.4.

$$\text{TBHP} + h\nu \rightarrow \text{OH(X)} + \text{products} \qquad \text{R 6.2}$$

$$\text{OH(X)} + h\nu \rightarrow \text{OH(A)} \qquad \text{R 6.3}$$

$$\text{OH(A)} \rightarrow \text{OH(X)} + h\nu\text{(LIF)} \qquad \text{R 6.4}$$

This phenomena was not observed when using the 5 kHz PRF laser system. The OH interference profile during the hydrocarbon decay was characterized and accounted for using the scavenger system described in section 2.2. At a time defined by the user, the *iso*-butane scavenger (20% in N_2) was injected into the FAGE cell for ~90 s at ~20 sccm. Typically 3 - 4 scavenger injections were completed per experiment and an empirical fit to the averaged signals was used to correct the measured OH signal from TBHP laser photolysis, shown here in Figure 6.4(b) compared to the inferred [OH] from the GC-FID. The type of fitting parameter (e.g. linear or exponential) was judged depending on the quality of data.

The calibration procedure was completed by plotting the OH signals, normalised for laser power, measured by FAGE as a function of the calculated OH concentrations from the hydrocarbon decays producing a calibration plot with C_{OH}, in units of counts cm^3 s^{-1} mW^{-1} $molecule^{-1}$, as the gradient. A typical calibration plot is shown in Figure 6.6; produced using the decay of *iso*-butene at 1000 mbar chamber pressure (see caption for detailed operating conditions).

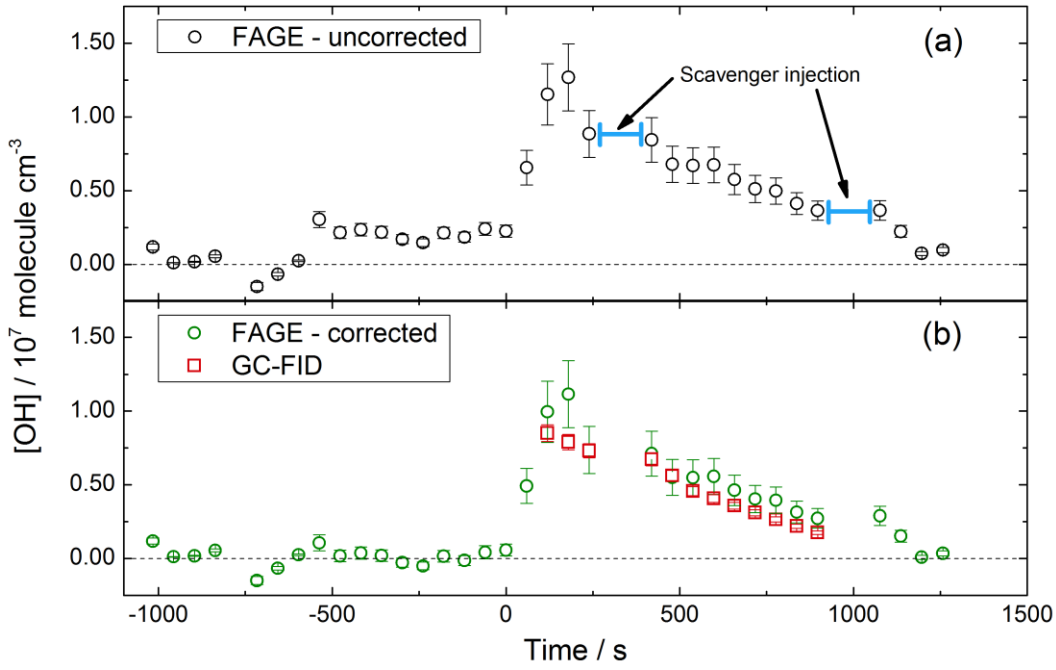

Figure 6.4: Comparison of [OH] traces measured using FAGE during the photoxidation of *n*-pentane at 1000 mbar and 293 K before, (a) and after, (b), correcting for laser generated OH due to TBHP photolysis in the OH fluorescence cell. The 200 Hz PRF laser system was used for these measurements. The uncorrected and corrected FAGE signal was converted to [OH] using C_{OH} = 3.6 × 10^{-8} counts cm^3 s^{-1} $molecule^{-1}$ mW^{-1} determined using the conventional calibration method for comparison with GC-FID data. The TBHP (3.2 × 10^{13} molecule cm^{-3}) and *n*-pentane (2.1 × 10^{13} molecule cm^{-3}) were introduced into the chamber at $t \approx -500$ s and the photolysis lamps were switched on at t = 0 s. The [OH] inferred from the HC decay method is also displayed in figure (b). Dashed line at y = 0 given for clarity..

6.3.2 Formaldehyde photolysis

Calibration of the HO_2 detection cell required only the generation of HO_2 radicals in the HIRAC chamber, and a measurement of their subsequent recombination using the FAGE instrument. Upon photolysis in air, HCHO produces two HO_2 radicals, the loss of which was characterised by the competing second and third order self-reactions (R 6.5 and R 6.6) and a first order wall loss parameter (R 6.7):

$$HO_2 + HO_2 \rightarrow H_2O_2 + O_2 \qquad \text{R 6.5}$$

$$HO_2 + HO_2 + M \rightarrow H_2O_2 + O_2 + M \qquad \text{R 6.6}$$

$$HO_2 \rightarrow \text{Loss} \qquad \text{R 6.7}$$

Therefore the rate of loss of HO_2 can be approximated by equation E 6.8:

$$\frac{d[HO_2]}{dt} = -\left(k_{loss}[HO_2] + 2k_{HO_2+HO_2}[HO_2]^2\right) \qquad \text{E 6.8}$$

where $k_{HO2+HO2}$ represents the sum of the pressure dependent and pressure independent rate coefficients (R 6.5 + R 6.6). Solving analytically for $[HO_2]_t$ at a given time, t, equation E 6.8 becomes:

$$\frac{1}{[HO_2]_t} = \left(\frac{1}{[HO_2]_0} + \frac{2 \cdot k_{HO_2+HO_2}}{k_{loss}}\right) \cdot e^{(k_{loss}t)} - \left(\frac{2 \cdot k_{HO_2+HO_2}}{k_{loss}}\right) \qquad \text{E 6.9}$$

The $[HO_2]$ in equation E 6.9 is unknown but is related to the normalized HO_2 signals measured by FAGE, S_{HO2}, and the instrument sensitivity to HO_2, C_{HO2}, through equation the relationship $S_{HO2} = C_{HO2} \times [HO_2]$ (chapter 5):

$$\left(S_{HO_2}\right)_t = \left(\left(\frac{1}{\left(S_{HO_2}\right)_0} + \frac{2 \cdot k_{HO_2+HO_2}}{k_{loss} \cdot C_{HO_2}}\right) \cdot e^{(k_{loss}t)} - \left(\frac{2 \cdot k_{HO_2+HO_2}}{k_{loss} \cdot C_{HO_2}}\right)\right)^{-1} \qquad \text{E 6.10}$$

where $(S_{HO2})_t$ and $(S_{HO2})_0$ are the HO_2 signal at time t and $t = 0$, respectively. The measured decay of S_{HO2} using FAGE and the fit described by equation E 6.10 are displayed in Figure 6.5 for a typical experiment (550 mbar, 298 K, <10 ppm $[H_2O]$ etc.). Both k_{loss} and C_{HO2} were determined by data fitting the S_{HO2} decay using equation E 6.10 with a Levenburg-Marquardt non-linear least squares algorithm by fixing the initial signal and $k_{HO2+HO2}$. The first ~100s of data were used, ensuring analysis after an almost complete decay of S_{HO2}. Fitting was improved by the inclusion of upper and lower bounds of ±10 % for the $(S_{HO2})_0$ into the fitting routine, which accounted for the uncertainty in the determination of $(S_{HO2})_0$.

The HO_2 recombination rate coefficient was calculated by combining both the pressure independent (R 6.5) and dependent (R 6.6) terms, including a correction for the H_2O vapour enhancement in accordance with the IUPAC recommended method (Atkinson et al., 2004). The pressure dependence can be explained by considering the formation of an H_2O_4 excited complex which can then form $H_2O_2 + O_2$ directly (bimolecular) as well

as after stabilisation by collision (termolecular). The H_2O chaperone effect accelerates the rate of reaction by forming a pre-reactive cyclic complex, and upon reaction with HO_2 or another cyclic complex, forms a vibrationally relaxed H_2O_4 intermediate (Stone and Rowley, 2005). For the experimental 440 – 1000 mbar pressure range at 0% H_2O, $k_{HO2+HO2}$ = 2.10 - 2.85 × 10^{-12} cm^3 $molecule^{-1}$ s^{-1} were used, respectively.

The wall loss rate, k_{loss}, was considered dependent on daily chamber conditions and was therefore determined as part of the fitting procedure along with C_{HO2}, typically between 0.032 - 0.073 with an uncertainty of ±10 % (2σ). Variations in the wall loss rates have implications for the uncertainty in C_{HO2} derivation (see section 6.5.2).

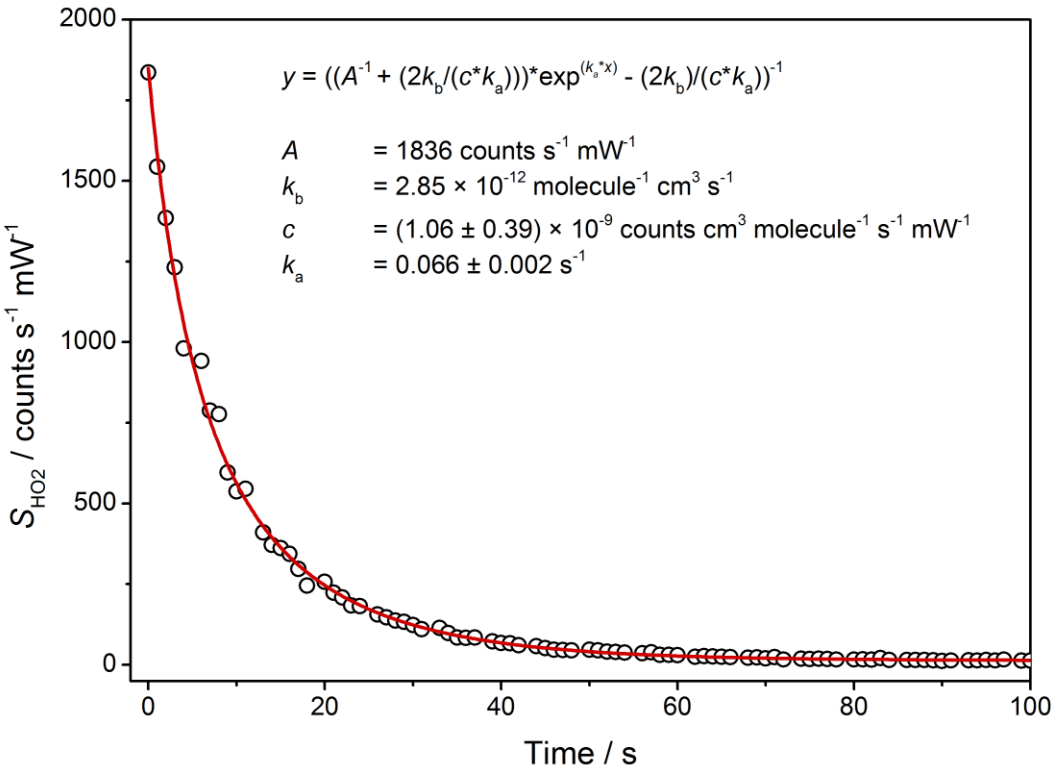

Figure 6.5: Normalised S_{HO2} decay for the HCHO photolysis calibration method at 1000 mbar chamber pressure using the aircraft based FAGE instrument operating at 5 kHz PRF; internal cell pressure = 2.53 ± 0.02 mbar; laser power = 8.25 ± 0.25 mW. Data were fitted with equation E 6.10 to give C_{HO2} where $A = (S_{HO2})_0$, $k_b = k_{(HO2+HO2)}$, $c = C_{HO2}$, $k_a = k_{loss}$, with uncertainties quoted to ±1σ. Parameters without quoted error were fixed.

6.4 Results and discussion

6.4.1 Hydrocarbon decay

Displayed in Figure 6.6 is a direct comparison of analysed data from the decay of *iso*-butene and H_2O vapour calibration method at ~3.80 mbar internal cell pressure (equivalent to 1000 mbar in HIRAC) using the 1.0 mm inlet pinhole and ~7 mW laser power. The C_{OH} was determined as $(2.1 \pm 1.1) \times 10^{-8}$ counts s^{-1} molecule-^{1} cm^3 mW^{-1} within error of the traditional H_2O vapour photolysis calibration (2σ) at the same pressure ($(2.62 \pm 0.91) \times 10^{-8}$ counts s^{-1} $molecule^{-1}$ cm^3 mW^{-1}). Error bars are representative of the total uncertainty at $\pm 1\sigma$.

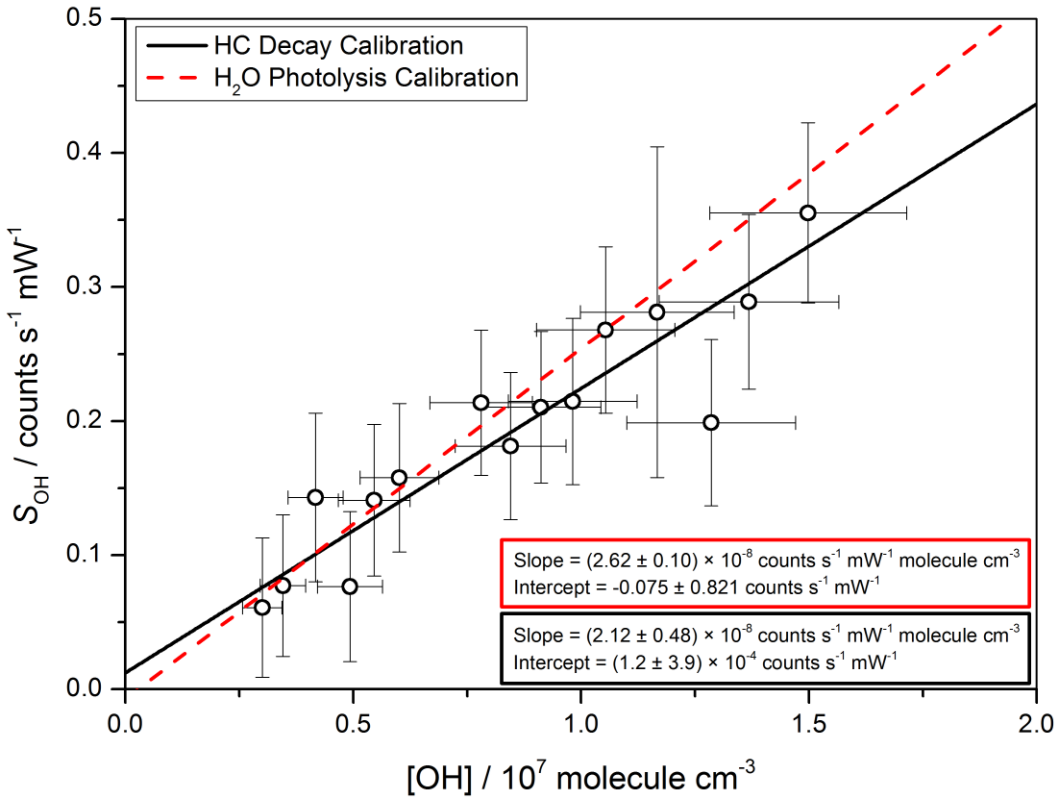

Figure 6.6: Calibration from the hydrocarbon decay method for *iso*-butene at 1000 mbar and 293 K chamber pressure using the 200 Hz PRF laser system; internal cell pressure = (3.81 ± 0.02) mbar; laser power = (7.0 ± 0.5) mW. Extrapolated calibration from the H_2O photolysis calibration technique for internal cell pressure = (3.79 ± 0.02) mbar, laser power = (6.0 ± 0.5) mW, $[H_2O]_{vapour}$ = (3900 ± 20) ppmv and [OH] = (0.5 - 1.5) × 10^9 molecule cm^{-3}. Both fits are weighted to errors in the *x* and *y* axes. Uncertainties quoted represent the precision of the calibration processes to $\pm 2\sigma$.

The HC decay calibration method has allowed the FAGE instrument to be calibrated at [OH] more representative of chamber experiments conducted in the HIRAC chamber. Confirmation that the calibration factor determined using the H_2O photolysis method is relevant at low [OH] through extrapolation was also very important as most ambient measurements are ~10^6 molecule cm^{-3}.

Displayed in Figure 6.7 and Table 6.2 are the values of C_{OH} as a function of internal cell pressure determined using the HC decay calibration method for *iso*-butene, cyclohexane and *n*-pentane. Error bars are representative of the total uncertainty at ±1σ. The HC decay calibration method was observed to be in agreement with the H_2O vapour photolysis calibration. The average of the ratio of calibration factors (conventional:alternative) was calculated for each alternative calibration point across the entire pressure range, $C_{OH(conv)}/C_{OH(alt)}$ = 1.19 ± 0.26, where $C_{OH(conv)}$ was determined from the fit to the H_2O photolysis data.

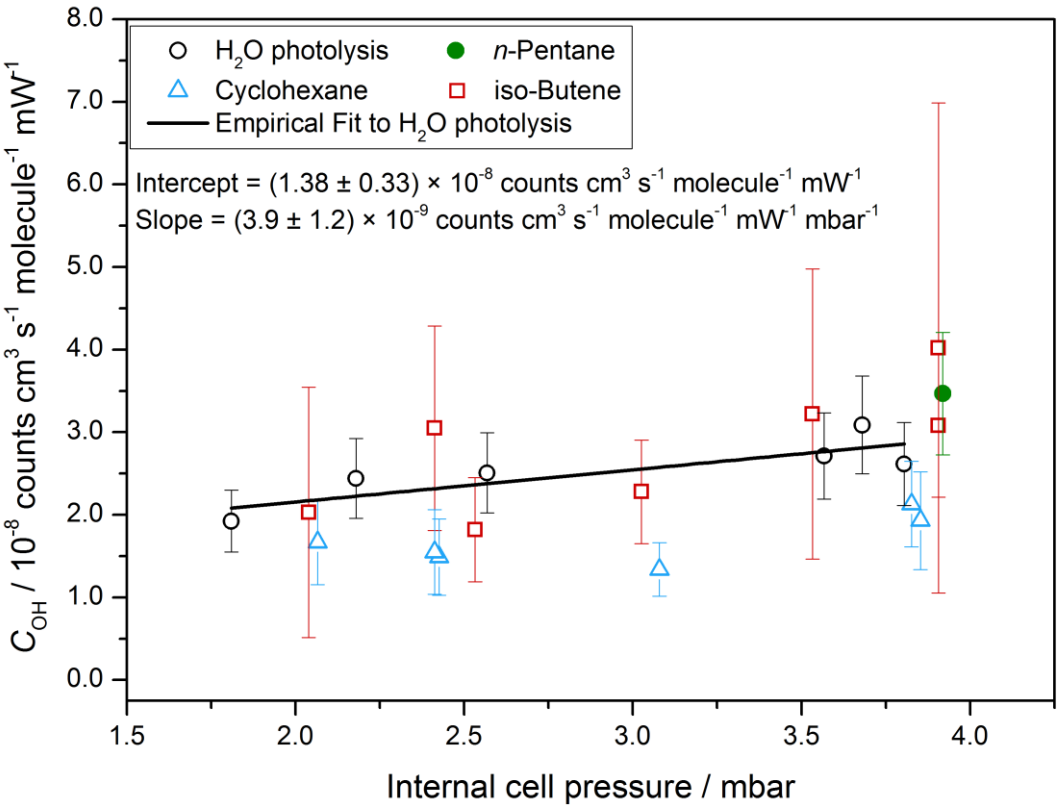

Figure 6.7. FAGE instrument sensitivity to OH, C_{OH}, as a function of internal detection cell pressure as determined by the H_2O photolysis and HC decay calibration techniques using the LITRON Nd:YAG pumped dye laser operating at 200 Hz PRF. All calibrations were conducted at laser powers between 6.0 - 9.5 mW. Error bars indicate the total uncertainty to ±1σ.

Hydrocarbon	Cell *P* (mbar)	Chamber *P* (mbar)	C_{OH}	Uncertainty (2σ)
n-pentane	3.92	1000	3.42	1.09
iso-butene	3.91	1000	3.08	0.86
	3.91	1000	4.02	2.97
	3.53	880	3.22	1.76
	3.03	750	2.28	0.63
	2.53	600	1.93	0.93
	2.41	550	3.05	1.24
	2.04	450	2.03	1.52
Cyclohexane	3.85	1000	1.93	0.59
	3.83	1000	2.13	0.52
	3.08	750	1.34	0.33
	2.43	550	1.49	0.46
	2.41	550	1.55	0.51
	2.07	450	1.67	0.51

Table 6.2: Tabulated data from the HC decay alternative OH calibration experiments. Uncertainties quoted to ±2σ and propogated as described in the main text. Pressure in mbar and C_{OH} and uncertainty in 10^{-8} counts s^{-1} molecule cm^3 mW^{-1}.

A large variability in the C_{OH} determined using the *iso*-butene decay was observed, with larger uncertainties associated with this calibration compared to cyclohexane and *n*-pentane, and the reason for this remains unclear. On average, the measured OH signals were closer to the detection limit of the FAGE instrument when using *iso*-butene. Initial concentrations of each of the hydrocarbons were 2.5×10^{13} molecule cm^{-3}, and hence a lower OH steady-state concentration is expected when *iso*-butene was present as the k_{OH} is an order of magnitude higher than those for *n*-pentane and cyclohexane. As S_{OH} approaches 0 counts s^{-1} mW^{-1}, the S_{OH} measurement becomes increasingly imprecise, and thus the uncertainty in the fitting of the calibration plot increases.

A general under-prediction of C_{OH}, compared to the H_2O vapour photolysis method, was observed when calculated using the decay of cyclohexane, $C_{OH(conv)}/C_{OH(Chex)} = 1.52 \pm 0.44$. The exact reason is unknown. Evaluation of the HC decay data with the k_{OH} adjusted at the upper limit of uncertainty recommended by Calvert et al. (2008) (25% (2σ), $k_{OH} = 8.04 \times 10^{-12}$ cm^3 $molecule^{-1}$ s^{-1}), brings the two datasets into better agreement, $C_{OH(conv)}/C_{OH(Chex)} = 1.21 \pm 0.22$. The cyclohexane

measurements were also affected to a greater extent by the chamber dilution due to the slower rate of reaction with OH, which contributed to 25 - 30 % of the total cyclohexane decay rate directly after the photolysis lamps were initiated, compared to 5 - 10 % for the iso-butene experiments. Correcting the cyclohexane data for a hypothetically enhanced chamber dilution could explain the lower sensitivity measurements (as the decay increases, $[OH]_{inf}$ increases), however the dilution rate was confirmed prior to photolysis of TBHP in each experiment.

6.4.2 Formaldehyde photolysis calibration

Figure 6.8 and Table 6.3 show the HIRAC FAGE instrument sensitivity to HO_2, C_{HO2}, as a function of internal cell pressure for the newly developed formaldehyde photolysis calibration technique. Each data point corresponds to the average of up to five HO_2 decay traces and the error bars are representative of the standard deviation in the average and the total calibration uncertainty to 1σ. All calibrations were completed using the 200 Hz PRF laser system at 6.0 ± 2.0 mW laser power. The alternative calibration was observed to be in good agreement with the conventional H_2O vapour photolysis calibration technique over the operating internal cell pressure range between 1.8 - 3.8 mbar ($C_{HO2(conv)}/C_{HO2(alt)}$ = 0.96 ± 0.18).

The kinetics of the HO_2 decay due to recombination and first order wall loss were confirmed by studying the HO_2 decay profile with the chamber mixing fans on and off using the University of Leeds aircraft based FAGE instrument. With the mixing fans off, the decay was accurately described by the recombination kinetics only, giving C_{HO_2} values within error of the fans on experiments, as shown in Figure 6.8(b). Good agreement between the conventional and alternative calibration methods was also observed across the 1.42 - 2.48 mbar internal cell pressure range and the overall correlation between conventional and alternative calibration methods was calculated as $C_{HO2(conv)}/ C_{HO2(alt)}$ = 1.07 ± 0.18.

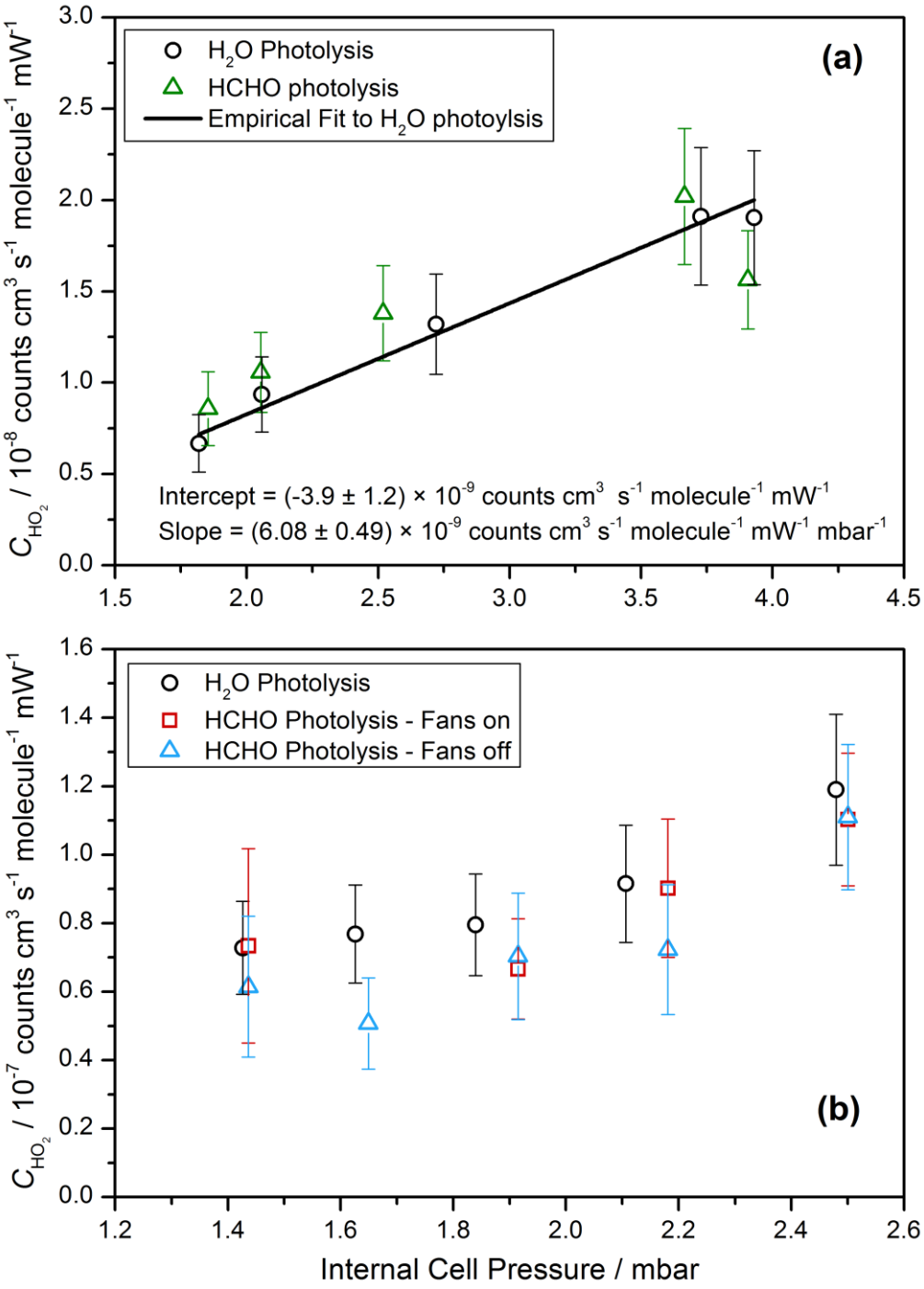

Figure 6.8. FAGE instrument sensitivity to HO_2, C_{HO2}, as a function of internal detection cell pressure as determined by the H_2O vapour and HCHO photolysis calibration techniques using the HIRAC FAGE instrument operating at 200 Hz PRF (a) and the aircraft FAGE instrument operating at 5 kHz PRF (b). Conventional calibrations were conducted at constant $[H_2O]_{vap}$ ((a) 4500 ± 600 ppmv, (b) 6000 ± 600 ppmv) whereas alternative calibrations were conducted under low $[H_2O]_{vap}$ (<15 ppmv). HIRAC chamber pressures between 440 - 1000 mbar were used to induce internal cell pressures between (a) 1.8 - 3.8 mbar and (b) 1.42 - 2.48 mbar. Error bars indicate the total uncertainty to ±1σ.

Cell *P* (mbar)	Chamber *P* (mbar)	C_{HO_2} ($\times 10^{-8}$)	Avg. C_{HO_2} ($\times 10^{-8}$)	Uncertainty ($\times 10^{-8}$) $\pm 2\sigma$
3.91	1000	1.54 1.37 1.72 1.47 1.63	1.55	0.52
3.67	880	1.71 1.96 1.65 2.51 2.26	2.02	0.74
2.52	550	1.57 1.27 1.35 1.32	1.38	0.52
2.05	410	0.68 1.78 0.98 0.78	1.06	0.44
1.85	350	1.12 0.67 0.78	0.86	0.40

Table 6.3: Tabulated data from the HCHO photolysis based alternative HO_2 calibration experiments. Uncertainties quoted to $\pm 2\sigma$ and propogated as described in the main text. Units for C_{HO2}, Avg C_{HO2} and Uncertainty = counts s^{-1} molecule cm^3 mW^{-1}.

6.5 Uncertainties

The overall uncertainty associated with the calibration methods presented here was calculated by the sum in quadrature of the accuracy and the precision terms of the calibration. The accuracy term accounted for any systematic uncertainty in each calibration method in the calculation of $[HO_x]$ or signal normalisation etc. and these are displayed in Table 6.4. The precision of the calibrations were defined as the random errors associated with each method and these are discussed in detail in the following sections.

H_2O + *hv*		**Hydrocarbon Decay**		**HCHO + *hv***	
Parameter	Uncertainty	Parameter	Uncertainty	Parameter	Uncertainty
$F_{184.9nm}$	32%	k_{OH+HC}	20 – 25 %	$k_{HO2+HO2}$	35%
Δt	2%	k_{dil}	10%	S_{HO2} initial	20%
$[H_2O]$	10%	Laser power	6%	Laser power	6%
$\sigma_{H2O,184.9nm}$	6%	Online Position	4%	Online Position	4%
Laser power	6%				
Online Position	4%				
Total	**35%**	Total	**24 - 28%**	Total	**41%**

Table 6.4: The systematic uncertainties in the various parameters that determine the accuracy in the OH and HO_2 calibration factors for all three calibration methods. Total accuracy is taken as the sum in quadrature of the individual uncertainties. Range of uncertainties in k_{OH+HC} and $k_{HO2+HO2}$ are discussed in sections 6.5.1 and 6.5.2, respectively.

6.5.1 Hydrocarbon Decay Calibration

The total uncertainty for the HC decay method was more varied than the flow tube calibration method due to the large variation in the random errors that defined the precision of the experiment. However, it should be noted that the systematic uncertainties associated with the HC decay method were smaller than the conventional H_2O photolysis method. The total uncertainty was therefore estimated at ~45 %.

The accuracy in the calibration was intrinsic to the hydrocarbon decay used, being dependent on the uncertainty in k_{OH} and k_{Dil}. The largest uncertainty was in k_{OH}, taken from data reviews from the Calvert series or IUPAC recommendations: *n*-pentane, ±20% (Calvert et al., 2008), cyclohexane, ±20% (Calvert et al., 2008), *iso*-butene, ±25%

(IUPAC, 2007). Uncertainty in k_{Dil} was calculated from repeated measurements of chamber dilution for the respective hydrocarbon, and induced errors in GC-FID measurements and calibration (4%).

The precision of the experiments for both *n*-pentane and cyclohexane was between 10 - 25%, whereas *iso*-butene showed much greater variation of between 13 - 69 %; possible reasons for which have been discussed in section 6.6.

6.5.2 Formaldehyde photolysis calibration

The total uncertainty for the HCHO photolysis calibration method has been estimated at ~41%, which is comparable to the conventional calibration method. The largest systematic uncertainty was in the HO_2 recombination rate constant (35%), taken from the IUPAC recommendation (IUPAC, 2007). The uncertainty in the initial S_{HO2} (i.e. S_{HO2} at t_0) chosen for the analysis was based on the standard deviation of the offline signal, which gives an estimation of the 1 second point-to-point variability for a chosen t_0 (~20%).

The error associated with the precision of the experiment is taken from the error propagation of the standard error terms from the Levenburg-Marquardt iterative fitting procedure for equation E 6.10 and Figure 6.5. This includes both the error in the C_{HO2} and k_{loss} parameters. The precision for this method was in line with the conventional flow tube calibration between 10 - 20 %.

6.6 Conclusions and further work

The first pressure dependent calibrations of a FAGE instrument for both OH and HO_2 have been successfully conducted using the HIRAC chamber. Previous pressure dependent aircraft measurements had been extracted by assuming that the calibration factor could be determined by simply calibrating at the required internal FAGE cell pressure. Assumptions were therefore made that variations in radical losses on the inlet and the nature of the expansion caused by the varying pressure differential inside and outside the FAGE cell were insignificant. The results displayed in Figure 6.7 and Figure 6.8 validate the conventional calibration method with the alternative hydrocarbon decay and HCHO photolysis methods over a range of internal FAGE cell pressures. As the calibration methods are quite different in principle, they are unlikely to be subject to the same systematic errors. The alternative calibration results presented here have been shown to be well within the uncertainty of their respective traditional calibration method, validating the pressure dependent flow tube calibration technique and improving confidence in FAGE measurements both in the field and in kinetics experiments. Both alternative methods have also shown that calibrations conducted under high $[H_2O]_{vap}$ conditionals (2000 - 4500 ppmv) can be applied to measurements at low $[H_2O]_{vap}$ (<15 ppmv).

The hydrocarbon decay method has shown that the FAGE instrument can be calibrated over a range of external pressures using different hydrocarbons. Compared to the conventional calibration method, where [HOx] are generated typically at $>10^8$ molecule cm^{-3}, the hydrocarbon decay method is conducted at a [HOx] relevant to chamber based experimental measurements (~10^7 molecule cm^{-3}). Currently the error associated with the hydrocarbon decay method is greater than that of the flow tube method (~45% vs 36%); the primary sources of error arise from uncertainties in the rate coefficients, detection of OH close to the detection limit of FAGE and the analysis of small changes in hydrocarbon concentration. Uncertainties in the rate coefficients could be reduced by a concerted laboratory study including relative rate and direct flash photolysis methods, with careful experimental design errors could be reduced to closer to 10% (Orkin et al., 2010; Carr et al., 2011; Glowacki et al., 2012). The benefit of increasing the steady state concentration of OH would be two-fold as OH fluorescence signals would be greater than the detection limit of the FAGE instrument, whilst a more marked decay in HC

would improve the determination of the inferred [OH]. The steady state OH concentration could be increased by increasing the 254 nm intensity in the chamber, using new lamps or more lamps, altering the OH precursor, e.g. O_3 + alkenes or photolysis of methyl nitrite, or by lowering the initial [HC]. The latter would require a more sensitive detection technique than GC-FID or FTIR than is currently available in HIRAC, e.g. a proton transfer mass spectrometer (PTR-MS). PTR-MS would also reduce the uncertainty in the hydrocarbon decay measurements (higher time resolution) and allow for easier simultaneous measurement of multiple hydrocarbons at low concentrations, effectively providing multiple independent estimates of C_{OH} from a single experiment. Studying a range of different volatile organics (e.g. aromatics) would also help improve confidence in the calibration technique, whilst determining the FAGE instrument response within HIRAC when exposed to high [HC] concentrations compared to ambient levels (> 1 ppmv). Expansion of the hydrocarbon decay method into a temperature dependent study is also planned in the near future in HIRAC to validate the external inlet temperature dependence observed here.

The HCHO photolysis method is quick and reproducible. The time taken to complete the analysis and the errors are comparable with the flow tube technique. An advantage of the HCHO photolysis method is that several runs can be completed in one fill of the chamber, compared to the HC decay method that requires one fill per experiment (although the proposed use of multiple HC decays will provide multiple estimates of C_{OH} from a single chamber fill). Temperature dependent C_{HO2} calibrations are also planned in the near future.

6.7 References

Atkinson, R. (1986). "Kinetics and mechanisms of the gas-phase reactions of the hydroxyl radical with organic compounds under atmospheric conditions." Chemical Reviews 86: 69.

Atkinson, R. (1994). "Gas-phase tropospheric chemistry of organic compounds." Journal of Physical ; Chemical Reference Data Monograph No. 2.

Atkinson, R. (2003). "Kinetics of the gas-phase reactions of OH radicals with alkanes and cycloalkanes." Atmospheric Chemistry and Physics 3: 2233-2307.

Atkinson, R., D. L. Baulch, R. A. Cox, J. N. Crowley, R. F. Hampson, R. G. Hynes, M. E. Jenkin, M. J. Rossi and J. Troe (2004). "Evaluated kinetic and photochemical data for atmospheric chemistry: Volume I - gas phase reactions of Ox, HOx, NOx and SOx species." Atmos. Chem. Phys. 4(6): 1461-1738.

Atkinson, R. and J. N. J. Pitts (1975). "Rate Constants for the Reaction of OH Radicals with Propylene and the Butenes over the Temperature Range 297 - 425 K." Journal of Chemical Physics 63(8): 3591 - 3595.

Baasandorj, M., D. K. Papanastasiou, R. K. Talukdar, A. S. Hasson and J. B. Burkholder (2010). "(CH3)3COOH (tert-butyl hydroperoxide): OH reaction rate coefficients between 206 and 375 K and the OH photolysis quantum yield at 248 nm." Physical Chemistry Chemical Physics 12(38): 12101-12111.

Bloss, W. J., J. D. Lee, C. Bloss, D. E. Heard, M. J. Pilling, K. Wirtz, M. Martin-Reviejo and M. Siese (2004). "Validation of the calibration of a laser-induced fluorescence instrument for the measurement of OH radicals in the atmosphere." Atmospheric Chemistry and Physics 4: 571-583.

Calvert, J. G., R. Atkinson, J. A. Kerr, S. Madronich, G. K. Moortgat, T. J. Wallington and G. Yarwood (2000). The Mechanism of Atmospheric Oxidation of the Alkenes. Oxford, OUP.

Calvert, J. G., R. G. Derwent, J. J. Orlando, G. S. Tyndall and T. J. Wallington (2008). Mechanisms of Atmospheric Oxidation of the Alkanes, Oxford University Press.

Campuzano-Jost, P., M. B. Williams, L. D'Ottone and A. J. Hynes (2004). "Kinetics and mechanism of the reaction of the hydroxyl radical with h(8)-isoprene and d(8)-isoprene: Isoprene absorption cross sections, rate coefficients, and the mechanism of hydroperoxyl radical production." Journal of Physical Chemistry A 108(9): 1537-1551.

Carr, S. A., M. A. Blitz and P. W. Seakins (2011). "Site-Specific Rate Coefficients for Reaction of OH with Ethanol from 298 to 900 K." Journal of Physical Chemistry A 115(15): 3335-3345.

Commane, R., C. F. A. Floquet, T. Ingham, D. Stone, M. J. Evans and D. E. Heard (2010). "Observations of OH and HO2 radicals over West Africa." Atmospheric Chemistry and Physics 10: 8783-8801.

Dusanter, S., D. Vimal and P. S. Stevens (2008). "Technical note: Measuring tropospheric OH and HO2 by laser-induced fluorescence at low pressure. A comparison of calibration techniques." Atmospheric Chemistry and Physics 8(2): 321-340.

Fuchs, H., T. Brauers, H. P. Dorn, H. Harder, R. Haseler, A. Hofzumahaus, F. Holland, Y. Kanaya, Y. Kajii, D. Kubistin, S. Lou, M. Martinez, K. Miyamoto, S. Nishida, M. Rudolf, E. Schlosser, A. Wahner, A. Yoshino and U. Schurath (2010). "Technical Note: Formal blind intercomparison of HO2 measurements in the atmosphere simulation chamber SAPHIR during the HOxComp campaign." Atmospheric Chemistry and Physics 10(24): 12233-12250.

George, L. A., T. M. Hard and R. J. O'Brien (1999). "Measurement of free radicals OH and HO2 in Los Angeles smog." Journal of Geophysical Research-Atmospheres 104(D9): 11643-11655.

Glowacki, D. R., A. Goddard, K. Hemavibool, T. L. Malkin, R. Commane, F. Anderson, W. J. Bloss, D. E. Heard, T. Ingham, M. J. Pilling and P. W. Seakins (2007). "Design of and initial results from a Highly Instrumented Reactor for Atmospheric Chemistry (HIRAC)." Atmospheric Chemistry and Physics 7(20): 5371-5390.

Glowacki, D. R., J. Lockhart, M. A. Blitz, S. J. Klippenstein, M. J. Pilling, S. H. Robertson and P. W. Seakins (2012). "Interception of excited vibrational quantum states by O2 in atmospheric association reactions." Science (Washington, D. C., 1883-) 337: 1066-1067.

Guggenheim, E. A. (1926). "On the determination of the Velocity Constant of a Unimolecular Reaction." Philos. Mag. 2(9): 538-543.

Hard, T. M., L. A. George and R. J. O'Brien (1995). "FAGE Determination of Tropospheric HO and HO2." Journal of the Atmospheric Sciences 52(19): 3354-3372.

Hard, T. M., L. A. George and R. J. O'Brien (2002). "An absolute calibration for gas-phase hydroxyl measurements." Environmental Science & Technology 36(8): 1783-1790.

Heard, D. E. and M. J. Pilling (2003). "Measurement of OH and HO2 in the Troposphere." Chemical Reviews 103: 5163-5198.

IUPAC. (2007). "Evaluated Kinetic Data." from www.iupac-kinetic.ch.cam.ac.uk.

Martinez, M., H. Harder, D. Kubistin, M. Rudolf, H. Bozem, G. Eerdekens, H. Fischer, T. Klupfel, C. Gurk, R. Koenigstedt, U. Parchatka, C. L. Schiller, A. Stickler, J. Williams and J. Lelieveld (2010). "Hydroxyl radicals in the tropical troposphere over the Suriname rainforest: airborne measurements." Atmos. Chem. Phys. 10(8): 3759-3773.

Orkin, V. L., L. E. Martynova and A. N. Ilichev (2010). "High-Accuracy Measurements of OH Reaction Rate Constants and IR Absorption Spectra: CH2=CF-CF3 and trans-CHF=CH-CF3." Journal of Physical Chemistry A 114(19): 5967-5979.

Park, J., C. G. Jongsma, R. Y. Zhang and S. W. North (2004). "OH/OD initiated oxidation of isoprene in the presence of O2 and NO." Journal of Physical Chemistry A 108(48): 10688-10697.

Pilling, M. J. and P. W. Seakins (1995). Reaction Kinetics. Oxford, Oxford University Press.

Sander, S. P., R. R. Friedl, J. P. D. Abbatt, J. Barker, D. M. Golden, C. E. Kolb, M. J. Kurylo, G. K. Moortgat, P. H. Wine, R. E. Huie and V. L. Orkin (2011). Chemical kinetics and photochemical data for use in atmospheric studies - Evaluation 17. Pasadena CA, Jet Propulsion Laboratory. 17.

Schlosser, E., T. Brauers, H. P. Dorn, H. Fuchs, R. Haseler, A. Hofzumahaus, F. Holland, A. Wahner, Y. Kanaya, Y. Kajii, K. Miyamoto, S. Nishida, K. Watanabe, A. Yoshino, D. Kubistin, M. Martinez, M. Rudolf, H. Harder, H. Berresheim, T. Elste, C. Plass-Dulmer, G. Stange and U. Schurath (2009). "Technical Note: Formal blind intercomparison of OH measurements: results from the international campaign HOxComp." Atmospheric Chemistry and Physics 9(20): 7923-7948.

Singh, S. and Z. J. Li (2007). "Kinetics investigation of OH reaction with isoprene at 240-340 K and 1-3 Torr using the relative rate/discharge flow/mass spectrometry technique." Journal of Physical Chemistry A 111(46): 11843-11851.

Stone, D. and D. M. Rowley (2005). "Kinetics of the gas phase HO2 self-reaction: Effects of temperature, pressure, water and methanol vapours." Phys. Chem. Chem. Phys. 7: 2156 - 2163.

Chapter 7. OH yield measurements from the reaction of acetylperoxy and HO_2 radicals

7.1 Introduction

Organic peroxy radicals, RO_2, play a key role in the tropospheric HOx (OH and HO_2) cycle (see chapter 1). The reaction of OH with VOCs produces RO_2 radicals which have two main destruction pathways: (i) reaction with NO and (ii) reaction with HO_2 or other RO_2 radicals. In areas where reaction with NO dominates RO_2 loss (typically when [NO] > 2×10^{10} molecule cm^{-3}), RO_2 radicals rapidly react with NO forming NO_2 and recycling OH (R 1.5 - R 1.7), through the creation and destruction of HO_2. NO_2 is extremely important in tropospheric chemistry as it is the only known source of O_3 *via* photolysis, a primary component in photochemical smog.

$$RO_2 + NO \rightarrow RO + NO_2 \qquad \text{R 7.1}$$

$$RO + O_2 \rightarrow R'R''CO + HO_2 \qquad \text{R 7.2}$$

$$HO_2 + NO \rightarrow OH + NO_2 \qquad \text{R 7.3}$$

However, in low NOx environments (e.g., remote forested areas) loss of RO_2 is dominated by reaction with other RO_2 and HO_2 radicals (R 7.4a-c); these have previously been considered as important radical termination processes (Lightfoot et al., 1992; Tyndall et al., 2001) with several possible products depending on the structure of the R group. For small alkylperoxy radicals such as methylperoxy (oxidation product of methane), reaction with HO_2 predominantly produces CH_3OOH through R 7.4a. This process is considered a radical sink in the atmosphere, as a fraction of the water soluble peroxide is lost before radicals are regenerated by photolysis. Organic peroxides (ROOH) can be used as an indication of the oxidative capacity of the troposphere (Phillips et al., 2013) and uptake onto aqueous aerosol may influence S(IV) to S(VI) conversion (Lee et al., 2000).

$$HO_2 + RO_2 \rightarrow ROOH + O_2 \qquad \text{R 7.4a}$$

$$\rightarrow ROH + O_3 \qquad \text{R 7.4b}$$

$$\rightarrow OH + RO + O_2 \qquad \text{R 7.4c}$$

However, more recent research has shown that radical termination may not be the exclusive reaction pathway for certain RO_2 radicals. Hasson et al. (2004) observed, using chamber studies and measuring stable products, that certain peroxy radical + HO_2 reactions (R 7.5a-c), such as the title reaction of acetylperoxy, $CH_3C(O)O_2$, can lead to the formation of OH radicals through a third channel (R 7.5c). Previous studies had

assumed radical termination through channels R 7.5a ($\alpha_{R\ 7.5a} = k_a/k = 0.8$) and b ($\alpha_{R\ 7.5_b} = k_b/k = 0.2$) (Moortgat et al., 1989; Lightfoot et al., 1992; Crawford et al., 1999), however an underestimated IR cross-section for peracetic acid, $CH_3C(O)OOH$ (R 7.5a), had led to the assignment of $\alpha_{(R\ 7.5a)}$ three times too high. Hasson et al. (2004) measured yields of (0.40 ± 0.16) : (0.20 ± 0.08) : (0.40 ± 0.16) for $\alpha_{R\ 7.5a}$: $\alpha_{R\ 7.5b}$: $\alpha_{R\ 7.5c}$, but for the equivalent reactions of the alkylperoxy radical, $C_2H_5O_2$, with HO_2 only channel (R 7.5a) producing $C_2H_5OOH + O_2$ was observed. Clearly the nature of the peroxy radical influences the branching ratio (Orlando and Tyndall, 2012).

$$CH_3C(O)O_2 + HO_2 \rightarrow CH_3C(O)OOH + O_2 \quad \text{R 7.5a}$$
$$\rightarrow CH_3C(O)OH + O_3 \quad \text{R 7.5b}$$
$$\rightarrow CH_3C(O)O + OH + O_2 \quad \text{R 7.5c}$$

Acetylperoxy radicals are of particular importance to tropospheric chemistry as they are formed from the oxidation and photolysis of several important VOCs. In high NOx environments, acetylperoxy leads to the formation of peroxyacetyl nitrate (PAN), a key contributor to long range NOx transport (Wayne, 1991). They are also a product of the OH initiated oxidation of methyl-vinyl ketone (Tuazon and Atkinson, 1989) which is a low NOx oxidation product of isoprene (C_5H_8). Isoprene is the most abundant VOC in certain forests and has been linked to an unexplainably high [OH] concentration in field campaigns (Lelieveld et al., 2008; Hofzumahaus et al., 2009; Lou et al., 2009; Pugh et al., 2010; Whalley et al., 2011; Stone et al., 2012).

Most OH measurements have been made using the fluorescence assay by gaseous expansion (FAGE) technique (Heard and Pilling, 2003) and uncertainties associated with the FAGE technique may account for a fraction of the discrepancy (Fuchs et al., 2011; Mao et al., 2012). However, a recent study in this laboratory has shown that instruments with a short residence time between sampling and probing should have very low interferences on the OH measurement channel (Whalley et al., 2013).

A number of mechanisms have also been postulated to explain the observed OH concentrations under low NOx conditions including the formation and subsequent photolysis of hydroperoxy-aldehyde (HPALD) species (Peeters et al., 2009; Peeters and Muller, 2010; Taraborrelli et al., 2012; Wolfe et al., 2012) and epoxides (Paulot et al., 2009). The OH yield from substituted $RO_2 + HO_2$ reactions has been put forward as a potential explanation for the shortfall in the [OH] prediction under these conditions

(Lelieveld et al., 2008; Taraborrelli et al., 2009; Taraborrelli et al., 2012) although at best it merely conserves total HOx concentrations. Stone et al. (2012) have shown that further amplification of OH in the isoprene mechanism is needed and recycling of OH through $RO_2 + HO_2$ chemistry is valid only in certain environments.

A number of studies on the title reaction have taken place with contradictory results and the temperature and pressure dependence of reaction R 7.5a-c has yet to be fully investigated. Le Crâne et al. (2006) reported real time measurements on reaction R 7.5a-c; flash photolysis of Cl_2 in the presence of $CH_3OH/CH_3CHO/O_2$ rapidly led to the formation of HO_2 and $CH_3C(O)O_2$ (see Experimental section 7.2 for details) with peroxy radicals being monitored on a millisecond timescale *via* UV absorption. OH in the system was indirectly identified through reaction with excess benzene where the formation of the C_6H_6OH radical was followed by a characteristic absorption at 290 nm. An upper limit of 0.1 for channel R 7.5c was reported. Jenkin et al. (2007) used a similar benzene radical trapping method to determine the branching ratio of R 7.5c, using FTIR analysis in a chamber study to measure a range of stable products including phenol from the trapping of OH with benzene. The results of Jenkin et al. (2007) are in excellent agreement with Hasson et al. (2004) reporting $\alpha_{R\ 7.5a}$: $\alpha_{R\ 7.5b}$: $\alpha_{R\ 7.5c}$ of $(0.38 \pm 0.13) : (0.12 \pm 0.04) : (0.43 \pm 0.10)$. Jenkin et al. (2007) highlighted several shortcomings of the Le Crâne et al. (2006) study, citing over-estimation of the stability of the C_6H_6OH radical as a possible reason for the assignment of a low yield for R 7.5c. After re-evaluating the data, Jenkin et al. (2007) showed that a chemical simulation with $\alpha_{R\ 7.5c} = 0.4$ was also a good fit to the observations of Le Crâne et al. (2006).

The first direct observation of OH from R 7.5c was made by Dillon and Crowley (2008) using calibrated laser induced fluorescence (LIF). They performed real time studies generating HO_2 and $CH_3C(O)O_2$ in a similar manner to Le Crâne et al. (2006), although flash photolysis of Cl_2 was performed by an excimer laser at 351 nm rather than a flash lamp. The study confirmed a significant OH yield of between 0.45 and 0.60 in experiments covering a range of pressures (100 – 700 mbar) at 298 K. No systematic variation was observed in the OH yield. Dillon and Crowley (2008) were also able to constrain the uncertainty on the overall rate coefficient for reaction R 7.5 to $k_{298} = (1.4 \pm 0.5) \times 10^{-11}$ cm^3 molecule^{-1} s^{-1}.

Two theoretical investigations into the reaction of acetylperoxy with HO_2 exist in the literature. First, Hasson et al. (2005) conducted theoretical calculations on the reaction potential energy surface (PES) using CBS-QB3 at the B3LYP/6-311G(2d,d,p) level. The reaction was shown as proceeding either *via* a triplet surface to $CH_3C(O)OOH + O_2$ (R 7.5a) or a singlet surface forming a hydrotetroxide intermediate which can decompose to form either $OH + CH_3C(O)O + O_2$ (R 7.5c) *via* HO_3 formation or $CH_3C(O)OH + O_3$ (R 7.5b) through hydrogen exchange. Further master equation calculations predicted that the R 7.5c channel was considerably less exothermic than the R 7.5b channel (−8.79 and −113.9 kJ mol^{-1} respectively). However, an amount of chemical activation of the initially formed HO_2-acetyl peroxy adduct combined with a higher entropy loose transition state, allowed for the experimentally observed results at 298 K and 1 atm to be rationalised. Secondly, in addition to experimental results, Le Crâne et al. (2006) constructed a similar PES using Density Functional Theory (DFT) at the B3LYP/6-31G(d,p) level. The small exothermicity of the R 7.5c channel (−12.98 kJ mol^{-1}) compared to the R 7.5b channel (−82.9 kJ mol^{-1}) was cited as the dominating factor in the experimentally low OH yields reported. It should be noted that the exothermicities of products, intermediates and transition states from two studies are not in agreement and the complex reaction dynamics require further study.

In a recent collaboration between the Max Planck Institut, Mainz, and the University of Leeds (with Dr. Terry Dillon and Christoph Gross under the Transnational Access program for EUROCHAMP2 (EUROCHAMP)), the reaction of $CH_3C(O)O_2 + HO_2$ (R 7.5a-c) was studied further. Reported here are the results from the first experiments, under ambient conditions, to simultaneously directly detect end-products from reaction R 7.5, using FTIR and an O_3 analyser for stable products from R 7.5a and b, and FAGE for OH radical detection from R 7.5c. This study combined the advantages of the previous chamber studies by Hasson et al. (2004) and Jenkin et al. (2007) and the direct OH detection experiments of Dillon and Crowley (2008).

7.2 Experimental

7.2.1 Chamber and instrumentation

Experiments were performed in the HIRAC chamber at 1000 mbar total pressure of a synthetic air mixture (4:1, N_2:O_2, Zero Grade BOC) at a constant temperature (293 ± 2 K). Details on HIRAC and the instrumentation are given in chapters 2 and 4, hence only a brief description and relevant operational conditions will be discussed here.

Acetic acid, $CH_3C(O)OH$, peracetic acid, $CH_3C(O)OOH$, formaldehyde, HCHO, and formic acid, HCOOH, along with chemical precursors acetaldehyde, CH_3CHO, and methanol, CH_3OH, were detected using FTIR. Inside HIRAC the multipass modified Chernin cell was optimised for 72 internal reflections giving an approximate path length of 144 m. Sample IR spectra were recorded as the average of 100 scans (~70 s per sample) at 0.5 cm^{-1} resolution. Reference spectra were taken of the pure compounds in the HIRAC chamber. Analysis of sample FTIR spectra was conducted mainly in the carbonyl region of the spectrum using the Quant2 iterative non-linear least squares fitting program. Example spectra and the development Quant 2 are shown in chapter 3. The carbonyl region was chosen as it was selective to the reactants and main products studied here. Methanol was measured at ~2000 cm^{-1} where the $2\nu_8$ overtone was observed, due to saturation of the fundamental absorptions at the high starting concentrations used. Examples of the FTIR analysis process for the methanol and carbonyl containing species are shown in chapter 3, along with example spectra.

Ozone concentrations were measured using a UV photometric O_3 analyser (TEC Model 49C, d.l. = 1.0 ppb) which operated over a 550 – 1000 mbar pressure range. A trace level chemiluminescence NO_x analyser (TEC Model 42C, d.l. = 50 pptv) was used to confirm that NOx (=NO + NO_2) were characteristically below the detection level of the apparatus during experiments.

The FAGE instrument coupled to HIRAC, was used to detect OH and HO_2 radicals for these experiments, using the 1.0 mm pinhole and pulsed Nd:YAG (JDSU Q201-HD) pumped dye laser (SIRAH Cobra) operating at 5 kHz pulse repetition frequency as described in chapter 2. The laser power (λ = 308 nm) entering each fluorescence cell

was typically 7 - 10 and 3 - 5 mW for the OH and HO_2 cells, respectively. FAGE was calibrated using the H_2O vapour photolysis method outlined in chapter 5.

7.2.2 Chemicals, sample preparation and gas handling

Liquid samples of CH_3OH (> 99.93%, Sigma Aldrich), HCOOH (> 98%, Sigma Aldrich), $CH_3C(O)OH$ (> 99%, Sigma Aldrich), $CH_3C(O)OOH$ (40% in acetic acid, Sigma Aldrich) were injected into the synthetic air filled HIRAC chamber directly using 100 (±5) and 10 (±0.5) µl syringes. Gas samples of CH_3CHO (> 99.5%, Sigma Aldrich), Cl_2 (99.9%, Gas Products Ltd.) and HCHO were expanded into the stainless steel delivery vessel before being flushed into HIRAC using high purity N_2, as described in chapter 2. Formaldehyde was prepared for gas delivery upon heating para-formaldehyde (99%, Sigma Aldrich). All species were purified through several freeze-pump-thaw cycles using liquid nitrogen before injection. Reactants were introduced into the chamber individually, allowing ~90 s mixing time before stability was confirmed by 5 - 10 FTIR measurement spectra and the photolysis lamps were turned on.

7.2.3 Radical generation and experimental process

Acetylperoxy and HO_2 radicals were generated through the chlorine initiated oxidation of CH_3CHO and CH_3OH respectively. Molecular chlorine was photolysed using black lamps *in situ* (Phillips, TL-D 36W/BLB, λ = 350 - 400 nm, chapter 2 for action spectrum):

$$Cl_2 + h\nu \rightarrow 2Cl \quad \text{R 7.6}$$

$$Cl + CH_3OH \rightarrow CH_2OH + HCl \quad \text{R 7.7}$$

$$CH_2OH + O_2 \rightarrow HCHO + HO_2 \quad \text{R 7.8}$$

$$Cl + CH_3CHO \rightarrow CH_3CO + HCl \quad \text{R 7.9}$$

$$CH_3CO + O_2\ (+M) \rightarrow CH_3C(O)O_2\ (+M) \quad \text{R 7.10}$$

The rate coefficients for the Cl atom reactions are well established (Seakins et al., 2004; Atkinson et al., 2008) and hence by varying the initial ratio of $[CH_3OH]_0$:$[CH_3CHO]_0$ it was possible to control the radical starting ratio of HO_2:$CH_3C(O)O_2$ (detailed in results section). The CH_3OH was kept in excess (~4:1) to make sure HO_2 was produced in excess, whilst preserving the lifetime of the CH_3CHO.

Experiments were conducted over a ~600 s time period to ensuring that measurements were taken during the initial stages of the reaction where $\Delta[CH_3CHO] < 50\%$. During this time, Cl atom concentrations were controlled by CH_3OH and CH_3CHO rather than reacting with products from reaction R 7.5.

Control experiments were conducted to characterise losses of products and reactants to the walls of the chamber and by photolysis. Samples were injected into the chamber at concentrations up to ~5×10^{13} molecule cm^{-3} in synthetic air and were monitored continuously by FTIR and FAGE through several lamps-on, lamps-off photolysis cycles with 2, 4 and 8 black lamps. Negligible decay due to photolysis was seen for any species. Trace levels of HO_2 (~10^8 molecule cm^{-3}) were observed upon illumination of HCHO with all 8 lamps, suggesting photolysis, however no decay was observed in the FTIR data over ~30 minutes. The black lamps were chosen as the emission spectrum falls outside of the UV absorption spectra of the majority of products and reactants used, whilst having a significant overlap with that of Cl_2. Appreciable wall loss was observed for the organic acids (~10^{-4} s^{-1}) and these were characterised and incorporated into the chemical model reaction scheme used (section 7.2.4).

Finally, a control reaction using a $Cl_2/CH_3OH/C_2H_6$ mixture was conducted, based on experiments by Hasson et al. (2004). From reaction with Cl in the presence of O_2, C_2H_6 formed the ethyl peroxy radical, $C_2H_5O_2$ (R 7.11 + R 7.12), for which reaction with HO_2 has been reported as a radical terminating step in the literature (IUPAC, 2007; Sander et al., 2011), forming ethyl hydrogen peroxide, C_2H_5OOH (R 7.13):

$$Cl + C_2H_6 \rightarrow C_2H_5 + HCl \qquad \text{R 7.11}$$

$$C_2H_5 + O_2 (+M) \rightarrow C_2H_5O_2 (+M) \qquad \text{R 7.12}$$

$$C_2H_5O_2 + HO_2 \rightarrow C_2H_5OOH + O_2 \qquad \text{R 7.13}$$

7.2.4 Chemical model

Numerical simulation of the system was necessary to gain quantitative information about $\alpha_{(R\ 7.5c)}$ as product yield analysis (Δ[product] as a function of Δ[reactant]) was not possible due to other $CH_3C(O)O_2$ radical removal reactions (e.g., through self-reaction) other than through reaction with HO_2. Additionally, the CH_3CHO precursor is not removed uniquely *via* reaction with Cl (R 7.9), but also reacts with OH and HO_2 present in the system, the latter forming $CH_3CH(OH)O_2$ in equilibrium (R 3.1). A similar reaction is also possible between HO_2 and HCHO, forming $HOCH_2O_2$:

$$CH_3CHO + HO_2 \leftrightarrow CH_3CH(OH)O_2 \qquad \text{R 7.14}$$

$$HCHO + HO_2 \leftrightarrow HOCH_2O_2 \qquad \text{R 7.15}$$

Chemical simulations were conducted using the Kintecus numerical integrator package (Ianni, 2002). The comprehensive model mechanism, displayed in Table 7.1, was constructed from reactions defined in the chamber studies by Hasson et al. (2004) and Jenkin et al. (2007), with updated rate constants where available from IUPAC and JPL (IUPAC, 2006; Sander et al., 2011). As $j(NO_2)$ had not yet been characterised using for the TL-D 36W/BLB lamps, $j(Cl_2)$ was determined for each experimental data set by fitting the model to the measured decay of the CH_3CHO and CH_3OH. The average determined $j(Cl_2)$ across all runs with 2 lamps was calculated at $\sim(1.7 \pm 1.0) \times 10^{-4}\ s^{-1}$. Simulated ratios $\alpha_{R\ 7.5a}:\alpha_{R\ 7.5b}:\alpha_{R\ 7.5c}$ were adjusted to optimise correlation with the experimentally determined products from R 7.5, backed up with an extensive rate of production and destruction analysis (ROPA/RODA), conducted by S. C. Orr. However, this work is still in progress and will be the subject of a further publication. As such, only the preliminary ROPA are given here.

Reaction	Branching Ratio	Rate Coefficient	
Chlorine Initiation			
$Cl_2 + h\nu \rightarrow 2Cl$		Varied. See text.	
$Cl + CH_3CHO\ (+O_2) \rightarrow CH_3C(O)O_2 + HCl$		8.0×10^{-11}	
$Cl + CH_3OH\ (+O_2) \rightarrow HCHO + HO_2 + HCl$		5.5×10^{-11}	
$Cl + HCHO\ (+O_2) \rightarrow CO + HO_2 + HCl$		$8.1 \times 10^{-11} \exp(-34/T)$	
Cl reactions			
$Cl + CH_3C(O)OOH \rightarrow CH_3C(O)O_2 + HCl$		4.5×10^{-15}	(a)
$Cl + CH_3C(O)OH\ (+O_2) \rightarrow CH_3O_2 + CO_2 + HCl$		2.65×10^{-14}	
$Cl + H_2O_2 \rightarrow HO_2 + HCl$		$1.1 \times 10^{-11} \exp(-980/T)$	
$Cl + CH_3OOH \rightarrow HCHO + OH + HCl$		5.9×10^{-11}	
$Cl + HCOOH\ (+O_2) \rightarrow CO_2 + HO_2 + HCl$		1.9×10^{-13}	
$Cl + HOCH_2OOH \rightarrow HCOOH + OH + HCl$		1.0×10^{-10}	(b)
$Cl + HOCH_2OH\ (+O_2) \rightarrow HCOOH + HO_2 + HCl$		1.0×10^{-10}	(b)
$Cl + CH_3CH(OH)OOH \rightarrow CH_3C(O)OH + OH + HCl$		1.0×10^{-10}	(b)
$Cl + CH_3CH(OH)_2\ (+O_2) \rightarrow CH_3C(O)OH + HO_2 + HCl$		1.0×10^{-10}	(b)
$Cl + O_3 \rightarrow ClO + O_2$		$2.8 \times 10^{-11} \exp(-250/T)$	
$ClO + HO_2 \rightarrow HOCl + O_2$		$2.2 \times 10^{-12} \exp(340/T)$	
$Cl + HO_2 \rightarrow HCl + O_2$	0.80	4.4×10^{-11}	
$\rightarrow ClO + OH$	0.20		
OH Reactions			
$OH + HO_2 \rightarrow H_2O + O_2$		$4.8 \times 10^{-11} \exp(250/T)$	
$OH + CH_3C(O)OH \rightarrow CH_3O_2 + CO_2 + H_2O$		$4.2 \times 10^{-14} \exp(855/T)$	
$OH + CH_3C(O)OOH \rightarrow CH_3C(O)O_2 + H_2O$		3.6×10^{-12}	(c)
$OH + H_2O_2 \rightarrow HO_2 + H_2O$		$2.9 \times 10^{-12} \exp(-160/T)$	
$OH + CH_3OOH \rightarrow CH_3O_2 + HO_2$	0.65	$2.9 \times 10^{-12} \exp(190/T)$	
$\rightarrow HCHO + OH + H_2O$	0.35		
$OH + HCOOH\ (+O_2) \rightarrow CO_2 + HO_2 + H_2O$		4.5×10^{-13}	
$OH + HOCH_2OOH \rightarrow HOCH_2O_2 + H_2O$	0.12	3.1×10^{-11}	(d)
$\rightarrow HCOOH + OH + H_2O$	0.88		
$OH + HOCH_2OH\ (+O_2) \rightarrow HCOOH + OH + H_2O$		1.1×10^{-11}	(d)
$OH + CH_3CH(OH)OOH \rightarrow CH_3C(O)OH + OH + H_2O$		6.0×10^{-11}	(d)
$OH + CH_3CH(OH)_2\ (+O_2) \rightarrow CH_3C(O)OH + HO_2 + H_2O$		2.4×10^{-11}	(d)
$OH + Cl_2 \rightarrow Cl + HOCl$		$3.6 \times 10^{-12} \exp(-1200/T)$	(a)
$OH + CO \rightarrow CO_2 + HO_2$		1.44×10^{-13} + 3.43×10^{-33} [M]	
$OH + HCl \rightarrow Cl + H_2O$		$1.7 \times 10^{-12} \exp(-230/T)$	(a)
$OH + O_3 \rightarrow HO_2 + O_2$		$1.7 \times 10^{-12} \exp(-940/T)$	
$OH + CH_3CHO \rightarrow CH_3C(O)O_2 + H_2O$		$4.4 \times 10^{-12} \exp(365/T)$	
$OH + CH_3OH \rightarrow HCHO + HO_2 + H_2O$		$2.85 \times 10^{-12} \exp(-345/T)$	
$OH + HCHO \rightarrow CO + HO_2 + H_2O$		$5.4 \times 10^{-12} \exp(135/T)$	
HO_2 Reactions			
$HO_2 + O_3 \rightarrow OH + O_2$		$2.03 \times 10^{-16} \times (T/300)^{4.57} \exp(693/T)$	
$HO_2 + CH_3CHO \rightarrow CH_3CH(OH)O_2$		4.4×10^{-14}	(e)
$CH_3CH(OH)O_2 \rightarrow HO_2 + CH_3CHO$		$2.3 \times 10^{13} \exp(-6925/T)$	(e)
$HO_2 + HCHO \rightarrow HOCH_2O_2$		$9.7 \times 10^{-15} \exp(625/T)$	
$HOCH_2O_2 \rightarrow HO_2 + HCHO$		$2.4 \times 10^{12} \exp(-7000/T)$	

HO_2 + RO_2 Reactions			
$HO_2 + HO_2 \rightarrow H_2O_2 + O_2$		$2.2 \times 10^{-15} \exp(600/T) + 1.9 \times 10^{-33}[M]\exp(980/T)$	
$CH_3C(O)O_2 + HO_2 \rightarrow CH_3C(O)OOH + O_2$		$5.2 \times 10^{-13} \exp(980/T)$	
$\rightarrow CH3C(O)OH + O_3$		(see text for branching)	
$(+O_2) \rightarrow CH_3O_2 + CO_2 + OH + O_2$			
$CH_3O_2 + HO_2 \rightarrow CH_3OOH + O_2$	0.90	$3.8 \times 10^{-13} \exp(780/T)$	
$\rightarrow HCHO + H_2O + O_2$	0.10		
$HOCH_2O_2 + HO_2 \rightarrow HOCH_2OOH + O_2$	0.50	$5.6 \times 10^{-15} \exp(2300/T)$	
$\rightarrow HCOOH + H_2O + O_2$	0.30		
$(+O_2) \rightarrow HCOOH+HO2+OH+O2$	0.20		
$CH_3CH(OH)O_2 + HO_2 \rightarrow CH_3CH(OH)OOH + O_2$	0.50	$5.6 \times 10^{-15} \exp(2300/T)$	(f)
$\rightarrow CH_3C(O)OH + H_2O + O_2$	0.30		
$(+O_2) \rightarrow HCOOH + CH_3O_2 + OH + O_2$	0.20		
RO_2 Self-Reactions			
$2CH_3C(O)O_2 (+O_2) \rightarrow 2CH_3O_2 + O_2 + CO_2$		$2.9 \times 10^{-12} \exp(500/T)$	
$2CH_3O_2 \rightarrow HCHO + CH_3OH + O_2$	0.63	$1.03 \times 10^{-13} \exp(365/T)$	
$(+2O_2) \rightarrow 2HCHO + 2HO_2 + O_2$	0.37		
$2HOCH_2O_2 \rightarrow HCOOH + HOCH_2OH + O_2$	0.12	5.7×10^{-12}	
$(+2O_2) \rightarrow 2HCOOH + 2HO_2 + O_2$	0.88		
$2CH_3CH(OH)O_2 \rightarrow CH_3C(O)OH + CH_3CH(OH)_2 + O_2$	0.12	5.7×10^{-12}	(f)
$(+2O_2) \rightarrow 2HCOOH + 2CH_3O_2 + O_2$	0.88		
RO_2 + RO_2 reactions			
$CH_3C(O)O_2 + CH_3O_2 \rightarrow CH_3C(O)OH + HCHO + O_2$	0.10	$2.0 \times 10^{-12} \exp(500/T)$	
$(+2O_2) \rightarrow CH_3O_2 + CO_2 + HCHO + HO_2 + O_2$	0.90		
$CH_3C(O)O_2 + HOCH_2O_2 \rightarrow CH_3C(O)OH + HCOOH + O_2$	0.10	$2.0 \times 10^{-12} \exp(500/T)$	(g)
$(+2O_2) \rightarrow CH_3O_2 + CO_2 + HCOOH + HO_2 + O_2$	0.90		
$CH_3C(O)O_2 + CH_3CH(OH)O_2 \rightarrow 2CH_3C(O)OH + O_2$	0.90	$2.0 \times 10^{-12} \exp(500/T)$	(g)
$(+2O_2) \rightarrow CH_3O_2 + CO_2 + HCOOH + CH_3O_2 + O_2$	0.10		
$CH_3O_2 + HOCH_2O_2 \rightarrow HCHO + HOCH2OH + O_2$	0.19	1.4×10^{-12}	(h)
$\rightarrow CH_3OH + HCOOH + O_2$	0.19		
$(+2O_2) \rightarrow HCHO + HCOOH + 2HO_2 + O_2$	0.62		
$CH_3O_2 + CH_3CH(OH)O_2 \rightarrow HCHO + CH_3CH(OH)_2 + O_2$	0.19	1.4×10^{-12}	(h)
$\rightarrow CH_3OH + CH_3C(O)OH + O_2$	0.19		
$(+2O_2) \rightarrow HCHO + HO_2 + HCOOH + CH_3O_2 + O_2$	0.62		
$HOCH_2O_2 + CH_3CH(OH)O_2 \rightarrow HCOOH + CH_3CH(OH)_2 + O_2$	0.06	5.7×10^{-12}	(h)
$\rightarrow HOCH2OH + CH_3C(O)OH + O_2$	0.06		
$(+2O_2) \rightarrow HCOOH + HO_2 + HCOOH + CH_3O_2 + O_2$	0.88		

Table 7.1: Reaction scheme used in the determination of branching ratios for the reaction of $CH_3C(O)O_2$ with HO_2. RO radical decomposition and reaction with O_2 are assumed instantaneous, indicated by $(+O_2)$ where appropriate. Rate coefficients sourced from IUPAC recommended values unless otherwise stated, all quoted in units = molecule^{-1} cm^3 s^{-1}. (Atkinson et al., 2004). (a) from Crawford et al. (1999); (b) Estimations from Jenkin et al. (2007), based on reactivity of Cl with other species containing -OOH, -OH, -CHO functional groups; (c) From Jenkin et al. (2007), estimation based on the reactivity of -OOH in CH_3OOH; (d) Taken from Jenkin et al. (2007), estimated based on SAR by Kwok and Atkinson (1995) and Saunders et al. (2003) ;(e) from Tomas et al. (2001); (f) Estimations from Jenkin et al. (2007), based on analogous reaction for similar α-hydroxy peroxy radicals; (g) Estimations from Jenkin et al. (2007), assumed equivalent to $CH_3C(O)O_2 + CH_3O_2$; (h)

Estimations from Jenkin et al. (2007), based on the geometric mean of self-reaction rate coefficients and branching ratios of participating peroxy radicals.

7.3 Results and Discussion

Presented here are the first experiments covering the reaction of $CH_3C(O)O_2$ with HO_2 (R 7.5) where products from all three branching pathways have been detected both directly and simultaneously. The branching ratios were studied at 1000 mbar and (293 ± 2) K (section 7.3.2) and the sensitivity of the experimental yields of R 7.5a, b and c to $[CH_3OH]_0$:$[CH_3CHO]_0$ and Cl_2 photolysis rate were investigated (sections 7.3.2.3 and 7.3.2.2). The chemical model was also thoroughly tested, examining the sensitivity of the predicted concentrations to uncertainties in the model and total $k_{R\ 7.5}$ (section 7.3.2.1). Discussed first is the control experiment conducted into the ethylperoxy + HO_2 reaction where no OH should be directly produced. Unless explicitly mentioned in the text, please refer to the chemical model listed in Table 7.1 for branching ratios for reactions with multiple pathways.

7.3.1 Reaction of $C_2H_5O_2$ with HO_2

The reaction of ethylperoxy with HO_2 was investigated at 1000 mbar of synthetic air and 293 K in a $Cl_2/CH_3OH/C_2H_6$ mixture where $[Cl_2] = 7.14 \times 10^{14}$ molecule cm^{-3}, $[CH_3OH] = 3.12 \times 10^{14}$ molecule cm^{-3} and $[C_2H_6] = 1.14 \times 10^{14}$ molecule cm^{-3}. The $[CH_3OH]_0$:$[C_2H_6]_0$ was maintained at 3.0. The decays of C_2H_6 and CH_3OH were monitored using FTIR and are shown in Figure 7.1. While $[CH_3OH]$ was analysed as described in section 7.2.1 using the Quant NLLSQ fitting software (see chapter 3), $[C_2H_6]$ was determined by manual subtraction. Figure 7.2a and b show the spectrum acquired before and after irradiation respectively, between 700 - 900 cm^{-1}. The resolved features are due to C_2H_6 and can be subtracted with some success. Figure 7.2c is the residual spectrum of the subtraction of (a) from (b), where (a) has been multiplied by a 0.63 scaling factor, equating to 7.18×10^{13} molecule cm^{-3}. The residual spectrum clearly shows the presence of unknown species which was qualitatively assigned to C_2H_5OOH identified from the investigation by Spittler et al. (2000) into the $C_2H_5O_2$ + HO_2 reaction

(R 7.13). Due to the lack of reference spectrum for C_2H_5OOH, no product yields for this species were calculated here.

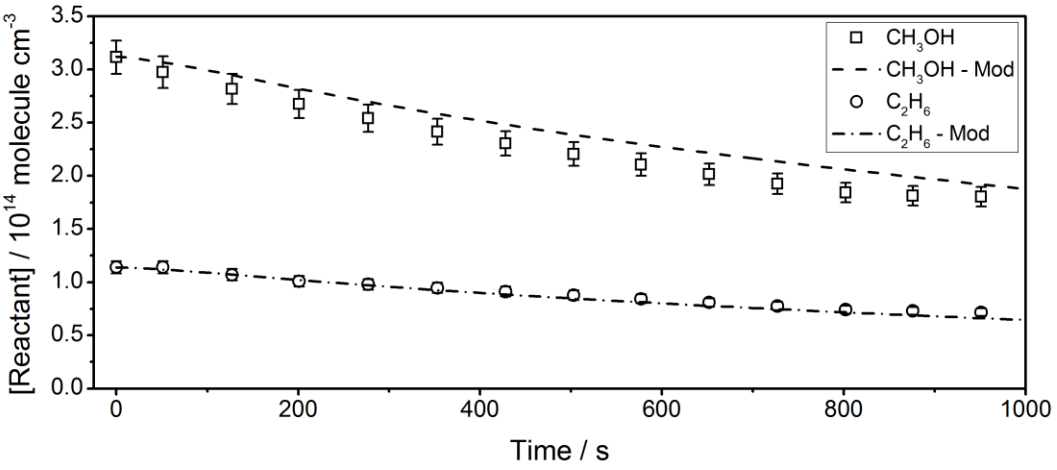

Figure 7.1: Decay of CH_3OH and C_2H_6 reactants due to primary reaction with Cl atoms in the HO_2 + $C_2H_5O_2$ reaction conducted in the HIRAC chamber at 1000 mbar and 293 K. $[Cl_2]_0 = 7.14\times 10^{14}$ molecule cm^{-3}, $[CH_3OH]_0 = 3.12\times 10^{14}$ molecule cm^{-3} and $[C_2H_6]_0 = 1.14 \times 10^{14}$ molecule cm^{-3}. Modelled concentrations determined *via* automated fitting of comprehensive mechanism in Table 7.1 to data using Kintecus (see section 7.2.4 for details).

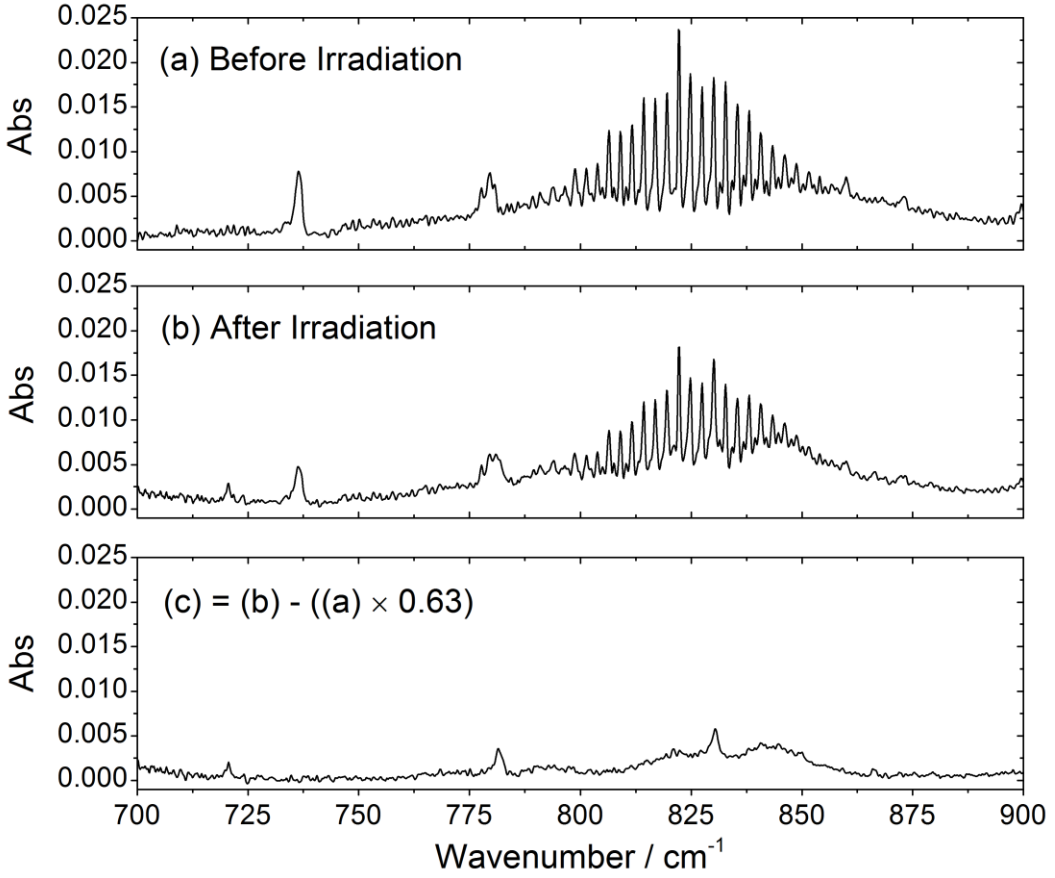

Figure 7.2: IR spectra taken (a) before photolysis lamps initiated photochemistry, (b) after ~900 s irradiation during the investigation into the HO_2 + $C_2H_5O_2$ reaction at 1000 mbar and 293 K. (c) shows the residual from subtraction of spectrum (a) due to C_2H_6 from (b). Spectral features in (c) were compared to the spectrum shown in Spittler et al. (2000) and qualitatively

assigned to C_2H_5OOH.

Profiles for OH (a), HO_2 (b), $CH_3C(O)OH$ (c), O_3 (d), CH_3CHO (e) and HCHO (f) are displayed in Figure 7.3. Profiles of HCHO and HO_2 indicate that oxidation of CH_3OH by Cl was efficient enough to produce high [HO_2] for the reaction. Trace levels of CH_3CHO were observed at later times, created predominantly from the Cl atom initiated oxidation of C_2H_5OOH (R 7.16), leading to the production of $CH_3C(O)OOH$, O_3 and $CH_3C(O)OH$ through HO_2 + $CH_3C(O)O_2$ (R 7.9 - R 7.10 and R 7.5). Unfortunately, reaction R 7.16 has been reported with a very large rate coefficient, $k_{R\,7.16} = 1.04 \times 10^{-10}$ cm^3 $molecule^{-1}$ s^{-1} (Wallington et al., 1989), and so there was an appreciable increase in OH at early times (Figure 7.3a) making the experiment unsuitable for a purely experimental data driven control reaction in HIRAC.

$$Cl + C_2H_5OOH \rightarrow CH_3CHO + OH + HCl \qquad \text{R 7.16}$$

A chemical model for the system was created, built on the mechanism employed in section 7.3.2 with supplementary reactions for the Cl initiated oxidation of C_2H_6, which are listed in Table 7.2. The model was constrained to the decay in C_2H_6 and CH_3OH, calculating $j(Cl_2)$ (as described in section 7.2.4) and is compared to the experimental data in Figure 7.1 and Figure 7.3 (Mod - (a)). Good agreement between measured and modelled reactants was observed over the ~1000 s reaction period (Figure 7.1). Predicted profiles for HO_2 and HCHO were in reasonable agreement with experimental data (Figure 7.3b and f), showing that the oxidation of CH_3OH was well described by the model. Products driven by the oxidation of C_2H_5OOH (R 7.16), however, were over-predicted by the chemical model (Figure 7.3a, c, d and e).

As no quantitative evaluation of C_2H_5OOH was completed; it was not possible to draw firm conclusions as to the nature of the over-prediction. Clearly further analysis of this dataset is required and the reproducibility needs to be tested, however some points can be made. The modelled OH, CH_3CHO and oxidation products thereof, were found to be sensitive to changes in the rate constant for Cl + C_2H_5OOH and $j(Cl_2)$. The decay in the reactants, whilst also dependent on $j(Cl_2)$, were found to be relatively insensitive and hence misassignment of [C_2H_6] or [CH_3OH] could be responsible for an inaccurate determination of $j(Cl_2)$ through the Kintecus fitting procedure. Repeat investigations into HO_2 + $C_2H_5O_2$ under similar conditions would highlight any random uncertainties associated with the measurements.

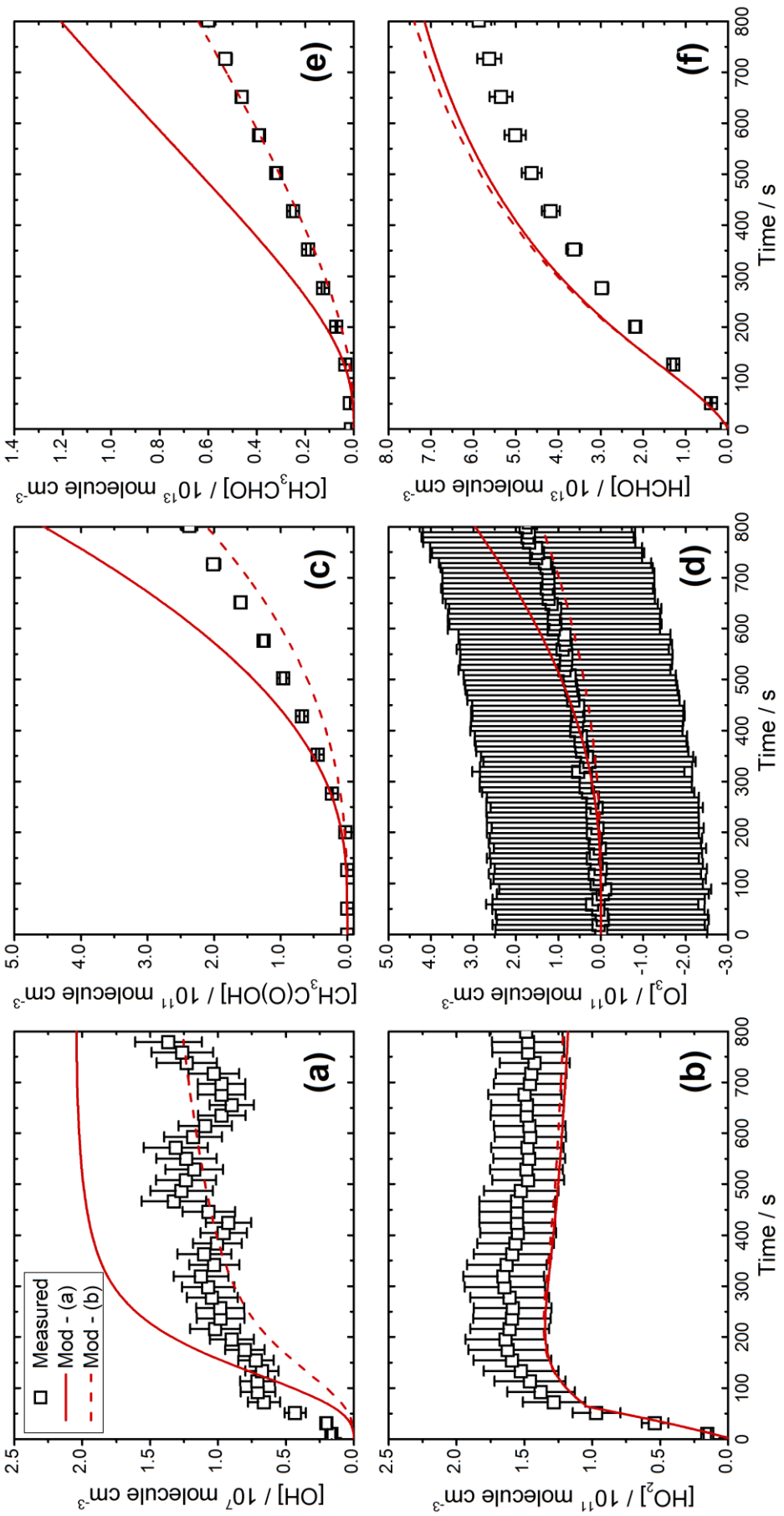

Figure 7.3: Measured product concentrations for OH (a), HO_2 (b), $CH_3C(O)OH$ (c), O_3 (d), CH_3CHO (e) and HCHO (f) as a function of time, for the reaction of $C_2H_5O_2$ with HO_2 at 1000 mbar, 293 K. Measured experimental data are compared to a chemical model based on the reactions in Table 7.1 and Table 7.2. Mod - (a) was constrained to k_R 7.16 = 1.04×10^{-10} cm^3 $molecule^{-1}$ s^{-1} while Mod - (b) was constrained to $k_{R\,7.16} = 4.0 \times 10^{-11}$ cm^3 $molecule^{-1}$ s^{-1}. All uncertainties quoted to ± 1σ.

The rate constant for (R 7.16) has, to date, only been measured by Wallington et al. (1989) using the relative rate method with C_2H_6 as a reference. The C_2H_5OOH decay was quantified using an IR reference spectrum measured in the same study (this was necessary due to the overlap with spectral features from C_2H_6 around 800 cm^{-1}, as in Figure 7.2). Spittler et al. (2000) also reported using an IR reference spectrum for C_2H_5OOH in the determination of products from HO_2 + $C_2H_5O_2$ (R 7.13), however Wallington et al. (1989) was quoted as the source. A visually better agreement between measured and predicted product concentrations was observed by revaluating the chemical model with $k_{R\ 7.16}$ = 4.0 × 10^{-11} cm^3 $molecule^{-1}$ s^{-1} (Figure 7.3, Mod - (b)), suggesting that the literature rate coefficient may be overestimated. Clearly confirmation of both the rate coefficient and the IR cross-section by other groups would be beneficial to validate the experiments conducted by Wallington et al. (1989).

In conclusion, the selected reaction of $C_2H_5O_2$ + HO_2 was not suitable for a non-OH producing peroxy radical control reaction in the HIRAC chamber. In the flow tube investigations of Dillon and Crowley (2008), where experiment times were short (< 10 ms), this reaction would be ideal as reactant + product chemistry is minimised and detection of products occurs at a much higher time resolution (μs as opposed to s). Repeat experiments into the ethylperoxy system would help evaluate reproducibility in the determination of $j(Cl_2)$ and experimental analysis could be improved by a direct measurement of the C_2H_5OOH product through used of an IR reference spectrum. This would help to further constrain the chemical model and properly evaluate the oxidation kinetics and products of C_2H_5OOH.

Reaction	**Branching ratio**	**Rate Coefficient**	
$Cl + C_2H_6 \rightarrow C_2H_5O_2 + HCl$		$8.3 \times 10^{-11} \exp(-100/T)$	(a)
$OH + C_2H_6 \rightarrow C_2H_5O_2 + H_2O$		$6.9 \times 10^{-11} \exp(-1000/T)$	(a)
$C_2H_5O_2 + HO_2 \rightarrow C_2H_5OOH + O_2$		$4.3 \times 10^{-13} \exp(870/T)$	(a)
$2C_2H_5O_2 \rightarrow 2CH_3CHO + O_2 + 2HO_2$	0.63	7.6×10^{-14}	(a)
$\rightarrow C_2H_5OH + CH_3CHO + O_2$	0.37		
$Cl + C_2H_5OH \rightarrow CH_3CHO + HO_2 + HCl$	0.95	9.6×10^{-11}	(b)
$\rightarrow HOC_2H_5O_2 + HCl$	0.05		
$OH + C_2H_5OH \rightarrow CH_3CHO + HO_2 + H_2O$	0.05	$3.0 \times 10^{-12} \exp(20/T)$	(a)
$\rightarrow CH_3CHO + HO_2 + H_2O$	0.95		
$\rightarrow HOC_2H_5O_2$	0.05		
$C_2H_5OOH + OH \rightarrow C_2H_5O_2 + H_2O$		$1.9 \times 10^{-12} \exp(190/T)$	(c)
$\rightarrow CH_3CHO + OH + H_2O$		8.0×10^{-12}	(c)
$C_2H_5OOH + Cl \rightarrow CH_3CHO + OH + HCl$		Varied - see text.	(d)
$C_2H_5O_2 + CH_3C(O)O_2 \rightarrow CH_3O_2 + CO_2 + CH_3CHO + HO_2 + O_2$	0.90	$5.0 \times 10^{-13} \exp(1070/T)$	(e)
$\rightarrow CH_3C(O)OH + CH_3CHO + O_2$	0.10		

Table 7.2: Reaction scheme added to the main chemical model (Table 7.1) used to simulate the $C_2H_5O_2$ + HO_2 reaction and others from the $Cl_2/CH_3OH/C_2H_6$ control experiment. Rate coefficient units = cm^3 $molecule^{-1}$ s^{-1}. Branching ratios listed to the left of rate constants. References: (a) IUPAC recommended (Atkinson et al., 2004); (b) JPL recommended (Sander et al., 2011); (c) MCM v3.2 (MCM, 2014); (d) taken from relative rate experiments conducted by Wallington et al. (1989); (e) taken from direct UV absorption experiments by Maricq and Szente (2000).

7.3.2 Reaction of $CH_3C(O)O_2$ with HO_2

Table 7.3 contains the starting conditions and assigned R 7.5 yields for experiments P1 - P5 conducted at 1000 mbar and 293 K for $[CH_3OH]_0$:$[CH_3CHO]_0 \approx 3.8$. Figure 7.4a, b and c show the product profiles of $CH_3C(O)OOH$, $CH_3C(O)OH$ and O_3 respectively as a function of decay in CH_3CHO ($\Delta[CH_3CHO]$) for all datasets, while Figure 7.4a and b show a typical OH and HO_2 time profiles for experiment P1, respectively. High steady state concentrations of $[HO_2]$ were observed in the first ~100 s of the reaction ensuring that enough HO_2 was present in the system to efficiently react with $CH_3C(O)O_2$ radicals. For a decrease in $[CH_3CHO]$ of ~50%, near linear increases in $[CH_3C(O)OOH]$, $[CH_3C(O)OH]$ and $[O_3]$ were observed, suggesting that the rate of formation of stable products through reaction R 7.5 remained roughly constant throughout the ~600 s reaction period. The monitored sharp increase in [OH] at early times to a steady state level of $\sim 10^7$ molecule cm^{-3} suggested a primary production channel that was also maintained throughout. However, more quantitative information was obtained through the use of the simulated chemical modelling scheme (section 7.2.4).

Expt	***P*[a]**	**$[Cl_2]_0$[b]**	**$[CH_3OH]_0$[b]**	**$[CH_3CHO]_0$[b]**	**$\alpha_{R\ 7.5a}$**	**$\alpha_{R\ 7.5b}$**	**$\alpha_{R\ 7.5c}$**
P1	1000	6.19	3.30	0.89	0.40 ± 0.02	0.15 ± 0.04	0.47 ± 0.08
P2	1000	6.93	3.30	0.88	0.36 ± 0.01	0.11 ± 0.03	0.53 ± 0.09
P3	1000	6.60	3.30	0.80	0.35 ± 0.01	0.11 ± 0.03	0.54 ± 0.09
P4[c]	1000	2.26	3.30	0.86	0.38 ± 0.02	0.12 ± 0.03	0.50 ± 0.09
P5[d]	1000	2.58	3.30	0.84	0.41 ± 0.02	0.15 ± 0.04	0.44 ± 0.08
				Average =	0.38 ± 0.03	0.13 ± 0.04	0.49 ± 0.10

Table 7.3: Experimental conditions for $CH_3C(O)O_2$ + HO_2 conducted in air at 1000 mbar HIRAC pressure. Yields for R 7.5 also listed, determined by optimising the match between the chemical simulation and experimental data, as described in section 7.2.4. [a] = pressure units in mbar; [b] = precursor concentrations in 10^{14} molecule cm^{-3}; [c] = reduced $[Cl_2]_0$ as experiment conducted using 4 photolysis lamps; [d] = reduced $[Cl_2]_0$ as experiment conducted using 8 photolysis lamps (all others conducted with 2 lamps).

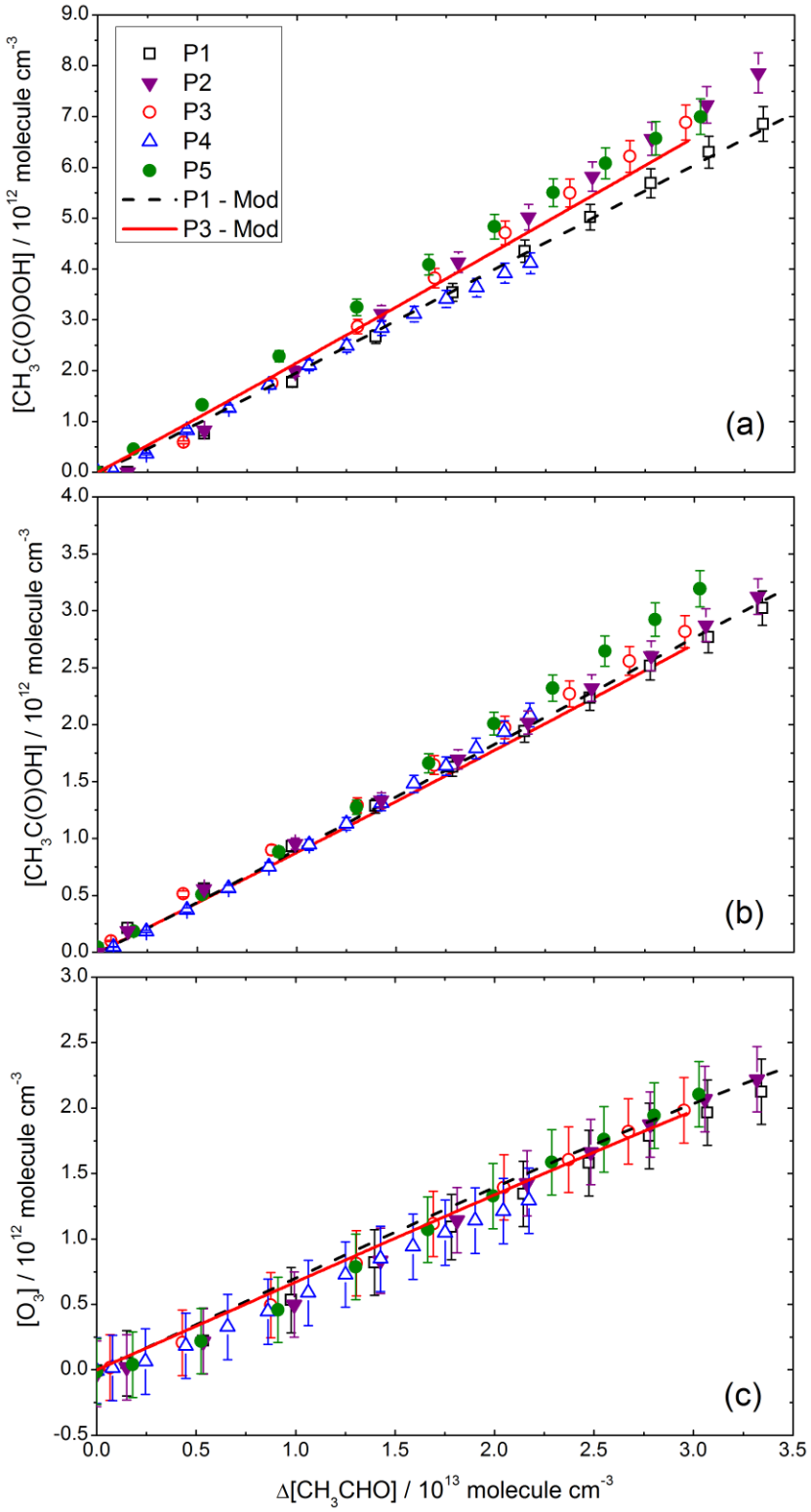

Figure 7.4: Products $CH_3C(O)OOH$, (a), $CH_3C(O)OH$, (b), and O_3, (c), as a function of $\Delta[CH_3CHO]$ for $[CH_3OH]_0$:$[CH_3CHO]_0 \approx 3.8$ in air at 1000 mbar and 293 K. Good agreement was observed between experimental data and the chemical model for all datasets with an average determined yield of $\alpha_{R\ 7.5a} = 0.38 \pm 0.03$, $\alpha_{R\ 7.5b} = 0.13 \pm 0.04$ and $\alpha_{R\ 7.5c} = 0.49 \pm 0.10$. Only model runs for experiments P1 and P3 are shown as examples, the optimised branching ratios for which are shown in Table 7.3. All uncertainties quoted to $\pm 1\sigma$.

Yields from the three branching pathways of $CH_3C(O)O_2$ + HO_2 (R 7.5) were assigned through application and optimisation of the chemical model to each experimental dataset, detailed in Table 7.3, leading to average branching ratios of $\alpha_{R\ 7.5_a} = 0.38 \pm 0.03$, $\alpha_{R\ 7.5_b} = 0.13 \pm 0.04$ and $\alpha_{R\ 7.5c} = 0.49 \pm 0.10$. Due to the crowded nature of the datasets presented in Figure 7.4, only the simulations for experiments P1 and P3 are shown as examples. Uncertainty in the branching ratio was calculated as a function of the precision error in repeated determinations along with any uncertainties in the FTIR cross-section and O_3 analyser and FAGE calibrations. Good agreement between measured and simulated data was achieved for all datasets at 1000 mbar with the results in Figure 7.4 and Figure 7.5 clearly showing the advantage of extra constraints to the possible determined yields through direct product measurement from all three branching pathways.

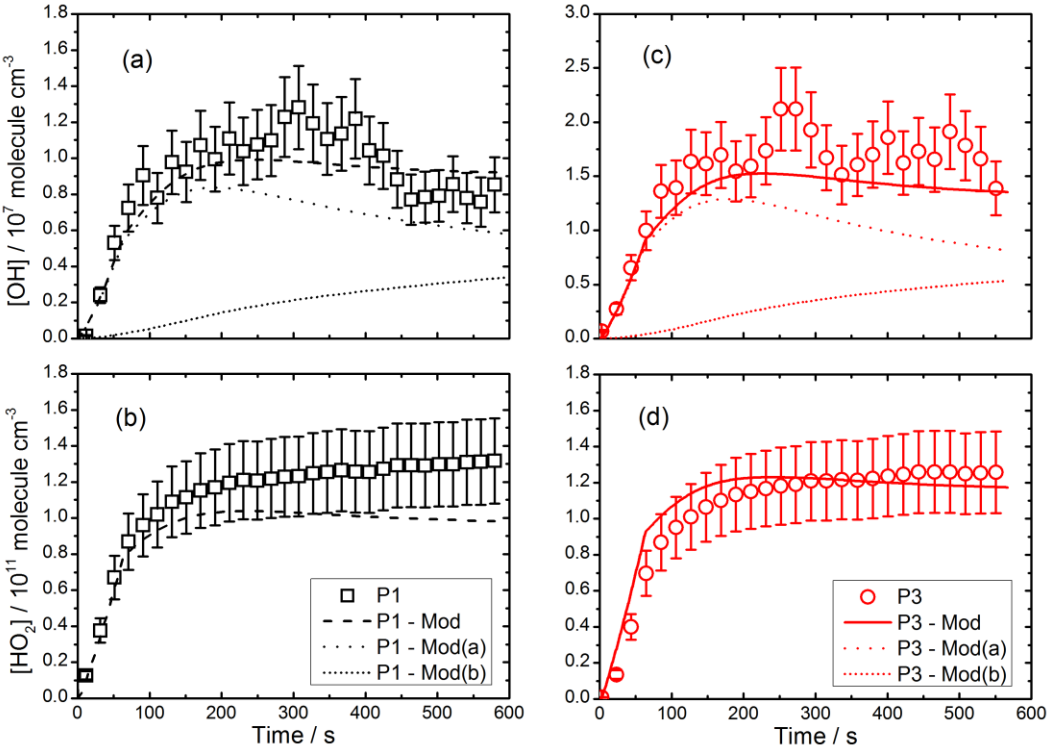

Figure 7.5: The OH (a + c) and HO_2 (b + d) time profiles during experiment P1 and P3 measured directly using the FAGE instrument at $[CH_3OH]_0$:$[CH_3CHO]_0$ ≈ 3.8, 1000 mbar in air and 293 K, where photolysis was initiated at t = 0 s. Chemical model predictions also shown (P1 – Mod and P3 – Mod) calculated using optimised branching ratios (P1) $\alpha_{R\ 7.5c}$ = 0.45 ± 0.08 and (P3) $\alpha_{R\ 7.5c}$ = 0.54 ± 0.09 calculated using the IUPAC recommended value for $k_{R\ 7.5}$. Contribution to total [OH] from reaction R 7.5c and all other secondary sources are shown in Mod(a) and Mod(b) traces respectively (i.e., Mod = Mod(a) + Mod(b)). Error bars represent uncertainty to ± 1σ in the FAGE calibration procedure.

Assignment of the yield for channel R 7.5c was found to be insensitive to the ratio of $\alpha_{R\ 7.5a}$:$\alpha_{R\ 7.5b}$. The ratio of $\alpha_{R\ 7.5a}$:$\alpha_{R\ 7.5c}$ was observed to affect the $CH_3C(O)OH$ yield, but not that of O_3, suggesting $\alpha_{R\ 7.5b}$ was also unaffected. Reaction R 7.5b was found to be the dominant production channel for $CH_3C(O)OH$ (~80%) with a ~19% yield from the reaction of $CH_3C(O)O_2$ with CH_3O_2 (R 7.18b). As the dominant production channel for CH_3O_2 in the system was the decomposition of acetylalkoxy radicals (R 7.17) produced alongside OH in R 7.5c (also produced here from R 7.18a), a certain sensitivity for $CH_3C(O)OH$ to $\alpha_{R\ 7.5c}$ can be expected. This also adds confidence to the determination of $\alpha_{R\ 7.5b}$ through measurement as agreement between measured and modelled concentrations of both O_3 and $CH_3C(O)OH$ is the first indication that effects of secondary chemistry are well accounted in the reaction scheme.

$$CH_3C(O)O\ (+O_2) \rightarrow CH_3O_2 + CO_2 \qquad \text{R 7.17}$$

$$CH_3C(O)O_2 + CH_3O_2 \rightarrow CH_3C(O)O + CH_3O + O_2 \qquad \text{R 7.18a}$$

$$\rightarrow CH_3C(O)OH + HCHO + O_2 \qquad \text{R 7.18b}$$

The only production source for $CH_3C(O)OOH$ and O_3 as well as OH at early times in the system was through R 7.5 and hence these species were more sensitive than $CH_3C(O)OH$ to changes in modelled yields. As mentioned previously, the prompt increase in measured [OH] suggests production from the primary $CH_3C(O)O_2 + HO_2$ reaction, and this is supported by the chemical simulation which shows >75% of total [OH] production through R 7.5c over the 600 s reaction period (Figure 7.5a, P1 - Mod(a)). The sum of OH sources from secondary $RO_2 + HO_2$ reactions (Figure 7.5a, P1 - Mod(b)) showed negligible impact on the measured [OH] until ~ 200 s, and in total were still the minor production channels (~40 %) even at t = 600 s. Secondary OH was mainly produced through the reaction of $HOCH_2O_2$ with HO_2 (R 7.19), the former the RO_2 radical from the HO_2:HCHO adduct (R 3.3).

$$HOCH_2O_2 + HO_2 \rightarrow HOCH_2O + OH + O_2 \qquad \text{R 7.19a}$$

$$\rightarrow HOCH_2OOH + O_2 \qquad \text{R 7.19b}$$

$$\rightarrow HCOOH + H_2O + O_2 \qquad \text{R 7.19c}$$

While the HO_2 + HCHO association reaction has received minor attention in the literature (Barnes et al., 1985; Veyret et al., 1989), to date the subsequent RO_2 reactions have only been studied by Jenkin et al. (2007). During their investigation of the title reaction, photolysis of Cl_2 was used with a CH_3OH/benzene mixture with the aim of detecting any OH produced from reaction R 7.19a, as large concentrations of both HO_2 and HCHO are produced from Cl + CH_3OH (R 7.7 and R 7.8), while benzene served as a chemical tracer for OH. Jenkin et al. (2007) deduced that the chemical model better reproduced the experimentally measured HCHO, HCOOH and OH upon inclusion of the $HOCH_2O_2$ self reaction (R 7.20), the assumed instantaneous reaction of the hydroxyl-alkoxy radical from R 7.19a and R 7.20a, with O_2 (R 7.21), and the Cl initiated oxidation of $HOCH_2OOH$ produced in R 7.19b (R 7.22 and R 7.23).

$$HOCH_2O_2 + HOCH_2O_2 \rightarrow HOCH_2O + HOCH_2O + O_2 \quad \text{R 7.20a}$$

$$\rightarrow HCOOH + HOCH_2OH + O_2 \quad \text{R 7.20b}$$

$$HOCH_2O + O_2 \rightarrow HCOOH + HO_2 \quad \text{R 7.21}$$

$$Cl + HOCH_2OOH \rightarrow HOCHOOH + HCl \quad \text{R 7.22}$$

$$HOCHOOH \rightarrow HCOOH + OH \quad \text{R 7.23}$$

As such, these reactions and their respective rate constants determined by Jenkin et al. (2007) have been included in the chemical model presented here. Both HCHO and HCOOH were detected in experiments P1 - P5 and are shown as a function of decay in CH_3OH, $\Delta[CH_3OH]$, in Figure 7.6a and b respectively. The good agreement between experimental and simulated HCHO and HCOOH helped to further constrain the kinetic evaluation of the title reaction, however, these two species showed the largest discrepancies between measured and modelled data overall.

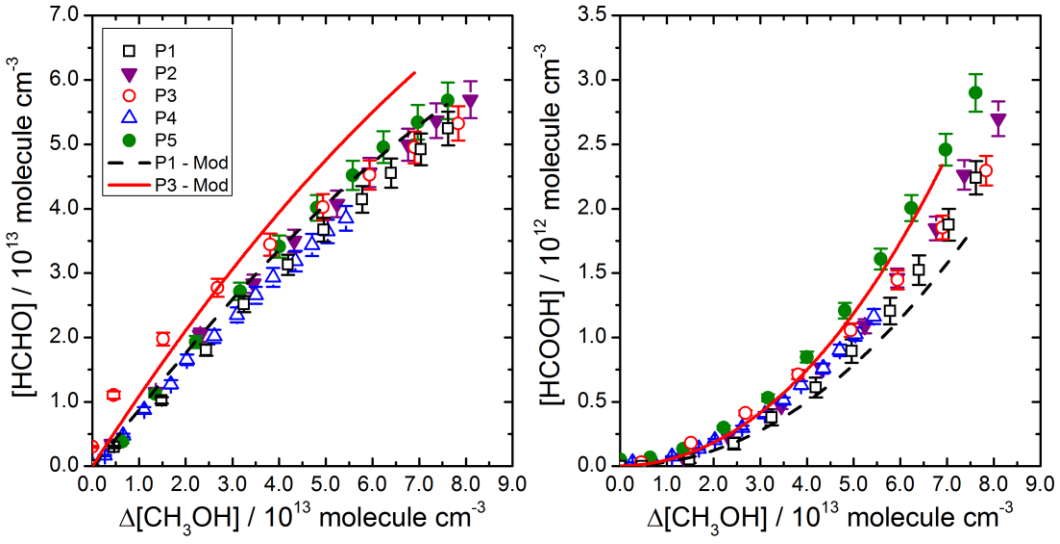

Figure 7.6. The [HCHO] and [HCOOH] profiles as a function of $\Delta[CH_3OH]$ for experiments P1 – P5, for $[CH_3OH]_0$:$[CH_3CHO]_0 \approx 3.8$ at 1000 mbar and 293 K. Only model runs for experiments P1 and P3 are plotted as examples, the optimised R 7.5 branching ratios for which are shown in Table 7.3. All uncertainties quoted to ± 1σ.

As few studies existed into the equilibrium between HO_2 + HCHO ↔ $HOCH_2O_2$ (R 3.3), IUPAC recommend uncertainties of ~75 % for both the forward and reverse reaction rate constants (IUPAC, 2002; IUPAC, 2005), and so the sensitivity of various

products to this uncertainty was investigated. Displayed in Figure 7.7 (overleaf) are the measured $CH_3C(O)OOH$ (a), O_3 (b), HCHO (c), HCOOH (d), OH (e) and HO_2 (d) yields as a function of $\Delta[CH_3CHO]$ (a + b), $\Delta[CH_3OH]$ (b + c) and time (d + e), for experiment P1. Also displayed is the optimised chemical model, determined using branching ratios of $\alpha_{R\ 7.5a} = 0.41 \pm 0.03$, $\alpha_{R\ 7.5b} = 0.15 \pm 0.02$ and $\alpha_{R\ 7.5c} = 0.44 \pm 0.04$ and the IUPAC recommended values for the forward, k_f and reverse, k_r, rate coefficients of the equilibrium reaction between HO_2 and HCHO (R 3.3, see Table 7.1). Shaded blue and red areas represent the range of concentrations predicted by the chemical model taking into account the uncertainty in the HO_2 + HCHO association n equilibrium for k_f and k_r respectively.

Clearly k_r has the largest effect on any of the simulated products shown as the effect of an increase in k_f is limited by the lifetime of $HOCH_2O_2$, controlled by the reverse dissociation reaction. An asymmetric change in yields was observed, shown by the model conducted with the IUPAC recommended rate constants, which sits close to the model runs using rate constants k_f and k_r calculated using the upper limit of uncertainty, due to the forward reaction becoming the rate limiting step at values of $k_r < 10^2\ s^{-1}$. As k_r decreases, $HOCH_2O_2$ has more chance to react, pushing the equilibrium towards RO_2 production and decreasing the [HCHO] and $[HO_2]$ in the system (Figure 7.7c and f). The decrease in $[HO_2]$ leads to a net yield decrease for $CH_3C(O)OOH$ and O_3 (Figure 7.7a and b) as more $CH_3C(O)O_2$ is consumed through reaction with itself (R 7.24), CH_3O_2 (R 7.18) and $HOCH_2O_2$ (R 7.25) rather than with HO_2. The yield of $CH_3C(O)OH$ has not been shown here as it was found to be insensitive to the change in HO_2 + HCHO equilibrium constant. This is due to a buffering system where $CH_3C(O)OH$ is increasingly produced from secondary sources where reaction of $CH_3C(O)O_2$ with the increased levels of CH_3O_2 (R 7.18b) and $HOCH_2O_2$ (R 7.25b) dominates due to the deficit in HO_2. The modelled OH was also sensitive to changes in k_f and k_r, and was observed to increase with a decrease in k_r, as production secondary to R 7.5c increased through R 7.19a and R 7.23. The largest effect was seen in the modelled HCOOH profile, where at the lower limit of k_r, the predicted [HCOOH] at 600 s was a factor of ~20 higher than when using the recommended IUPAC value for k_r (see inset plot in Figure 7.7d). Clearly this is not the case, and the chemical model using the IUPAC recommended rate constants provides a satisfactory prediction of the secondary chemistry in the system generated by the HO_2 + HCHO reaction. More work

is required into the equilibrium and further reactions of the RO_2 produced however, and this is the topic of interest for future research for the HIRAC group (see section 7.5).

$$2CH_3C(O)O_2 \rightarrow 2CH_3C(O)O + O_2 \quad \text{R 7.24}$$

$$CH_3C(O)O_2 + HOCH_2O_2 \rightarrow CH_3C(O)O + HOCH_2O + O_2 \quad \text{R 7.25a}$$

$$\rightarrow CH_3C(O)OH + HCOOH + O_2 \quad \text{R 7.25b}$$

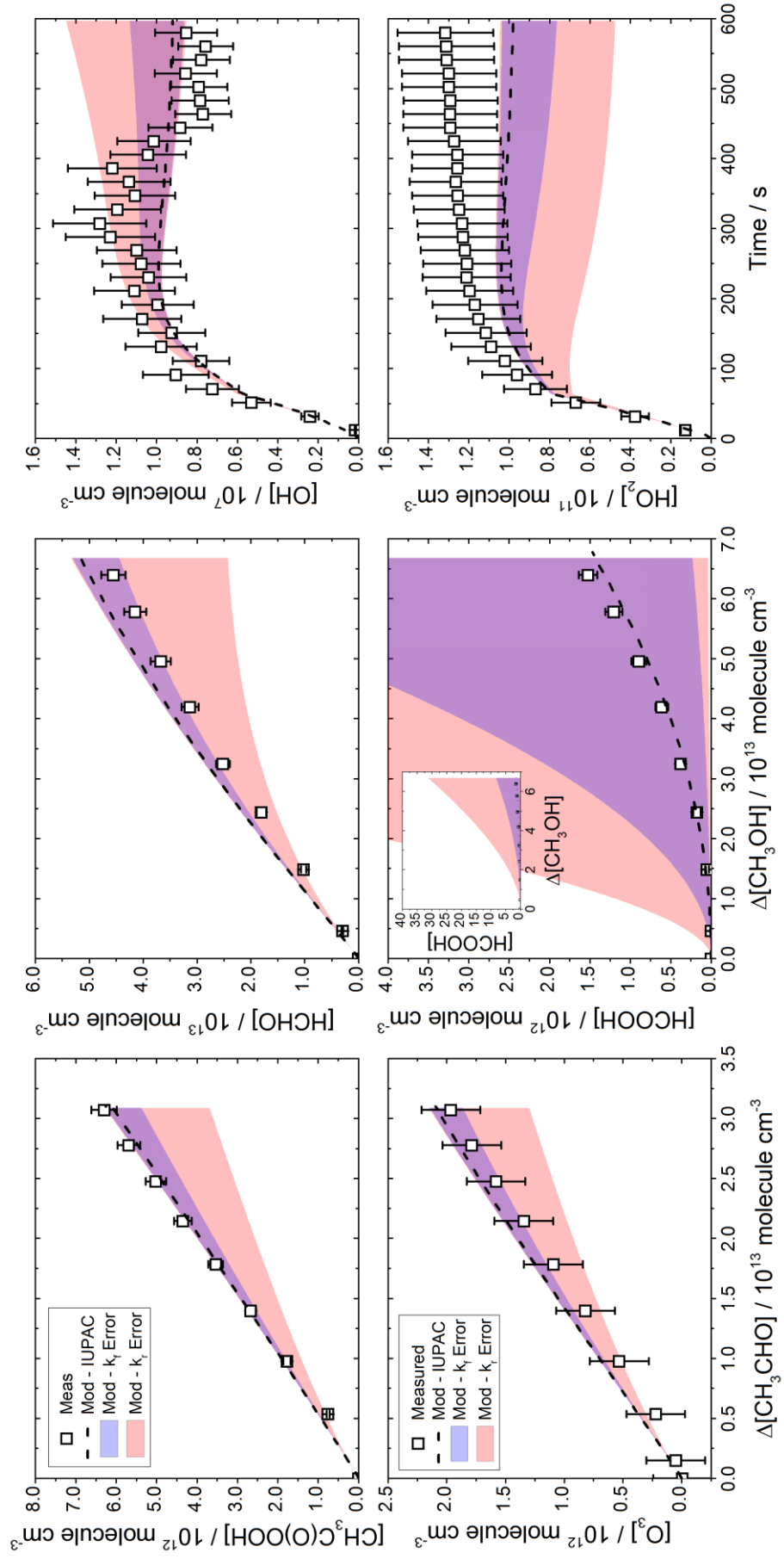

Figure 7.7. Measured product concentrations for $CH_3C(O)OOH$ (a), O_3 (b), HCHO (c), HCOOH (d), OH (e) and HO_2 (f) as a function of $\Delta[CH_3CHO]$ (a + b), $\Delta[CH_3OH]$ (c + d) and time (e + f), for experiment P1 where $[CH_3OH]_0$:$[CH_3CHO]_0 \approx 3.8$ at 1000 mbar in air, 293 K and $\alpha_{R\ 7.5a} = 0.41 \pm 0.03$, $\alpha_{R\ 7.5b} = 0.15 \pm 0.02$ and $\alpha_{R\ 7.5c} = 0.44 \pm 0.04$. Shaded areas represent the range of concentrations predicted by the chemical model taking into account the uncertainty in the HO_2 + HCHO association equilibrium (R 3.3) where k_f and k_r represent he forward and reverse reactions respectively. Axes units for insert plot in (d) are the same as the parent plot and all uncertainties quoted to ± 1σ.

The sensitivity of the uncertainty in the analogous HO_2 association with CH_3CHO on the measured products was also investigated. As only one study exists into the equilibrium (Tomas et al., 2001), it was conceivable that uncertainty in forward and reverse rate constants could impact on OH and $CH_3C(O)OH$ yields through further reactions of the $CH_3CH(OH)O_2$ radical (R 3.1) with $HOCH_2O_2$ and CH_3O_2 (see Table 7.1). The chemical model showed that the dominating pathway for removal of CH_3CHO was through reaction with HO_2 at ~90%. However, the rate of dissociation from $CH_3C(OH)O_2$ back to CH_3CHO and HO_2 was > 99% of the total $CH_3C(OH)O_2$ loss. Hence, negligible concentrations of $CH_3C(OH)O_2$ were able to react with other RO_2 species or HO_2, and the model was found to be insensitive to the removal of this pathway from the mechanism. A small sensitivity to the upper and lower limits of uncertainty in this equilibrium was observed in OH and $CH_3C(O)OH$, however the deviation was well within the measurement uncertainties and hence the importance of this reaction under the operating conditions at 293 K was limited.

7.3.2.1 Sensitivity of experimental yields from R 7.5 to $k_{R\ 7.5}$

The sensitivity of the yields of R 7.5 to the overall rate constant was investigated. Whilst the modelled yields using the IUPAC recommended rate constant (1.48×10^{-11} cm^3 molecule^{-1} s^{-1}) matched the data well using $\alpha_{R\ 7.5a} = 0.38 \pm 0.03$, $\alpha_{R\ 7.5b} = 0.13 \pm 0.02$ and $\alpha_{R\ 7.5c} = 0.49 \pm 0.10$, in general there was a minor under-prediction of OH concentrations. Whilst the modelled yields fell within the uncertainties of the FAGE measurements (except in the case of the higher photolysis rate experiments, see section 7.3.2.2), a visually better correlation between measured and modelled OH was achieved by fitting the model to the measured data from all three branching pathways from the $CH_3C(O)O_2 + HO_2$ reaction. The model was constrained to the decay in reactants and photolysis rate and a non-linear least squares iterative fitting routine built into the Kintecus package was used to determine the best fit rate coefficients by judging the reduced χ^2 (determined using the Powell method (Press et al., 1992; Ianni, 2002)). An increase in rate coefficient for channel R 7.5c was observed, whilst the sum of $k_{R\ 7.5a}$ and $k_{R\ 7.5b}$ remained constant (within uncertainty), leading to an overall increase in $k_{R\ 7.5} = (1.76 \pm 0.25) \times 10^{-11}$ cm^3 molecule s^{-1}. Uncertainties were

taken as the quoted standard errors in the fitting routine to ± 1σ. The predicted OH yields using the fitted rate constants are also presented in Figure 7.8, showing the improvement in correlation to the measured OH data for experiments P4 and P5. Predicted concentrations of all other measured products were found to be insensitive to the increased rate constant. The revised branching ratios for experiments P1 - P5 are shown in Table 7.4 with the rate constants derived from the fitting procedure and these are discussed further with reference to literature data in section 7.4.

Expt	$\alpha_{R\ 7.5a}$	$\alpha_{R\ 7.5b}$	$\alpha_{R\ 7.5c}$	k_a/k_b	$k_a + k_b$ [a]	k_c [a]	k_{tot} [a]
P1	0.40	0.14	0.46	2.86	0.81	0.69	1.50
P2	0.35	0.10	0.55	3.50	0.72	0.88	1.60
P3	0.32	0.10	0.59	3.20	0.71	0.99	1.68
P4[b]	0.32	0.10	0.58	3.20	0.86	1.19	2.05
P5[c]	0.36	0.11	0.53	3.27	0.94	0.92	2.00
	0.35 ± 0.03	0.11 ± 0.02	0.54 ± 0.05	3.21	0.81	0.93	1.76 ± 0.25

Table 7.4. Yields for R 7.5 determined by fitting the chemical model to the experimental data, allowing the chemical simulation to optimise $k_{R\ 7.5a}$, $k_{R\ 7.5b}$ and $k_{R\ 7.5c}$ independently. The total rate coefficient was determined from the fitting procedure also listed (k_{tot}). The bottom row displays average values and calculated standard deviations (± 1σ). a = rate coefficient units in cm^3 $molecule^{-1}$ s^{-1}; b = experiment conducted using 4 photolysis lamps; c = experiment conducted using 8 photolysis lamps. All other experiments conducted using 2 photolysis lamps.

7.3.2.2 Sensitivity of experimental yields from R 7.5 to $j(Cl_2)$

The target reaction was studied using 2, 4 and 8 photolysis lamps in experiments P1 - P3, P4 and P5 respectively, preserving $[CH_3OH]_0$:$[CH_3CHO]_0 \approx 3.8$. All runs were conducted at 1000 mbar and 293 K. Photolysis rates for P4 and P5 have been estimated at (3.4 ± 1.0) and (5.9 ± 1.0) × 10^{-4} s^{-1} respectively. Doubling the number of photolysis lamps should in principle double the photolysis rate, however the output of each lamp was not identical as the number of operational hours was different leading to a degradation in output intensity. The initial $[Cl_2]_0$ was lowered in experiments P4 and P5 to maintain the overall Cl atom and radical density inside the chamber, compared to the

P1 - P3 runs. The stable product yields ($CH_3C(O)OOH$, $CH_3C(O)OH$ and O_3) from runs P4 and P5 were found to be in excellent agreement with the P1 - P3 experiments conducted at a lower photolysis rate and hence have been included in Figure 7.4.

Discrepancies between measured and simulated OH and HO_2 radicals were observed using both 4 and 8 lamps, displayed in Figure 7.8. The model was found to under-predict both OH and HO_2. The HO_2 model deficiency (= $[HO_2]_{mod}/[HO_2]_{meas}$) increased with photolysis rate: from 47% (P4) to 69% (P5).

It was possible that heterogeneous reactions taking place on the steel chamber walls and warm walls of the quartz tubes used to house the photolysis lamps were contributing to the increase in $[HO_2]$ initiated by reaction with the high levels of radicals in the system, leading to HO_2 formation directly or indirectly through RO_2 chemistry. The increased [OH] at higher $j(Cl_2)$ (~2×10^7 compared to ~1×10^7 molecule cm^{-3}) suggests that even with reduced $[Cl_2]_0$ the radical density in the system was increased, and this was confirmed by the chemical model where [Cl] ≈ 0.9 and 1.2×10^7 molecule cm^{-3} for experiments P1 and P5 respectively. Photolysis of species trapped on the chamber walls was unlikely as the only known species that could possibly photolyse at λ ≈ 360 nm was HCHO, and control tests showed that with 8 photolysis lamps at $[HCHO]_0 = 3 \times 10^{13}$ molecule cm^{-3}, low levels of $[HO_2]$ just above the detection limit of the FAGE instrument were observed (d.l. ≈ 10^8 molecule cm^{-3}).

However, it should be noted that after the full run of experiments was completed, a malfunction in the mass flow controller (MFC) that controls the NO injection into the FAGE HO_2 detection cell was detected. A blockage caused the controller to flow erratically, changing the conversion efficiency of the HO_2 to OH, which ultimately impacted on instrument sensitivity. It is possible that the results from P4 and P5, conducted towards the end of the experimental period, were therefore subject to a malfunctioning MFC, and this could explain the under-estimation in HO_2 for these experiments.

The OH model deficiency was estimated at ~0.60 (= $[OH]_{mod}/[OH]_{meas}$) for both experiments P4 and P5, suggesting that the discrepancy was not related to the increase in photolysis rate. Also shown in Figure 7.8 are the modelled [OH] for a higher $k_{R\ 7.5c}$ (= 1.01×10^{-11} cm^3 $molecule^{-1}$ s^{-1}) determined through fitting of the data using Kintecus as described in section 7.3.2.

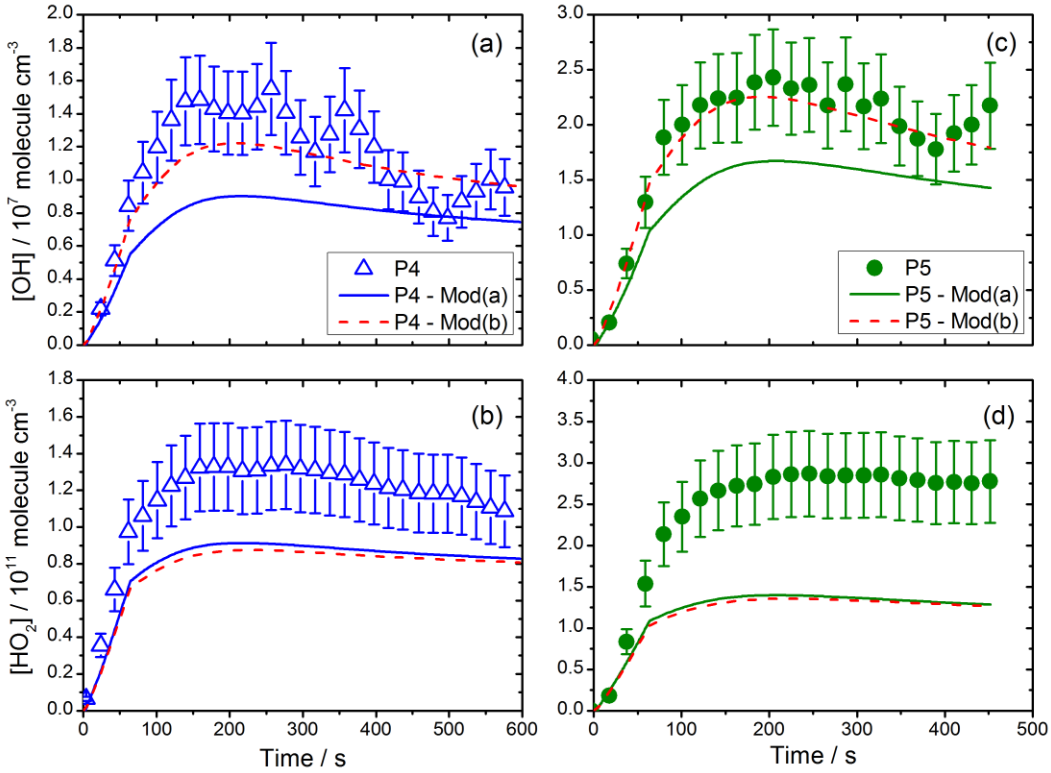

Figure 7.8: The OH (a + c) and HO_2 (b + d) time profiles during experiment P4 and P5 measured directly using the FAGE instrument at $j(Cl_2)$ = (3.4 ± 1.0) and (5.9 ± 1.0) × 10^{-4} s^{-1} respectively. Experiments conducted at $[CH_3OH]_0$:$[CH_3CHO]_0 \approx 3.8$, 1000 mbar and 293 K, and photolysis was initiated at t = 0 s. Chemical model predictions also shown (P4 – Mod(a) and P5 – Mod(a)) calculated using optimised branching ratios (P4) $\alpha_{R\ 7.5c} = 0.45 \pm 0.08$ and (P5) $\alpha_{R\ 7.5_c} = 0.54 \pm 0.09$ for recommended IUPAC value of $k_{R\ 7.5}$ (see text). Model runs labelled (b) show predicted OH and HO_2 calculated using $k_{R\ 7.5}$ = 2.05 and 2.00 × 10^{-11} cm^3 $molecule^{-1}$ s^{-1} for runs P4 and P5. Error bars represent uncertainty to ± 1σ in the FAGE calibration procedure.

7.3.2.3 Sensitivity of experimental yields from R 7.5 to $[CH_3OH]_0$:$[CH_3CHO]_0$

By manipulating the starting ratio of $[CH_3OH]_0$:$[CH_3CHO]_0$ it was possible to control the ratio of HO_2:$CH_3C(O)O_2$ during a given experiment. Table 7.5 lists the starting conditions for all the experiments studied at four $[CH_3OH]_0$:$[CH_3CHO]_0$ ratios between 0.0 - 5.6, with the observed $CH_3C(O)OOH$, $CH_3C(O)OH$ and O_3 experimentally determined product yields (relative to decay in CH_3CHO). Yields were calculated as the gradient from the linear regression of a respective [product] vs. $\Delta[CH_3CHO]$ plot. The yields are graphically displayed as a function of $[CH_3OH]_0$:$[CH_3CHO]_0$ in Figure 7.9. Measurements of O_3 at ratios of 1.2 and 5.6 were not completed due to an O_3 analyser malfunction. The product yields were observed to remain constant between ratios of 1.2 and 5.6, with yields decreasing for experiments where no methanol was added (ratio = 0.0). This indicated that experiments P1 – P5 were conducted at a ratio of precursors that did not negatively impact on the total observed yield of products from R 7.5 and in an excess of HO_2.

The chemistry in experiment P8, where $[CH_3OH] = 0$, is solely driven by the Cl atom initiated oxidation of CH_3CHO, and hence RO_2 chemistry outside of reaction with HO_2 (as in experiments with CH_3OH) drives product formation. The initial dominating loss for $CH_3C(O)O_2$ is self-reaction, followed closely by CH_3O_2, produced through reactions R 7.24 and R 7.17. The HO_2 radicals were produced at later times from the Cl initiated oxidation of HCHO (R 7.26), itself produced from reaction for CH_3O_2 with $CH_3C(O)O_2$ (R 7.18b). As the HCHO is produced quickly, no delay in R 7.5 product formation was observed on the timescale of the measurements presented here, however the reduced yields were calculated as there was no excess of HO_2 in the system. This trend has been reported and reproduced in the literature (Hasson et al., 2004; Jenkin et al., 2007).

$$Cl + HCHO + O_2 \rightarrow CO + HO_2 + HCl \qquad \text{R 7.26}$$

Expt	$[Cl_2]_0$	$[CH_3OH]_0$	$[CH_3CHO]_0$	Ratio	$Y_{CH3C(O)OOH}$	$Y_{CH3C(O)OH}$	Y_{O3}
P1	6.19	3.30	0.89	3.7	0.21 ± 0.02	0.09 ± 0.04	0.05 ± 0.08
P2	6.93	3.30	0.88	3.7	0.25 ± 0.01	0.09 ± 0.03	0.07 ± 0.09
P3	6.60	3.30	0.80	3.8	0.24 ± 0.01	0.09 ± 0.03	0.07 ± 0.09
P4	2.26	3.30	0.86	3.8	0.20 ± 0.02	0.10 ± 0.03	0.06 ± 0.09
P5	2.58	3.30	0.84	3.9	0.23 ± 0.02	0.10 ± 0.04	0.07 ± 0.08
P6	6.36	5.00	0.89	5.6	0.27 ± 0.01	0.10 ± 0.03	-
P7	6.78	1.00	0.85	1.2	0.22 ± 0.02	0.08 ± 0.03	-
P8	7.00	0.00	0.83	0.0	0.13 ± 0.02	0.05 ± 0.04	0.02 ± 0.08

Table 7.5: Yields of $CH_3C(O)OOH$, $CH_3C(O)OH$ and O3 as a function of decay in $[CH_3CHO]$ where $Y_x = [X] / \Delta[CH_3CHO]$ taken from the linear regression of the respective [X] vs. $\Delta[CH_3CHO]$ plot (see Figure 7.4 and Figure 7.10). Precursor concentrations shown for reference (units = 10^{14} molecule cm^{-3}). Ratio column calculated as $[CH_3OH]_0 / [CH_3CHO]_0$. No O_3 was measured for ratios 1.2 and 5.6 due to an analyser malfunction. All uncertainties calculated as the standard error in the linear regression to ± 1σ.

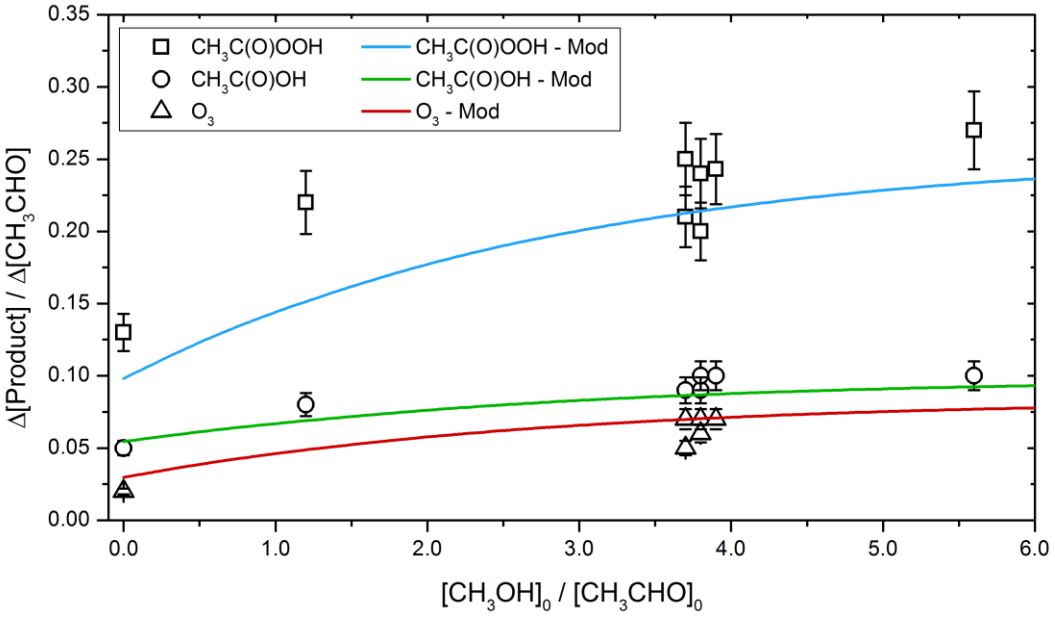

Figure 7.9. Experimentally determined product yields (relative to decay in CH_3CHO) for $CH_3C(O)OOH$, $CH_3C(O)OH$ and O_3 as a function of the $[CH_3OH]_0$:$[CH_3CHO]_0$ ratio where each point represents one experiment. Model predictions for each species yield also displayed for comparison. No O_3 data collected at $[CH_3OH]_0$:$[CH_3CHO]_0$ = 1.2 and 5.6 due to an O_3 analyser malfunction. Uncertainties calculated to 1σ from linear regression of respective [product] vs. $\Delta[CH_3CHO]$ plot.

Each experiment was simulated using the chemical mechanism in Table 7.1, using the average branching ratios calculated for the IUPAC recommended $k_{R\ 7.5}$ in the P1 – P5 experiments. By fixing the branching ratios for R 7.5, discrepancies in the chemical model compared to the experimental data could be more easily identified, as the rate of the R 7.5 pathways should be independent of precursor concentration. Displayed in Figure 7.10 are the measured and modelled product yields of $CH_3C(O)OOH$ (a), $CH_3C(O)OH$ (b), O_3 (c), HCHO (d) and HCOOH (e) as a function of $\Delta[CH_3CHO]$ (a + b + c) and $\Delta[CH_3OH]$ (d + e) for experiments P3 and P6 – P8. The model was in good agreement with the measured data at ratios > 1.0, however poor agreement for $CH_3C(O)OH$ and O_3 was obtained for the 0.0 ratio experiment (i.e., $[CH_3OH]_0$ = 0) where simulations over predicted concentrations by a factor of ~2 towards the end of the reaction period (~600 s, see Figure 7.11).

As described in section 7.3.2, the two main production channels for $CH_3C(O)OH$ are through the HO_2 + $CH_3C(O)O_2$ (R 7.5b) and CH_3O_2 + $CH_3C(O)O_2$ (R 7.18b), and in experiment P8 the chemical model predicted both channels were in competition for the

first ~200 s of the reaction (R 7.18b > R 7.5b by ~25%). In an experiment conducted at $[CH_3OH]_0$:$[CH_3CHO]_0$ > 1.0, loss of $CH_3C(O)O_2$ from reaction with HO_2 was the dominating pathway for the entire reaction, leading to <20% production of the measured $CH_3C(O)OH$. Modifying the branching ratio for R 7.18b in the chemical simulation from 0.1 to 0.05 showed better agreement with measured data in experiment P8 (Figure 7.11 - Mod (b)) and kept the branching ratio well within the IUPAC recommended uncertainty of ± 0.1. Models conducted for $[CH_3OH]_0$:$[CH_3CHO]_0$ > 1.0 were found to be insensitive to the change in branching ratio.

An over-prediction of CH_3O_2 in the chemical model could also increase $CH_3C(O)OH$ through reaction R 7.18. However, measurement of HCHO and CH_3OH in experiment P8 (Figure 7.11a and b) were well matched by the modelled profiles, calculated through the primary production reactions R 7.18a + R 7.28 and self-reaction of CH_3O_2 (R 7.27 + R 7.28), suggesting the methoxy chemistry in the system was well understood under these conditions.

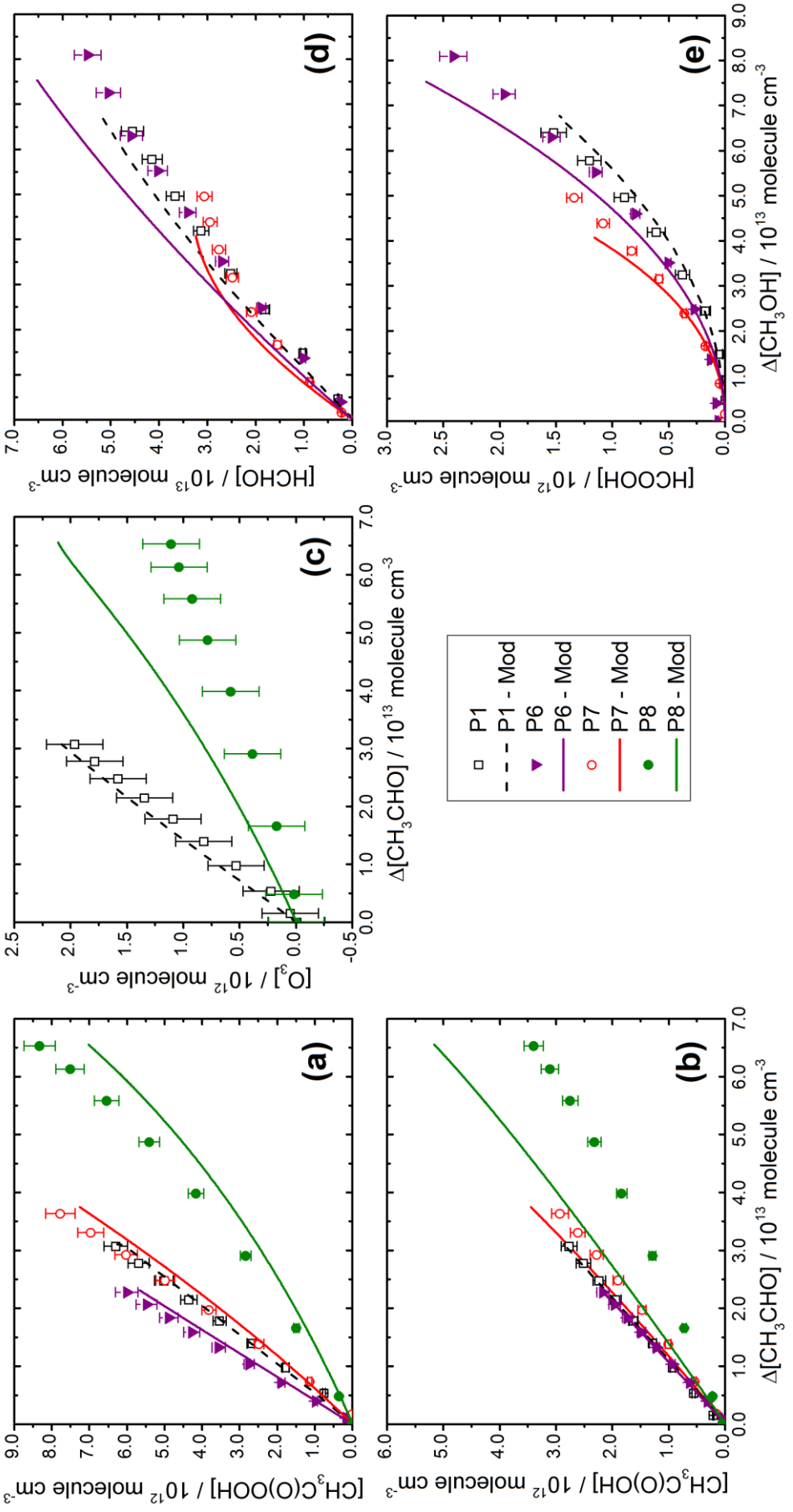

Figure 7.10: Experimental results for $CH_3C(O)OOH$, (a), $CH_3C(O)OH$, (b), and O_3, (c), HCHO (d), HCOOH (e) as a function of $\Delta[CH_3CHO]$ (a + b + c) and $\Delta[CH_3OH]$ (d + e) for $[CH_3OH]_0$:$[CH_3CHO]_0$ ratios 0.0 – 5.6 at 1000 mbar and 293 K. Measurements of O_3 were not conducted at ratios 1.2 and 5.6 due to an analyser malfunction. Yields for R 7.5 were fixed at $\alpha_{R\ 7.5a} = 0.38 \pm 0.03$, $\alpha_{R\ 7.5b} = 0.13 \pm 0.02$ and $\alpha_{R\ 7.5c} = 0.49 \pm 0.10$. Data not included for experiment P8 as no CH_3OH was introduced (see Figure 7.11 for time profiles). All uncertainties quoted to $\pm 1\sigma$.

$$2CH_3O_2 \rightarrow 2CH_3O + O_2 \quad \text{R 7.27a}$$

$$\rightarrow CH_3OH + HCHO + O_2 \quad \text{R 7.27b}$$

$$CH_3O + O_2 \rightarrow HCHO + HO_2 \quad \text{R 7.28}$$

Formation of HCHO and HO_2 ultimately leads to the creation of $HOCH_2O_2$ radicals through reaction R 3.3 and good agreement between measured and modelled HCOOH and OH yields confirms that formation reactions of the $HOCH_2O_2$ radical are well characterised in the HIRAC chamber at 1000 mbar and 293 K.

While the discussion above examines the validity of the RO_2 chemistry that could explain the measured $CH_3C(O)OH$, the measured O_3 was harder to predict. The main production channel in all experiments conducted is through the title reaction. An over estimation of HO_2, (Figure 7.11) could explain both the discrepancy in $CH_3O(O)OH$ and O_3, however the measured $CH_3C(O)OOH$ and OH have been modelled well, suggesting that reaction R 7.5 is well described by the model. Experiment P8 was the first to be conducted following the O_3 analyser malfunction so there is a possibility that the device was still not working correctly, however more recent calibrations have confirmed the pre-experimental calibration factor.

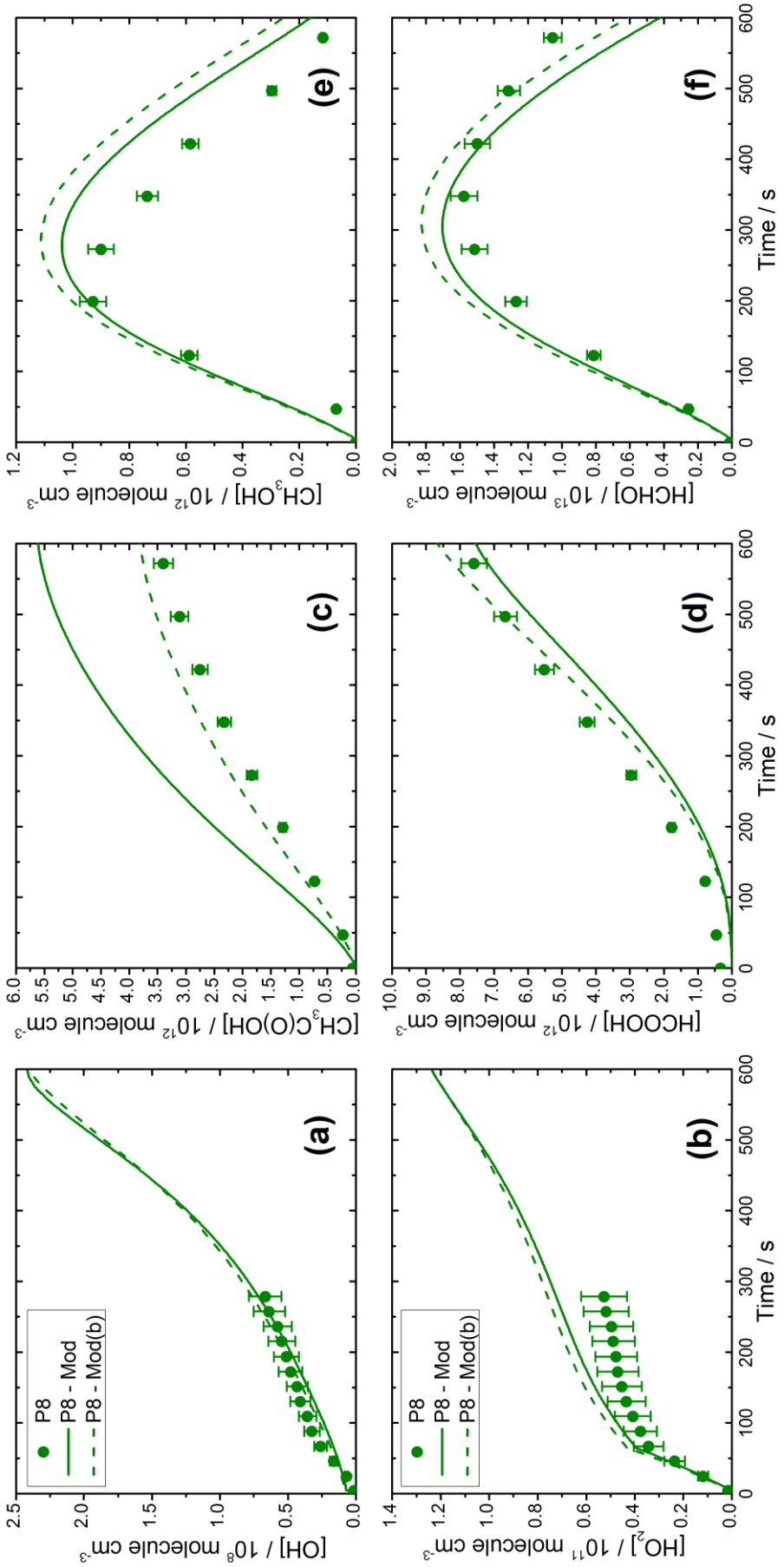

Figure 7.11: Experimental results for OH, (a), HO_2, (b), $CH_3C(O)OH$, (c), HCOOH (d), CH_3OH (e) and HCHO, (f) as a function of time (in s) for $[CH_3OH]_0$:$[CH_3CHO]_0$ = 0.0 at 1000 mbar and 293 K. Yields for R 7.5 were fixed at α_R 7.5_a = 0.38 ± 0.03, $\alpha_{R\ 7.5b}$ = 0.13 ± 0.02 and $\alpha_{R\ 7.5c}$ = 0.49 ± 0.10. Chemical simulations conducted using the base model reaction scheme shown in Table 7.1 (Mod - (a)) and predictions investigating the sensitivity of $CH_3C(O)OH$ production through CH_3O_2 + $CH_3C(O)O_2$ (Mod - (b), see text for details) are shown for comparison. All uncertainties quoted to ± 1σ.

7.4 Comparison with literature data

7.4.1 Branching ratios

The average branching ratios determined for reaction R 7.5 at 1000 mbar and 293 K using the recommended IUPAC value for $k_{R\ 7.5}$ as well as those determined using the fitting of the chemical model are presented in Table 7.6.

Author	$\alpha_{R\ 7.5a}$	$\alpha_{R\ 7.5b}$	$\alpha_{R\ 7.5c}$	k_a / k_b	$k_{R\ 7.5}$[a]
This work	0.38 ± 0.03	0.13 ± 0.04	0.49 ± 0.10	3.00 ± 0.28	1.4[b]
(floated $k_{R\ 7.5}$)	0.35 ± 0.03	0.12 ± 0.02	0.54 ± 0.09	3.21 ± 0.23	1.76 ± 0.25
Dillon and Crowley (2008)	-	-	0.50 ± 0.20	-	1.4 ± 0.5
Jenkin et al. (2007)	0.38 ± 0.13	0.12 ± 0.04	0.43 ± 0.10	3.16 ± 0.48	1.4[b]
Le Crâne et al. (2006)	-	0.20 ± 0.01	< 0.1	-	1.50 ± 0.08
Hasson et al. (2004)	0.40 ± 0.16	0.20 ± 0.08	0.40 ± 0.16	2.00 ± 0.57	2.2
Tomas et al. (2001)	-	0.20 ± 0.02	-	-	1.51 ± 0.07
Crawford et al. (1999)	(0.72)[c]	0.12 ± 0.04	-	7.3 (2.6)[c]	4.4 ± 1.6
Horie and Moortgat (1992)	-	-	-	2.7	-
Moortgat et al. (1989)	-	0.33 ± 0.07	-	-	1.3 ± 0.3
Niki et al. (1985)	~ 0.75	~ 0.25	-	~ 3	-

Table 7.6: Comparison of the results determined in this study with those present in the literature. Authors are referenced as they appear in the bibliography and tilde symbols indicate where a value was not measured directly. Data previous to Hasson et al. (2004) had not considered a third branching pathway ($\alpha_{R\ 7.5c}$) but are included here to compare the ratio of k_a and k_b as well as the overall rate constant for $CH_3C(O)O_2 + HO_2$ ($k_{R\ 7.5}$). [a] = units for $k_{R\ 7.5}$, molecule^{-1} cm^3 s^{-1}; [b] = experiments assumed IUPAC recommended value for $k_{R\ 7.5}$ [c] = bracketed data from Crawford et al. (1999) corrected for erroneous absorption cross section for $CH_3C(O)OOH$ by Orlando et al. (2000).

The branching ratio results presented here showed an OH yield from R 7.5c in agreement with the only other study to directly detect OH by Dillon and Crowley (2008). Whilst the Dillon and Crowley (2008) study was insensitive to the products from R 7.5a and b, the shorter timescale experiments conducted in a flash photolysis cell were not subject to heterogeneous uptake of radicals onto wall surfaces or potential interferences from RO_2 chemistry on longer timescales (> 5 ms), giving more robust results. Studies by Hasson et al. (2004) and Jenkin et al. (2007) inferred the OH channel through detection of CH_3OOH, from the reaction of HO_2 with CH_3O_2 (produced in the decomposition of $CH_3C(O)O$ (R 7.17) from reaction R 7.5c), and C_6H_5OH, from the OH initiated oxidation of a benzene scavenger. The slight underestimation of $\alpha_{R\ 7.5c}$ compared to the results from direct OH detection could be due to assumptions and estimations made in the complex chemical model used to predict the R 7.5c branching ratio. Although, it should be noted that the $\alpha_{R\ 7.5c}$ reported here were within the uncertainty of both the Hasson et al. (2004) and Jenkin et al. (2007) investigations.

Previous measurements of $k_{R\ 7.5}$ by Moortgat et al. (1989), Crawford et al. (1999), Tomas et al. (2001) and Le Crâne et al. (2006) were completed using the measurements of peroxy radicals by UV absorption spectroscopy. The convoluted UV signal was fit using predetermined absorption cross-sections and a numerical model simulation, which were likely to add uncertainty as no radical recycling channel was considered. Re-evaluation of the data reported by Tomas et al. (2001) and Le Crâne et al. (2006) by Jenkin et al. (2007) suggested this to be the case. The recent determination of $k_{R\ 7.5}$ by Dillon and Crowley (2008) relied on the more sensitive and specific LIF detection of OH, removing the need for UV action spectra. However, the calibration of the LIF setup, calculation of peroxy radical concentrations and chemical modelling of the system all relied on the determination of $[Cl]_0$ through a Joule meter reading of laser fluence, resulting in the ±30 % uncertainty in $k_{R\ 7.5}$ quoted by the authors.

The ratio of the R 7.5a and R 7.5b rates (= k_a / k_b**)** has been estimated at ~3 across the majority of studies, back to the first investigation of the reaction by Niki et al. (1985) which was originally insensitive to the R 7.5c channel. The high measurement of $k_{R\ 7.5a}$ by Crawford et al. (1999) was corrected for the $CH_3C(O)OOH$ absorption cross-section by Orlando et al. (2000), calculating k_a / k_b = 2.6, in line with other reported values. The preservation of this ratio in the work presented here helps substantiate a higher rate

constant for R 7.5c, leading to an overall increased $k_{R\ 7.5}$ compared to the IUPAC recommendation.

7.5 Conclusions, atmospheric implications and further work

The experiments presented here were successful in directly measuring yields from all three branching pathways of the reaction of HO_2 with $CH_3C(O)O_2$ using FAGE coupled to the HIRAC chamber. The reported yields for R 7.5 were optimised using a higher rate constant ($k_{R\ 7.5}$ = 1.76 × 10^{-11} molecule^{-1} cm^3 s^{-1}) than the current IUPAC recommended rate coefficient with $\alpha_{R\ 7.5a}$ = 0.35 ± 0.03, $\alpha_{R\ 7.5b}$ = 0.12 ± 0.02 and $\alpha_{R\ 7.5_c}$ = 0.54 ± 0.09. Considering the experimental uncertainty in the previously reported determinations, the overall rate constant was within the quoted uncertainty in the literature (section 7.4).

The implications of OH recycling for a host of carbonyl-containing RO_2 radicals is important in atmospheric systems where RO_2 radical reactions dominate over reaction with NO. Work has been conducted into the modelling shortfall in OH compared to field measurements in highly forested areas (Stone et al., 2012), and while the OH yield from these types of reactions is significant, it does not account for the total discrepancy (> 3 - 4). Further study into a series of different carbonyl-containing RO_2, pertinent to isoprene oxidation, have also recently been published confirming the trend (Hasson et al., 2012). This reaction could also play an important role in OH recycling in the upper troposphere, however to date no temperature dependent studies into the OH yield from substituted RO_2 + HO_2 radical reactions exist.

The results presented here are part of an on-going study into the reaction of HO_2 with $CH_3C(O)O_2$. The sensitivity to the determination of yields from R 7.5 to the uncertainties in the secondary RO_2 chemistry around the target reaction, particularly in the reaction of HO_2 with HCHO, have been investigated using a comprehensive chemical model. However, direct measurements of OH and HCOOH from Cl_2/CH_3OH and Cl_2/HCHO mixtures in HIRAC are planned to help constrain the branching ratios of these RO_2 reactions, the only study of which has been completed by Jenkin et al.

(2007). Further investigation into the pressure dependence of the title reaction is also planned in HIRAC, to help validate the results observed by Dillon and Crowley (2008). A more in depth study of the uncertainties in the fitted rate constants is also required to assess the impact of poorly described rate constants in the comprehensive model on the predicted yields. This work is on-going using the Bootstrapping method in Kintecus (section 7.3.2.1), however the process is computer-time intensive and was not ready for this publication. To date, no temperature dependent yields for this reaction have been reported and work in this direction would help determine the importance of this reaction at altitudes across the troposphere or even in different parts of the boundary layer and aid the development of reaction databases, such as the MCM, used in the complex modelling of our atmosphere.

7.6 References

Atkinson, R., D. L. Baulch, R. A. Cox, J. N. Crowley, R. F. Hampson, R. G. Hynes, M. E. Jenkin, M. J. Rossi and J. Troe (2004). "Evaluated kinetic and photochemical data for atmospheric chemistry: Volume I - gas phase reactions of O-x, HOx, NOx and SOx species." Atmospheric Chemistry and Physics **4**: 1461-1738.

Atkinson, R., D. L. Baulch, R. A. Cox, J. N. Crowley, R. F. Hampson, R. G. Hynes, M. E. Jenkin, M. J. Rossi, J. Troe and T. J. Wallington (2008). "Evaluated kinetic and photochemical data for atmospheric chemistry: Volume IV gas phase reactions of organic halogen species." Atmos. Chem. Phys. **8**(15): 4141-4496.

Barnes, I., K. H. Becker, E. H. Fink, A. Reimer, F. Zabel and H. Niki (1985). "FTIR spectroscopic study of the gas-phase reaction of HO_2 with H_2CO." Chemical Physics Letters **115**(1): 1-8.

Crawford, M. A., T. J. Wallington, J. J. Szente, M. M. Maricq and J. S. Francisco (1999). "Kinetics and mechanism of the acetylperoxy plus HO_2 reaction." Journal of Physical Chemistry A **103**(3): 365-378.

Dillon, T. J. and J. N. Crowley (2008). "Direct detection of OH formation in the reactions of HO_2 with $CH_3C(O)O_2$ and other substituted peroxy radicals." Atmospheric Chemistry and Physics **8**: 4877-4889.

EUROCHAMP. "EUROCHAMP." from http://www.eurochamp.org/.

Fuchs, H., B. Bohn, A. Hofzumahaus, F. Holland, K. D. Lu, S. Nehr, F. Rohrer and A. Wahner (2011). "Detection of HO_2 by laser-induced fluorescence: calibration and interferences from RO_2 radicals." Atmospheric Measurement Techniques **4**(6): 1209-1225.

Hasson, A. S., K. T. Kuwata, M. C. Arroyo and E. B. Petersen (2005). "Theoretical studies of the reaction of hydroperoxy radicals (HO_2) with ethyl peroxy ($CH_3CH_2O_2$), acetyl peroxy ($CH_3C(O)O_2$) and acetonyl peroxy ($CH_3C(O)CH_2O_2$) radicals." Journal of Photochemistry and Photobiology A-Chemistry **176**(1-3): 218-230.

Hasson, A. S., G. S. Tyndall and J. J. Orlando (2004). "A product yield study of the reaction of HO_2 radicals with ethyl peroxy, acetyl peroxy and acetonyl peroxy radicals." Journal of Physical Chemistry A **108**: 5979-5989.

Hasson, A. S., G. S. Tyndall, J. J. Orlando, S. Singh, S. Q. Hernandez, S. Campbell and Y. Ibarra (2012). "Branching Ratios for the Reaction of Selected Carbonyl-Containing Peroxy Radicals with Hydroperoxy Radicals." Journal of Physical Chemistry A **116**(24): 6264-6281.

Heard, D. E. and M. J. Pilling (2003). "Measurement of OH and HO_2 in the Troposphere." Chemical Reviews **103**: 5163-5198.

Hofzumahaus, A., F. Rohrer, K. D. Lu, B. Bohn, T. Brauers, C. C. Chang, H. Fuchs, F. Holland, K. Kita, Y. Kondo, X. Li, S. R. Lou, M. Shao, L. M. Zeng, A. Wahner

and Y. H. Zhang (2009). "Amplified Trace Gas Removal in the Troposphere." Science **324**(5935): 1702-1704.

Horie, O. and G. K. Moortgat (1992). "Reactions of $CH_3C(O)O_2$ Radicals with CH_3O_2 and HO_2 between 263 and 333 K – a Product Study." Journal of the Chemical Society-Faraday Transactions **88**(22): 3305-3312.

Ianni, J. C. (2002). "Kintecus, Windows Version 2.80, www.kintecus.com." from www.kintecus.com.

IUPAC. (2002). "IUPAC Subcommittee on Gas Kinetic Data Evaluation – Data Sheet HOx_VOC58." from http://www.iupac-kinetic.ch.cam.ac.uk/datasheets/pdf/HOx_VOC58_HO2_HCHO.pdf.

IUPAC. (2005). "IUPAC Subcommittee on Gas Kinetic Data Evaluation – Data Sheet HOx_VOC59." from http://www.iupac-kinetic.ch.cam.ac.uk/datasheets/pdf/HOx_VOC59_HOCH2OO.pdf.

IUPAC (2006). Gas Kinetics Data Evaluation, IUPAC.

IUPAC. (2007). "Evaluated Kinetic Data." from www.iupac-kinetic.ch.cam.ac.uk.

Jenkin, M. E., M. D. Hurley and T. J. Wallington (2007). "Investigation of the radical product channel of the $CH_3C(O)O_2$+HO_2 reaction in the gas phase." Physical Chemistry Chemical Physics **9**(24): 3149-3162.

Kwok, E. S. C. and R. Atkinson (1995). "Estimation of hydroxyl radical reaction rate constants for gas-phase organiccompounds using a structure-reactivity relationship - an update." Atmospheric Environment **29**(14): 1685-1695.

Le Crâne, J. P., M. T. Rayez, J. C. Rayez and E. Villenave (2006). "A reinvestigation of the kinetics and the mechanism of the $CH_3C(O)O_2$ + HO_2 reaction using both experimental and theoretical approaches." Physical Chemistry Chemical Physics **8**(18): 2163-2171.

Lee, M. H., B. G. Heikes and D. W. O'Sullivan (2000). "Hydrogen peroxide and organic hydroperoxide in the troposphere: a review." Atmospheric Environment **34**(21): 3475-3494.

Lelieveld, J., T. M. Butler, J. N. Crowley, T. J. Dillon, H. Fischer, L. Ganzeveld, H. Harder, M. G. Lawrence, M. Martinez, D. Taraborrelli and J. Williams (2008). "Atmospheric oxidation capacity sustained by a tropical forest." Nature **452**(7188): 737-740.

Lightfoot, P. D., R. A. Cox, J. N. Crowley, M. Destriau, G. D. Hayman, M. E. Jenkin, G. K. Moortgat and F. Zabel (1992). "Organic Peroxy-Radicals - Kinetics, Spectroscopy and Tropospheric Chemistry." Atmospheric Environment Part A-General Topics **26**(10): 1805-1961.

Lou, S., F. Holland, F. Rohrer, K. Lu, B. Bohn, T. Brauers, C. C. Chang, H. Fuchs, R. HÃ¤seler, K. Kita, Y. Kondo, X. Li, M. Shao, L. Zeng, A. Wahner, Y. Zhang, W. Wang and A. Hofzumahaus (2009). "Atmospheric OH reactivities in the Pearl River Delta â€“ China in summer 2006: measurement and model results." Atmos. Chem. Phys. Discuss. **9**(4): 17035-17072.

Mao, J., X. Ren, L. Zhang, D. M. V. Duin, R. C. Cohen, J.-H. Park, A. H. Goldstein, F. Paulot, M. R. Beaver, J. D. Crounse, P. O. Wennberg, J. P. DiGangi, S. B. Henry, F. N. Keutsch, C. Park, G. W. Schade, G. M. Wolfe, J. A. Thornton and W. H. Brune (2012). "Insights into hydroxyl measurements and atmospheric oxidation in a California forest." Atmospheric Chemistry and Physics **12**: 8009-8020.

Maricq, M. M. and J. J. Szente (2000). "Kinetics of the Reaction between Acetylperoxy and Ethylperoxy Radicals." Journal of Physical Chemistry A **104**(31): 7239-7245.

MCM. (2014). "Master Chemical Mechanism Version 3.2 (http://mcm.leeds.ac.uk/MCM)."

Moortgat, G. K., B. Veyret and R. Lesclaux (1989). "Kinetics of the reaction of HO_2 with $CH_3C(O)O_2$ in the temperature range 253–368 K." Chemical Physics Letters **160**(4): 443-447.

Niki, H., P. D. Maker, C. M. Savage and L. P. Breitenbach (1985). "FTIR study of the kinetics and mechanism for chlorine-atom-initiated reactions of acetaldehyde." Journal of Physical Chemistry **89**: 588-591.

Orlando, J. J. and G. S. Tyndall (2012). "Laboratory studies of organic peroxy radical chemistry: an overview with emphasis on recent issues of atmospheric significance." Chemical Society Reviews **41**(19): 6294-6317.

Orlando, J. J., G. S. Tyndall, L. Vereecken and J. Peeters (2000). "The atmospheric chemistry of the acetonoxy radical." Journal of Physical Chemistry A **104**(49): 11578-11588.

Paulot, R., J. D. Crounse, H. G. Kjaergaard, A. Kurten, J. M. St. Clair, J. H. Seinfeld and P. O. Wennberg (2009). "Unexpected epoxide formation in the gas-phase photooxidation of isoprene." Science (Washington, D. C., 1883-) **325**: 730 - 733.

Peeters, J. and J. F. Muller (2010). "HOx radical regeneration in isoprene oxidation via peroxy radical isomerisations. II: experimental evidence and global impact." Physical Chemistry Chemical Physics **12**(42): 14227-14235.

Peeters, J., T. L. Nguyen and L. Vereecken (2009). "HOx radical regeneration in the oxidation of isoprene." Physical Chemistry Chemical Physics **11**: 5935-5939.

Phillips, G. J., N. Pouvesle, J. Thieser, G. Schuster, R. Axinte, H. Fischer, J. Williams, J. Lelieveld and J. N. Crowley (2013). "Peroxyacetyl nitrate (PAN) and peroxyacetic acid (PAA) measurements by iodide chemical ionisation mass spectrometry: first analysis of results in the boreal forest and implications for the measurement of PAN fluxes." Atmospheric Chemistry and Physics **13**: 1129-1139.

Press, W., S. Teukolsky, W. Vetterling and B. Flannery (1992). Numerical recipes in C (2nd ed.): the art of scientific computing, Cambridge University Press.

Pugh, T. A. M., A. R. MacKenzie, C. N. Hewitt, B. Langford, P. M. Edwards, K. L. Furneaux, D. E. Heard, J. R. Hopkins, C. E. Jones, A. Karunaharan, J. Lee, G. Mills, P. Misztal, S. Moller, P. S. Monks and L. K. Whalley (2010). "Simulating atmospheric composition over a South-East Asian tropical rainforest: performance of a chemistry box model." Atmospheric Chemistry and Physics **10**(1): 279-298.

Sander, S. P., R. R. Friedl, J. P. D. Abbatt, J. Barker, D. M. Golden, C. E. Kolb, M. J. Kurylo, G. K. Moortgat, P. H. Wine, R. E. Huie and V. L. Orkin (2011). Chemical kinetics and photochemical data for use in atmospheric studies - Evaluation 17. Pasadena CA, Jet Propulsion Laboratory. **17**.

Saunders, S., M. Jenkin, R. Derwent and M. Pilling (2003). "Protocol for the development of the Master Chemical Mechanism, MCM v3 (Part A): tropospheric degradation of non-aromatic volatile organic compounds." Atmos. Chem. Phys. **3**: 161–180.

Seakins, P. W., J. J. Orlando and G. S. Tyndall (2004). "The Rate Coefficients and Fraction of Vibrationally Excited HCl from the Reactions of Chlorine Atoms with Methanol, Ethanol, Acetaldehyde and Formaldehyde." Physical Chemistry Chemical Physicis **6**: 2224-2229.

Spittler, M., I. Barnes, K. H. Becker and T. J. Wallington (2000). "Product Study of the $C_2H_5O_2$ + HO_2 reaction in 760 Torr of air at 284-312 K." Chemical Physics Letters **321**(1-2): 57-61.

Stone, D., L. K. Whalley and D. E. Heard (2012). "Tropospheric OH and HO2 radicals: field measurements and model comparisons." Chem Soc Rev **41**(19): 6348-6404.

Taraborrelli, D., M. G. Lawrence, T. M. Butler, R. Sander and J. Lelieveld (2009). "Mainz Isoprene Mechanism 2 (MIM2): an isoprene oxidation mechanism for regional and global atmospheric modelling." Atmospheric Chemistry and Physics **9**(8): 2751-2777.

Taraborrelli, D., M. G. Lawrence, J. N. Crowley, T. J. Dillon, S. Gromov, C. B. M. Gross, L. Vereecken and J. Lelieveld (2012). "Hydroxyl radical buffered by isoprene oxidation over tropical forests." Nature Geoscience **5**(3): 190-193.

Tomas, A., E. Villenave and R. Lesclaux (2001). "Reactions of the HO_2 Radical with CH_3CHO and $CH_3C(O)O_2$ in the Gas Phase." Journal of Physical Chemistry A **105**: 3505-3514.

Tuazon, E. C. and R. Atkinson (1989). "A Product Study of the Gas-Phase Reaction of Methyl Vinyl Ketone with the OH Radical in the Presence of NOx." International Journal of Chemical Kinetics **21**(12): 1141-1152.

Tyndall, G. S., R. A. Cox, C. Granier, R. Lesclaux, G. K. Moortgat, M. J. Pilling, A. R. Ravishankara and T. J. Wallington (2001). "Atmospheric chemistry of small organic peroxy radicals." Journal of Geophysical Research-Atmospheres **106**(D11): 12157-12182.

Veyret, B., R. Lesclaux, M. T. Rayez, J. C. Rayez, R. A. Cox and G. K. Moortgat (1989). "Kinetics and mechanism of the photo-oxidation of formaldehyde. 1. Flash photolysis study." Journal of Physical Chemistry **93**(6): 2368-2374.

Wallington, T. J., C. A. Gierczak, J. C. Ball and S. M. Japar (1989). "Fourier Transform Infrared Study of the Self Reaction of $C_2H_5O_2$ Radicals in Air at 295 K." International Journal of Chemical Kinetics **21**(11): 1077-1089.

Wayne, R. P. (1991). Chemistry of atmospheres : an introduction to the chemistry of the atmospheres of Earth, the planets, and their satellites. Oxford, Clarendon.

Whalley, L. K., M. A. Blitz, M. Desservettaz, P. W. Seakins and D. E. Heard (2013). "Reporting the sensitivity of Laser Induced Fluorescence instruments used for HO_2 detection to an interference from RO_2 radicals and introducing a novel approach that enables HO_2 and certain RO_2 types to be selectively measured." Atmospheric Measurement Techniques **6**: 3425-3440.

Whalley, L. K., P. M. Edwards, K. L. Furneaux, A. Goddard, T. Ingham, M. J. Evans, D. Stone, J. R. Hopkins, C. E. Jones, A. Karunaharan, J. D. Lee, A. C. Lewis, P. S. Monks, S. J. Moller and D. E. Heard (2011). "Quantifying the magnitude of a missing hydroxyl radical source in a tropical rainforest." Atmospheric Chemistry and Physics **11**(14): 7223-7233.

Wolfe, G. M., J. D. Crounse, J. D. Parrish, J. M. S. Clair, M. R. Beaver, F. Paulot, T. P. Yoon, P. O. Wennberg and F. N. Keutsch (2012). "Photolysis, OH reactivity and ozone reactivity of a proxy for isoprene-derived hydroperoxyenals (HPALDs)." Physical Chemistry Chemical Physics **14**(20): 7276-7286.